University of Iowa
Iowa Research Online

Theses and Dissertations

Summer 2015

Modeling stream discharge and nitrate loading in the Iowa-Cedar River basin under climate and land use change

Lance Olot Le
University of Iowa

Recommended Citation
Le, Lance Olot. "Modeling stream discharge and nitrate loading in the Iowa-Cedar River basin under climate and land use change." PhD (Doctor of Philosophy) thesis, University of Iowa, 2015.
https://doi.org/10.17077/etd.vjr7kly3

MODELING STREAM DISCHARGE AND

NITRATE LOADING IN THE IOWA-CEDAR RIVER BASIN

UNDER CLIMATE AND LAND USE CHANGE

by

Lance Olot Le

A thesis submitted in partial fulfillment of
the requirements for the Doctor of Philosophy
degree in Civil and Environmental Engineering
in the Graduate College of The University of Iowa

August 2015

Thesis Supervisor: Professor Jerald L. Schnoor

Graduate College
The University of Iowa
Iowa City, Iowa

CERTIFICATE OF APPROVAL

_____

PH.D. THESIS

_____

This is to certify that the Ph.D. thesis of

Lance Olot Le

has been approved by the Examining Committee
for the thesis requirement for the Doctor of Philosophy
degree in Civil and Environmental Engineering at the August
2015 graduation.

Thesis Committee:_____
                    Jerald L. Schnoor, Thesis Supervisor

                    _____
                    David Bennett

                    _____
                    Craig L. Just

                    _____
                    Marian Muste

                    _____
                    Richard L. Valentine

ABSTRACT

A Soil and Water Assessment Tool (SWAT) model was developed for the Iowa-Cedar River Basin (ICRB), a 32,660 km^2 watershed dominated by agricultural land cover (~70%) to simulate hydrology and water quality for the prediction of stream discharge, nitrate loads, and nitrate concentration under climate and land use change scenarios. Iowa exports as much as 20% of the nitrogen entering the Gulf of Mexico at the mouth of the Mississippi, contributing to Gulf hypoxia as well as local threats to water quality in the ICRB. The model utilized a combined autocalibration and sensitivity procedure incorporating Sequential Uncertainty Fitting (SUFI) and generalized additive models. This procedure resulted in Nash-Sutcliffe Efficiency (NSE) goodness-of-fit statistics that met literature guidelines for monthly mean stream discharge (NSE$\geq$0.60) and daily nitrate load (NSE$\geq$0.50). Artificial neural networks coupled with SWAT stream discharges aided in the simulation of daily mean nitrate concentrations that met the literature guideline (NSE$\geq$0.50).

The North American Regional Climate Change Assessment Program (NARCCAP) provided an ensemble of 11 climate change scenarios. NARCCAP is a multi-institutional effort to simulate climate change at the mesoscale by downscaling global circulation models (GCM) with regional climate models (RCM). The resulting GCM-RCM produced synthetic precipitation and temperature time-series that drove the SWAT simulations and scenarios. The land use scenarios were a collaboration with the U.S. Army Corps of Engineers, using a rule-based GIS method to generate scenarios that (1) maximized agricultural productivity, (2) improved water quality and reduced flooding, and (3) enhanced local biodiversity. The SWAT simulations and ensemble climate change scenarios resulted in a warmer and wetter climate with greater and more extreme discharge in all seasons except summer where the models indicate a somewhat higher probability of extreme low flows (p-value<0.05). The land use scenarios for SWAT showed that nitrate load and discharge positively and linearly scale with percent of agricultural land area (p-value<0.05).

PUBLIC ABSTRACT

Climate change manifests not merely as global warming; the latter term only starts to describe the impact of human activities on the planet. Extreme floods and droughts are another facet of climate change that are becoming accepted in the scientific discourse as not just independent events, but part of a growing trend. Naturally, different locales will weather different effects under climate change and how those effects emerge depend on how humans shape and use their land. Iowa has a fully developed agrarian economy infamous for releasing large amounts of nutrients into the waters of the United States. Nitrate, a major component and end-product of fertilizer application, is a threat to local water supplies, increasing the cost of drinking water treatment as the source water becomes more contaminated. Nitrate exiting Iowa eventually enters the Gulf of Mexico, accelerating algal blooms that subsequently suffocate the coastal waters deprived of oxygen. This research projects the future by building a computational model capable of simulating water quantity and water quality on the order of decades through the use of the Soil and Water Assessment Tool (SWAT). The model developed succeeded at simulating the past, a test that all models must pass. Applying scenarios created by leading institutions that study climate and land use change, the model foresees the possibility of greater flooding events and nitrate loads in a wetter and warmer future. No prediction is so exact to give the time and place of such events, but what SWAT can give is a sense of the average. An increase in the average implies an increase in the larger values of greater discharge and nitrate runoff.

TABLE OF CONTENTS

LIST OF TABLES

LIST OF FIGURES

xi

xiii

CHAPTER 1: INTRODUCTION AND RESEARCH
OBJECTIVES

<u>Introduction</u>

The looming impacts of a changing climate may already be underway as the public and policymakers focus with concern on what appear to be more frequent extreme weather events in the form of flood intensities and drought durations (IPCC, 2013). The midwestern United States has suffered crop losses in the very recent past from the 2012 drought (USDA, 2014). In addition to drought more losses may be compounded from flood damage (Rosenzweig et al., 2002). While the flood events were local or regional, the downstream effects on water quality were apparent with the well-known Gulf of Mexico hypoxia catalyzed by runoff from nitrogen fertilizer and agricultural land use (Goolsby, 2000). Eastern Iowan watersheds contributed as much as 20% of the nitrogen discharge from the Mississippi-Atchafalaya River Basin (Goolsby et al., 1999).

During intense rainfall events like the historic June 2008 Eastern Iowa flood, nitrogen loading from flood events accounted for 22-46% of annual nitrogen flux for agricultural basins (Hubbard et al., 2011). Yet to consider these episodic events as indicators for climate change could be a scientifically dubious practice (Seneviratne, 2012). The science of climate change is not so precise nor computation so cheap that one could predict a particular extreme event over another in any specific area (Katz, 2010). Instead one must rely on many models, general global statistical trends, and potential scenarios to arrive at a likely estimate (Tebaldi & Knutti, 2007).

The National American Regional Climate Change Assessment Program (NARCCAP) provided eleven Regional Climate Models embedded in General Circulation Models (RCM-GCM) combinations (Mearns et al., 2007). The combinations simulated the Intergovernmental Panel on Climate Change (IPCC) A2 emission scenario that depicts a heterogeneous world where regional economic interests predominate along with continuously increasing population. At the half century mark, the A2 scenario was also the midpoint of the different IPCC emission

1

scenarios (Figure 1-1). NARCCAP modeled a historical period (1971-1998) and a projected period (2041-2068) for calibration and comparison purposes. The same time-frames were utilized for hydrologic and water quality modeling in this dissertation.

The climate models by design simulated multi-decadal time-scales and thus the watershed responses were modeled accordingly. For large watersheds the computational requirements for a fine-resolution and completely physically-based modeling were vast, and individual stakeholders in the watershed lacked the resources to meet these requirements. The alternative route was to employ a less computationally intense watershed model that can simulate large spatial and temporal scales. The Soil and Water Assessment Tool or SWAT was one option (Douglas-Mankin, 2010). Another option existed in coupling physically based models with data-driven models that have no explicit form prior to being fed data. Examples of these data-driven models were regression trees, fuzzy logic systems, genetic algorithms, and artificial neural networks (Solomatine & Ostfeld, 2008). The data-driven model chosen was the artificial neural network due to the wide literature supporting its usage in hydrological research (Hsu et al., 1995).

The SWAT model was built on several models of crop growth (EPIC), rainfall-runoff hydrology (CREAMS), and water quality (QUAL2E); the intention of this consolidation was to simulate specifically agricultural watershed dynamics in regards to both water yields and constituent loading of nutrients, sediment, and pesticides (Gassman et al., 2007). The current version of SWAT can also incorporate land use change. Land use change represented the human system component responding to climate change scenarios. The use of SWAT in combination with climate model data generated from NARCCAP was advantageous in sketching out possible future scenarios where both climate and land use have changed.

<u>Research Questions</u>

(1)   Is SWAT an appropriate watershed model to simulate large spatial and temporal scales in regards to stream discharge, nitrate loading, and nitrate concentrations?

2

(2) If SWAT is unable to simulate acceptably any of the observed quantities of interest in (1), can an alternative and equally or less computationally intensive data-driven method compensate for SWAT?

(3) When applied to SWAT does the ensemble of climate models show agreement with respect to simulating the historical and projected seasonal precipitation, stream discharge, evapotranspiration, and nitrate loads in eastern Iowa?

(4) What is the influence of modifying agricultural land area on stream discharge and nitrate loads in the NARCCAP projected time-frame in 2041-2048?

<u>Hypotheses</u>

H1a   SWAT simulates well the multi-decadal monthly mean stream discharge with goodness-of-fit statistics that meet or exceed the minimum-acceptable criteria reported in the model literature.

H1b   SWAT simulates daily nitrate loadings well with goodness-of-fit statistics that meet or exceed the minimum reported in the model literature.

H1c   SWAT simulates daily nitrate concentrations poorly due to the model structure being only semi-physically based with different granularities for different model components. SWAT is unable to simulate spikes in nitrate concentration exceeding the EPA drinking water limit of 10 mg/L nor do the goodness of fit statistics meet the guidelines set in the model literature.

3

H2   Artificial neural networks (ANNs) can compensate for SWAT's poor performance in simulating nitrate concentrations on large spatial scales by weakly coupling ANNs with SWAT's stream discharge outputs.

H3a   The ensemble of NARCCAP climate models and SWAT simulations show agreement in modeling precipitation, discharge, evapotranspiration and nitrate loads in the historical (1971-1998) when compared to historical precipitations and SWAT simulated discharge, evapotranspiration, and nitrate load driven by the observed climate.

H3b   The SWAT simulations driven by NARCCAP's projected period are significantly different (α=0.05) from SWAT simulations driven by NARCCAP's historical period.

H3c   The ensemble of NARCCAP climate models and SWAT simulations show agreement in modeling precipitation, discharge, evapotranspiration and nitrate loads in the projected (2041-2068) time frame.

H4   Land use change incorporated into SWAT simulations with NARCCAP input data show a linear trend in the annual mean stream discharge and nitrate loads with increasing agricultural land area in the historical period.

Organization

This dissertation is organized into eight chapters to address the research objectives and hypotheses with the first chapter introducing and providing organizing context to the dissertation. Chapter 2 contains a description and history of the study area in the Iowa-Cedar River Basin, a comprehensive description of the SWAT model and the underlying theory, and a general literature review on hydrological modeling related to the basin or areas similar or

4

geographically near. More in-depth literature review related to the artificial neural networks, climate change models, and land use change scenarios can be found in their respective chapters.

Chapter 3 details the development of a SWAT model for the Iowa-Cedar River Basin with description of input data and discretization choices for the model development. Chapter 4 describes a novel approach in model calibration by using a combined sensitivity and autocalibration procedure derived from the SWAT-CUP software. The results of the sensitivity analysis and autocalibration are included in this chapter for the monthly mean discharge at eight USGS stream gauges from years 1973-2012 and the mean daily nitrate loads and concentrations at two USGS gauges for the years 2008-2013, excluding all or parts of January, February, and March where the nitrate sensors are inactive.

Chapter 5 describes the artificial neural networks in detail and reviews literature of its application in and outside the field of watershed modeling. The artificial neural network method had two applications in this dissertation. The first purpose was filling in data gaps for the daily nitrate concentrations so that monthly loads could be calculated and that the autocalibration procedure for nitrogen may have more data with which to work. The second purpose was exploratory research into combining SWAT's strength in hydrology with neural networks to compensate for the poor nitrate simulations found in the results of Chapter 4. Chapter 6 describes the application of the NARCCAP climate models to drive SWAT simulations for the historical 1971-1998 and projected 2041-2068 periods. This chapter also includes a literature review of climate change models in hydrological research and briefly touch on the mathematics and physics of the models. A more detailed evaluation of the NARCCAP climate models is beyond the scope of this dissertation.

Chapter 7 details the land use change scenarios and the methodology to develop the scenarios. United States Army Corps of Engineers (USACE) developed the raw input data for the scenarios. This chapter describes the procedure to transform the raw data into a form usable by SWAT and shows the results from the simulations as well as the climate change projections for each land use scenario. Finally, Chapter 8 summarizes the results from all the simulations and

5

discusses the possible interpretations together with potential future research. Chapter 8 also attempts to re-organize and parse this dissertation into a series of peer-review journal articles that have the submission potential. The Appendix section contains raw data or charts in case the raw data were too numerous to be included in the main body.
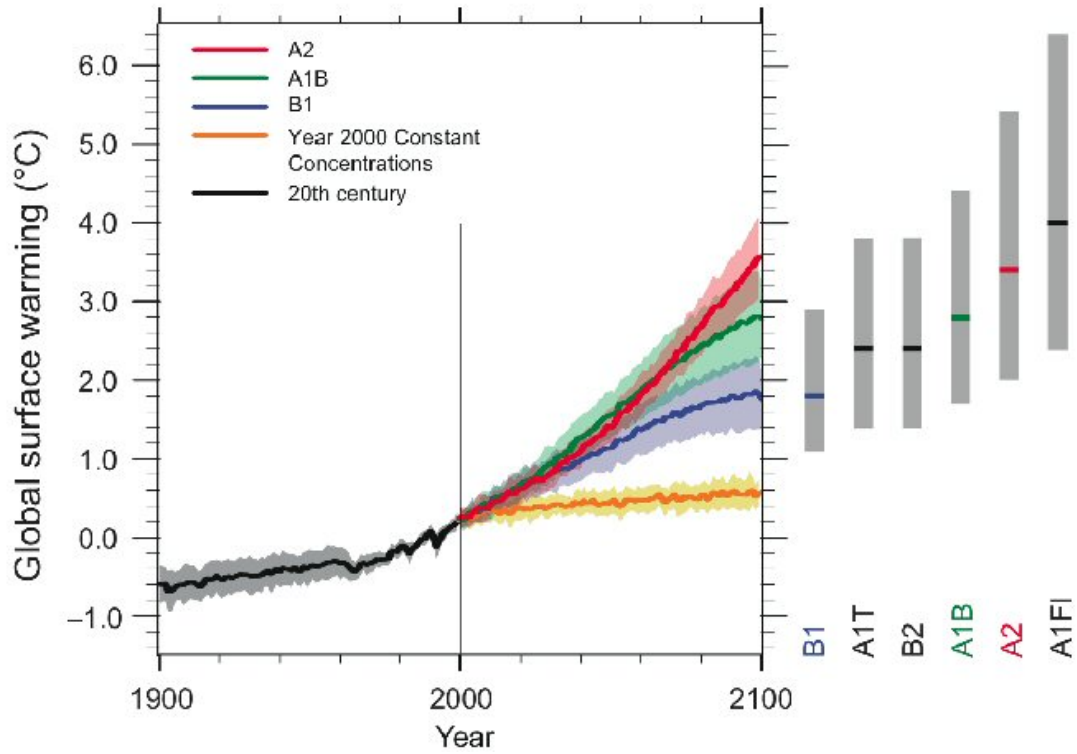
Figure 1-1   IPCC emission scenarios with potential surface warming. Scenario A2 of which the GCM-RCM combinations utilize was the midpoint warming scenario at half century which is the projected period of simulation of 2041-2068 (Nakicenovic & Swart, 2000)

CHAPTER 2: SITE DESCRIPTION AND MODEL
LITERATURE REVIEW

<u>Site Description</u>

The Iowa-Cedar River Basin (ICRB) is a 32,660 km^2 watershed dominated by corn and
soybean row crop agriculture. The watershed starts at an elevation of 441m above sea level on
the border between north-central Iowa and south-central Minnesota and drains into the
Mississippi River at 165m above sea level. The Iowa and Cedar Rivers are two major river
systems that form independent basins until their confluence in Columbus Junction, IA. The
longitudinal extent of the ICRB has the watershed occupying two major climate zones: the cool
humid continental in the north and warm humid continental in the south. Annual mean
precipitation for the basin from 1970-2010 was approximately 895 mm. The runoff or discharge
proportion of the atmospheric water input was approximately 32 percent or 286 mm for the same
period.

Opened to non-Native American settlement in 1833 from the Black Hawk Purchase, the
history of agriculture in the ICRB and Iowa in general (Throne, 1949) started from subsistence
with crops of wheat, corn, and oats, barley or flax and perhaps a few hogs and pack animals.
Abundant forests east of the Mississippi river provided timber and construction materials for the
expansions of these settlements. The native Iowa landscape was tall-grass prairie, and forests
were clustered mostly in riparian zones, leading to the use of sod for prairie houses during the
early subsistence era (Bogue, 1963). Because of the relatively large temperature extremes
between the seasons, the population remained small and the farms likewise. The agricultural
landscape at this time had minimal impacts on the environment and local ecology (Foster et al.,
2003).

The introduction of farm machinery reduced the difficulty of tilling the fertile, but deeply
vegetated prairie soils, expanding the size of individual farms. Wheat as a dominant crop gave
way to corn as the harsh Iowa winters killed fall wheat and the hot summers burned spring wheat

8

(Ross, 1951). The expansion of railroads into Iowa and transcontinental networks such as the Pacific Railroad helped to settle western Iowa increased population growth (Cole, 1921). The tributaries of the Upper Mississippi River Basin (UMRB) allowed inexpensive shipping downstream, and so the links from farm to rail to river steamboats provided a transportation infrastructure to transition the agricultural landscape to that of expansive industrial agriculture (Page & Walker, 1991).

The twentieth century advance in the Haber-Bosch process (ammonium production from the nitrogen in air and hydrogen, a natural gas byproduct) further bolstered industrial agriculture as large-scale production increased in the proceeding decades. In less than two centuries the native Iowan prairie grasslands disappeared into marginal remnants and small preserves, replaced by agriculture with corn as the primary cash crop with soybean rotations to maintain soil productivity (Karlen et al., 1991). As of 2012 the land cover distribution in the ICRB was approximately 42% corn, 26% soybeans, 15% rangeland, 8% urban or developed, 2% wetlands, 1% open water, and the remaining 6% split amongst other crops (USDA, 2012).

Due to extensive fertilizer applications throughout the basin in recent years, nitrogen load from eastern Iowa watersheds had been approximately 74.2×10^3 metric tons per year, and 77% of that load was in the form of nitrate (Goolsby et al., 2001). The watershed contained nineteen US Geological Survey (USGS) gage stations that measure discharge and four of those stations collected 15 minute, high-frequency measurements of combined nitrate plus nitrite concentrations. Eight gage stations were used for model calibration for stream discharge, and two stations were used for calibrating nitrogen concentrations and loadings. The discharge stations chosen were spatially representative of the watershed and spanned multiple stream orders, covering small streams such as Old Man's Creek in Iowa City and the larger Cedar and Iowa Rivers.

The high frequency nitrate plus nitrite data from the Cedar Rapids and Wapello stations only covered the years 2009-2013, and the instruments were inactive during the months of December, January, and February and were frequently inactive during other months due to

9

technical problems, resulting in numerous data gaps even in periods of activity. Figure 2-1 shows the geographic extent of the watershed, locations of the USGS gage stations, and locations of the climate stations used in this dissertation for model development. Table 2-1 summarizes the discharge data at the eight stations and Table 2-2 and Table 2-3 summarize the nitrogen concentration and load data at Cedar Rapids and Wapello, respectively.

<div align="center">SWAT Description</div>

The Soil and Water Assessment Tool (SWAT) was a time-continuous distributed hydrologic model that incorporated several modules to simulate the atmospheric, land, subsurface, and in-stream processes for the watershed. SWAT was not a singular model, but a package of several that consolidated around the Simulator for Water Sources in Rural Basins (SWRRB), developed by the USDA Agriculture Research Service (ARS) (Williams et al., 1985) The other models or modules were the CREAMS (Chemicals, Runoff, and Erosion from Agricultural Management Systems) (Knisel, 1980), GLEAMS (Groundwater Loading Effects on Agricultural Management Systems) (Leonard et al., 1987), and EPIC (Erosion-Productivity Impact Calculator) (Williams et al., 1984). Because of the agricultural slant of these models, SWAT was the most appropriate choice for simulating the ICRB.

SWAT split its processes into two components: the land or soil phase and the water or in-stream phase. The land phase operated the EPIC crop growth modules and routed surface water into the subsurface through a discretized series of soil layers constituting a soil column. Beneath the column was the groundwater system with the shallow aquifer being the physical system directly simulated. The deep aquifer was an abstraction created through a coefficient that diverts total recharge. Vadose zone hydrology was indirectly simulated by plant uptake of water between the soil surface and shallow aquifer. The outputs of the land phase modules entered the stream network in the water phase. Water bodies such as reservoirs or lakes were optional components, user-defined, and links with the in-stream hydrology and water quality modules. The modules previously mentioned simulated the land component and their outputs entered the

stream phase. The water quality module in SWAT was QUAL2E, a one dimensional model developed by the US EPA (Brown & Barnwell, 1987).

Aside from the whole watershed, SWAT had three levels of computation, each operating differently depending on the user configuration: the subbasin, the reach, and the Hydrologic Response Unit (HRU). A subbasin was a spatially explicit construct that was determined by flow accumulation on a digital elevation map (DEM). The number of subbasins for a watershed was based on user discretion either by specifying a minimum catchment area if automatically delineating the watershed through public domain software such as ArcHydro (Maidment, 2002) or by manual configuration. Each subbasin had one reach or channel running through its lowest elevation. SWAT assumed the dimensions of the reach to be longitudinally uniform in cross-sectional area, side slope, longitudinal slope, and bed roughness. Aside from ponds abstracted as a fraction of a subbasin area, the reach was the water phase's smallest unit of computation, realized as an implicit backward-difference finite difference scheme.

The smallest unit of computation for the land modules was the (HRU). An HRU was a unique combination of land use, slope class, and soil type. Chapter 3 details the development of an HRU and what data can be used to determine an HRU. The user had the option of defining an entire subbasin as an HRU or have more than one HRU in a subbasin. The model lost granularity when computing each subbasin as an HRU, but computation time for simulations greatly decreased. If the user chose to have multiple HRUs, the model gains greater granularity and longer computation times; however, the HRUs are not spatially explicit. The HRUs were abstracted as fractions of a subbasin's area. Thus the input of constituent loads and water into a reach were the area weighted sum of the HRUs' outputs:

Equation 2-1 $$Input_n = \sum_{i=1}^{N_{HRU}} f_{m,n} HRU_{m,n}$$

Input_n was the input into the *n*'th subbasin's reach. *HRU_{m,n}* was an output from the *m*'th HRU in the *n*'th subbasin. *f_{m,n}* was the fraction of the total subbasin area that the *m*'th HRU takes up.

Figure 2-2 shows a set of flow charts for a SWAT model simulation. If a given subbasin contained more than one HRU, then the land subroutine must be completed for each HRU before the loads into the water phase began. Because the HRUs were abstracted as area fractions, SWAT did not route overland flow and constituents between HRUs within a single subbasin. One compromise was to have a large number of small subbasins that are also HRUs, but the computation time would greatly increase.

The following subsections detail the theory and mathematics underlying the SWAT model. Only the equations that pertained to the objectives of this dissertation were explained in detail. The equations and variables were modified from the SWAT Theoretical Documentation (Neitsch et al., 2011) to be more direct and accessible. The major variables related to soil hydrology are listed in Table 2-4, soil nitrogen dynamics variables in Table 2-5, and in-stream nitrogen dynamics variables in Table 2-6. Figure 2-3 shows the water balance for land and water phases and how the two phases interact. Figure 2-4 shows nitrogen dynamics between the various pools, sources, and sinks in both the land and water phase.

Model Theory

Soil Hydrology

The land phase hydrology was based on the soil water balance equation (Arnold et al., 1998):

Equation 2-2
$$SW_t = SW_0 + \sum_{i=1}^{t} \left(P_i - Q_{surf,i} - ET_i - w_{seep,i} - Q^*_{gw,i} - Q^*_{lat,i} \right)$$

In units of mm H_2O and for the *i*'th day, SW_t was the final soil water content, SW_0 the initial soil water content, P_i the precipitation, $Q_{surf,i}$ the surface runoff, ET_i the evapotranspiration, and $w_{seep,i}$ the water percolation exiting the soil bottom. $Q^*_{gw,i}$ was the sum of the ground water processes such as revap and baseflow from the shallow aquifer. $Q^*_{lat,i}$ was the sum of lateral flow from saturated soil layers and flow from tile drains. Additional processes were canopy storage from

vegetation available for evapotranspiration and bypass flow for clay-heavy soils. SWAT offered numerous methods for modeling the processes and the user set the methods. The default methods and settings were used for model development and modified during the calibration phase.

Surface Runoff

Surface run off was calculated with the runoff curve number method initially developed by the Natural Resource Conservation Service (NRCS) (USDA, 1985):

Equation 2-3

$$Q_{surf} = \begin{cases} 0 & P < I_a \\ \dfrac{(P - I_a)^2}{P - I_a - S} & P > I_a \end{cases}$$

I_a was the initial amount of water that includes surface storage, canopy interception, and infiltration before runoff (mm H_2O). S was the maximum soil moisture retention after runoff begins (mm H_2O). I_a and S were determined with the runoff curve number CN:

Equation 2-4

$$S = \frac{1000}{CN} - 10$$

Equation 2-5

$$I_a = 0.2S$$

CN had a range between 30 and 100 where values increase with runoff potential. CN was determined empirically and based on NRCS soil groupings, surface characteristics such as vegetation cover or impervious surface area, and antecedent soil moisture conditions.

Evapotranspiration

The Penman-Monteith equation determined evapotranspiration or ET (mm H_2O) (Monteith, 1965):

Equation 2-6

$$ET = \frac{\Delta(R_n - G) + \rho_a c_p g_a \delta e}{\Delta L_v + L_v \gamma (1 + \frac{g_a}{g_s})}$$

13

R_n was the net irradiance (W·m^{-2}), G the ground heat flux (W·m^{-2}), ρ_a the dry air density (kg·m^{-3}), c_p the specific heat capacity of air (J·kg^{-1}·K^{-1}), g_a the conductivity of air (m·s^{-1}), g_s the conductivity of plant stoma (m·s^{-1}), δe the specific humidity (Pa), L_v the volumetric latent heat of vaporization (2453 MJ·m^{-3} for water), γ the psychometric constants (~66 Pa·K^{-1}) and Δ the rate of change of saturation specific humidity with air temperature (Pa·K^{-1}).

Evaporative demand took into account the soil layer's depth below the surface (z_s):

Equation 2-7
$$ET_j = ET \cdot \frac{z_{s,j}}{z_{s,j} + e^{2.374 - .00713 z_{s,j}}}$$

Because the evaporative demand was different at the lower and upper boundary of the soil layer, the actual evapotranspiration was calculated as:

Equation 2-8
$$ET_{act,j} = ET_{j,l} - ET_{j,u} \cdot esco$$

$ET_{j,l}$ and $ET_{j,u}$ were evaporative demand at the lower and upper boundary of the soil layer and *esco* was the unitless soil evaporation compensation coefficient that varies between 0 and 1.

Soil Water

SWAT simulated water flow in the soil by discretizing the column into layers, and the parameters such as bulk density, porosity, and hydraulic conductivity were based on the soil type of that layer. The soil type followed USDA conventions where the percent of silt, sand, clay determine the properties (Soil Survey Staff, 1993). The soil type yielded two parameters that control soil water storage: the field capacity (*FC*) and the permanent wilting point (*WP*). Both parameters had units as fractions of total soil volume or mm H$_2$O when used to calculate water content. *FC* was soil type-specific and informally defined as the water content held in soil after excess water has drained way and the rate of downward movement has decreased, typically after 2-3 days of rain or irrigation (Israelson & West, 1922). Physically defined, *FC* was the bulk water content retained in the soil at -33 kPa or -3.37 mm of hydraulic head. *WP* was nominally

crop-specific and defined as the water content found when plants growing in the soil wilted and did not recover if their leaves were kept in a humid atmosphere overnight (Veihmeyer & Hendrickson, 1928).

SWAT estimated the *WP* for the *j'*th layer as a function of the clay content (m_c, %) and the bulk density (ρ_b):

Equation 2-9 $$WP_j = 0.40 \frac{m_c \rho_b}{100}$$

The field capacity for the *j'*th layer was determined as the sum of the plant-available water capacity (*AWC*) and WP_i:

Equation 2-10 $$FC_j = WP_j + AWC_j$$

AWC was an input from the user, but had default values based on soil type and land cover. Surface runoff occurred when the water content of the soil exceeds field capacity. SWAT simulated saturated flow directly and assumed water was uniformly distributed within a layer. Unsaturated flow between layers was modeled indirectly by plant water uptake and soil water evaporation due to surface heat or pressure. Water remaining after surface runoff occurred (or not) was available for percolation, lateral flow, or tile flow unless soil temperature was below 0°C and the layer was frozen.

Percolation was calculated for each layer and occurred when saturation was met for one layer and the layer below was not saturated. Water percolation ($w_{perc,j}$, mm H_2O) was a function of *SW*, *FC*, the time step (Δt) and the travel time through the layer:

Equation 2-11 $$w_{perc,j} = \left(SW_j - FC_j\right)\left(1 - e^{\frac{-\Delta t}{t_{trav}}}\right)$$

Travel time t_{trav} was determined by the water content at complete saturation (SAT_j, mm H_2O), the FC_j, and the saturated hydraulic conductivity for that layer ($K_{sat,j}$, mm·hr^{-1}):

15

$$\text{Equation 2-12} \qquad t_{trav} = \frac{SAT_j - FC_j}{K_{sat,j}}$$

Water that percolated through all soil layers entered the vadose zone between the bottom of the soil profile and the top of the shallow aquifer.

A perched water table formed in areas whose soil profiles contain an impervious layer (z_{imp}, mm), a parameter set by the user or a default of six meters. If z_{imp} was above the depth of the lowest layer, then no percolation into the vadose zone occurred. If z_{imp} was below the soil profile, then the percolation out of the bottom layer (w_{seep}) was a function of the difference between the lowest layer depth and the impervious layer depth ($\Delta z_{imp,jmax}$) and the percolation out of the lowest layer calculated from Equation 2-11 ($w_{perc,jmax}$):

$$\text{Equation 2-13} \qquad w_{seep} = w_{perc_{jmax}} \frac{\Delta z_{imp,j_{max}}}{\Delta z_{imp,j_{max}} + e^{8.833 - 2.598\Delta z_{imp,j_{max}}}}$$

Under saturated conditions water may move upward from a perched water table and fill overlying layers. The height of the perched water table (z_w, mm) was a function of the soil profile's SW, FC, porosity (ϕ), the air-filled porosity (ϕ_{air}) and z_{imp}:

$$\text{Equation 2-14} \qquad z_w = z_{imp} \frac{\sum_{j=1}^{j_{max}} SW - \sum_{j=1}^{j_{max}} FC}{\left(\phi - \sum_{j=1}^{j_{max}} FC\right)(1 - \phi_{air})}$$

Lateral flow was water entering the stream perpendicular to the longitudinal direction; the source of lateral flow was the saturated zone due to a perched water table. SWAT simulated lateral flow as a kinematic storage model (Sloan & Moore, 1984) based on the continuity equation on the hillslope and its soil columns as the control volume. The excess soil water in a layer available for lateral flow ($SW_{j,lat}$) was a function of the drainable porosity (ϕ_d, mm·mm^{-1}), saturated thickness normal to the hillslope, expressed as a fraction of the total layer thickness (H_0, mm·mm^{-1}), and the length of the hillslope (L_{hill}, m):

16

Equation 2-15 $$SW_{j,lat} = 10^3 \cdot \frac{H_o \phi_d L_{hill}}{2}$$

The drainable porosity was calculated as the total porosity of the layer minus the porosity at field capacity: $\phi_d = \phi_{soil} - \phi_{FC}$. The net lateral flow ($Q_{lat}$, mm H$_2$O·day^{-1}) at the hillslope outlet was a function of the saturated thickness H_o, the slope of the control volume (θ_{hill}), and the saturated hydraulic conductivity (K_{sat}, mm·hr^{-1}):

Equation 2-16 $$Q_{lat} = 24 H_o K_{sat} \theta_{hill}$$

Rearranging Equation 2-15 and combining with Equation 2-16 yielded the following equation for lateral flow in the *j*'th soil layer:

Equation 2-17 $$Q_{lat,j} = 0.024 \cdot \left(\frac{2 SW_{j,lat} K_{sat,j} \theta_{hill}}{\phi_{d,j} L_{hill}} \right)$$

Tile drainage behaved similarly as lateral flow with z_{drain} the height of tile drain (mm) and t_{drain} was the time required to drain the soil to field capacity (hr):

Equation 2-18 $$Q_{tile} = \frac{z_w + z_{drain}}{z_w}(SW - FC)\left(1 - e^{\frac{-24}{t_{drain}}}\right)$$

Groundwater

SWAT simulated shallow aquifers with the water balance being:

Equation 2-19 $$aq_{sh,i} = aq_{sh,i-1} + w_{rchrg,sh} - Q_{gw} - w_{revap} - w_{pump,sh}$$

In units of mm H$_2$O, $aq_{sh,i}$ was the water stored in the shallow aquifer on day i, $aq_{sh,i-1}$ the water stored in the shallow aquifer on day i-1, $w_{rchrg,sh}$ the recharge entering the shallow aquifer, Q_{gw} the groundwater flow out of the shallow aquifer and into the main channel, w_{revap} water moving through the soil in response to water deficiencies, and $w_{pump,sh}$ the water removed by pumping. SWAT simulated inputs into the deep aquifer from the shallow aquifer, but the water moving

into that zone was treated as lost to the system and not considered for subsequent calculations in the soil hydrology. The water balance for the deeper aquifers was:

Equation 2-20 $\qquad aq_{dp,i} = aq_{dp,i-1} + w_{rchrg,dp} - w_{pump,dp}$

In units of mm H$_2$O, $aq_{dp,i}$ was the water stored in the deep aquifer on day i, $aq_{dp,i-1}$ the water stored in the shallow aquifer on day i-1, $w_{rchrg,dp}$ the recharge entering the deep aquifer, and $w_{pump,dp}$ the water removed by pumping. While water can enter the soil system from the deep aquifer through pumping, this water did not come from the original balance in Equation 2-2. Pumping was implemented in the simulations and scenarios.

Recharge for a given day ($w_{rchrg,i}$) was function of a user-defined groundwater delay or drainage time (δ_{gw}, days) with a default of 31 days, percolation from the soil profile (w_{seep}), and recharge from the previous day ($w_{rchrg,i-1}$):

Equation 2-21 $\qquad w_{rchrg} = w_{seep} \left(1 - e^{\frac{-1}{\delta_{gw}}} \right) + w_{rchrg,i-1} e^{\frac{-1}{\delta_{gw}}}$

Recharge split into deep and shallow aquifers by way of a coefficient (β_{dp}):

Equation 2-22 $\qquad w_{rchrg,dp} \quad = \beta_{dp} w_{rchrg}$

Equation 2-23 $\qquad w_{rchrg,sh} \quad = w_{rchrg} - w_{rchrg,dp}$

Groundwater or baseflow into the reach occurred when water stored in the shallow aquifer exceeds a user-defined threshold ($aq_{sh,t,gw}$, mm H$_2$O). The steady-state solution to groundwater flow was a function of the hydraulic conductivity of the shallow aquifer ($K_{sat,aq}$, mm·d^{-1}), the distance from the subbasin divide to the main channel (L_{gw}, m), and the height of the water table (z_w, m) (Arnold et al., 1993) was:

Equation 2-24 $\qquad Q_{gw} = z_w \dfrac{8000 K_{sat,aq}}{L_{gw}^2}$

18

With the inclusion of time-varying water table height and a non-steady state aquifer recharge, the ground water flow to the stream on the *i*'th day ($Q_{gw,i}$) was calculated as:

Equation 2-25

$$Q_{gw,i} = \begin{cases} Q_{gw,i-1}e^{-\alpha_{gw}\Delta t} + w_{rchrg,sh}\left(1 - e^{-\alpha_{gw}\Delta t}\right) & \text{if } aq_{sh} > aq_{sh,t,gw} \\ Q_{gw,0}e^{-\alpha_{gw}t} & \text{if } w_{rchrg,sh} = 0 \\ 0 & \text{otherwise} \end{cases}$$

$Q_{gw,i-1}$ was the groundwater flow from day *i-1*, *Δt* the time step, α_{gw} the baseflow recession constant, and $Q_{gw,0}$ the groundwater flow at the start of the recession, defined as the period after recharge has stopped. The baseflow recession constant was a direct index of groundwater flow response to changes in recharge (Smedema & Rycroft, 1983). Graphically, the recession was approximated by the length of time a hydrograph fell to and remained at some minimal flow after a storm event. This parameter could be estimated from streamflow records by calculating the record-derived number of days (*N*) since the start of the recession and the groundwater flow at day *N* ($Q_{gw,N}$).

Equation 2-26

$$\alpha_{gw} = \frac{1}{N}\ln\left[\frac{Q_{gw,N}}{Q_{gw,0}}\right]$$

Revap was the process by which water from the shallow aquifer diffuses upward during periods where the overlying layers were dry due to low rainfall or excess evapotranspiration. Revap was also a function of land cover as deep root plants may draw directly from the shallow aquifer and some parameters depended on the plant or crop. The maximum amount of water removed from the aquifer due to revap ($w_{rvp,max}$, mm H_2O) was a function of a revap coefficient (β_{rvp}) and the potential evapotranspiration (*ET*):

Equation 2-27

$$w_{rvp,max} = \beta_{rvp}ET$$

The actual revap depended on a user-defined threshold value ($aq_{sh,t,r}$, mm H_2O) for the shallow aquifer volume that must be met before revap occured:

19

Equation 2-28
$$w_{rvp,i} = \begin{cases} 0 & \text{if } aq_{sh} \leq aq_{sh,t,r} \\ w_{rvp,max} - aq_{sh,t,r} & \text{if } aq_{sh} \in (aq_{sh,t,r}, aq_{sh,t,r} + w_{rvp,max}) \\ w_{rvp,max} & \text{if } aq_{sh} \geq (aq_{sh,t,r} + w_{rvp,max}) \end{cases}$$

Soil Nitrogen

Nitrogen dynamics were simulated separately in the land and in-stream phases. The land phase had five pools: the organic pools consisting of "active", "fresh", and "stable" organic nitrogen and the mineral pools of ammonium and nitrate (Figure 2-4a). Active organic nitrogen increased from organic nitrogen fertilizer, decreased with mineralization into nitrate, and could transfer to and from stable organic nitrogen. Stable organic nitrogen was not available for mineralization and acted as storage for humic organic nitrogen. Fresh organic nitrogen was the nitrogenous plant residue. The fresh organic nitrogen could only exist on the top 10 mm or the surface layer of the soil column.

The nitrate pooled increased from inorganic fertilizer, organic nitrogen mineralization, and atmospheric deposition and decreased through denitrification, plant uptake, and leaching into the groundwater systems. SWAT did not have a pool for nitrite in the soil phase of the nitrogen cycle (Neitsch et al., 2011). Ammonium entered the soil as fertilizer and atmospheric deposition and left through volatilization into the gas phase or nitrification via the two-step biological oxidation by bacteria.

Equation 2-29
$$2NH_4^+ + 3O_2 \rightarrow 2NO_2^- + 2H_2O + 4H^+$$

Equation 2-30
$$2NO_2^- + O_2 \rightarrow 2NO_3^-$$
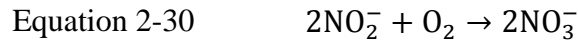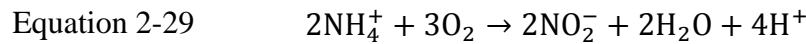
Plant uptake of nitrate was modeled separately as part of the EPIC crop growth module. This module also coded for atmospheric nitrogen fixation, which directly enters the plant biomass instead of residing in the soil. For brevity the following equations and processes were for each layer in a soil column of an HRU except for inputs from a specific layer denoted with j.

20

Organic Nitrogen

Stable and active organic nitrogen pools were initially grouped together as nitrogenous humus or $N_{org,s}$ (mg·kg^{-1}). The soil organic nitrogen concentration was a function of the soil organic carbon content or C_{org} (%) in the j'th soil layer, under the assumption of a 14:1 ratio of carbon to nitrogen in humus:

Equation 2-31 $$N_{org,s} = 10^4 \left(\frac{C_{org}}{14}\right)$$

The initial active ($N_{org,actv}$, mg·kg^{-1}) and stable ($N_{org,stab}$, mg·kg^{-1}) organic nitrogen pools were partitioned as fractions of $N_{org,s}$. The initial fraction ($f_{N,act}$) of active nitrogen in the nitrogenous humus was 0.02. The fresh organic nitrogen pool or $N_{org,frsh}$ (mg·kg^{-1}) was set to 0.15% of the total plant residue mass (R_{surf}, kg·ha^{-1}).

Equation 2-32 $$N_{org,actv} = N_{org}f_{N,act}$$

Equation 2-33 $$N_{org,stab} = N_{org}(1 - f_{N,act})$$

Equation 2-34 $$N_{org,frsh} = 1.5 \times 10^{-3} \cdot R_{surf}$$

Decomposition of the fresh nitrogenous plant residue into humus, the microbial mineralization of active organic nitrogen or plant residue to inorganic nitrogen available for plant uptake, and the assimilation of inorganic to unavailable organic nitrogen all depended on the residue or humic ratio of carbon to nitrogen ($\varepsilon_{C:N}$) and soil water content, a proxy for aerobic conditions. Bacteria break down humus for energy and cell growth; if nitrogen in the humus was low ($\varepsilon_{C:N} > 30:1$), bacteria would draw NH_4^+ and NO_3^- from the soil. Bacteria released inorganic nitrogen into the soil when the nitrogen content was high ($\varepsilon_{C:N} < 20:1$) (Seligmand & van Keulen, 1981). SWAT soil phase simulated net mineralization of organic nitrogen, incorporating assimilation to limit the rate, but SWAT did not allow net organic nitrogen production from

bacterial processes. The modeled assumed the organic nitrogen from bacterial cells (alive and dead) was negligible compared to plant matter.

The exchange between active, stable, and fresh organic, and their decomposition to nitrate was a function of the following unitless variables: a transfer rate constant between active and stable organic nitrogen ($\beta_{stab,actv}$), a mineralization rate constant (β_{min}), crop-specific rate constants for plant residue decomposition (β_R), a soil temperature parameter (γ_T), a water content parameter (γ_w), and a plant residue composition parameter (γ_n). γ_n was a function of $\varepsilon_{C:N}$, humus carbon to phosphorous ratio ($\varepsilon_{C:P}$), and the residue content for the j'th layer (R_j):

Equation 2-35 $\qquad \gamma_T \quad = 0.9 \dfrac{T_{soil}}{T_{soil} + e^{9.93 - 0.312 \cdot T_{soil}}} + 0.1$

Equation 2-36 $\qquad \gamma_w \quad = \dfrac{SW}{FC}$

Equation 2-37 $\qquad \gamma_n \quad = \min \begin{cases} e^{-0.693 \frac{\varepsilon_{C:N} - 25}{25}} & | \; \varepsilon_{C:N} = \dfrac{0.58 R_j}{N_{org,frsh} + NO_3^-} \\ e^{0.693 \frac{\varepsilon_{C:P} - 200}{200}} & | \; \varepsilon_{C:P} = \dfrac{0.58 R_j}{P_{org,frsh} + P_{sol}} \\ 1.0 \end{cases}$

T_{soil} (˚C) was the temperature of the soil, SW the water content (mm H_2O) of the soil layer, and FC the water content at field capacity. The rate constants were user defined while the parameters were directly calculated; γ_T and γ_w have minimum values of 0.1 and 0.05, respectively. Phosphorous dynamics were structured similarly to nitrogen, but was only mentioned here because γ_n was dependent on the fresh organic phosphorous ($P_{org,frsh}$) and soluble inorganic phosphorus (i.e. phosphate: $H_nPO_4^{3-n}$). The overall decomposition of plant residue into humus was a function of a decay rate constant, δ_R:

Equation 2-38 $\qquad \delta_R = \beta_R \gamma_n \sqrt{\gamma_T \gamma_w}$

22

The change in active organic nitrogen occurred through transfer from stable organic nitrogen and the decomposition of fresh organic nitrogen. $N_{org,fert,j+1}$ refers to the addition of active organic nitrogen due to percolation from the layer immediately above.

Equation 2-39
$$\Delta N_{org,actv} = N_{org,stab} - \beta_{stab,act} N_{org} \left(1 - \frac{1}{f_{N,act}}\right) + 0.2 N_{org,frsh} \delta_R + N_{org,fert,j+1}$$

Inorganic Nitrogen

Initial soil NO_3^- could be user defined or calculated as a function of soil layer depth z:

Equation 2-40
$$NO_3^-{}_s = 7e^{-\frac{z}{1000}}$$

Atmospheric deposition occurred only for the top 10 mm layer of the soil and expressed as:

Equation 2-41
$$NH_4^{+}{}_{j=0}^{atm} = 0.01 NH_4^+{}_P P_i + NH_4^+{}_{dry}$$

Equation 2-42
$$NO_3^{-}{}_{j=0}^{atm} = 0.01 NO_3^-{}_P P_i + NO_3^-{}_{dry}$$

P_i was the daily precipitation (mm H_2O), $NH_4^+{}_p$ the rainfall ammonium concentration (mg·L^{-1}), $NO_3^-{}_{,P}$ the rainfall nitrate concentration (mg·L^{-1}),), $NH_4^+{}_{dry}$ the ammonium dry deposition rate, and $NO_3^-{}_{,dry}$ the nitrate dry deposition rate. The inorganic nitrogen from the atmosphere could be considered fertilizer input upon reaching the soil surface.

Nitrification and denitrification processes were dependent on the soil denitrification rate coefficient (β_{den}), temperature parameter (η_T), water content parameter (η_w), volatilization depth parameter (η_z), and the volatilization cation exchange parameter that was set to a constant value of $\eta_c = 0.15$.

Equation 2-43
$$\eta_T = 0.41 \frac{T_{soil} - 5}{10} \quad \text{if } T_{soil} > 5$$

23

Equation 2-44 $\eta_w = \begin{cases} \dfrac{SW - WP}{0.25(FC - WP)} & \text{if } SW < 0.25FC - .75WP \\ 1.0 & \text{otherwise} \end{cases}$

Equation 2-45 $\eta_z = 1 - \dfrac{z_{m,j}}{z_{m,j} + e^{4.706 - 0.305 z_{m,j}}}$

WP was the wilting point water content and $z_{m,i}$ was the depth from the surface to the middle of the j'th layer. The total amount of ammonium gained or lost for the j'th soil layer was calculated as:

Equation 2-46 $\Delta NH_4^+{}_s = NH4_4^+{}_{fert,j+1} - NH_4^+(1 - e^{\eta_T(\eta_w - \eta_z \eta_c)})$

The second term accounted for both volatilization and nitrification. To partition that term into their respective loss processes, two additional parameters were needed: the estimated fractions lost to volatilization (f_{vol}) and nitrification (f_{nit}).

Equation 2-47 $f_{nit} = 1 - e^{-\eta_T \eta_w}$

Equation 2-48 $f_{vol} = 1 - e^{-\eta_T \eta_z \eta_c}$

The ammonium lost to nitrification ($\Delta NH_4^+{}_{nit}$) and volatilization ($\Delta NH_4^+{}_{vol}$) were calculated as:

Equation 2-49 $NH_4^+{}_{nit} = \dfrac{f_{nit}}{f_{nit} + f_{vol}} \cdot NH_4^+(1 - e^{\eta_T(\eta_w - \eta_z \eta_c)})$

Equation 2-50 $NH_4^+{}_{vol} = \dfrac{f_{vol}}{f_{nit} + f_{vol}} \cdot NH_4^+(1 - e^{\eta_T(\eta_w - \eta_z \eta_c)})$

Denitrification occurred during anoxic conditions in the soil when the water content increased at the expense of air. The point at which the soil water content reached a user defined threshold value ($\gamma_{w,t}$) to allow denitrification was relative to the water content parameter (γ_w). Nitrate lost ($NO_3^-{}_{den}$, kg·ha^{-1}) to denitrification was calculated as:

Equation 2-51 $NO_3^-{}_{den} = NO_3^-\left(1 - e^{-\beta_{den} \gamma_T C_{org}}\right)$ if $\gamma_w \geq \gamma_{w,t}$

24

SWAT simulated the soil-to-surface movement of nitrate ($NO_3^-{}_{evap}$, kg·ha^{-1}) as:

Equation 2-52 $\qquad NO_3^-{}_{evap} = 0.1 NO_3^-{}_{i=1} \frac{E_{a,i=1}}{SW_{i=1}}$

$NO_3^-{}_{i=1}$ was the nitrate content in the first soil layer (kg N·ha^{-1}), $E_{a,i=1}$ the evaporation of water from the first soil layer (mm H$_2$O), and $SW_{i=1}$ the soil water content in the first layer (mm H$_2$O). With the omission of soil-to-surface movement because it applies only to the first soil layer, the general the nitrate balance in a soil layer for was:

Equation 2-53
$$\Delta NO_3^-{}_s = NO_3^-{}_{fert,j+1} + 0.8 N_{org,frsh} \delta_n + \beta_{min} N_{org,actv} \sqrt{\gamma_T \gamma_w}$$
$$+ NH_4^+{}_{nit} - NO_3^-{}_{plant} - NO_3^-{}_w$$

The first term, $NO_3^-{}_{fert,i+1}$, accounted for fertilizer from the upper layers. The second and third term accounted for the mineralization of fresh and active organic nitrogen, respectively. $NO_3^-{}_{plant}$ was the plant uptake of nitrogen, which was a function of the crop or land cover at the surface, plant growth stage, root depth, and plant health. $NO_3^-{}_w$ was the sum of nitrate transported with water in the soil column whose processes are described in the *Nitrogen Transport* subsection.

Nitrogen Transport

Nitrate

Nitrate may move with surface runoff ($NO_3^-{}_{surf}$), lateral flow ($NO_3^-{}_{lat,j}$), or percolation ($NO_3^-{}_{perc,j}$). Nitrate in tile flow was equivalent to that of lateral. The amount of water (w_{mobile}) that nitrate moved with was different for the surface and the lower soil layers:

Equation 2-54 $\qquad w_{mobile} = \begin{cases} Q_{surf} + Q_{lat,j} + w_{perc,j} & \text{if } j = 0 \\ Q_{lat_j} + w_{perc,j} & \text{if } j > 0 \end{cases}$

In units of mm H$_2$O, Q_{surf} was the surface runoff, $Q_{lat,j}$ was the lateral flow for the *j*'th layer, $w_{perc,j}$ was percolation from the *j*'th layer. The concentration of transportable nitrate ($NO_3^-{}_t$, kg N·mm^{-1}) in these three processes was calculated as:

Equation 2-55
$$NO_3^-{}_t = \frac{NO_3^-{}_j\left(1-e^{\frac{-w_{mobile}}{SAT_j(1-\theta_e)}}\right)}{w_{mobile}}$$

$NO_3^-{}_j$ was the amount of nitrate in the j'th soil layer (kg N·ha^{-1}), θ_e the fraction of porosity from which anions are excluded, and SAT_j the saturated water content in the j'th layer (mm H$_2$O). The nitrate removed from the surface runoff and lateral flow was calculated using a nitrate percolation coefficient (β_{NO3}); lateral flow nitrate depended on soil depth. Nitrate may transport with percolation ($NO_3^-{}_{perc,j}$, kg N·ha^{-1}).

Equation 2-56
$$NO_3^-{}_{surf} = \beta_{NO3}NO_3^-{}_t Q_{surf}$$

Equation 2-57
$$NO_3^-{}_{lat,j} = \begin{cases} \beta_{NO3}NO_3^-{}_t Q_{lat,j} & \text{if } j = 0 \\ NO_3^-{}_t Q_{lat,j} & \text{if } j > 0 \end{cases}$$

Equation 2-58
$$NO_3^-{}_{perc,j} = NO_3^-{}_t w_{perc,j}$$

Nitrate may enter the groundwater systems, recharging into either the shallow or deep aquifer or moving out of the groundwater system via revap or groundwater flow into the main channel. Nitrate may travel with recharge on the i'th day ($NO_3^-{}_{rchrg,i}$, kg N·ha^{-1}) and followed Equation 2-21 for shallow aquifer water recharge where $NO_3^-{}_{seep}$ was the nitrate exiting the lowest soil layer:

Equation 2-59
$$NO_3^-{}_{rchrg,i} = NO_3^-{}_{seep}\left(1 - e^{\frac{-1}{\delta_{gw}}}\right) + NO_3^-{}_{rchrg,i-1}e^{\frac{-1}{\delta_{gw}}}$$

Once in the shallow aquifer nitrate movement followed the general equation:

Equation 2-60
$$NO_3^-{}_x = x\frac{NO_3^-{}_{sh,i-1} + NO_3^-{}_{rchrg,i}}{aq_{sh,i} + Q_{gw,i} + w_{rvp,i} + w_{rchrg,dp,i}} \mid x \in (aq_{sh}, Q_{gw}, w_{rvp}, w_{rchrg,dp})$$

The placeholder x denoted a part of the groundwater system: aq_{sh} for shallow aquifer, Q_{gw} for groundwater flow into the stream, w_{rvp} for revap into the upper layers, and $w_{rchrg,dp}$ for recharge

26

to the deep aquifer. Nitrate removal in the shallow aquifer due to microbial processes was modeled as a first order decay:

Equation 2-61
$$NO_{3\ sh,t}^- = NO_{3\ sh,0}^- e^{-k_{NO3,sh}t} \ | \ k_{NO3,sh} = \frac{0.693}{\lambda_{1/2,NO3,sh}}$$

$NO_{3\ sh,t}^-$ was the nitrate content (kg N·ha^{-1}) at time t, $NO_{3\ sh,0}^-$ the initial nitrate content, $k_{NO3,sh}$ the decay rate constant (day^{-1}), and $\lambda_{1/2,NO3,sh}$ a user-defined half-life of nitrate in the shallow aquifer (days). Of these groundwater components, only the groundwater flow directly contributed to in-stream nitrate; the aquifers are sinks and revap indirectly affected the streams by adding to the nitrate pool in the soil layers for lateral flow or surface runoff.

Organic Nitrogen

The concentration of organic nitrogen on the soil surface ($N_{org,conc}$) layer was calculated as the sum of the surface active, fresh, and stable organic nitrogen pools (kg·ha^{-1}) divided by the first soil layer's bulk density ($\rho_{b,j=1}$) and surface depth ($z_0 = 10$mm):

Equation 2-62
$$N_{org,conc} = 100 \frac{N_{org,frsh,surf} + N_{org,stab,surf} + N_{org,actv,surf}}{\rho_{b,j=1}z_0}$$

Organic nitrogen may enter the streams as a part of sediment loading in soil erosion in surface runoff ($N_{org,surf}$) and calculated with a loading function (McElroy et al., 1976):

Equation 2-63
$$N_{org,surf} = 10^{-3} \cdot N_{org,conc}\varepsilon_{N:sed} \frac{M_{sed}}{A_{HRU}}$$

M_{sed} was the mass of sediment yield on a given day, A_{HRU} the area of the HRU (ha), and $\varepsilon_{N:sed}$ the nitrogen enrichment ratio. The enrichment ratio was calculated as (Menzel, 1980):

Equation 2-64
$$\varepsilon_{N:sed} = 0.78\left(\frac{M_{sed}}{10A_{HRU}Q_{surf}}\right)^{-.2468}$$

27

SWAT and QUAL2E modeled the channel cross-section as a trapezoid and the dimensions varied by reach and subbasin. These values were derived from the input data pre-processing steps detailed in Chapter 3. The stream flow rate (Q_s) and velocity were calculated with Manning's equation for open channel flow:

Equation 2-65
$$Q_s = \frac{R^{\frac{2}{3}} S^{\frac{1}{2}}}{n}$$

A was the cross-sectional area, *R* the hydraulic radius (the ratio of the cross-sectional area and wetted perimeter), *S* the energy slope, and *n* the roughness coefficient.

Water (V_{rch}, m^3) entering the stream network from a given HRU was based on a balance:

Equation 2-66
$$V_{rch} = 10 A_{HRU}\left(Q_{surf} + \Sigma_j Q_{lat} + Q_{gw} + Q_{tile}\right) - V_{irr}$$

A_{HRU} was the area of the HRU (ha). In units of mm H$_2$O, Q_{surf} was the surface runoff (Equation 2-3), Q_{lat} the lateral flow (Equation 2-17), Q_{gw} the groundwater flow from the shallow aquifer (Equation 2-25), Q_{tile} the flow from tile drains (Equation 2-18), and V_{irr} the volume withdrawn for irrigation. Irrigation was not included in the ICRB model development. Variable storage method simulated water routing between reaches, a method based on the continuity equation for a given stream reach segment (Williams, 1969):

Equation 2-67
$$\Delta V_{rch} = V_{in} - V_{out} = \Delta t \left(\frac{Q_{in,1} + Q_{in,2}}{2} - \frac{Q_{out,1} + Q_{out,2}}{2}\right)$$

V was the volume in the reach, *Δt* the time step, $Q_{in,1}$ and $Q_{in,2}$ the inflow at the beginning and end of the time step, respectively, and $Q_{out,1}$ and $Q_{out,2}$ were the outflow at the beginning and end of the time step, respectively.

The outputs from the land module plus nitrogen from a previous stream reach were the initial values for the in-stream nitrogen that had four pools: organic nitrogen, ammonium, nitrite, and nitrate (Figure 2-4b). The in-stream phase incorporated the QUAL2E water quality model managed by the US Environmental Protection Agency (Chapra et al., 2006), Rate constants and coefficients were relative to a water temperature (T_w) of 20°C and SWAT adjusted these numbers with changes in temperature.

Organic nitrogen increased from the conversion from algae death and decreased through hydrolysis to ammonium and settling into the sediment phase:

Equation 2-68 $$\frac{\Delta N_{org,w}}{\Delta t} = \alpha_N \rho_a Algae - \beta_1 N_{org,w} - \sigma_{s,N_{org}} N_{org,w}$$

α_N was the fraction of algal biomass that is nitrogen, ρ_a was the local algal algal rate (hr^{-1}), β_1 was the rate constant for hydrolysis of organic nitrogen to ammonium (hr^{-1}), and $\sigma_{S,Norg}$ was the settling rate coefficient for organic nitrogen (hr^{-1}). Adjusted to water temperature, the rate coefficients or constants were:

Equation 2-69 $$\beta_1 = \beta_{1,T_w=20} 1.047^{T_w-20}$$

Equation 2-70 $$\sigma_{s,N_{org}} = \sigma_{s,N_{org},T_w=20} 1.024^{T_w-20}$$

Ammonium nitrogen increased from hydrolysis of organic nitrogen and sediment or benthic diffusion. Ammonium decreased with assimilation by algae and nitrification.

Equation 2-71 $$\frac{\Delta NH_4^+{}_w}{\Delta t} = \beta_1 N_{org} - \beta_2 NH_4^+ - \frac{\sigma_{S,NH_4^+}}{z_{rch}} - f_{NH_4^+} \alpha_N \mu_a Algae$$

Equation 2-72 $$\beta_2 = \beta_{2,T_w=20}(1 - e^{-0.6O_2}) \cdot 1.083^{T_w-20}$$

Equation 2-73 $$\sigma_{s,NH_4^+} = \sigma_{s,NH_4^+,T_w=20} 1.074^{T_w-20}$$

29

β_2 was the rate constant for biological oxidation of ammonium to nitrite (hr^{-1}), $\sigma_{S,NH4+}$ the sediment source rate for ammonium (mg N·m^{-2}·day^{-1}), z_{rch} the water depth of the stream reach, f_{NH4+} the fraction of algal nitrogen uptake from the ammonium pool, and μ_a the local rate of algae growth. O_2 was the dissolved oxygen concentration in the stream (mg·L^{-1}). Nitrite increased with ammonium oxidation and decreased with oxidation of nitrite to nitrate with β_3 as the rate constant for biological oxidation of nitrite to nitrate (hr^{-1}):

Equation 2-74
$$\frac{\Delta NO_2^-}{\Delta t} = \beta_2 NH_4^+ - \beta_3 NO_2^-$$

Equation 2-75
$$\beta_3 = \beta_{3,T_w=20}(1 - e^{-0.6O_2}) \cdot 1.047^{T_w-20}$$

Nitrate increased from oxidation of nitrite and lost through algal uptake:

Equation 2-76
$$\frac{\Delta NO_3^-}{\Delta t} = \beta_3 NO_2^- - \left(1 - f_{NH_4^+}\right)\alpha_N\mu_a Algae$$

SWAT simulated algae growth and the process featured prominently in the in-stream nitrogen dynamics, specifically as the only sink for nitrate:

Equation 2-77
$$\frac{\Delta Algae}{\Delta t} = Algae\left(\mu_a - \rho_a - \frac{\sigma_{s,algae}}{z_{rch}}\right)$$

σ_S was the local settling algal settling rate (m·day^{-1}) and all other variables were defined previously.

<u>Literature Review</u>

The use of SWAT was not new to hydrological studies of the ICRB and other Iowan watersheds. One of the first SWAT studies inside the ICRB was the simulation of alternative management scenarios in Walnut Creek (Vaché et al., 2002; Santelman et al. 2004) and their impacts on surface water discharge, sediment and nitrate loads. Walnut Creek was a small watershed (51.3 km^2), but the initial scenario-driven studies showed that only widespread

adoption of a best management practices such as riparian buffers, filter strips, and engineered wetlands would result in a substantial (>50%) decrease in nitrate export. The first variety of SWAT studies in the ICRB was scenario driven where a watershed was subjected to alternative land use or management scenarios to assess effects on non-point source pollution from agriculture.

The second variety of SWAT studies in the ICRB was methodological, often involving watersheds larger than Walnut Creek. These studies manipulated model development to evaluate SWAT's robustness at different spatial configurations (Jha et al., 2004) or sensitivity to input data. The sensitivity to input data was especially important considering one of SWAT's strength lies in long-term simulations. During a model calibration, the initial inputs such as land use should change lest the model results be misinterpreted (Schilling et al., 2008). Methodological studies more specific to the ICRB were those evaluating relevant and newer subroutines such as tile flow (Moriasi et al., 2012). For example the 775 km^2 South Fork Iowa River within the ICRB had approximately 80% tile drain coverage (Green et al., 2006).

The more recent scenario studies have now shifted to a climate change focus (Chattopadhyay & Jha, 2015), the incorporation of extra-watershed factors such as crop prices (Hendricks et al., 2014), and trade-off studies between land use and water quality or other parameters (Yaeger et al., 2014). As SWAT matured the methodological studies explored modification through coupling with other models (Wu & Liu, 2014). For watersheds that have experienced successful SWAT implementations, the attention focused on improving model performance to more accurately and precisely simulate observed conditions. These studies looked at alternative calibration procedures to reduce uncertainty and aid in calibration (Harmel et al., 2010). The examples given explicitly related to the ICRB and other watersheds in Iowa, but the trends were literature-wide: improve calibration and simulate future scenarios. The need for additional calibration techniques may only grow, especially because SWAT branched out into running more varied and complex scenarios in climate and land use change.

31

Table 2-1   Summary statistics for eight USGS gage stations for stream discharge in units of $m^3 \cdot s^{-1}$

Gage Station	Minimum	25%	Median	Mean	75%	Maximum
Charles City	1.69	6.82	11.5	23.1	24.2	864
New Providence	0.003	0.396	1.76	5.04	5.15	167
Marshalltown	0.133	7.16	16.6	33.2	39.6	632
Cedar Rapids	3.96	49.3	87.5	150	176	3908
Iowa City	1.39	17.8	42.2	73.5	105.9	1158
Old Man's Creek	0.011	0.538	1.76	4.66	4.39	249
Lone Tree	1.95	22.9	56.1	97.8	139	1560
Wapello	13.0	96.3	186	289	368	4870

Table 2-2   Summary statistics for nitrate plus nitrite loading (metric tons $N \cdot day^{-1}$) at Cedar Rapids in the Cedar River Basin and Wapello gage   in the Iowa River Basin

Gage Station	Minimum	25%	Median	Mean	75%	Maximum
Cedar Rapids	0.134	19.8	93.1	155	199	1620
Wapello	0.452	5.59	93.4	214	313	2882

Table 2-3   Summary statistics for nitrate plus nitrite concentrations ($mg \cdot L^{-1}$ as N) at Cedar Rapids in the Cedar River Basin and Wapello gage station on the Iowa River Basin

Gage Station	Minimum	25%	Median	Mean	75%	Maximum
Cedar Rapids	0.1	2.97	6.03	5.81	8.16	18.5
Wapello	0.1	1.03	3.62	4.26	6.71	15.4

Table 2-4   List of variables for computation of soil and in-stream hydrology

Symbol	Definition	Units	Derivation
aq_{sh}	water in shallow aquifer	mm H_2O	calculated
$aq_{sh,t,gw}$	threshold water content in shallow aquifer before groundwater can flow	mm H_2O	user defined
$aq_{sh,t,r}$	threshold water content in shallow aquifer before revap can occur	mm H_2O	user defined
$AWCj$	plant-available water capacity	fraction	database
CN	curve number for surface runoff	mm H_2O	database
ET	evapotranspiration	mm H_2O	calculated
FC_j	field capacity of layer j	fraction	calculated
I_a	initial surface soil water	mm H_2O	calculated
$K_{sat,j}$	saturated hydraulic conductivity for layer j	mm·hr^{-1}	database
n	Manning's roughness coefficient	unitless	user defined
P_i	precipitation on day i	mm H_2O	user defined
Q_{gw}	groundwater flow into streams	mm H_2O	calculated
$Q_{lat,j}$	lateral flow from layer j	mm H_2O·day^{-1}	calculated
Q_s	flow in channel from Manning's equation	m^3·s^{-1}	calculated
Q_{surf}	surface runoff	mm H_2O	calculated
Q_{tile}	flow from subsurface tile drains	mm H_2O	calculated
S	maximum soil moisture retention	mm H_2O	calculated
SW_j	soil water content at layer j	mm H_2O	calculated
V_{rch}	water volume in a reach	m^3	calculated
$w_{perc,j}$	percolation from layer j	mm H_2O	calculated
w_{rchrg}	recharge into shallow deep aquifer	mm H_2O	calculated
w_{rvp}	upward, subsurface diffusion of water from saturated zone	mm H_2O	calculated
w_{seep}	percolation out of soil profile	mm H_2O	calculated
w_{mobile}	amount of water that can carry nitrate out of the soil column	mm H_2O	calculated
z_{imp}	depth to impervious layer	mm	user defined
z_w	height of the perched water table	mm	calculated
α_{gw}	baseflow recession constant	day^{-1}	user defined
β_{dp}	deep aquifer recharge partitioning coefficient	fraction	user defined
β_{rvp}	revap coefficient	unitless	user defined
δ_{gw}	groundwater delay time	day	user defined

33

Table 2-5   List of variables for computation of soil nitrogen dynamics

Symbol	Definition	Units	Derivation
C_{org}	soil organic carbon in layer j	%	database
$f_{N,act}$	fraction of active organic nitrogen in nitrogenous humus	fraction	calculated
f_{nit}	fraction of ammonium lost to nitrification	fraction	calculated
f_{vol}	fraction of ammonium lost to volatilization	fraction	calculated
$N_{org,actv}$	active organic nitrogen	mg·kg^{-1}	calculated
$N_{org,frsh}$	nitrogenous plant residue	mg·kg^{-1}	calculated
$N_{org,stab}$	stable organic nitrogen	mg·kg^{-1}	calculated
$N_{org,s}$	nitrogenous humus	mg·kg^{-1}	calculated
$NH_4^+{}_s$	soil ammonium	mg·kg^{-1}	calculated
$NH_4^+{}_p$	ammonium concentration in rainfall	mg·L^{-1}	user defined
$NO_3^-{}_p$	nitrate concentration in rainfall	mg·L^{-1}	user defined
$NO_3^-{}_{den}$	nitrate loss due to denitrification	kg·ha^{-1}	calculated
$NO_3^-{}_p$	nitrate concentration in rainfall	mg·L^{-1}	user defined
$NO_3^-{}_s$	soil nitrate	mg·kg^{-1}	calculated
R_j	total plant residue in layer j	kg·ha^{-1}	calculated
R_{surf}	total plant residue at surface	kg·ha^{-1}	calculated
$\beta_{stab,actv}$	transfer rate between stable and active organic nitrogen	unitless	constant (10^{-5})
β_{min}	organic nitrogen mineralization constant	unitless	user defined
β_R	crop-specific rate constant for plant residue decomposition to humus	unitless	database
β_{den}	Soil denitrification rate coefficient	unitless	user defined
γ_T	soil temperature parameter for nutrient dynamics	unitless	calculated
γ_w	soil water parameter for nutrient dynamics	unitless	calculated
γ_n	plant residue composition parameter	unitless	calculated
δ_R	plant residue to humus decay rate constant	unitless	calculated
$\varepsilon_{C:N}$	carbon to nitrogen ratio in humus	ratio	calculated
$\varepsilon_{C:P}$	carbon to phosphorous ratio in humus	ratio	calculated
η_T	Nitrification/volatilization temperature parameter	unitless	calculated
η_w	Nitrification soil water parameter	unitless	calculated
η_z	ammonium volatilization depth parameter	unitless	calculated
η_c	soil cation exchange capacity	unitless	constant (0.15)

Table 2-6   List of variables for computation of in-stream nitrogen dynamics

Symbol	Definition	Units	Derivation
$Algae$	in-stream algae concentration	mg·L^{-1}	calculated
f_{NH4+}	fraction of algal nitrogen uptake from the ammonium pool	fraction	user defined
$N_{org,w}$	in-stream organic nitrogen concentration	mg N·L^{-1}	calculated
$NH_4^+{}_w$	in-stream ammonium concentration	mg N·L^{-1}	calculated
$NO_3^-{}_w$	in-stream nitrite concentration	mg N·L^{-1}	calculated
O_2	dissolved oxygen	mg ·L^{-1}	calculated
T_w	water temperature	°C	calculated
z_{rch}	water depth in the reach	m	database
α_N	nitrogenous algal biomass fraction	fraction	user defined
β_1	organic nitrogen hydrolysis rate constant	hr^{-1}	calculated
$\beta_{1,20}$	organic nitrogen hydrolysis rate constant at 20°C	hr^{-1}	user defined
β_2	rate constant for biological oxidation of NH$_4^+$ to NO$_2^-$	hr^{-1}	calculated
$\beta_{2,20}$	rate constant for biological oxidation of NH$_4^+$ to NO$_2$ at 20°C	hr^{-1}	user defined
β_3	rate constant for biological oxidation of NO$_2^-$ to NO$_3^-$	hr^{-1}	calculated
$\beta_{3,20}$	rate constant for biological oxidation of NO$_2^-$ to NO$_3^-$ at 20°C	hr^{-1}	user defined
μ_a	algae growth rate	hr^{-1}	calculated
ρ_a	algae death rate	hr^{-1}	calculated
$\sigma_{s,Norg}$	settling rate coefficient for organic nitrogen	hr^{-1}	calculated
$\sigma_{s,Norg,20}$	settling rate coefficient for organic nitrogen at 20°C	hr^{-1}	user defined
$\sigma_{S,NH4+}$	sediment source rate for ammonium	mg N·m^{-2} ·day^{-1}	user defined
$\sigma_{s,algae}$	settling rate for algae	m·day^{-1}	calculated
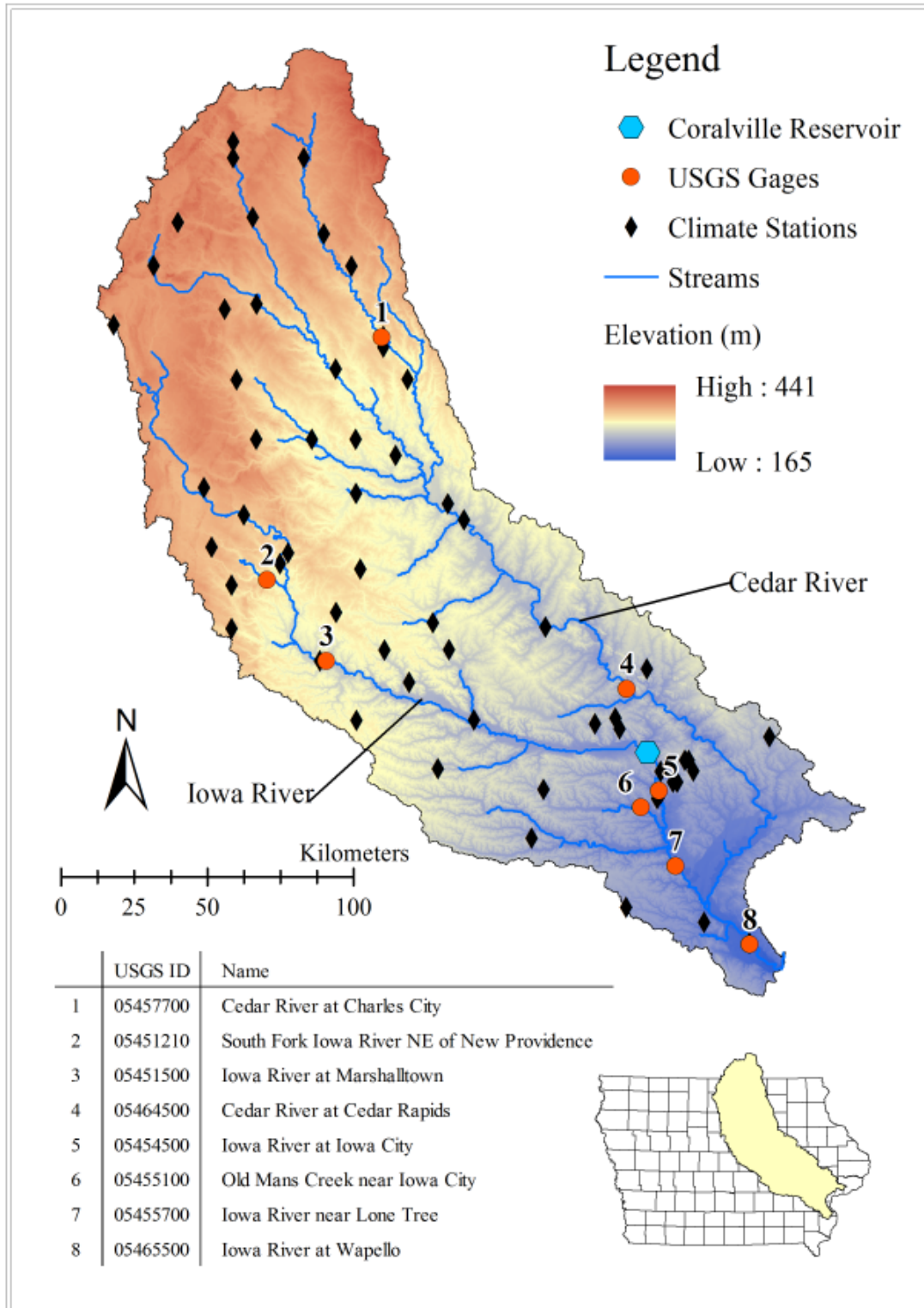
Figure 2-1   Map of the Iowa-Cedar River basin, locations of the USGS gage stations and climate stations.

The legend and table within the figure read:

Legend
- Coralville Reservoir
- USGS Gages
- Climate Stations
- Streams

Elevation (m)
- High : 441
- Low : 165

Cedar River

Iowa River

N

Kilometers
0   25   50   100

	USGS ID	Name
1	05457700	Cedar River at Charles City
2	05451210	South Fork Iowa River NE of New Providence
3	05451500	Iowa River at Marshalltown
4	05464500	Cedar River at Cedar Rapids
5	05454500	Iowa River at Iowa City
6	05455100	Old Mans Creek near Iowa City
7	05455700	Iowa River near Lone Tree
8	05465500	Iowa River at Wapello

Figure 2-2   Computational diagram of SWAT
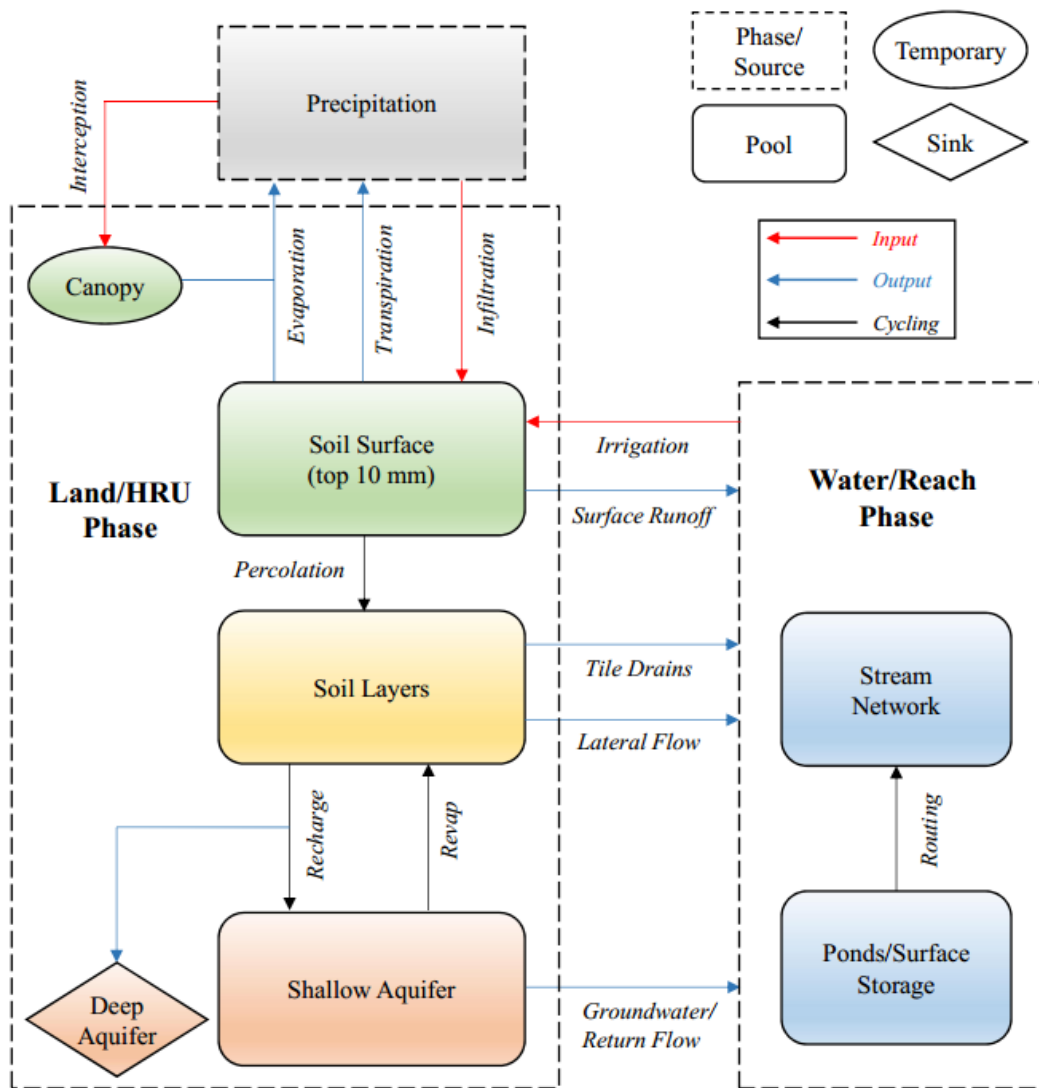
Figure 2-3   SWAT soil and stream water balance schematic
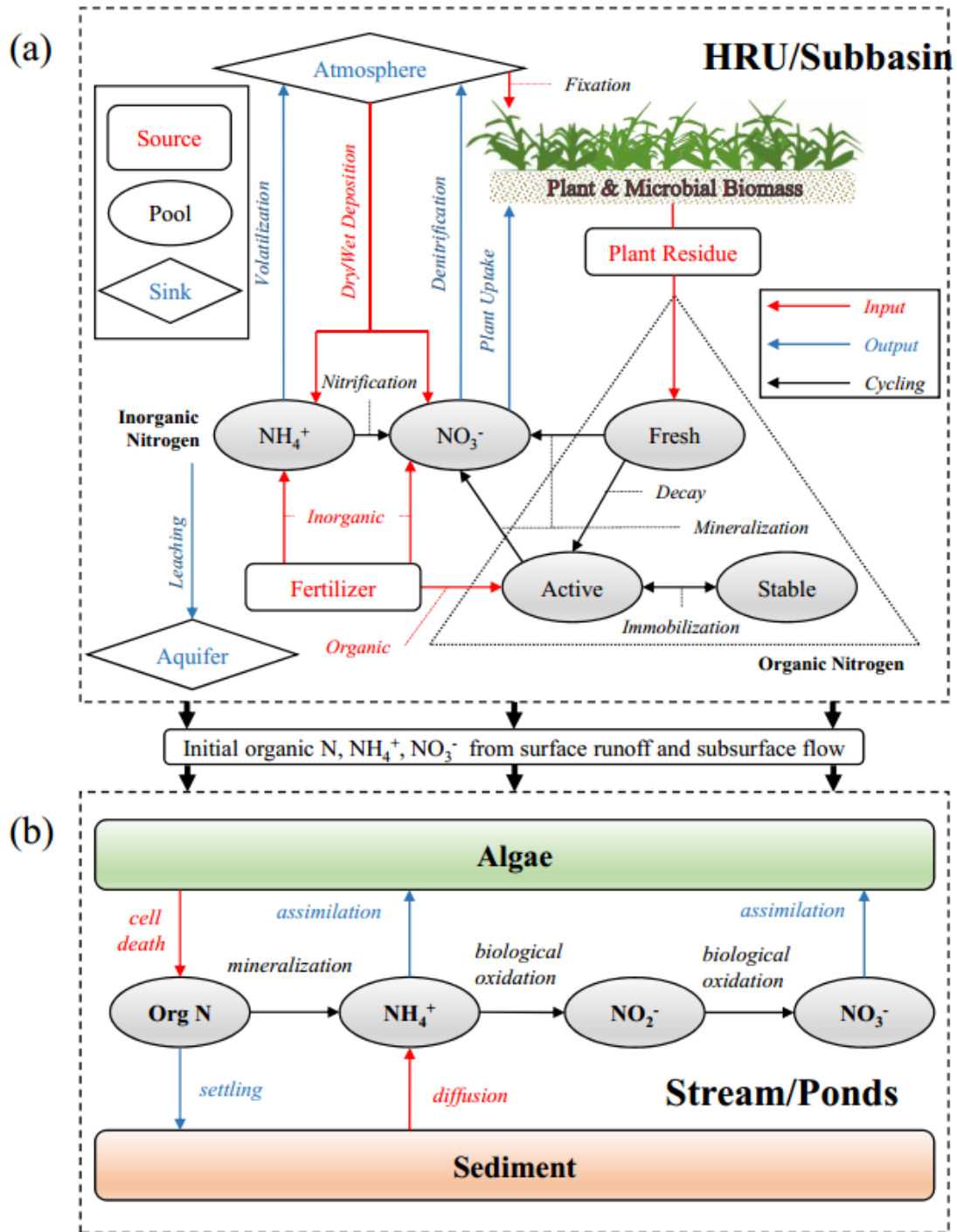
Figure 2-4   SWAT nitrogen dynamics for the (a) land phase and (b) in-stream phase.

Introduction

SWAT required four general inputs: (1) elevation or surface geometry, (2) soil type and characteristics, (3) land use or cover, and (4) climatic and meteorological records. Aside from the climate datasets, the inputs were in the form of digital maps and geodatabases. Geodatabases contained data tied with spatial coordinates along with other properties such as geographic projection, spatial units, and associated metadata describing their source and development. The climatic data were not from geodatabases, but downloaded as comma delimited files (USDA, 2010b) accompanied by a metadata text file with the stations' geographic coordinates.

The procedure for developing the SWAT model used a Geographic Information Science (GIS) approach through the application of the ArcSWAT extension for ESRI ArcGIS software (Winchell et al., 2009). The SWAT model itself was an executable compiled from the FORTRAN scientific programming language, but ArcSWAT provided all the necessary tools and databases to write and edit the initial input files. From the context of ArcSWAT, the main steps in developing the model were: (1) watershed delineation, (2) HRU definition, and (3) editing or adding details to suit the user's purpose. The details in step (3) were specific land management operations such as timing of planting or tilling for crops and the land use update module.

Input Data

Surface Geography

The surface features came from a Digital Elevation Model (DEM), sourced from the USGS National Elevation Dataset or NED (USGS, 2013). The NED had multiple resolutions and the resolution chosen for this model's development was one arc-second, resulting in a pixel edge of approximately 30 meters at the ICRB's geographical location (Gesh et al., 2002). The DEM

40

data had a raster grid format that was equivalent to images whose pixels have spatial coordinates and units; attribute tables for the pixels and metadata accompanied the raster datasets. The DEM was required for delineating the watershed, creating the reach network, and computing the subbasins' surface characteristics. The calculated average slope grid was a necessary component in the HRU definition process. The slopes were binned into classes as HRU definition requires categorical variables. The slope class definition was arbitrary and given that Iowa lies in the Great Plains region of the United States, the slope classes were narrow and uniformly separated: 0-2%, 2-4%, 4-6%, 6-8% and 8%+ grade. The percent area of the ICRB of these classes were 46.8, 24.9, 13.0 6.6, and 8.7 percent, respectively. The higher slope classes were found mostly in the southern portion of ICRB and along the riparian zones. Figure 3-1 summarizes the slope class distribution.

Soil Characteristics

The USDA STATSGO2 (Soil Survey Staff, n.d.) is a broad-based inventory of soil types across the United States. The STATSGO2 database sub-divided types by state and further differentiated into 37 different soil series (Figure 3-2). As a map the soil types were irregular polygons whose attribute tables contained the soil taxonomy and their column/layer characteristics. The main and relevant characteristics to the watershed were listed in

Table 3-2. Examples of these characteristics were number of soil layers, their depths, the total column depth, the particle size distribution (sand, silt, clay, rock) by layer, and soil organic carbon content by layer. ArcSWAT, a software extension for SWAT described in the Model Development subsection, incorporated the STATSGO database and transformed the attributes into input variables for SWAT. These attributes were the source of the "database" values in Table 2-4 through Table 2-6.

For runoff calculations using the SCS curve number method, the soil taxa were binned into Hydrologic Soil Groups from A to D (Miller & White, 1998). Group A soils were primarily sand or sandy loam with high infiltration rates and low runoff potential. Group B soils were loam or silt loams with moderate infiltration and a moderate fine or moderate coarse texture. Group C soils were sandy clay loams with low infiltration rates when nearing water saturation and their

41

textures are moderately fine to fine. Group D soils were primarily clay types and had the highest runoff potential with frequent ponding due to a high and permanent water table. Hydrologic Soil Group B covered approximately 95.9 percent of the ICRB. Group A soils covered 2.7 percent cluster around riparian areas, especially for the Cedar River. Group C at 0.8 percent and Group D at 0.6 percent were found in the far north in the headwaters of ICRB. Table 3-1 summarizes the soil characteristics and their distribution.

Land Use and Cover

Land use and land cover (LULC) were the third component of the HRU definition (Figure 3-6), constituting the crops for agricultural land, types of urban land uses, and other land covers not specified. This dissertation utilized three LULC maps or datasets for model development: the Iowa Department of Natural Resources (DNR) (Iowa DNR, 2012), the Multi-Resolution Land Characteristics Consortium's (MRLC), National Land Cover Dataset (NLCD) (Fry et al., 2011), and the USDA's Crop Data Layer (CDL) (USDA, 2012). The datasets had different spatial and temporal range and the combination of three help cover data gaps. To use any one particular dataset from one time point ignored the fact that land use changes. Conversion of native landscape to cultivation or urban development was one major example and crop rotation in agricultural land was another case that varies land use on a year-to-year and periodic basis.

Each data source classified LULC differently and in varying degrees of detail. The NLCD was the most general with no classes for specific crops (Table 3-5), the Iowa DNR (Table 3-4) included alfalfa, corn, and soybeans as they were important crops or cover crops for Iowa, and the CDL (Table 3-6) was the most extensive with every crop grown in the United States. Because of its breadth and similarity to SWAT's LULC classes, the CDL's classes were the basis for the LULC distribution in the model. SWAT had its own internal crop database (Table 3-3) for use in EPIC, the crop growth module. A "look-up table" was required to transform the LULC

42

classes in the data source to a SWAT equivalent; Table 3-3 through Table 3-6 were effectively the look-up tables for these data sources.

The Iowa DNR provided the earliest land use map in 1985, despite the period of simulation starting in 1971. Because of the lack of digital and georeferenced datasets before 1985 for Iowa, the model used the 1985 LULC map as a baseline for 1971 onwards until 1990 when the next available dataset was available. SWAT2009 and SWAT2012 (the version used in this dissertation) allowed updating of land use by changing the proportion of area an HRU occupies in a subbasin. The *Land Use Update* subsection described the procedure to combine the three data sources into a composite LULC time-series.

<div align="center">Climatic Data</div>

SWAT required the following climate or meteorological inputs: daily precipitation, minimum/maximum temperatures, relative humidity, wind speed, and solar radiation. The model contained the WXGEN weather generator module that created synthetic inputs given an existing record of at least twenty years (Sharpley & Williams, 1990). The weather generator was used for relative humidity, wind speed, and solar radiation while the temperature and precipitation data were observations originally sourced from the National Weather Service (NWS) Cooperative Observer Program (COOP), the Weather Bureau Army Navy (WBAN), and the Iowa Environmental Mesonet (IEM).

The generated solar radiation was based on a weak stationary process whose covariance does not change with time (Matalas, 1967); the generated values were a function of the probability distribution of the recorded dataset and correlations between solar and daily minimum/maximum temperatures derived from 31 locations in the United States (Richardson, 1982). The daily relative humidity was generated from a triangular probability distribution that relied on the monthly mean, maximum, minimum relative humidity, and a random number between 0.0 and 1.0 (Richardson, 1981).Wind speed was generated by an exponential function of the mean monthly wind speed and a random number between 0.0 and 1.0. Observed precipitation

43

and temperatures came from 48 stations in the COOP and WBAN networks covering the ICRB. Gaps existed in these records and the USDA Agricultural Research Service (ARS) used inverse distance weighted interpolation to fill in these gaps by referencing the nearest five stations that had datum for that day. The WBAN and COOP data covered the simulation period up to 2010 and the values for 2011-2013 were exclusively estimates from the IEM. The IEM itself used the NWS climate data to estimate values for arbitrary geographic locations (Herzmann et al., 2013).

Model Development

Watershed Delineation

ArcSWAT incorporated the ArcHydro extension for watershed delineation (Maidment, 2002). Figure 3-4 diagrams the procedure for delineation. ArcHydro required the DEM as input data, a polygon or raster mask covering the study area, and a user-defined minimum catchment area threshold. The minimum catchment threshold determined the number of subbasins and reaches in the model in an automated delineation procedure (Jenson & Domingue, 1988). The catchment area defined for model development was 1% of the total watershed area or 327 km^2; that catchment threshold and resulting subbasin output was sufficient for simulating the hydrologic and nitrogen processes in this dissertation (Jha et al., 2004).

The delineation process followed the general workflow: (1) identify sinks or depression areas in the DEM, (2) fill the sinks, (3) calculate flow direction based on surrounding grids, (4) calculate flow accumulation based on flow direction, and (5) define the initial stream network and their segmentation using the mask, catchment area threshold, and flow accumulation, (6) add or remove outlets and (7) calculate subbasin and channel geometry to finalize the watershed polygon. Steps (1) and (2) were skipped because the DEMs from the NED have been pre-processed or hydro-flattened. Raw or bare-earth DEMs contained the elevations of all points on the surface including that of stream obstructions, bridges, wave elevations, depending on the resolution of the DEM. Were the obstructions not flattened, the flow direction and accumulation

44

steps may not perform efficiently or may generate small catchments that do not drain to the subbasin or whole watershed outlet (Martz & Garbrecht, 1998). Steps 4 and 5 were performed for the grids within the bounding mask. Step 4 generated a raster grid of slope values that will be a necessary input dataset for the *HRU Definition* stage.

The outlets added in step 6 represented the USGS gage stations; while the stations are geographic locations, each additional outlet created a subbasin and stream segment upstream of the point. The nutrient loads and water discharge exiting these points were the simulated values for comparison to the observed dataset during calibration. A gage station may be located near an existing outlet generated in step (5) and that nearby point was removed to avoid having a small subbasin between the existing point and the stream gage station. The subbasin would only increase computation time without providing any substantial granularity to the model. The removal of nearby existing points may not be preferred if they were confluences for large or otherwise independent upstream subbasins. Such removals may combine upstream subbasins into a larger subbasin, losing granularity.

Step (6) also allowed the addition of point sources and pools that are similar to but do not function as subbasin outlets. Point sources added water discharge and constituents much like outlets from upstream reaches; however, the source of the loadings or discharge was not from the HRU but from an external user-supplied data, synthetic or observed. No point sources were added to the watershed for this dissertation. Pools or other small water bodies were abstracted in a way that resembles an HRU. SWAT defined and simulated three types of pools: reservoirs, perennial wetlands/ponds, and depression/potholes. They had no explicit spatial location like HRUs and received loadings and flow from some fraction of the subbasin area. The exception was a reservoir, which was placed on the main channel network and thus received inputs from all upstream subbasins. Volume in the pool may increase with precipitation and decrease through evaporation. A separate QUAL2E module simulated nutrient dynamics in the pools. Computationally, pools in SWAT functioned as HRUs without soil layers and can undergo water-phase nutrient dynamics and transformation. The discharge and mass loading, which exits

45

a pool, entered the stream for the subbasin in which the pool exists or downstream of the main stem in the case of reservoirs.

Only one pool was added to the model: the Coralville Reservoir. This reservoir was a controlled water body with protocols that govern discharge external to surface geography; the protocols must be explicitly defined by the user. The Army Corps of Engineers Rock Island District managed this reservoir and provided some general protocols that correspond to the parameters that SWAT requires for reservoir simulation: the target storage in the reservoir for various times in the year and the reservoir volume until the water level reaches the principal and emergency spillway to avoid flooding of the area in proximity to the reservoir. The water level and target storage governed the discharge rate into the downstream reach. Table 3-7 summarizes the parameters for Coralville Reservoir.

After the outlets/gages were removed/added and the reservoir defined, the last user step was manually defining the location of the whole watershed or terminal outlet for the basin. ArcHydro finished the delineation process by eliminating outlets and reaches that do not connect to the main stream network, resulting in the final stream network and reach segmentation. The boundaries of the subbasins were defined by the edge of first order grids of flow direction and accumulation. The remaining geometry such as channel width, depth, and average slope were also calculated using the DEM. Table A-1 in the Appendix and Figure 3-5 summarizes the resulting watershed and channel geometry of 67 subbasins and their corresponding reach channels.

HRU Definition

As explained before SWAT had two distinct, but linked computational phases on the land/subsurface and in the streams/ponds. The separation allowed the two phases to operate at different granularities. The model configuration for this dissertation was that of approximately HUC-8 scale subbasins with multiple HRUs per subbasin. The HRUs were a combination of three categorical variables: slope class, soil type, and LULC. The first step was to overlay the

46

four maps containing the subbasins, slope classes, soil types, and LULC into one map. For each subbasin the grid cells for each slope-soil-LULC combination were summed and divided by the total number of cells for the subbasin. This process abstracted HRUs as area fractions of the subbasin and two or more subbasins may contain identical HRUs. An HRU's characteristics governed its hydrologic and nutrient processes, but its subbasin controlled where the outputs route.

Given the numerous LULC and soil types in the basin, the number of unique HRUs for a given subbasin can be large, numbering in the thousands. Many of these HRUs' area fractions can be very small, possibly on the scale of one grid cell. Because HRUs were not spatially explicit and depended on their area fraction, the contribution of such small individual HRUs were miniscule and well below the uncertainty of the observed dataset to which the model calibrated. Thus another step was the defining a threshold for the slope, soil, and LULC maps. If a class from these three variables falls below the area coverage of a given subbasin, ArcSWAT removed that HRU and distributed its area to the remaining HRUs proportional to their size. The threshold used for the model development was 5% for all three variables.

For example HRU 1 in Subbasin 2 was defined as 8%+ slope, Lester soil type, and rye LULC. Rye covers less than 5 percent of Subbasin 2's area and so ArcSWAT removed HRU 1 from the subbasin. The removal process repeats for all such HRUs whose classes fell under 5 percent. The sum area fraction of the removed HRUs were then distributed to the remaining HRUs proportional to their fractions:

Equation 3-1
$$f_j \sum_i^n A_i = \Delta A_j \mid f_j = \frac{A_j}{\sum_j^m A_j}$$

A_i was the area of a removed HRU, A_j the area of the j'th remainder HRU, ΔA_j the addition of area to the j'th remainder HRU, and the f_j the fraction of HRU j over the sum of all remaining HRUs.

47

After this procedure the model shrank considerably, reducing the total number of HRUs from 26,841 to 2,538 HRUs. As each HRU consumed the equivalent amount of computation time, with small differences depending on the number of soil layers, the reduction allowed a multi-decadal simulation to be run on the order of minutes versus hours for a full model on a personal computer. The downside to the thresholding procedure was the loss of rare slope, soil, or LULC classes for a subbasin. Once a class was removed from the model, the user had two options: restart the HRU definition process or, after generating the SWAT input files, edit each HRU-level file to match the characteristics of the lost classes. To properly incorporate land use change into SWAT, two models were created, with and without threshold, or henceforth *sparse* and *full* models. The sparse model was used in calibration to reduce the simulation time, the number of simulations, and the number of input files or HRUs modified. The full model was used for simulating LULC or climate scenarios, using the calibrated parameters from the sparse model. The calibration modified parameters on a subbasin and reach scale, but the structure remains the same for both sparse and full models.

Land Management

The next step for the ArcSWAT mediated model development was the generation of solar radiation, relative humidity, and wind speed from ArcSWAT's internal weather databases and formatting precipitation and temperature time-series into a form that the SWAT executable can read. With all inputs entered, ArcSWAT next generated a database containing the input files and model configuration with default values for all the modules. At this stage the user may edit the database to change parameters or specify management operations on HRUs. Most of these management operations focused heavily on agriculture: dates for planting, fertilizing, tilling, and harvest. In particular tiles were added to all corn and soybean HRUs at a depth of one meter below the surface. Areas with urban land cover may also have management options for activities such as street cleaning. The reservoir parameters may be modified or added here as well. The user had a wide array of options to pursue, depending on his or her objectives.

48

For the purpose of this dissertation, the management operations can be classified into two types: agricultural and non-agricultural. The agricultural lands include all crops—with the exception of alfalfa and pasture—and non-agriculture is everything else. All agricultural lands have the following sequence of management: (1) auto-fertilization, (2) planting/start of growing season, (3) harvest/end of growing season, and (4) generic fall tillage. Auto-fertilization was a subroutine that added nitrate salts as fertilizer whenever a crop undergoes nitrogen stress, i.e. the soil does not contain enough available nitrogen for optimal plant growth. The exact fertilizer setting in SWAT was "elemental nitrogen," which was equivalent to the direct application of nitrate to the soil. The application quantity (kg/ha) and nitrogen stress depended on the crop and ArcSWAT provided a database for these values. The timing of these sequence was based on heat units. A heat unit (HU) was the accumulated temperature or growing degree days (GDD) above some base temperature (T_{base}), usually 20°C, over time.

Equation 3-2 $$HU = GDD = \frac{T_{max} + T_{min}}{2} - T_{base}$$

T_{max} and T_{min} are the maximum and minimum daily temperatures, respectively. If the average daily temperature is below 20°C, then no HU was added to the accumulated total for that day.

Each crop had a HU value for which "maturity" is reached. Given a temperature time-series, the model can schedule the operations by specifying them as fractions (HUSC) relative to the crop's maturity HU. For example corn required 1500 HU to mature. The user scheduled the fertilization at 0.01 HUSC, planting at 0.15 HUSC, harvest at 1.2 HUSC and fall till at 1.5 HUSC. Translating into a HU reference: fertilization began at 15 HU or when the accumulated mean daily temperature above 20°C was equal to 15 (nominally in units of °C). Planting began at 225 HU, harvest at 1800 HU, and fall till at 2250 HU. The HU counter reset with the last operation for that year. For non-agricultural HRUs the only difference was the absence of fertilization and tillage. The harvest operation removed part of the plant biomass out of the system and allowed the remaining biomass to become plant residue for soil nutrient dynamics.

49

For unmanaged vegetation such as forests, the non-harvested biomass was considered to be the portion of the plant that does not die and stays dormant during the non-growing season. Urban HRUs were part of the non-agricultural land areas and typically had some grass or turf; because urban land area was relatively small in the ICRB, fertilizer application was not included in their management operations. Once the user specifies the management operations, ArcSWAT automatically generated SWAT input files into the proper format used by the SWAT executable. The simulation period was set by the user in a master control file. The simulation period cannot be longer than the observed data's time period.

Land Use Update

The last step before properly starting the historical or control time-period simulation was the incorporation of historical land use change. SWAT simulated land use change as the modification of HRU area fraction within a subbasin. SWAT2009_LUC (Pai & Saraswat, 2011) was a tool developed at the University of Arkansas to process raster LULC grids into SWAT input files that redefined HRU area fraction over time. The tool used the watershed and subbasin boundaries to count the number of cells that an LULC occupies in a new map and assigned a new area fraction. This process was done separately for the sparse and full model. SWAT2009_LUC summed the grid cells with LULC that do not exist in the subbasin and reassigned them to the remaining HRUs, which was the same process for HRU definition with thresholds.

The Iowa DNR had data for 1990, 1992, and 2002. The CDL had data continuously from 2002 through the present year; however, the earlier maps were not complete and lacked large parts of the ICRB. The Iowa DNR maps themselves were incomplete and missed a small portion of the watershed that lies in Minnesota. Because the SWAT2009_LUC tool required inputs raster grids that included the boundary of the watershed, a methodology was developed to composite the maps into a complete LULC time-series (Figure 3-7).

The user started with a mask that was equivalent to the watershed boundary and a LULC map that may or may not be complete. The mask clipped the LULC map for any area that the

50

mask covered. If the LULC clipped area covered the mask, then the clipped LULC map fed directly into the SWAT2009_LUC module. If the clipped area did not cover the entire watershed, then that portion which was missing sourced data from a map of the previous or next year, depending on whichever is available. The missing area was clipped from a different year's map and then composited into a complete map to be fed into SWAT2009_LUC. The process was repeated for all years until the last year for which LULC data were available. For years where large portions of the watershed were missing, a LULC update was not created for that year. For example, the 2003 CDL map covered only the area of the ICRB in Minnesota.

The results could be quite disjointed such as the DNR maps with their Minnesota portion clipped from a CDL map. The process was not perfect, but given that HRUs were not spatially explicit and the need to account for crop rotation and periodicity, a spatially broken LULC map which accounts for some LULC change was perhaps better than assuming no change at all. The land use change scenarios in Chapter 7 exploited SWAT's LULC update capability by either feeding new maps or manipulating the area fractions directly. With the final step for model development done, calibrating the model parameters to best fit the observations came next.

Table 3-1   Soil type distribution in the ICRB

Series Name	Area Coverage (%)	Hydrologic Soil Group	Layers Simulated	Maximum Depth (mm)
Bassett	0.46	B	3	1854
Bixby	0.02	B	3	1524
Blooming	0.52	B	4	1524
Blue earth	0.31	B	3	1524
Canisteo	0.97	B	4	1524
Clarion	12.2	B	3	1524
Clinton	2.48	B	3	2032
Clyde	0.80	B	4	1524
Coland	1.47	B	3	1524
Colo	9.43	B	3	1524
Dinsdale	11.5	B	3	1854
Downs	5.77	B	4	1524
Estherville	0.45	B	3	1524
Fayette	0.02	B	3	1854
Hayden	0.09	B	3	1524
Kenyon	10.8	B	3	1930
Kilkenny	0.46	B	3	1524
Kossuth	1.03	B	3	1524
Ladoga	1.35	B	3	1524
Lester	3.25	B	3	1524
Mahaska	0.97	B	3	1778
Marna	0.52	C	3	1524
Marshan	0.81	B	4	1524
Maxcreek	0.47	B	4	1600
Maxfield	0.11	B	3	1676
Otley	3.76	B	3	1854
Readlyn	1.23	B	3	1524
Rockton	1.68	B	4	813
Rossfield	0.03	B	3	1524
Sargeant	0.43	D	4	1625
Skyberg	0.29	C	4	1676
Sparta	2.70	A	3	1524
Spillville	6.44	B	2	1524
Tama	14.9	B	3	1524
Titus	0.42	B	3	1575
Tripoli	1.12	B	3	1676
Udolpho	0.54	B	5	1524

52

Table 3-2   ArcSWAT modification on STATSGO database

Characteristic Name	SWAT Variable from Chapter 2	Description
NLAYER	$j_1, j_2, \ldots, j_n$	Number of layers
HYDGRP	not in Chapter 2	Hydrologic group for *CN* classification
SOL_ZMX	$z_{j,max}$	total soil column depth
SOL_ALB	not in Chapter 2	moist soil albedo for temperature calculations
ANION_EXCL	θ_e	fraction of porosity from which anions are excluded
USLE_K	not in Chapter 2	soil erodibility factor for universal soil loss equation
SOL_Z(j)	z_j	depth of soil layer j
SOL_CLAY(j)	m_c	clay content in the j'th layer
SOL_SILT(j)	not in Chapter 2	silt content in the j'th layer
SOL_SAND(j)	not in Chapter 2	clay content in the j'th layer
SOL_ROCK(j)	not in Chapter 2	rock fragment in the j'th layer
Texture	(not used by SWAT)	USDA soil texture descriptor
SOL_BD(j)	ρ_b	soil bulk density in the j'th layer
SOL_AWC(j)	*AWC*	plant-available water capacity
SOL_K(j)	$K_{sat,j}$	saturated hydraulic conductivity in the j'th layer
SOL_CBN(j)	C_{org}	organic carbon content in the j'th layer
SOL_EC3(j)	not in Chapter 2	electrical conductivity in the j'th layer

Table 3-3   SWAT land use and cover classes in the ICRB

Code	Area (%)	Name	Plant Equivalent for EPIC Crop Growth Model
AGRL	0.19	Agricultural Land—Generic	Grain Sorghum
AGRR	2.40	Agricultural Land—Row Crops	Corn
ALFA	1.93	Alfalfa	-
BARR	0.05	Barren	none
CORN	42.94	Corn	-
FRSD	0.05	Deciduous Forest	Oak
FRSE	0.06	Evergreen Forest	Pine
FRST	<0.01	Mixed Forest	Oak
LIMA	0.02	Lima Beans	-
OAK	4.40	Oak	-
OATS	<0.01	Oats	-
PAST	5.04	Pasture	Alamo Switchgrass
PEAS	0.02	Peas	-
RNGB	0.25	Range-brush	Little Bluestem
RNGE	15.06	Range-grass	Little Bluestem
RYE	<0.01	Rye	-
SGBT	0.00	Sugarbeet	-
SOYB	24.28	Soybeans	-
SWHT	0.00	Spring Wheat	-
UIDU	0.72	Industrial/Commercial	Bermuda Grass
URBN	1.06	General Urban/Residential	Bermuda Grass
URHD	<0.01	High-Density Residential	Bermuda grass
URLD	0.02	Low-Density Residential	Bermuda Grass
URMD	<0.01	Medium-Density Residential	Bermuda Grass
UTRN	0.51	Infrastructure/Transportation	Bermuda Grass
WATR	0.74	Open Water	none
WETF	0.12	Forested Wetland	Oak
WETN	0.13	Non-Forested Wetland	Alamo Switchgrass
WWHT	<0.01	Winter Wheat	-

54

Table 3-4   Iowa DNR land use classes and SWAT equivalent

Iowa DNR LULC	SWAT LULC Code	SWAT LULC Name
water	WATR	Open Water
wetland	WETN	Non-Forested Wetland
bottomland forest	OAK	Oak
coniferous forest	FRST	Pine
deciduous forest	OAK	Oak
ungrazed grassland	RNGE	Range-grass
grazed grassland	PAST	Pasture
alfalfa	ALFA	Alfalfa
corn	CORN	Corn
soybeans	SOYB	Soybeans
other rowcrop	AGRR	Agricultural Land—Row Crops
roads	UTRN	Infrastructure/Transportation
commercial industrial	UIDU	Industrial/Commercial
residential	URBN	General Urban/Residential
barren	BARR	Barren

Table 3-5   2001 NLCD Land use classes and SWAT equivalent

NLCD LULC	SWAT LULC Code	SWAT LULC Name
Open Water	WATR	Open Water
Developed, Open Space	URLD	Low-Density Residential
Developed, Low Intensity	URLD	Low-Density Residential
Developed, Medium Intensity	URMD	Medium-Density Residential
Developed, High Intensity	URHD	High-Density Residential
Deciduous Forest	OAK	Oak
Evergreen Forest	PINE	Pine
Mixed Forest	OAK	Oak
Shrub/Scrub	RNGB	Range-shrub
Grassland/Herbaceous	RNGE	Range-grass
Pasture/Hay	PAST	Pasture
Cultivated Crops	AGRR	Agricultural Land—Row Crops
Woody Wetlands	WETF	Forested Wetland
Emergent Herbaceous Wetland	WETN	Non-Forested Wetland

55

Table 3-6   2012 USDA CDL land use classes and SWAT equivalent

CDL LULC	SWAT LULC Code	SWAT LULC Name
Open Water	WATR	Open Water
Barren	BARR	Barren
Deciduous Forest	OAK	Oak
Evergreen Forest	PINE	Pine
Mixed Forest	OAK	Oak
Developed/Open Space	URLD	Low-Density Residential
Developed/Low Intensity	URLD	Low-Density Residential
Developed/Med Intensity	URMD	Medium-Density Residential
Developed/High Intensity	URHD	High-Density Residentia
Grassland Herbaceous	RNGE	Range-grass
Shrubland	RNGB	Range-brush
Herbaceous Wetlands	WETN	Non-Forested Wetlands
Woody Wetlands	WETF	Forested Wetlands
Corn	CORN	Corn
Lima Beans	LIMA	Lima Beans
Oats	OAT	Oats
Peas	PEAS	Peas
Soybeans	SOYB	Soybean
Sugarbeet	SGBT	Sugabeet
Sweet Corn	CORN	Corn
Rye	RYE	Rye
Spring Wheat	SWHT	Spring Wheat
Winter Wheat	WWHT	Winter Wheat
Alfalfa	ALFA	Alfalfa
Pasture/Hay	PAST	Pasture
Other Hay/Non Alfalfa	PAST	Pasture

56

Table 3-7　　Reservoir parameters provided the U.S. Army Corps of Engineers

SWAT Variable	Value	Units	Description
RES_EVOL	51929	$10^4 \, m^3$	Volume of water needed to fill reservoir to emergency spillway
RES_PVOL	3462	$10^4 \, m^3$	Volume needed to fill reservoir to principal spillway
STARG(1)	3462	$10^4 \, m^3$	Target reservoir storage for January
STARG(2)	3067	$10^4 \, m^3$	Target reservoir storage for February
STARG(3)	2374	$10^4 \, m^3$	Target reservoir storage for March
STARG(4)	1942	$10^4 \, m^3$	Target reservoir storage for April
STARG(5)	2482	$10^4 \, m^3$	Target reservoir storage for May
STARG(6)	3462	$10^4 \, m^3$	Target reservoir storage for June
STARG(7)	3462	$10^4 \, m^3$	Target reservoir storage for July
STARG(8)	3462	$10^4 \, m^3$	Target reservoir storage for August
STARG(9)	3889	$10^4 \, m^3$	Target reservoir storage for September
STARG(10)	4316	$10^4 \, m^3$	Target reservoir storage for October
STARG(11)	4316	$10^4 \, m^3$	Target reservoir storage for November
STARG(12)	3876	$10^4 \, m^3$	Target reservoir storage for December
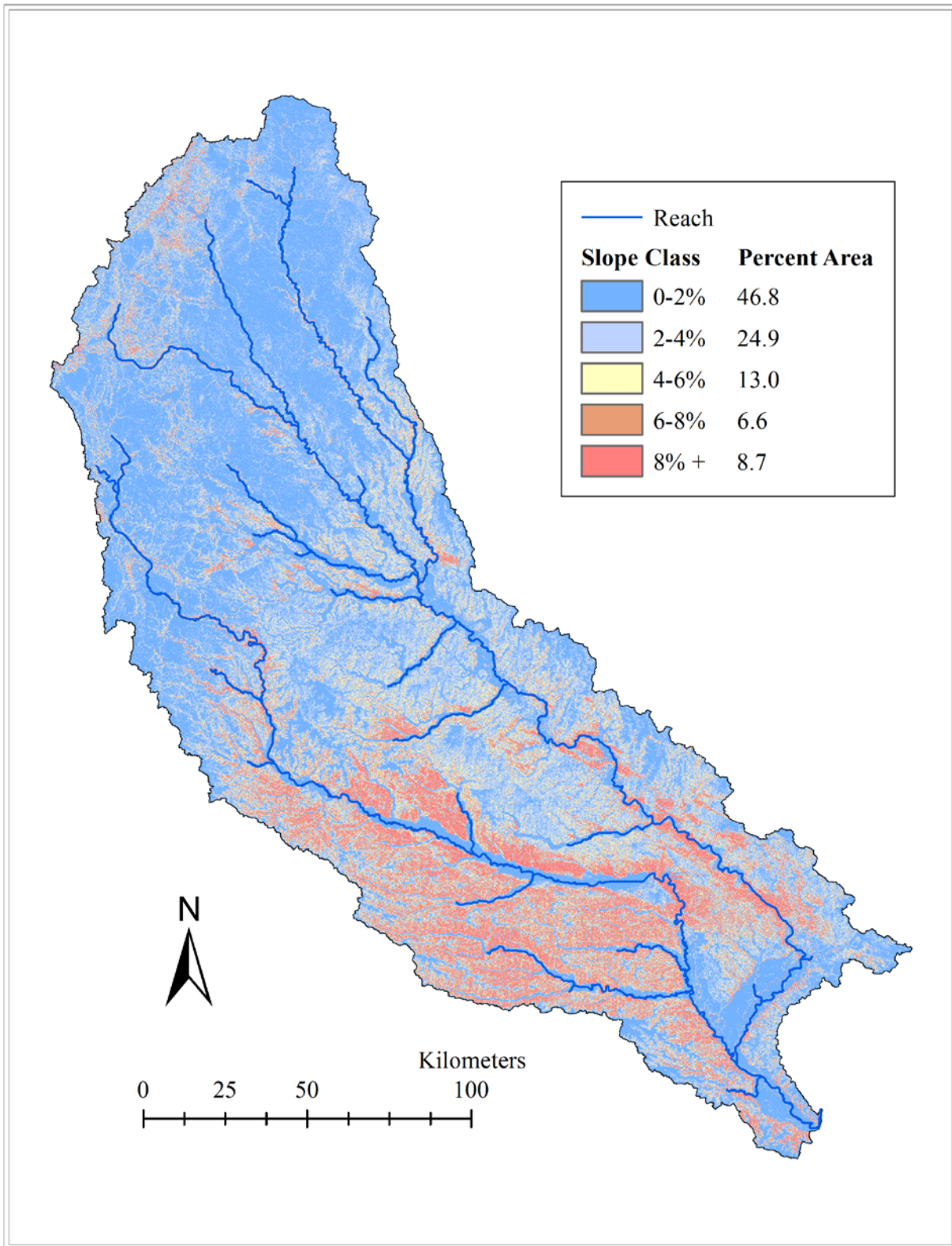
Figure 3-1   Slope class distribution for ICRB
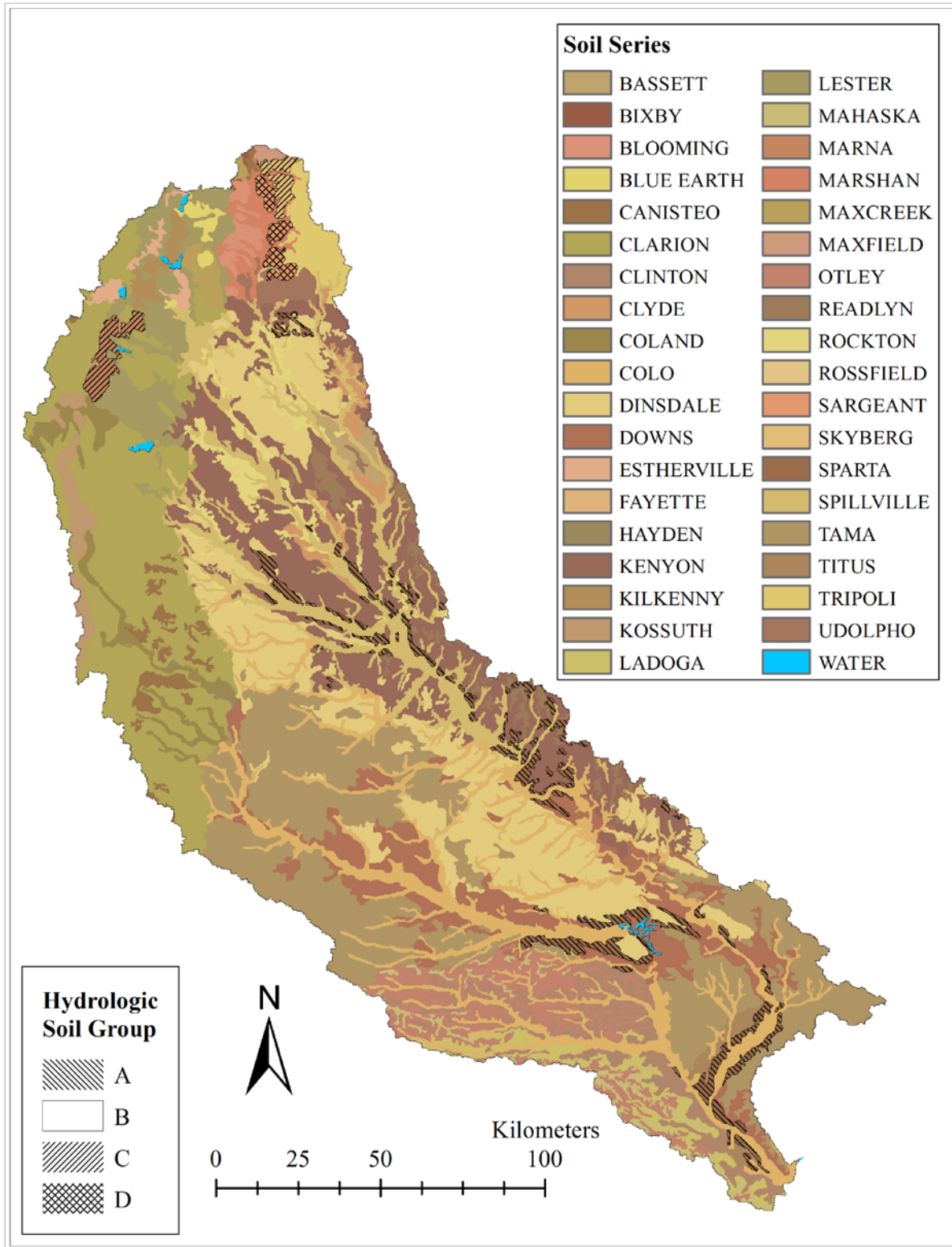
Figure 3-2   STATSGO soil type distribution for ICRB

1985 Land Use and Cover

General Urban		Pasture	
Transportation		Oak	
Industrial		Forest-Evergreen	
Wetlands-Non-Forested		Forest-Deciduous	
Wetlands-Forested		Corn	
Open Water		Barren	
Soybean		Alfalfa	
Range-Grasses		Row Crops	
Range-Brush		Agriculture (Other)	
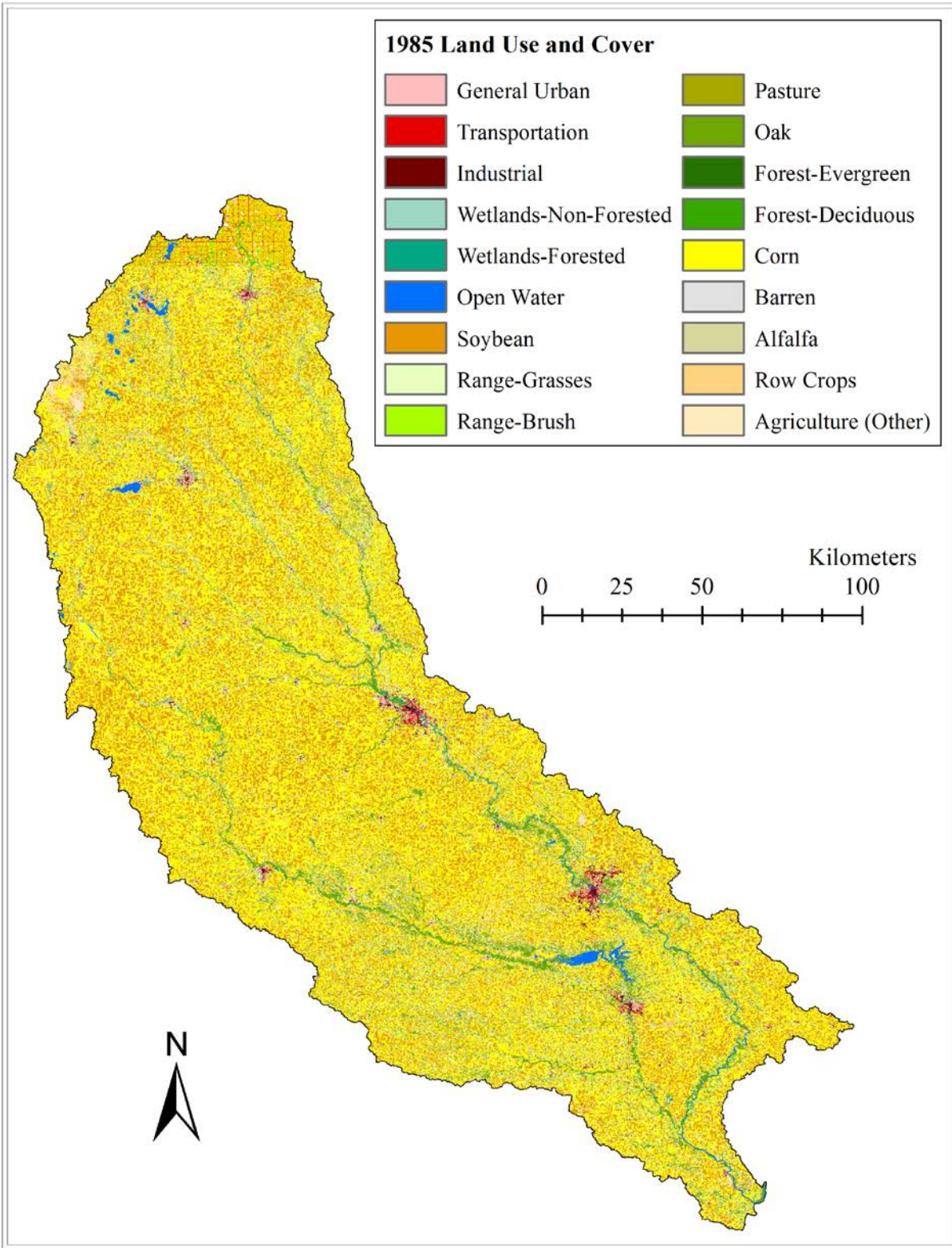
Figure 3-3   Land use or cover distribution for the ICRB in 1985 and at the start of the historical simulation period
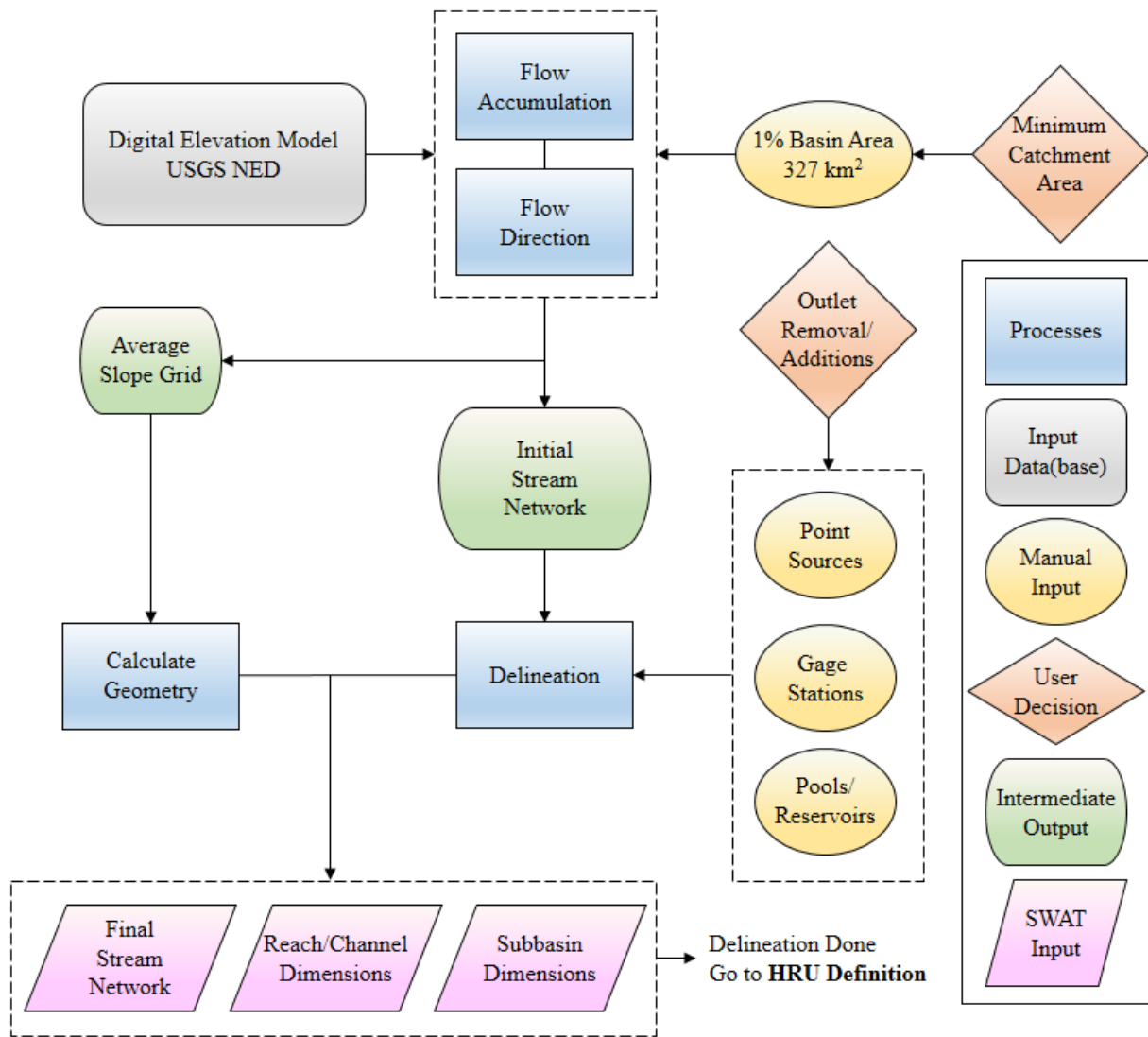
Figure 3-4   Watershed delineation flowchart, summarized from the ArcHydro software
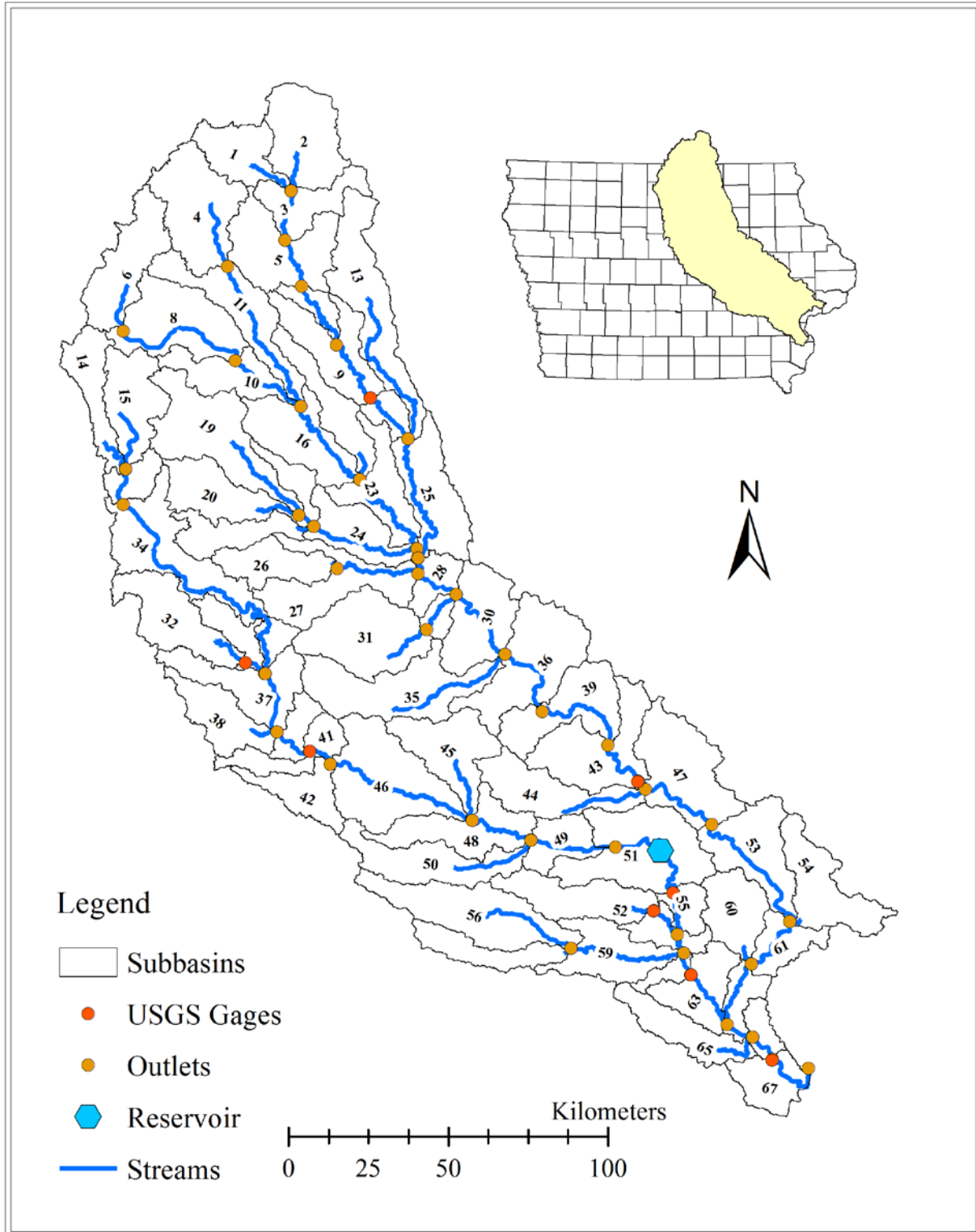
Figure 3-5   Results from watershed delineation
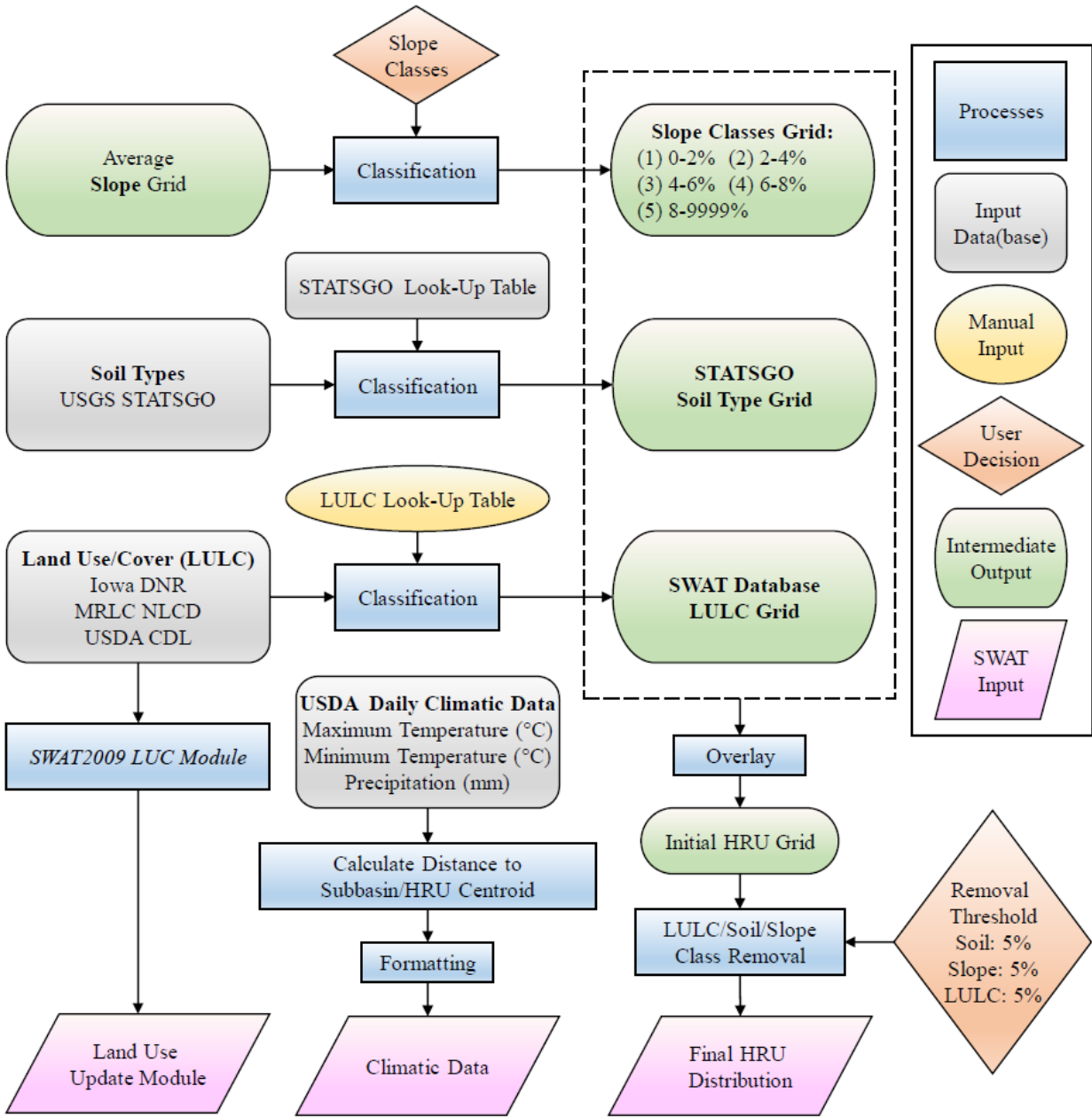
Figure 3-6   HRU definition flowchart using ArcSWAT software
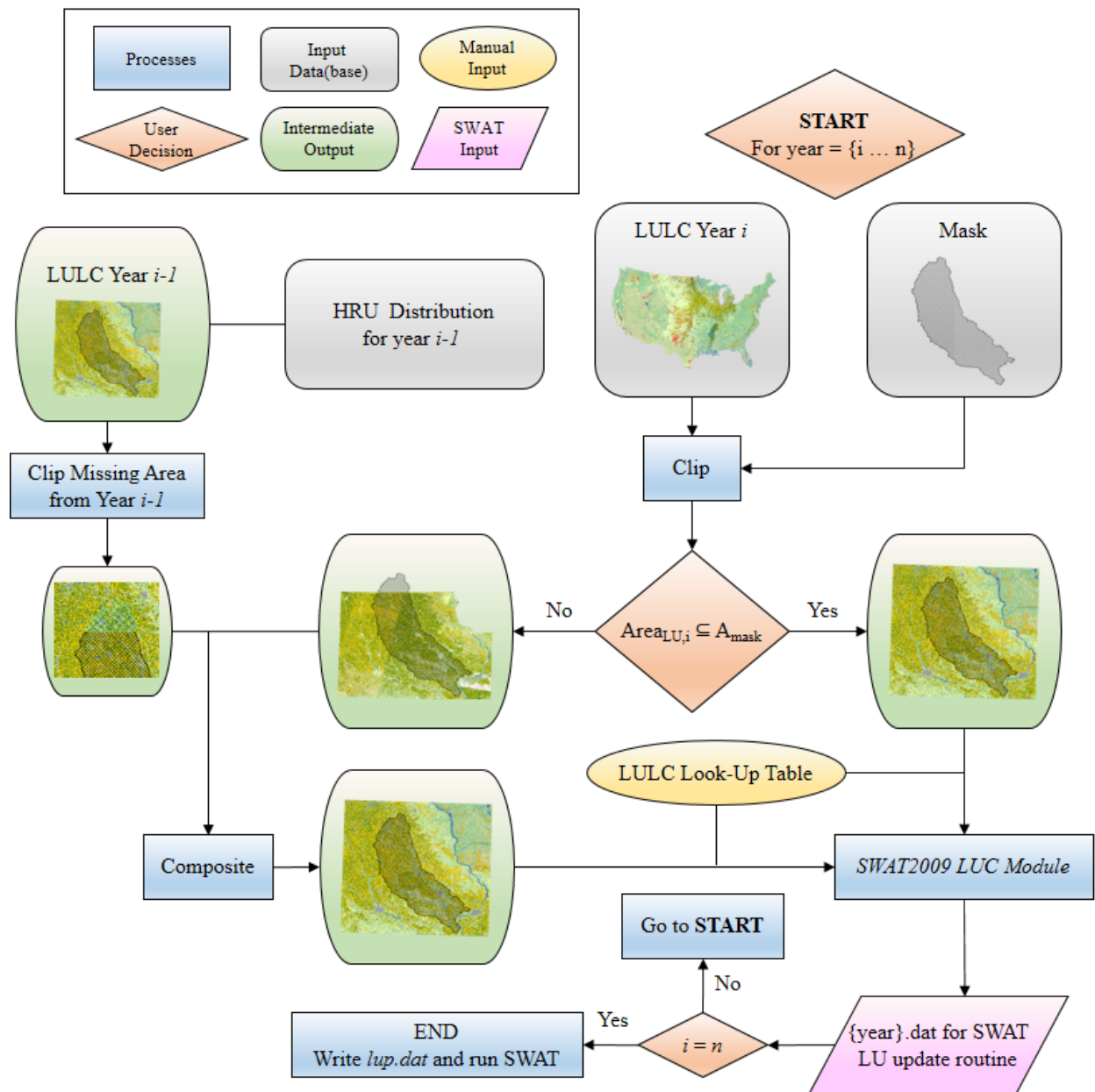
Figure 3-7   Algorithm to generate land use rasters from multiple sources with temporal and spatial gaps
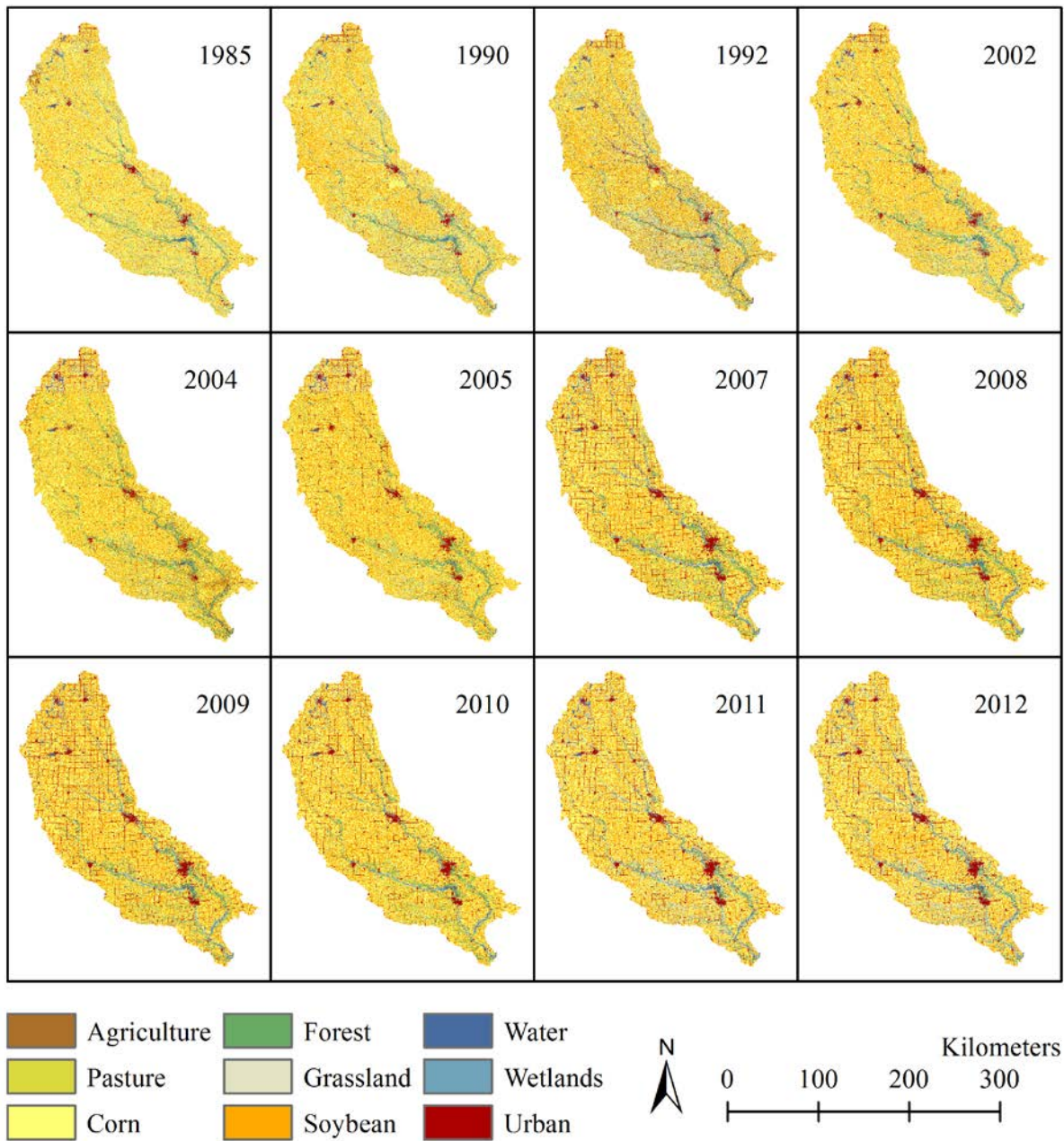
Figure 3-8   LULC rasters generated from USDA-CDL, NLCD, and Iowa DNR from
algorithm described in Land Use Update

CHAPTER 4: MODEL CALIBRATION AND SENSITIVITY'

Introduction

SWAT was a highly parameterized model with many modules, often based on empirical relationships (Whittaker et al., 210). The databases included in ArcSWAT contained the accumulated research for the behavior of soil and plant types (Harmel et al., 2006); those parameters that were not empirical could be coarse in resolution (Cotter et al., 2003). Calibration was the procedure for tuning these parameters to values that yielded a simulation that best fit the observation datasets. Preceding calibration was parameter selection because the model displayed different sensitivities to different parameters, especially as one considered the study area's characteristics. The ICRB was a large basin and collecting detailed data for these parameters was prohibitively expensive and any field data that were collected would be sparse and spatially unrepresentative.

One path to account for the model's complexity and the ICRB's size and variation was a procedure automating calibration and sensitivity analysis simultaneously. The sensitivity analysis portion of the combined procedure initializes with an exhaustive list of relevant parameters pulled from the literature and the numerical ranges that these parameters would be expected to fall under for the study area. These parameters were drawn from Table 2-4, Table 2-5, Table 2-6, and Table 3-2 and described in previous chapters. The procedure evaluated the model sensitivity to a parameter after each "iteration" or a series of runs that sampled from the n-dimensional parameter "space" where parameter ranges lie with n being the number of parameters. The sensitivity analysis culled those parameters whose sampled values had small or negligible changes to the "objective" function between the observed and simulated values, a metric to evaluate the model's performance. The combined procedure blurred the distinction between sensitivity analysis and calibration because each iteration incorporated both.

The autocalibration algorithm employed was Sequential Uncertainty Fitting (SUFI) (Abbaspour et al., 2004) and executed with the SWAT Calibration and Uncertainty Procedures

66

software suite (SWAT-CUP) (Abbaspour et al., 2007a). The sensitivity analysis employed a generalized additive model (GAM), a non-parametric regression technique to detect non-linear relationships between explanatory variables (the parameters) and the objective function outputs from an iteration's simulation. The combined autocalibration and sensitivity procedure first operated on a calibration or control period and then validates using those parameters that remain after a sensitivity analysis with a validation or test period. The validation step was a separate and parallel iteration initiated by the user after an arbitrary number of iterations covering the calibration period. The validation used the same parameter sample sets and the results of the validation iteration only informed whether the user should go back to a previous calibration iteration, thus having no direct influence on the final parameter values. For mean monthly stream discharge, the calibration period was 1978-2002 and the validation period 2003-2012. For mean daily nitrate loading and concentrations, the calibration period was 2009-2011 and the validation period 2012-2013.

Methods

Objective Functions

Objective functions measure a model's performance with respect to how well the model simulates the observations. The autocalibration steps ran multiple simulations for an iteration and calculated those simulations' objective function outputs. The outputs then determined the parameter space of the next iteration. Thus the choice of objective function was a critical part in employing autocalibration methods as the path that the calibration took and the parameter values that they converged to were predicated on the objective function (Legate & McGabe, 1999). The same could be said for sensitivity analyses that use objective functions to evaluate parameter sensitivity. Performance of the model with respect to objective functions were collectively measured by goodness-of-fit (GOF) statistics.

67

The objective function was the minimization of errors between the model results and the observations, a metric used by the Nash-Sutcliffe Efficiency (NSE) goodness of fit statistic where Q is discharge or any other parameter:

Equation 4-1
$$\text{NSE} = 1 - \frac{\sum_i^n \left(Q_{sim}^i - Q_{obs}^i\right)^2}{\sum_i^n \left(\bar{Q}_{obs}^i - Q_{obs}^i\right)^2} \in (-\infty, 1]$$

The NSE measured the ratio of the mean-squared-error (MSE) between the observations and simulated outputs to the variance of the observations. The NSE was a robust measure of GOF in hydrologic modeling (McCuen et al., 2006). The "acceptable" GOF for SWAT simulations depended on the statistic, the simulation's time-step, and the output of interesting. The SWAT literature (Moriasi et al., 2007) reported the acceptable values for stream discharge at NSE=0.60 for the monthly time-step and NSE=0.50 for the daily time-step. For daily nitrate loading or concentrations, the acceptable value was NSE=0.50.

While NSE was the GOF statistic for the autocalibration and sensitivity analysis, other statistics are important for evaluating model performance. Another GOF statistic this dissertation used was the percent bias (PBIAS), which calculated the ratio of the summed absolute model errors to the sum of the observations:

Equation 4-2
$$\text{PBIAS} = 100 \times \frac{\sum_i^n \left(Q_{sim}^i - Q_{obs}^i\right)}{\sum_i^n Q_{obs}^i} \in (-\infty, +\infty)$$

PBIAS was a general measure of the model's performance, evaluating the absolute magnitude of the model errors relative to the observations, giving the user a sense of whether the model was under- or over-predicting the observations. A PBIAS approaching zero was a good indicator of model performance.

Widespread in pure statistical models, the squared Pearson product-moment correlation coefficient or the coefficient of determination (R^2) was also present for comparison:

Equation 4-3
$$R^2 = \left[\frac{\sum_i^n (Q_{obs}^i - \bar{Q}_{obs})(Q_{sim}^i - \bar{Q}_{sim})}{\sqrt{\sum_i^n (Q_{obs}^i - \bar{Q}_{obs})^2 \sum_i^n (Q_{sim}^i - \bar{Q}_{sim})^2}} \right]^2 \in [0,1]$$

R^2 measured the linear correlation or statistical dependence between the observations and simulations. The acceptable R^2 in the SWAT literature for stream discharge was 0.70 at the monthly time-step and 0.60 at the daily time-step. The acceptable nitrogen discharge R^2 for the daily time-step was 0.60. While well-known and widely used, the pitfalls of using R^2 as the GOF statistic for calibration were that the statistic measured the degree of linear dependence irrespective of the difference in magnitudes between the observations and simulations. Equation 4-3 demonstrated this aspect: the simulated values Q_{sim} appeared in both the denominator and numerator whereas NSE (Equation 4-1) had only the observed values Q_{obs} in the denominator. Thus if the simulations and observations were consistently off by an order of magnitude, a good R^2 statistic would still result but the NSE would report otherwise (Krause et al., 2005).

Parameter Sampling

For the *k*'th *run* or single simulation of an iteration, the model required a parameter set $\vec{P}_k$. The parameter set contained the changes or replacement to the parameters of interest, explicitly tied to one run of one iteration. All parameter sets for an iteration were determined before the iteration begins by sampling values from each parameter's range, a user-defined interval. The collective ranges for all parameters were called the parameter *space*. The sampling method was the Latin hypercube that sampled from the parameter space equally probable values (McKay et al., 1979). For example in a two-parameter sample space where a square grid represented all parameter value combinations, a Latin square was one where the sample positions are such that there was only one sample location in each row and column. The "hypercube" generalized to higher order dimensions or when the number of parameters exceed three.

69

Because some parameters depended on HRU and subbasin characteristics, the change had two methods. One method was the "relative" change or: $p_{new} = p_{init} \times (1+r)$ where p was the parameter's numerical value and r was a factor in the interval [-0.5, 0.5]. The other method was "replace" where the sampled value was in the same units as the parameter and applied over the subbasin or entire basin for global parameters. In general if a parameters' values varied with HRU or subbasin, the relative method was used. If the parameter was constant for the entire basin regardless of location, then the replace method was used. The initial list of parameters was drawn from the Table 2-4, Table 2-5, Table 2-6, and Table 3-2. The initial iteration contained the parameters that were either user-defined or came from a database.

Sensitivity Analysis

The typical approach to model calibration required performing the sensitivity analysis first and then adjusting those sensitive parameters (White & Chaubey, 2005). In these cases a one-at-a-time (OAT) analysis was the most basic method where the model, given default parameter values, was allowed to vary one parameter while others are kept constant. The relative sensitivity was then calculated from available observational output data from the gage stations (Saltelli et al., 2000):

Equation 4-4 $$S_r = \left(\frac{x_0}{y_0}\right)\left(\frac{\Delta y}{\Delta x}\right)$$

S_r was the relative sensitivity, x_0 the initial parameter value, y_0 the initial objective function output for an observed variable, Δx an arbitrary change in the parameter value, and Δy the change in the objective function with respect to the parameter change. Being a local technique, relative sensitivity did not account for interactions between variables.

The Latin hypercube parameter sampling method yielded parameters sets that were equally probable and distributed in the parameter space. The runs from these sets produced outputs and a set of NSEs. To account for interactions between parameters, one can develop a

70

multivariate regression where the parameters were the explanatory variables and the objective function the response variable: $\text{NSE} \sim \beta_0 + \sum_i^n P_i \cdot \beta_i$. This multivariate regression assumed that the parameters have linear and additive effects with the β_i coefficients acting as weights. For a complex model with many modules and nonlinear components, linearity may not be appropriate (Cukier et al., 1978). To account for non-linear parameter influences in the sensitivity, a generalized additive model (GAM) was used as the basis of the sensitivity analysis.

Generalized additive models were non-parametric forms of the generalized linear model (GLM), which expanded the ordinary least squares regression to response variables whose error or residual distributions were not normal (Hastie & Tibshirani, 1990). A parametric model had an explicit form; e.g. $y \sim \beta_0 + \beta_1 x + \beta_2 x^2 + \dots$. The coefficients were determined by minimizing the sum of squared errors between the model and observations. A non-parametric model relaxed this requirement and had the explanatory variables be an unknown smooth function. The smooth functions themselves may contain coefficients or parameters, but these coefficients had no explicit connections to the physical system being modeled. For example an ordinary regression of population against with time may yield a coefficient equal the growth rate per unit time. The coefficients of the smooth functions would have little have direct meaning and they could change in number or form as the input data changes.

The GAM took the following form:

Equation 4-5
$$g(\text{E}[y]) \sim \beta_0 + \sum_i^n f_i(x_i) + \sum_j^m f_j(x_1, x_2, \dots, x_n)$$

The left hand side or the $g(\text{E}[y])$ represented the *link* function that provided the relationship between the explanatory variables and the mean of the objective function output. The link function allowed for the residuals following a non-normal distribution. The right hand side of the equation contained a constant value β_0, the sum of the smooth functions $f_i(x_i)$, and the optional sum of multivariate smooth functions—e.g. $f(x_1, x_2) = x_1 x_2$.

71

The construction of a GAM in this dissertation produced smooth functions using cubic splines as the basis. A penalized iteratively reweighted least squares (IRLS) method fitted the splines of all the smooth functions to the response variable simultaneously (Holland & Welsh, 1977). IRLS was a type of optimization algorithm related to the Gauss-Newton algorithm that treats the coefficients of the splines as weights and iterates through different weights until converging to a best fit (Wood & Agustin, 2002). Each smooth function underwent IRLS and penalties were added to the regression splines as the number of knots in the splines increase; that is, too smooth of a function would have little predictive ability outside the input data (Ruppert & Carroll, 1999). Statistical significance or the *p*-values were calculated from the smooth functions through the Wald test by comparing a smooth function to its null form: i.e. $f_i(x_i) = 0$. The changes to the response variable between the null and smooth functions used the normal or, alternatively, the χ^2 distribution to calculate the *p*-value (Wood, 2013). The Wald test was a parametric test evaluating the significance of the smooth function and had no role in developing the GAM.

The GAM was the model used in the sensitivity and parameter space reduction phase in Figure 4-1. The response variable was the NSE for an iteration. Smooth functions of the parameter values for a single iteration were the explanatory variables. The link function was the identity function, implying normally distributed residuals. Multivariate smooth functions were not considered because the requirement for their inclusion would increase the number of runs in an iteration and total computation time. The GAM regressed NSE against the sum of single variable smooth functions of the parameters plus a constant:

Equation 4-6 $$\text{NSE} \sim \beta_0 + \sum_{i}^{n} f_i(P_i)$$

From Figure 4-1 the end of an iteration's set of runs started the sensitivity analysis loop where the GAM was developed and *p*-values for the smooth functions calculated. Any *p*-values for a parameter's smooth functions that were above a significance level $\alpha=0.10$ would be subjected to a trial simulation to check the GAM-mediated sensitivity and parameter reduction

72

test. One simulation was run with the best parameter set from an iteration, but that run excluded the parameter whose smooth function p-value was above α. If the NSE of this trial simulation differed by more than 10^{-3} or 0.1%, then the parameter was re-added to the parameter space for the next iteration. The loop repeated this step for every parameter that fails the initial GAM p-value test. After each iteration the parameter space reduced until settling to the most sensitive parameters: 8 related to discharge and 14 related to nitrate. Table 4-3 and Table 4-4 listed these parameters. Discharge calibration was performed by gage station and with eight stations, the total number of discharge parameters was 64. Nitrate had 5 global parameters and two stations with 9 parameter each, totaling 23 parameters for nitrate.

<center>*Sequential Uncertainty Fitting (SUFI)*</center>

The suite of tools in SWAT-CUP offered multiple autocalibration techniques and the software was heavily utilized to streamline the autocalibration steps outside of sensitivity and parameter space reduction. The general autocalibration procedure was a variation of the Sequential Uncertainty Fitting (SUFI) algorithm having the following workflow: (1) define initial parameter ranges and space, (2) sample from space using Latin hypercube method, (3) run *M* simulations for an iteration, (4) perform a multivariate regression whose *t*-score and covariance matrix determine the boundaries of the next iteration's parameter ranges. The number of simulations per iteration was chosen as being at least one hundred times the number of unique parameters being sampled. The initial number of unique parameters were 18 for discharge and 21 for nitrate parameters. With eight discharge gage, two nitrate gages, and 5 global parameters, the total number of initial parameters were 181, giving 18,100 initial simulations. However, the first iteration started with the most upstream gage station and only calibrated discharge so the actual "first" iteration had 1800 simulations. The initial parameters can be found on Table 2-4, Table 3-2 for discharge and Table 2-5, Table 2-6 for nitrate; only those parameters that were described as "database" or "user defined" were modified.

This variation on SUFI had the initial iteration containing a large number of parameters and required the most time. The statistical significance of the GAM test step winnowed the number of parameters that determine whether a particular parameter may continue on to the next iteration. If the parameter did not pass the GAM step, it was reset to its initial value for the remainder of the autocalibration procedure. Before the next iteration proceeds, the parameter ranges were reduced as a means to converge to the optimal parameter values or range. This step used a different and less computationally intensive methodology compared to GAM.

SWAT-CUP performed a multiple linear regression of the NSE against the parameter values and calculated a sensitivity matrix $\mathbf{J}$ from an iteration's NSEs and the parameters that produced them:

Equation 4-7
$$J_{j,i} = \frac{\Delta NSE_j}{\Delta P_i} \; \Big| \; \begin{array}{ll} \Delta NSE_j & = \beta_i P_i \\ \Delta P_i & = P_0 - P_i \end{array}$$

$J_{j,i}$ was the entry for the j'th row and the i'th column of the sensitivity matrix. ΔP_i the change in the i'th parameter from its original P_0; in the case of relative changes, the original would be $P_0 = 0$. ΔNSE_j was the partial contribution to the NSE in the j'th run from the i'th parameter. The partial contribution was calculated from a regression output when all coefficients in the regression were zero except for the i'th parameter's coefficient. The number of rows in the sensitivity matrix was equal to the number of runs in the iteration and the column length was equal to the number of parameters sampled.

The parameter covariance matrix was then the approximated using the inverse of an equivalent Hessian matrix ($\mathbf{J^T J}$) and the variance of the NSE from the iteration (Press et al., 1992).

Equation 4-8
$$\mathbf{C} = \sqrt{s_{NSE}^2 (\mathbf{J^T J})^{-1}}$$

The estimated standard deviation of the i'th parameter ($s_{P,i}$) was the square root of the diagonal term from the covariance matrix $\mathbf{C}$. From $s_{p,i}$ the 95% confidence interval of the parameter value

74

from the best simulation was calculated with b^*_i being the parameter from the run with the best NSE:

Equation 4-9 $\qquad s_{P_i} \qquad = \sqrt{C_{ii}}$

Equation 4-10 $\qquad P_{i,lower} \quad = P_i^* - t_{v,0.025}s_{P_i}$

Equation 4-11 $\qquad P_{i,upper} \quad = P_i^* + t_{v,0.025}s_{P_i}$

$b_{i,lower}$ and $b_{i,upper}$ were the upper and lower 2.5 and 97.5 percent confidence intervals and $t_{v,0.025}$ was the standard, two-sided t-score at a significance level of 0.05. The new parameter range after an iteration was:

Equation 4-12 $\qquad P_{i,min}^{new} \quad = P_{i,lower} - \max\left(\dfrac{P_{i,lower} - P_{i,min}}{2}, \dfrac{P_{j,max} - P_{i,upper}}{2}\right)$

Equation 4-13 $\qquad P_{i,max}^{new} \quad = P_{i,upper} + \max\left(\dfrac{P_{i,lower} - P_{i,min}}{2}, \dfrac{P_{j,max} - P_{i,upper}}{2}\right)$

$P_{i,min}$ and $P_{i,max}$ were the current iteration's minimum and maximum values. The parameter update's regression included all parameters, including the ones that failed the sensitivity test. Only after the new ranges were calculated did the number of parameters updated. The combined SUFI and GAM loops repeat until two conditions were met: (1) a run produced an NSE that met the acceptable literature value (0.60 for monthly stream discharge) and (2) the ratio of the maximum and minimum parameter range values was sufficiently small (≤0.05). The ratio was met for every parameter and was not a mean of the parameter range ratios. These conditions ensured that autocalibration produced a good simulation and had a narrow parameter range (Abbaspour, 2005).

For stream discharge the model parameters were calibrated sequentially starting with the most upstream gage station and its contributing subbasins. Every gage station underwent its own autocalibration loop where the only parameters modified were those related to the subbasins and HRUs that contribute to the gage station. For example in Figure 4-3, subbasin group $\mathbf{G_1} = \{1, 2, 3, 5, 7, 9\}$'s nearest downstream contributing gage station is Charles City (Figure 4-3). The

75

combined autocalibration and sensitivity modified G_1's parameter space while minimizing the differences (expressed as NSE) between the observed and simulated values at that gage station. After G_1's parameter space shrank with an acceptable NSE for the best simulation at Charles City, the next subbasin group G_4 underwent autocalibration and sensitivity with the Cedar Rapids gage station. The autocalibration of G_4 includes G_1's parameters, but G_1's parameters neither underwent the GAM sensitivity culling nor were they included in calculating the number of runs for an iteration in G_4's autocalibration. Nevertheless, G_1 contributed to G_4 and thus the simulation GOF for the Cedar Rapids gage station depends on G_1's parameters values.

In a sequential calibration the user must be careful not to overly narrow the parameter ranges for an upstream subbasin group. The autocalibration for G_1 could "overfit" to Charles City, skewing the parameter space for G_4 to compensate. Overfitting occurred when the parameter range for an upstream basin was too narrow and simulated that gage station's observation well, but impacted the performance of the next gage station. For example a wide initial parameter range for G_1 going into G_4's autocalibration would avoid overfitting. Meaning, the second stop condition where parameter range was sufficiently small (≤0.05) was not required to stop the autocalibration and sensitivity loops for the upstream gage stations. This stop condition only applied at the terminal gage station.

The goal is that by the most downstream or terminal gage station G_8, all parameters have converged to a narrow range and reached satisfactory statistics. Figure 4-2 summarizes the contributing subbasins' spatial distribution with color coding to indicate the sequence and contribution. The stream discharge calibration period covered 1978-2002 for monthly mean discharges and the validation period covered 2003-2012. Not all stations had complete coverage of the calibration period.

For nitrogen load and concentration autocalibrations, the observations came from the Cedar Rapids and Wapello USGS gage stations. The stations employed high-frequency sensors that measure combined nitrate and nitrite concentrations every 15 minutes in units of $mg \cdot L^{-1}$. Nitrite concentrations in streams are small (Peterson et al., 2001) and thus nitrite is lumped in

www.manaraa.com

with nitrate for autocalibration. The nitrate sensors did not operate for the winter months of December, January, and February. Because SWAT's driving input was daily precipitation, the autocalibration used the mean daily nitrate concentrations as observations. The nitrate loads were simply the product of the mean daily stream discharge and nitrate concentrations. Because the record at the time of autocalibration spanned only 2009-2012, the daily concentrations and loads were used in the autocalibration to supply the procedure a sufficient amount of data. The two outputs also served different purposes: load was important when considering total nitrogen export from the basin and concentration was important for water quality standards.

The nitrate calibration was not done sequentially like discharge because of the inclusion of basin-wide or global parameters. Still, some parameters were separated into subbasin groups as shown by the dashed-line boxes in Figure 4-3. $G_{4,N}$ subbasins contributing to Cedar Rapids gage station encompasses the stream discharge groups **G₁** and **G₄**. $G_{8,N}$ subbasins encompasses the remaining groups. The calibration period for nitrate covered 2009-2011 and the validation period coverd 2012-2013. Some nitrate "observations" were originally missing or were gaps in the record. With the exception of the winter months, these gaps were filled using artificial neural networks described in Chapter 5. Because the gaps were few and had excellent fits to the actual observations (Table 5-3), the influence of synthetic data in the calibration and validation dataset on the autocalibration was negligible considering the gap treatment only used time and observed discharge as explanatory variables.

For either stream discharge or nitrate, the user may run a validation iteration after an arbitrary number of SUFI and GAM iterations. This dissertation allowed the autocalibration to have three calibration iteration for every validation iteration. The validation run simply repeated SUFI and GAM with simulations using the parameter sets from the calibration period's third iteration. The results from the validation run were not incorporated into the overall autocalibration scheme and served only as a manual evaluation on the autocalibration progress. If the third iteration's parameter sets produced low NSEs for the validation, then the autocalibration

took a step backwards, re-sampling from a previous iteration's parameter space and re-starting the autocalibration procedure from that point.

The first iteration included both calibration and validation periods as baselines to compare NSEs in future validation runs. The validation was run independent of the autocalibration, provided it used the same parameter set as the calibration run. Once both calibration and validation loops yielded an iteration whose parameter ranges are small and the NSE meets the acceptable value, the combined autocalibration and sensitivity procedure stops. The midpoint in the range for each parameter in the final calibration period iteration was then the "final" calibration parameter values applied to scenario runs in Chapter 5 and Chapter 6. Table 4-3 and Table 4-4 listed the final parameter values for the calibrated model for discharge and nitrate, respectively.

<u>Results and Discussion</u>

Sensitivity

The stream discharge parameters that survived the GAM sensitivity culling were the HRU runoff curve number at (CN2 or *CN* from Table 2-4), depth to impervious layer (DEP_IMP, z_{imp}), evaporation compensation coefficient (ESCO, *esco*). The groundwater parameters, which were also at the HRU scale, were the groundwater delay time (GW_DELAY, δ_{gw}) and the threshold water content in shallow aquifer before groundwater can flow (GWQMN, $aq_{sh,t,gw}$). The soil parameters at the HRU scale were the soil layers' available water capacity (SOL_AWC, AWC_j) and soil layer thicknesses (SOL_Z, z_j). The Manning's roughness coefficient (CH_N2, *n*) in the main channel was the only parameter at subbasin scale. Each HRU had different CN2, SOL_AWC, and SOL_Z values and so their changes were relative. SOL_AWC and SOL_Z had values for each soil layer in each HRU and so their changes were applied to all layers; e.g. the thicknesses of all soil layers in all HRUs of the subbasins

contributing downstream to gage station at Wapello were decreased by 18.9%. These subbasins were in orange or group **G₈** in Figure 4-2 and Figure 4-3.

The global nitrate parameters were the soil denitrification exponential rate coefficient (CDN, β_{den}), the organic nitrogen mineralization rate constant (CMN, β_{min}), the nitrate percolation coefficient (β_{NO3}), the nitrate concentration in the rain (RCN, $NO_3^-{}_{,P}$), and the threshold value for the nutrient cycling factor for denitrification to occur ($\gamma_{w,t}$). On HRU scale the soil parameters were a fraction of porosity that excludes anions (ANION_EXCL, θ_e), the initial nitrogenous soil humus or organic matter (SOL_ORGN, $N_{org,s}$), and the amount of organic carbon in the soil layers (SOL_CBN, $C_{org,j}$). The half-life of nitrate in the shallow aquifer (HLIFE_NGW, $\lambda_{\frac{1}{2},NO3,sh}$) was the only groundwater parameter for nitrate autocalibration. The management parameters were the maximum annual amount of fertilizer applied in SWAT's auto-fertilization operation (AUTO_NYR), the fertilizer application efficiency, (AUTO_EFF) the fraction of fertilizer applied to the top 10mm of the soil (ARFT_SURFACE), the biological mixing efficiency in a soil column (BIOMIX), and the soluble nitrogen concentration in runoff from urban HRUs (SOLN_CON).

Stream Discharge

SWAT-CUP was utilized to optimize the most sensitive parameters based on NSE, a goodness-of-fit (GOF) measure between the model simulation results and observations at the same location and time. During the validation period, parameter sets were fixed (not optimized further) and NSE computed once again. Table 4-5 summarizes the calibration and validation GOF statistics for stream discharge at the eight USGS gage stations from the simulation whose parameter set yielded the highest NSE in the final iteration. The calibration period NSE ranged from a low of 0.60 at the Iowa City station on the Iowa River to a high of 0.75 at the terminal gage at Wapello (below where the Cedar and Iowa Rivers join). The validation NSE ranged from a low of 0.55 at Old Man's Creek, a small tributary of the Iowa River, and high of 0.88 at the Cedar Rapids station on the Cedar River. The calibration R^2 ranged from a low of 0.73 at Charles

79

City on the Cedar River and a high of 0.83 at Lone Tree on the Iowa River. The validation R^2 ranged from a low of 0.73 at two locations: South Fork Iowa River near Providence and Old Man's Creek. The high validation R^2 of 0.90 was also found at two locations: Lone Tree and Wapello. The calibration PBIAS had the greatest magnitude difference from zero at Old Man's Creek, where the best (optimal) parameters generally under-predicted the discharge by -40.3%. The lowest magnitude calibration PBIAS was found at Cedar Rapids where the best parameters generally over-predicted the discharge by 1.8%. The validation PBIAS had the same location trend but different signs: Old Man's Creek was -49.1% under prediction and Cedar Rapids was -4.8% under prediction.

Aside from Old Man's Creek, Charles City, and New Providence, the validation statistics were better than the calibration. These three gage stations were also upstream or lower order gages and the first to be calibrated. At most gage stations the simulations improved for the 2003-2012 validation period, with markedly higher values in the downstream gages at Cedar Rapids and Wapello. The curve number was one of the more sensitive parameters when calculating runoff; these two stations saw the highest modification of their curve numbers with an increase in 22.1 and 24.8 percent in Cedar Rapids and Wapello, respectively. Aside from the curve number influence, the parameters in Table 4-3 did not show an obvious pattern with respect to the gage's location in the watershed. As for the broad improvement in GOF statistics, one explanation could be that the input data were more accurate in the validation period. Land use and land cover (LULC) updated more frequently after 2003 with a total of eight maps. The calibration period only had updates in 1990, 1992, 1995, and 2002; the 1985 map was the model's base LULC map. The early years would not have accurate LULC data and therefore one could expect the early years to not have as accurate statistics. The difference between the periods' statistics were unexpected, but fortunate that accuracy during the validation periods seemed to out-perform that of the calibration period.

Figure 4-4 through Figure 4-11 show the results for the combined autocalibration and sensitivity procedure for the stream discharge as a time-series with the observations, the best

simulation with the highest NSE from the calibration period, and the 95% parameter uncertainty (95PPU) from the final iteration. The top time-series were for the calibration period and the bottom time-series were for the validation period. The 95PPU was calculated from an empirical cumulative distribution function (ECDF) for each time step. For example, say a gage location had N observations to compare to simulated values from M runs for the final iteration, yielding an $N{\times}M$ matrix. Each row in the matrix was sorted in ascending order and cumulatively added to produce an ECDF from which the 2.5^{th} and 97.5^{th} percentiles were interpolated from M values. The result was an $N{\times}2$ matrix of simulated time series with N time-steps. Plotted along with the values from the best simulation, the ECDF gave a zone that approximates a confidence interval without assuming a probability distribution for the variable at each time-step.

Charles City had data gaps between from 1996 and 2000 for stream discharge and the simulated values were not drawn. Old Man's Creek and New Providence's discharge records started in late 1984 and late 1995, respectively, so the calibration periods were shorter than the other stations. Qualitatively the simulation time series tended to under-predict the observations, especially at gages on lower order streams such as Charles City, New Providence, and Old Man's Creek. This under-prediction trend decreased with higher order gages with the peaks flows being very close to the observed as was the case with the 1993 and 2008 floods at Cedar Rapids and Wapello stations. In general the validation performed better than the calibration with the trend most pronounced on higher order gages. This trend could be seen numerically in GOF statistics and graphically on the time series plots.

Nitrate

Table 4-6 and Table 4-7 summarize the GOF statistics for nitrate load and concentration, respectively, for the Cedar Rapids and Wapello gage stations from the simulation whose parameter sets yielded the highest NSE in the final iteration. Because the nitrate autocalibration was simultaneously performed, the NSE from Wapello determined the stopping point. The autocalibration was not successful in finding a simulation for nitrate concentration that met the

81

stopping condition (NSE $\geq$ 0.50). Instead, the concentration and loading NSEs for Wapello were averaged and that was used as the stopping point for both variables.

The calibration period NSEs for nitrate loads were 0.25 and 0.62 at Cedar Rapids and Wapello, respectively. The R^2 statistics were 0.52 and 0.71. The PBIAS generally under-predicted at Cedar Rapids and Wapello, -42.4 and -26.4 percent, respectively. The validation period NSEs for nitrate loads were 0.52 and 0.70. The R^2 statistics were 0.73 and 0.79. The validation PBIAS also under-predicted at -44.4 and -27.4 percent. Nitrate load was the product of concentration and discharge. The variance of discharge was much larger than that of nitrate: discharge can vary between 0 and 2500 $m^3 \cdot s^{-1}$ while the maximum nitrate concentration for either gage stations was 18.5 $mg \cdot L^{-1}$. Thus if the model simulates discharge well, then nitrate loads should follow accordingly. In this case a comparison between discharge and nitrate load statistics cannot be directly made as the discharge statistics were monthly averages over three decades while nitrate had only five year daily averages. A model's ability to simulate nitrogen dynamics using estimated loads (Q x C) relied too much on the discharge (Q), and so looking at the independent nitrate concentrations was considered to be more appropriate.

The calibration period NSEs for nitrate concentrations were -0.35 and 0.48 at Cedar Rapids and Wapello, respectively. The R^2 statistics were 0.29 and 0.49. The PBIAS under-predicted at -22.9 and -0.90 percent. The validation period NSEs for nitrate loads were 0.15 and 0.37 at Cedar Rapids and Wapello, respectively. The R^2 statistics were 0.16 and 0.42. The validation PBIAS over-predicted at 0.30 and 21.4 percent. The model performed rather poorly for nitrate concentrations given these GOF statistics. Neither station made the cut-off point of NSE=0.50, and Cedar Rapids reported a negative NSE for the calibration period, indicating that the model errors were larger than the observations' variance.

The sensitivity procedure also eliminated the in-stream nitrogen parameters as none were statistically significant in the GAM and neither did they induce change in the NSE. This behavior could be explained from the stream network having fewer computational parts than the HRUs. With each subbasin having only one reach from which many HRUs export their outputs, in-

stream parameters drove the model's in-stream nitrogen dynamics less. One of the most sensitive parameters was the nitrogen rainfall concentration (RCN) that originally veered into a "too high" 4-5 ppm range, leading to a re-start of the autocalibration procedure. The impact of RCN can be explained by how the model applies rainfall: each subbasin located the nearest climate station and used the precipitation time-series from that station for all HRUs. Any increase in RCN would lead to a large input into the system. The model default was 1 ppm and the autocalibration settled to 1.34 ppm, a more acceptable number than 4 ppm, which would be representative of high-density automobile and industrial emissions.

Figure 4-12 and Figure 4-13 show time-series for nitrate loads at Cedar Rapids and Wapello, respectively. Figure 4-14 and Figure 4-15 show time series for the concentrations. These plots had the same configuration as the stream discharge figures: observation, best simulation, and the ECDF-derived 95PPU. The nitrate concentration plots also show two horizontal lines: the dashed is the EPA's drinking water standard or Maximum Contaminant Level (MCL) at $10 \text{ mg} \cdot \text{L}^{-1}$ for nitrate, and the dotted line the instrument detection limit for nitrate concentration from the manufacturer report for a HACH Nitratax sensor (HACH, 2011) The USGS reported detection limits for nitrate concentration as $0.1\text{-}1.0 \text{ mg} \cdot \text{L}^{-1}$, depending on instrument (Pellerin et al., 2013). Given that $<1.0 \text{ mg} \cdot \text{L}^{-1}$ were approved for public release by the USGS, the instrument deployed was likely to have the lower detection limits. Therefore, the calibration included concentrations below $1.0 \text{ mg} \cdot \text{L}^{-1}$ in the calculation of GOF statistics, despite not knowing the actual instrument being deployed at these sites.

Simulated nitrate loads at Cedar Rapids consistently underestimated the observations. Results at Wapello were similar but to a lesser degree. The 95PPU for the nitrate loads were also wider, compared to the stream discharge plots where the 95PPU were so narrow as not be seen on the plot. Wapello results showed a wider 95PPU during periods of high nitrate loads. The wide 95PPU reflected difficulty in the autocalibration procedure with finding optimal parameters. Because loads were correlated with discharge, one could see that 2012 was a drought year with very low loads, at or near zero during late summer. The following year saw a spike in

83

nitrate loads higher than that of the calibration years. The mechanism could be that with low rainfall, nitrogen fertilizer remained in the soil and at the break of drought, the fertilizer flushed out all at once in addition to new N-applications for 2013. The model did seem to predict this behavior well, even if the spikes in loading were lower. Here one could say the model successfully simulated daily discharge and the persistence of soil nitrogen during the drought period.

The concentration time-series told a similar story as the load plots, only with less accuracy and precision. The calibration years showed concentrations generally following the observations: dipping and rising as observations dipped and rose. The Cedar Rapids time-series had a more erratic pattern with 2011 calibration year showing the best fit. Wapello's calibration performed better, but the 95PPU was wider, indicating less precision. Going into the validation period with the 2012 drought showed an important facet for the model's behavior. At both Cedar Rapids and Wapello the simulated concentrations never went below 1 mg·L^{-1} as they did for the observations. The model did not seem to behave well at low flows, overestimating the observed concentrations and also could not simulate the spike in May, 2012 when the observation went above 10 mg·L^{-1}. Going into 2013 the increase in daily concentrations due to 2012's fertilizer could be seen in the observations rising above the EPA standard for multiple days in May and June. Cedar Rapids simulations followed the dips and rises, but do not accurately simulate the observations. Wapello performed better. In both cases the model was able to simulate high nitrate concentrations. Still, the wide 95PPU at both stations throw in some doubt whether the model can perform these simulations precisely.

Conclusion

The combined autocalibration procedure using SUFI and sensitivity analysis using GAM regressions successfully simulated stream discharge and nitrate loads at the monthly and daily time-step, respectively. The most sensitive parameters were related to the apportionment of runoff between infiltration and retention as soil moisture. For monthly average stream discharge,

84

the NSE statistic for all stations met, and at downstream gages exceeded, the minimum of NSE=0.60 in both calibration and validation periods. The validation period showed improved statistics over the calibration; this behavior could be attributed to input data being more accurate for later years or possibly an artifact of the calibration period being much longer. The longer calibration period would encompass more inter-annual variability that SWAT may not be able to capture. The model also performed better as one approached the outlet or as the number of contributing subbasins increased, indicating a law of large numbers effect where the sum of smaller contributing areas that do not behave as well independently lead to a good summation statistic. Physically speaking, the smaller streams were flashier and these dynamics were not captured well by SWAT, but the integration into larger streams muted these dynamics.

Nitrate loads met the minimum acceptable NSE for the daily time-step (NSE=0.50) at the Wapello outlet, but not at the mid-basin gage station at Cedar Rapids. The parameters most sensitive in the autocalibration related to nitrogen dynamics and movement in the soil column or HRU, the management of fertilizer in agricultural land uses, and the sole atmospheric parameter of rainfall nitrogen concentration. Nitrate concentrations do not perform so well, and none of the stations in either period met the NSE=0.50 minimum. An explanation for this would be the model granularity not being equivalent at the in-stream scale and that SWAT does not simulate nitrogen very well during periods of low flow like 2012. The management operations which dictated the application of fertilizer in this model were simplistic because they were set to default settings. The default fertilization scheme was inorganic nitrogen applied, the same for all agricultural HRUs. While the SWAT documentation dictates that the inorganic nitrogen includes both nitrate and ammonia, the reality was that the fertilizer input was almost entirely nitrate upon inspection of the output files not used in the calibration.

The justification for using the default settings was the lack of spatial data detailing the types of fertilizer, when or how they were applied, and in what quantities. The autocalibration incorporated these parameters out of necessity, but due to the spatial scales of the calibration—only eight management changes corresponding to eight subbasin groups and gages—SWAT

85

would be unable to capture the true spatial heterogeneity in management practices in the ICRB. One group of parameters not included in the calibration were the heat units that scheduled dates when crops were planted, fertilized, or harvested. These parameters would have an impact on crop yields and fresh organic nitrogen (plant matter) inputs into the soil. One unexpected behavior the simulation had was that the accumulated heat units sometimes did not reach the required amount to initiate harvest. Thus harvest only occurred at the very end of year in the dead of winter, a most unrealistic practice. The harvest operation also added to the dead plant material, which increased total nitrogen in the soil. Additionally, if the harvest operation did not occur during the year, the yields would be zero and the organic nitrogen inputs into the soil would likewise follow suit. Thus the under-prediction of nitrate and the undue influence of rainfall nitrogen could be from the inaccurate scheduling of management operations by heat units. Extending this phenomenon further, the heat units not making the required harvest point would indicate a problem with the climate input data.

Nevertheless, the calibrated model generally followed the observations, if not at exactly the correct time points, and the calibration also produced peaks in concentrations similar to the observations. More interestingly, the calibrated SWAT model emulated the response of nitrate loads to rainfall-runoff patterns, where a drought year followed by a wet year faithfully produced spikes in concentration and loads for the next year. Due to the poor performance in simulating nitrate concentrations, an alternative method was devised. The GAM used in the sensitivity analysis was non-parametric and could flexibly simulate complex systems, if at the expense of the user's understanding of the regression model's components. Artificial neural networks (ANN) took the idea of non-parametric models to their limit, producing a black-box of weights and numbers that simulate complex systems. The next chapter details the use of ANNs to compensate for SWAT's poor nitrate concentration simulations.

Table 4-1   Discharge-related parameters that survived the sensitivity and autocalibration procedure with the parameter name, units, initial range, and description

SWAT Parameter	Units	Minimum	Maximum	Description
CH_N2	unitless	0.01	0.3	Manning's roughness coefficient for the main channel
CN2	unitless	35	98	Runoff curve number for an HRU; relative change has range of [-0.25,0.25]
DEP_IMP	mm	1000	6000	Depth to impervious layer
ESCO	unitless	0	1	Soil evaporation compensation coefficient
GW_DELAY	day	1	90	Groundwater delay time
GWQMN	mm	0	5000	Threshold water content in shallow aquifer before groundwater can flow
SOL_Z	mm	0	3500	Soil layer thickness; relative change has range of [-0.25,0.25]
SOL_AWC	mm H2O/ mm soil	0	1	Soil available water capacity; relative change has range of [-0.5,0.5]

87

Table 4-2   Nitrate-related parameters that survived the sensitivity and autocalibration procedure with the parameter name, units, initial range, and description

Parameter	Units	Default	Min.	Max.	Description
ANION_EXCL	unitless	0.5	0.5	0.99	Fraction of porosity that excludes anions
ARFT_SURFACE	unitless	0.2	0.2	1	Fraction of fertilizer applied to top 10 mm of soil column
AUTO_EFF	unitless	1.3	1	2	Nitrogen fertilizer application efficiency
AUTO_NYR	kg N/ha	300	300	600	Maximum allowable annual nitrate fertilizer for corn
BIOMIX	unitless	0.2	0.2	0.9	Biological mixing efficiency
CDN	unitless	1.4	0	3	Soil denitrification rate coefficient
CMN	unitless	0.0003	0.0001	0.003	Rate factor for organic nitrogen mineralization
HLIFE_NGW	days	0	0	200	Half-life of nitrogen in groundwater from Equation 2-61
NPERCO	unitless	0.2	0.5	1	Nitrogen percolation coefficient
RCN	ppm	1	1	1.5	Concentration of nitrate in rainfall
SDNCO	unitless	1.1	0.5	1.1	Nutrient cycling factor v for denitrification to occur
SOL_CBN	% soil	varies	-0.5	1	Soil organic carbon content, varies on HRs; relative change has range of [-0.5,1]
SOL_ORGN	mg/kg	0	0	100	Initial organic nitrogen concentration in the soil
SOLN_CON	ppm	0	0	5	Soluble nitrogen concentration from urban runoff

88

Table 4-3   Final parameter values after autocalibration for stream discharge.

Parameter	CH_N2	CN2	DEP_IMP	ESCO	GW_DELAY	GWQMN	SOL_AWC	SOL_Z
Units	unitless	unitless	mm	unitless	day	mm	mm H_2O/ mm soil	mm
Change	replace	relative	replace	replace	replace	replace	relative	relative
Charles City	0.117	0.008	1383	0.966	71.43	24.09	-0.134	-0.245
New Providence	0.149	-0.182	1565	0.995	47.99	463.94	-0.294	0.079
Marshalltown	0.187	-0.095	1491	0.993	86.18	187.35	-0.46	-0.245
Cedar Rapids	0.192	0.221	3026	0.961	59.75	805.38	-0.174	0.000
Iowa City	0.182	-0.134	4437	0.998	22.27	353.27	-0.437	-0.229
Old Man's Creek	0.149	0.010	2813	0.948	30.72	44.85	-0.236	0.054
Lone Tree	0.148	0.194	2390	0.921	89.78	570.46	-0.45	0.123
Wapello	0.163	0.248	4593	0.847	51.60	778.45	0.131	-0.189

89

Table 4-4   Final parameter values after autocalibration for nitrate loading and concentration.

Parameter	Units	Change	Whole Basin	Cedar Rapids	Wapello
ANION_EXCL	unitless	replace	-	0.900	0.861
ARFT_SURFACE	unitless	replace	-	0.236	0.531
AUTO_EFF	unitless	replace	-	1.770	1.706
AUTO_NYR	kg N/ha	replace	-	440	541
BIOMIX	unitless	replace	-	0.279	0.211
CDN	unitless	replace	0.562	-	-
CMN	unitless	replace	0.000672	-	-
HLIFE_NGW	days	replace	-	143	91
NPERCO	unitless	replace	0.836	-	-
RCN	ppm	replace	1.344	-	-
SDNCO	unitless	replace	0.993	-	-
SOL_CBN	% soil	relative	-	0.590	0.98
SOL_ORGN	mg/kg	replace	-	35.76	65.88
SOLN_CON	ppm	replace	-	2.59	0.94

90

Table 4-5   Goodness of fit statistics for monthly average stream discharge at eight USGS gage stations for the calibration and validation period

	Calibration			Validation		
Station	NSE	R^2	PBIAS	NSE	R^2	PBIAS
Charles City	0.62	0.73	-32.2	0.61	0.79	-35.5
New Providence	0.64	0.76	-46.1	0.66	0.73	-32.2
Marshalltown	0.71	0.82	-35.9	0.81	0.89	-32.2
Cedar Rapids	0.66	0.67	1.8	0.88	0.89	-4.8
Iowa City	0.60	0.76	-40.3	0.64	0.86	-45.5
Old Man's Creek	0.65	0.82	-51.0	0.55	0.73	-49.1
Lone Tree	0.63	0.83	-41.0	0.67	0.90	-43.8
Wapello	0.75	0.76	-11.7	0.86	0.90	-17.7

Table 4-6   Goodness of fit statistics for daily nitrate loading at Cedar Rapids and Wapello gage stations

	Calibration			Validation		
Gage Station	NSE	R^2	PBIAS	NSE	R^2	PBIAS
Cedar Rapids	0.25	0.52	-42.4	0.52	0.73	-44.4
Wapello	0.62	0.71	-26.4	0.70	0.79	-27.4

Table 4-7   Goodness of fit statistics for daily nitrate concentrations at Cedar Rapids and Wapello gage stations

	Calibration			Validation		
Gage Station	NSE	R^2	PBIAS	NSE	R^2	PBIAS
Cedar Rapids	-0.35	0.29	-22.9	0.15	0.16	0.30
Wapello	0.48	0.49	-0.90	0.37	0.42	21.4
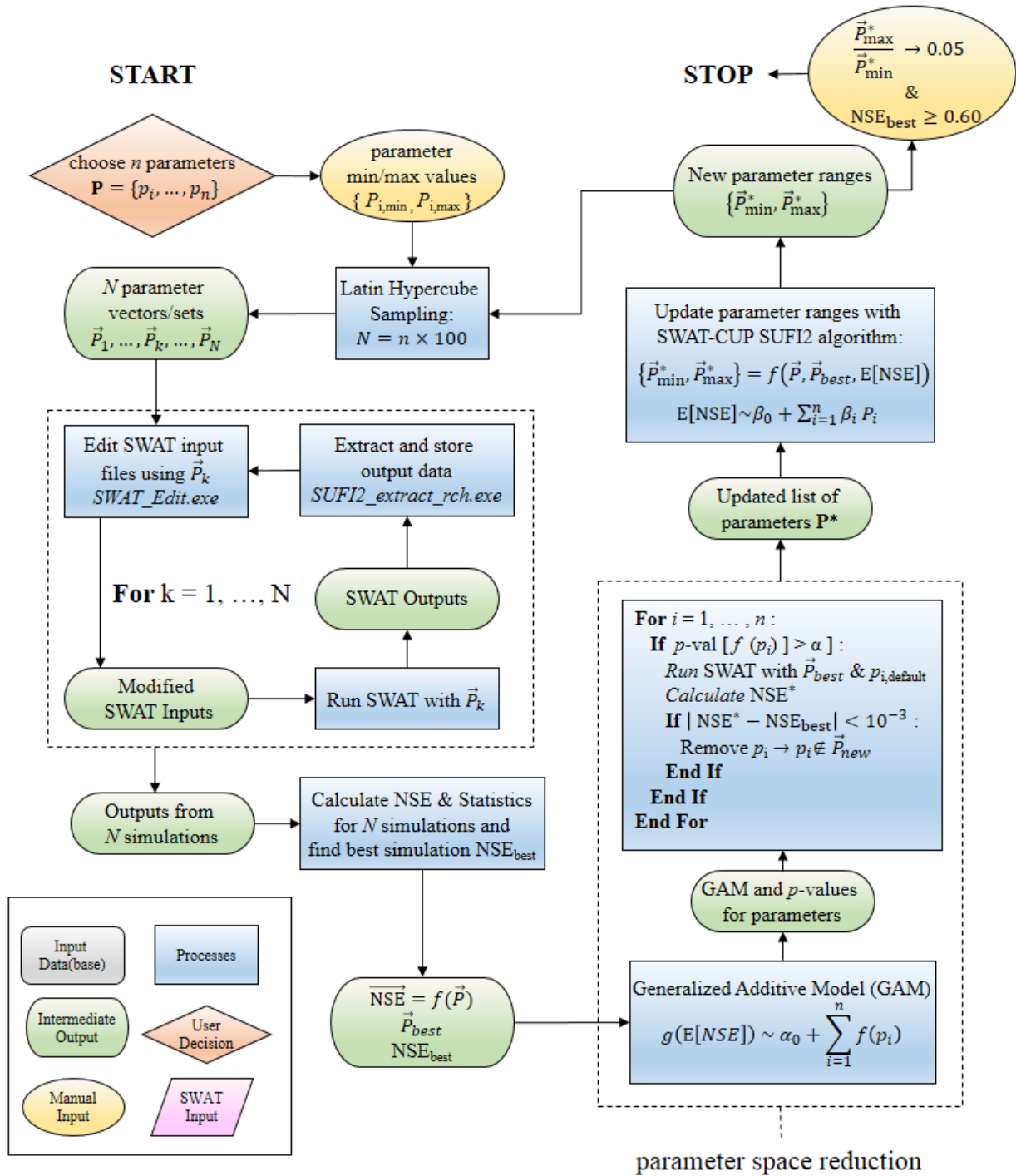
Figure 4-1   Combined autocalibration and sensitivity analysis workflow. The SUFI2 autocalibration parts are described in Abbaspour et al. (2007a).
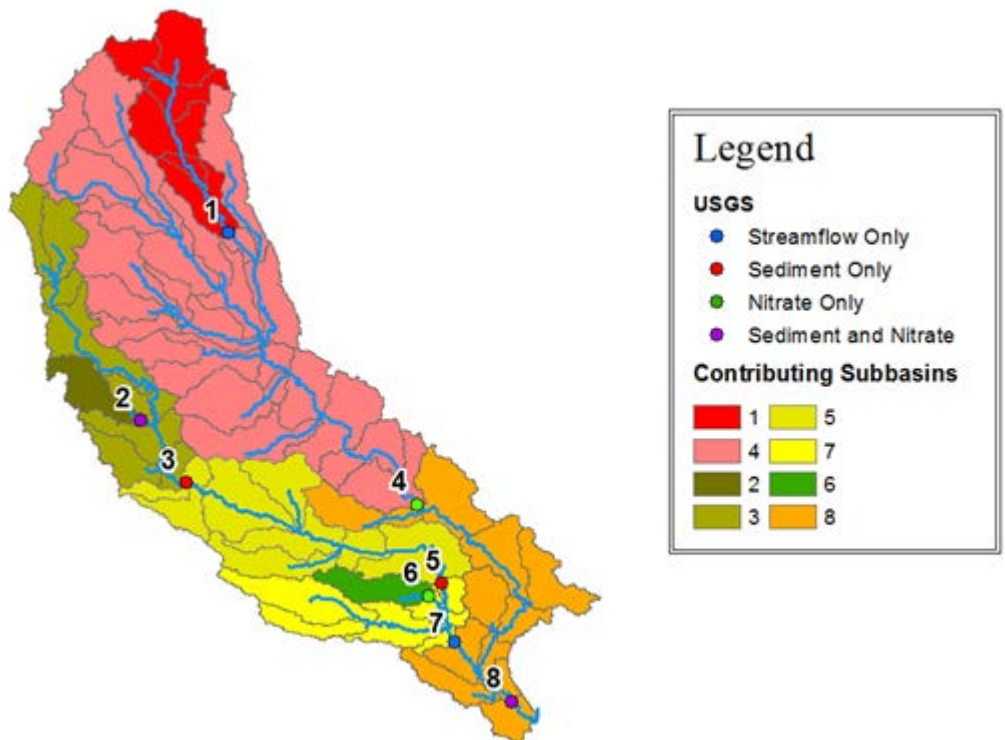
Figure 4-2   Order of sequential calibration spatially defined
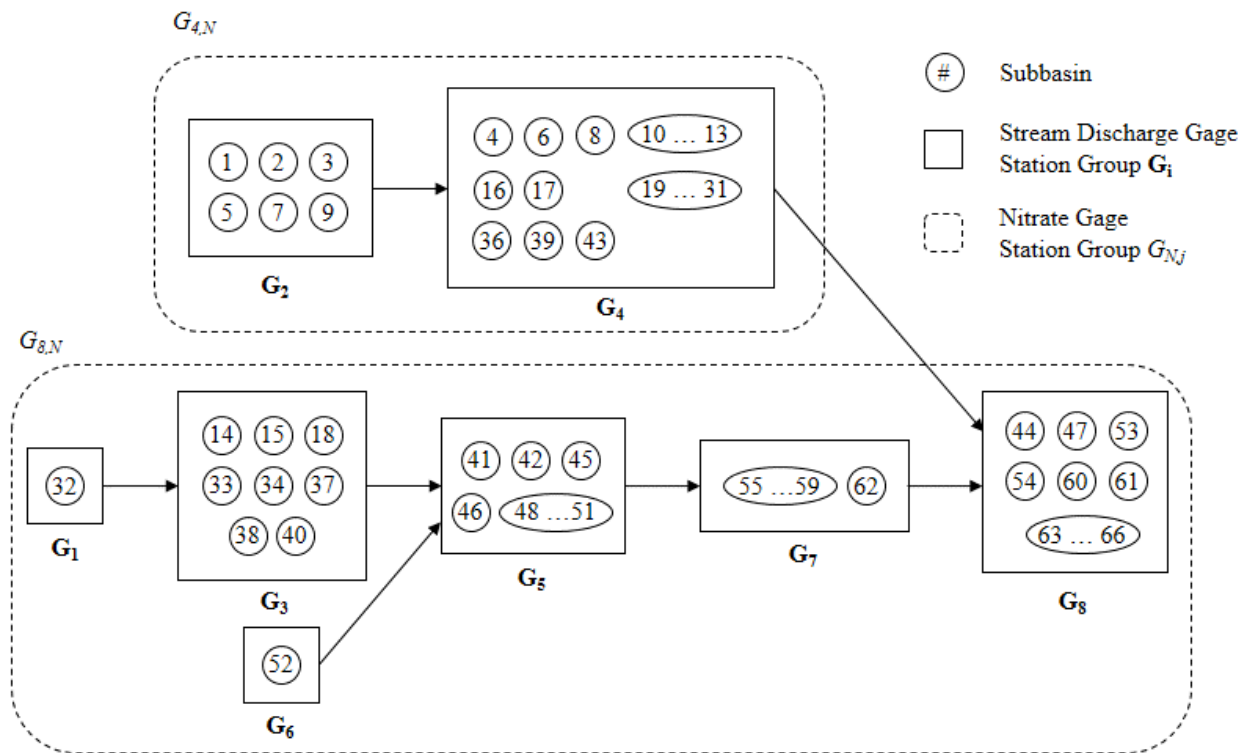
Figure 4-3   Order of sequential calibration diagramed by subbasin
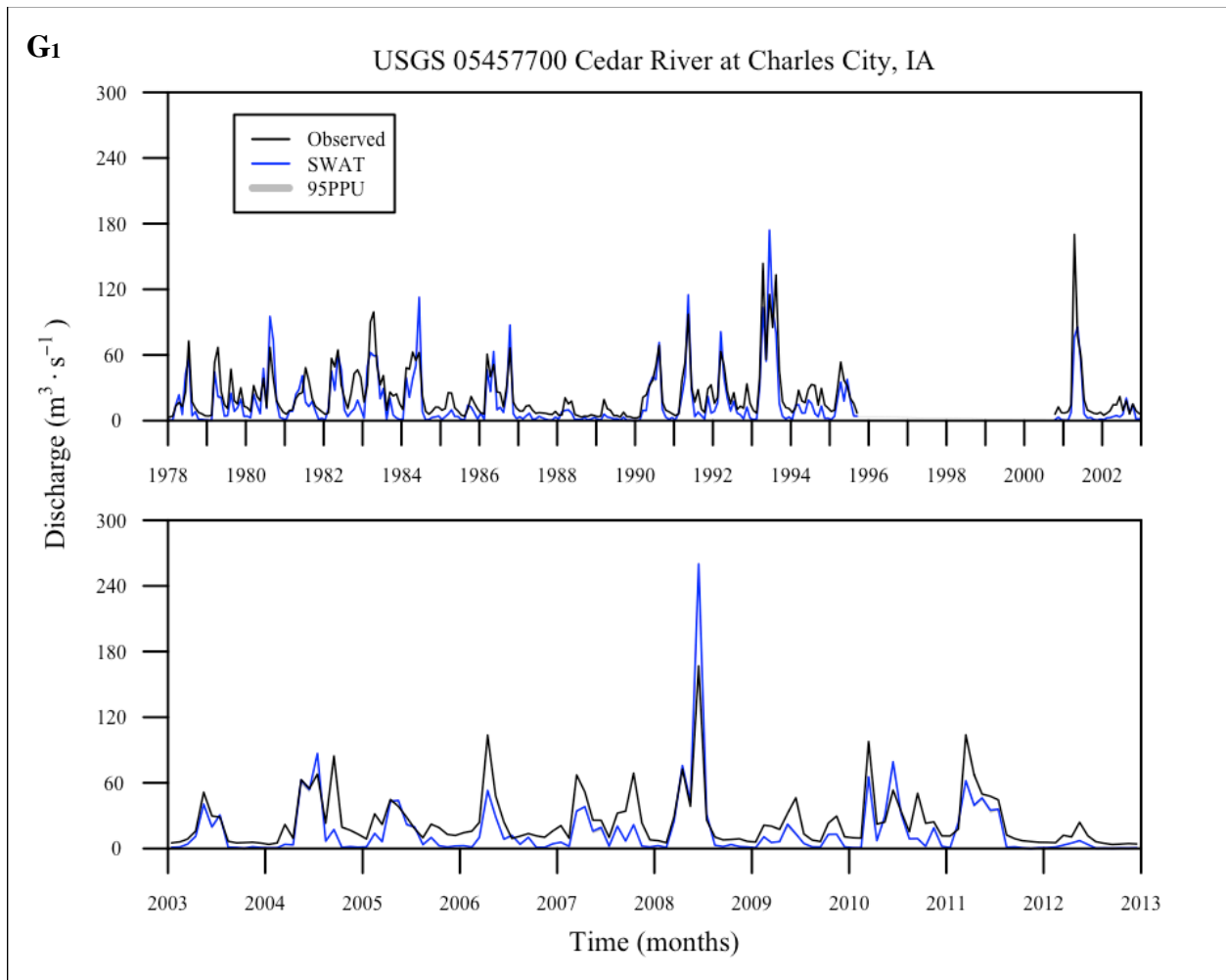
Figure 4-4   Simulated and observed stream discharge at gage station USGS 05457700 Cedar River at Charles City, IA for (top) calibration period and (bottom) validation period

94
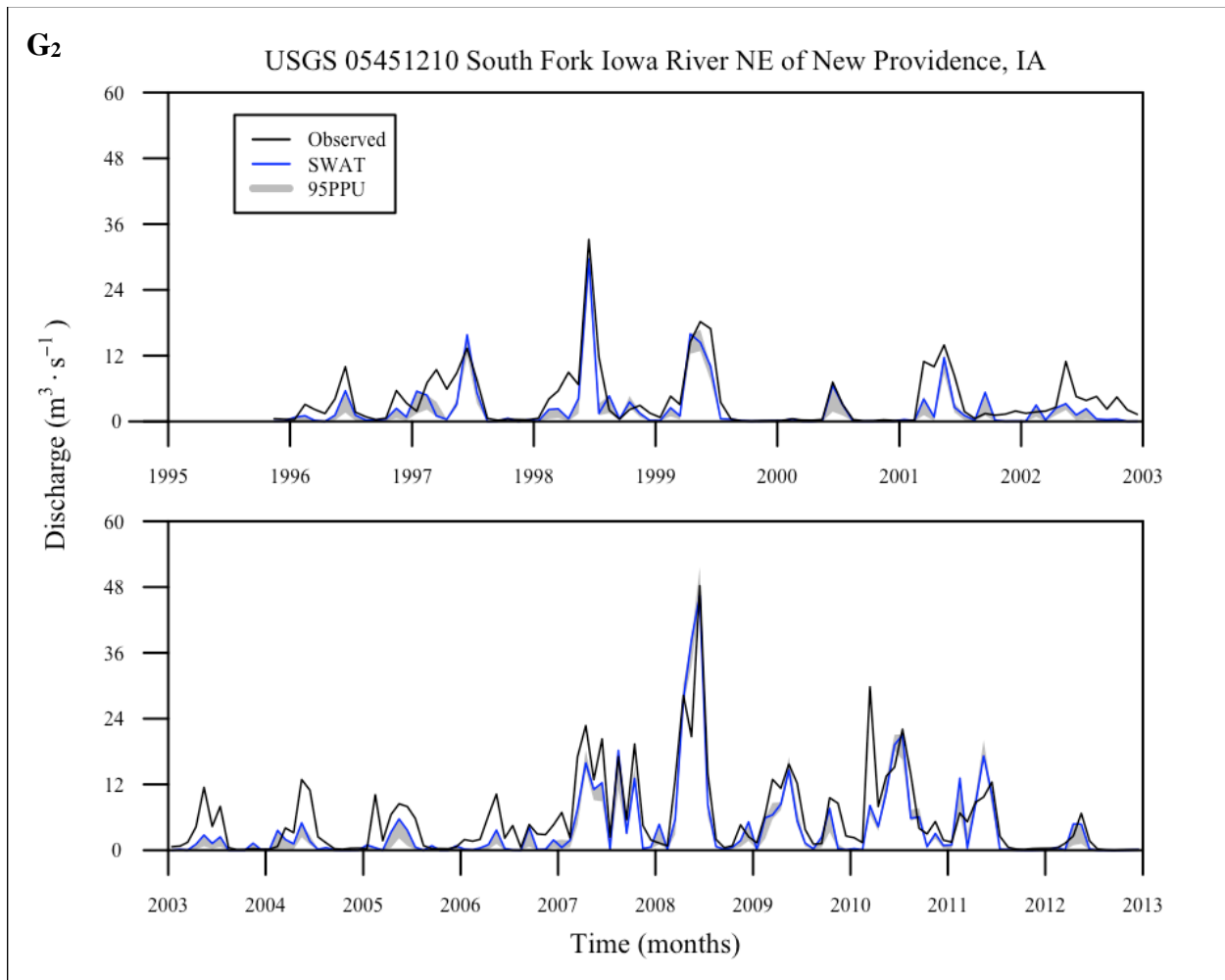
Figure 4-5   Simulated and observed stream discharge at gage station USGS 05451210 South Fork Iowa River NE of New Providence, IA for (top) calibration period and (bottom) validation period.
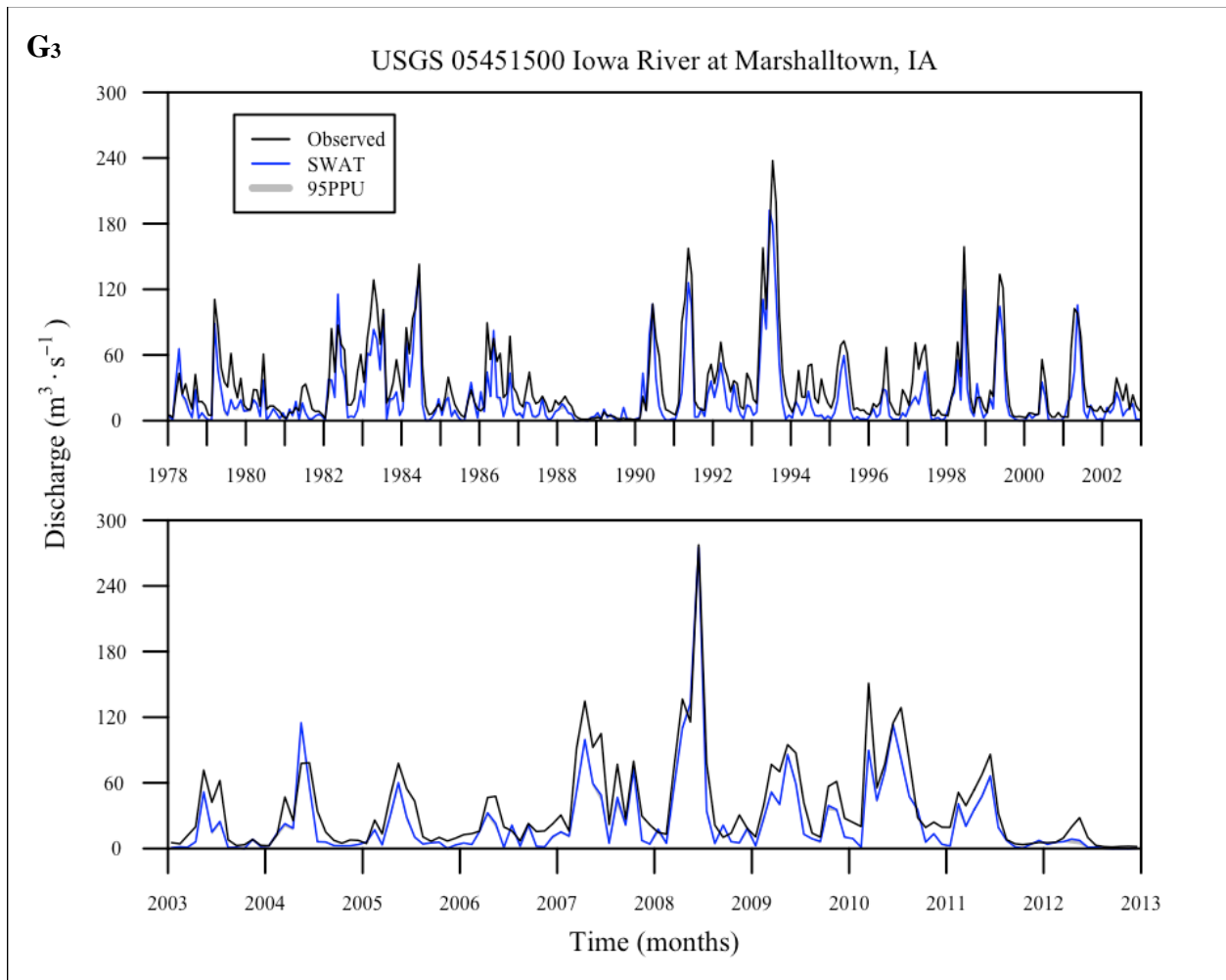
Figure 4-6   Simulated and observed stream discharge at gage station USGS 05451500 Iowa River at Marshalltown, IA for (top) calibration period and (bottom) validation period.
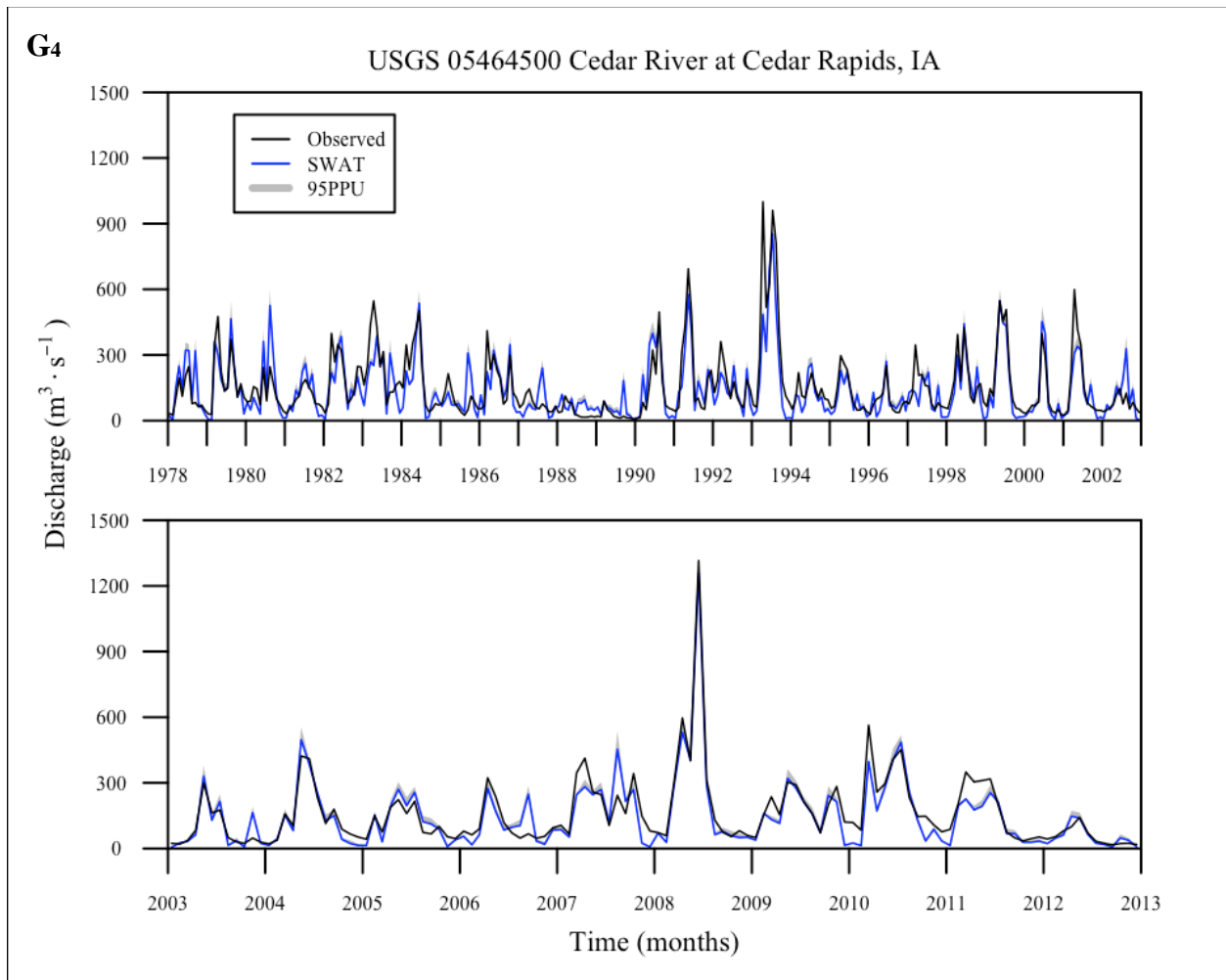
Figure 4-7   Simulated and observed stream discharge at gage station USGS 0546500 Cedar River at Cedar Rapids, IA for (top) calibration period and (bottom) validation period.
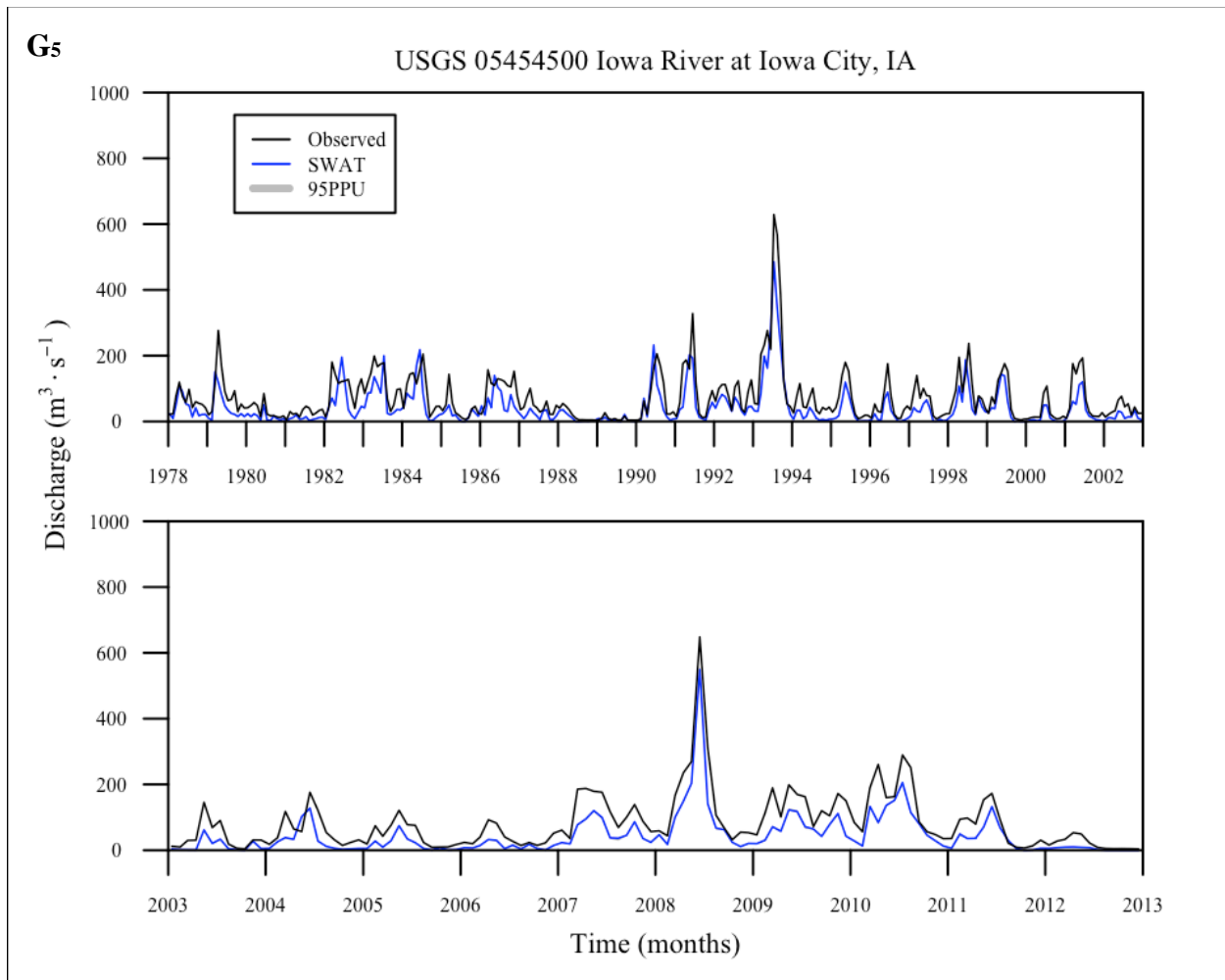
Figure 4-8   Simulated and observed stream discharge at gage station USGS 05454500 Iowa
River at Iowa City, IA for (top) calibration period and (bottom) validation period.
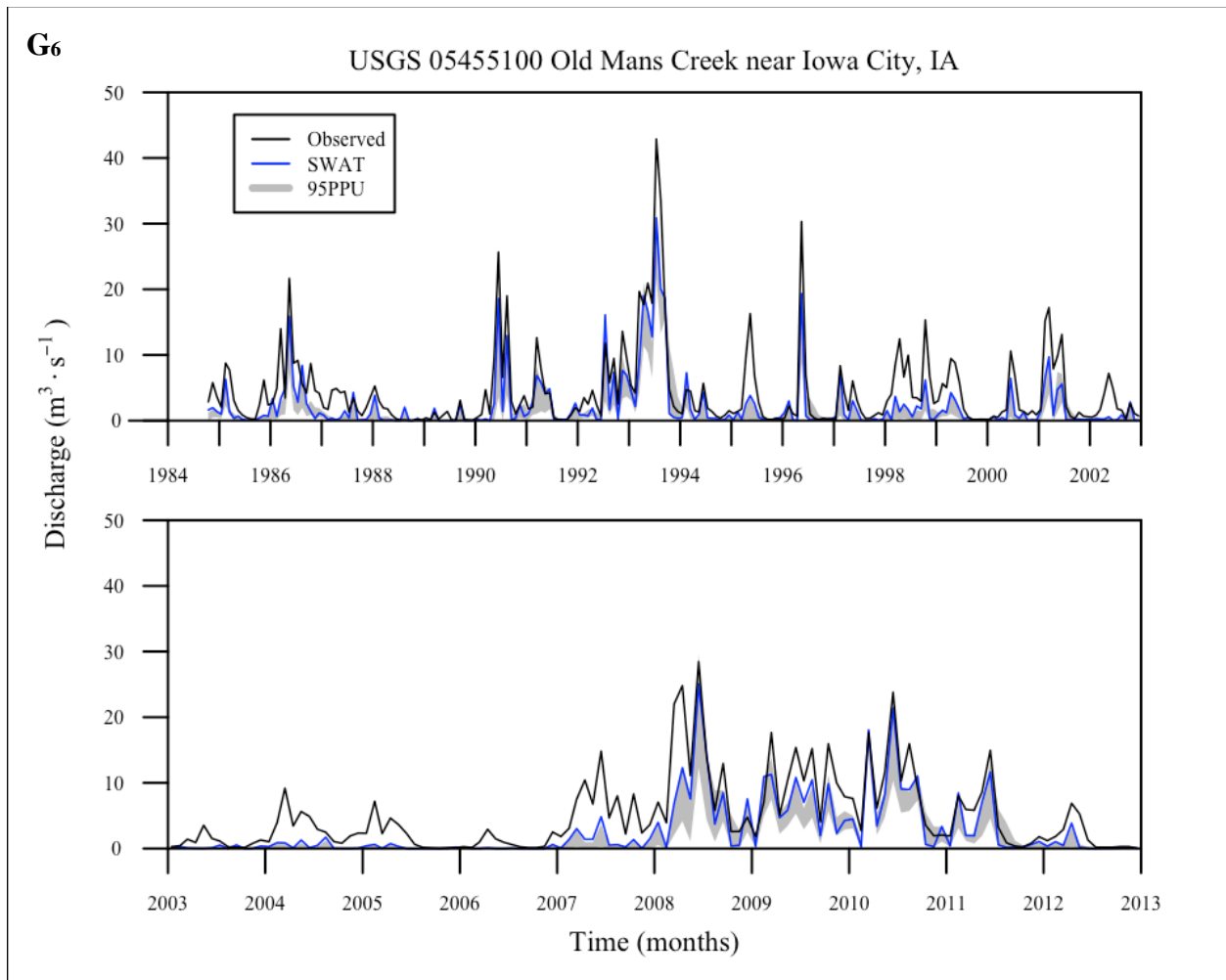
Figure 4-9   Simulated and observed stream discharge at gage station USGS 05455100 Old
              Man's Creek near Iowa City, IA for (top) calibration period and (bottom)
              validation period
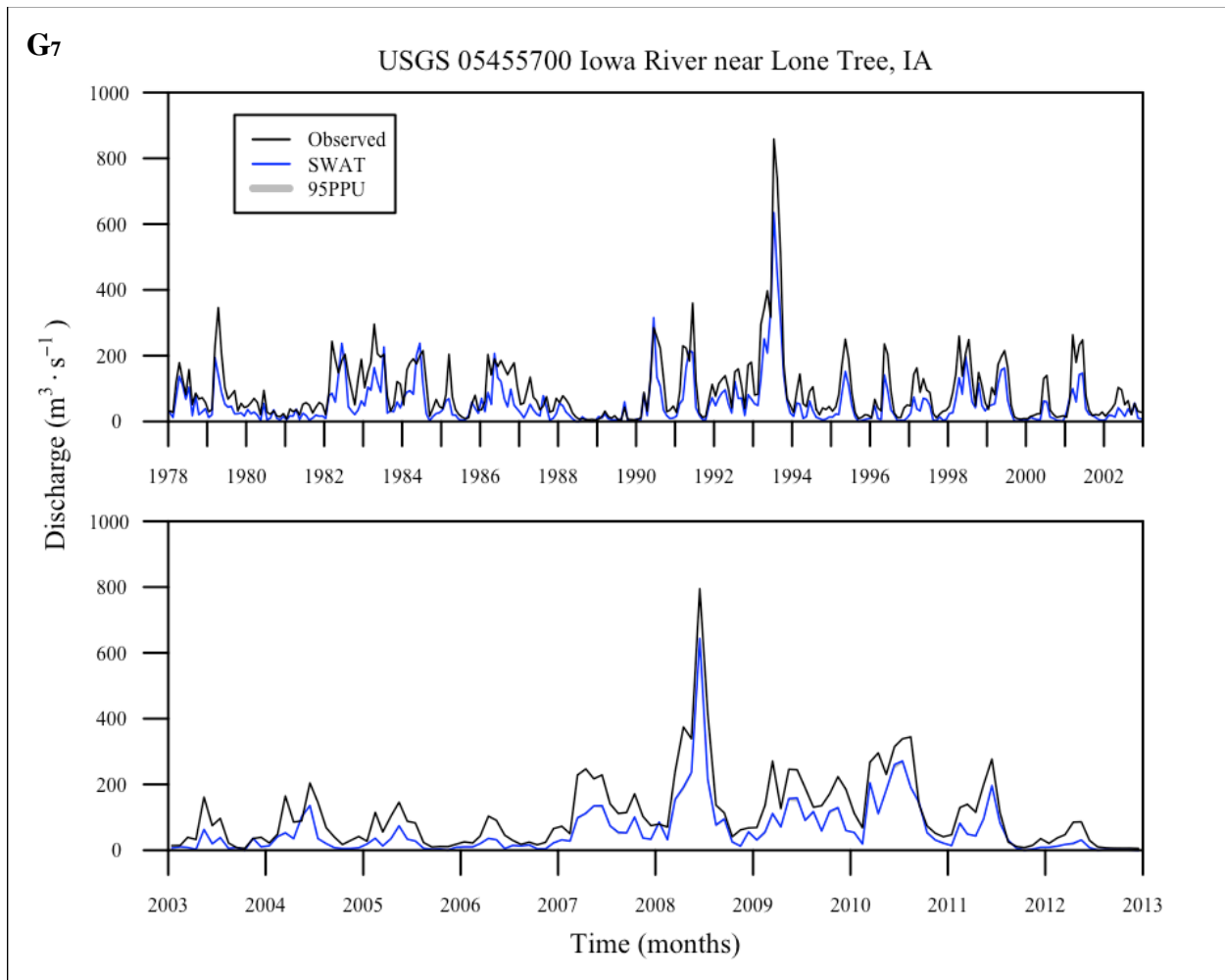
Figure 4-10   Simulated and observed stream discharge at gage station USGS 05455700 Iowa
River near Lone Tree, IA for (top) calibration period and (bottom) validation
period
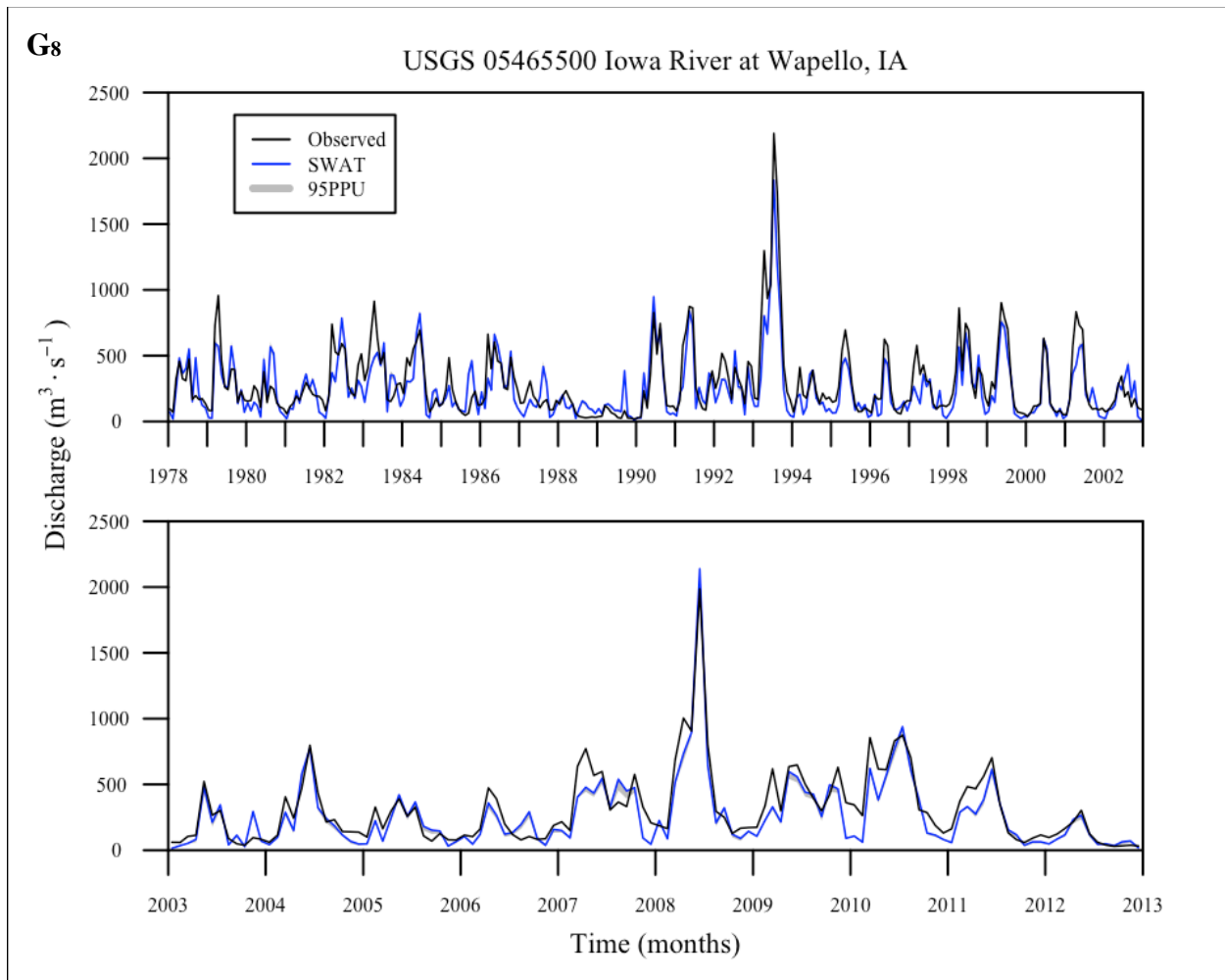
Figure 4-11   Simulated and observed stream discharge at gage station USGS 0546550 Iowa
               River at Wapello, IA for (top) calibration period and (bottom) validation period
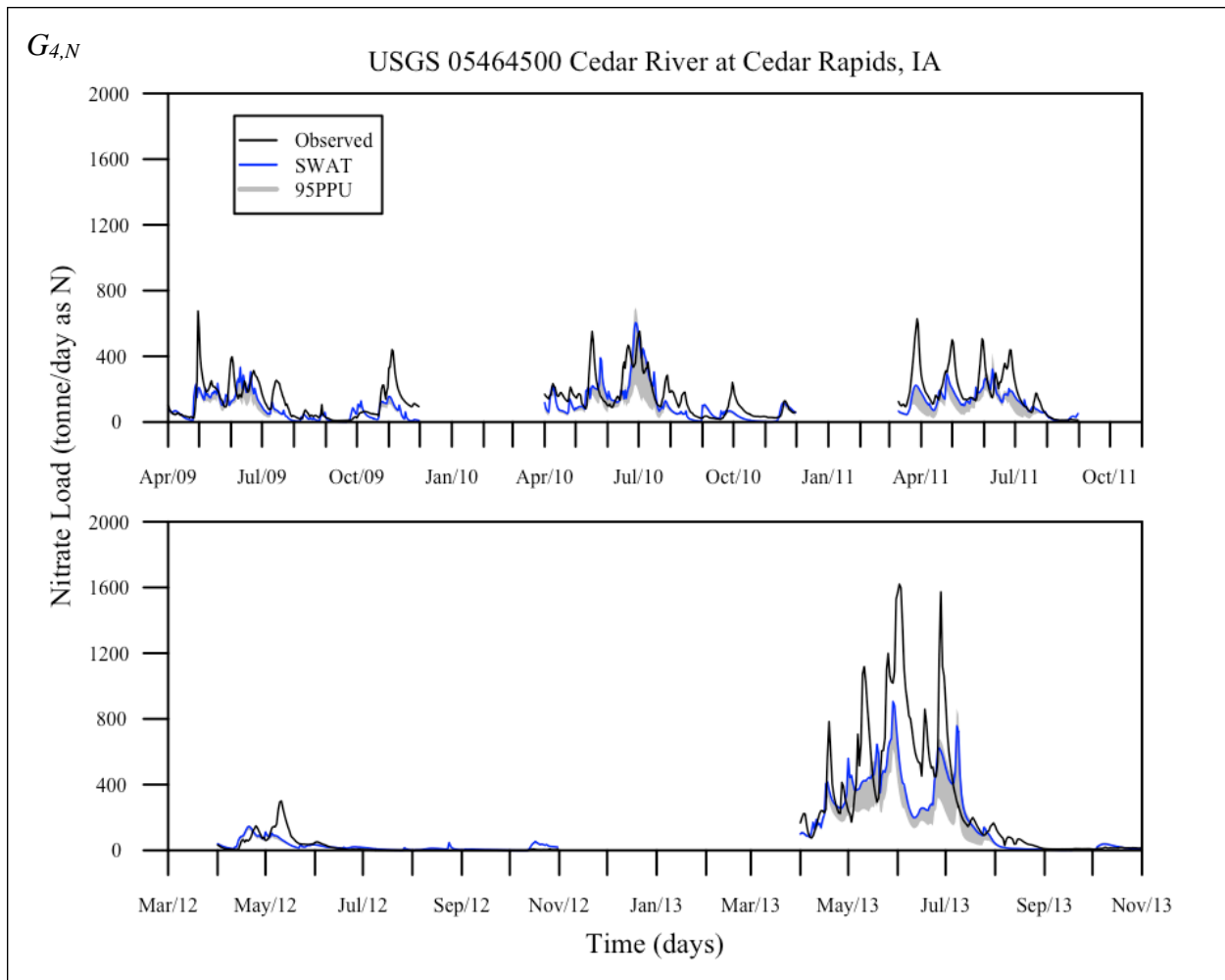
Figure 4-12   Simulated and observed nitrate load (tonne/day) at gage station USGS 05464500
Cedar River at Cedar Rapids, IA for (top) calibration period and (bottom)
validation period
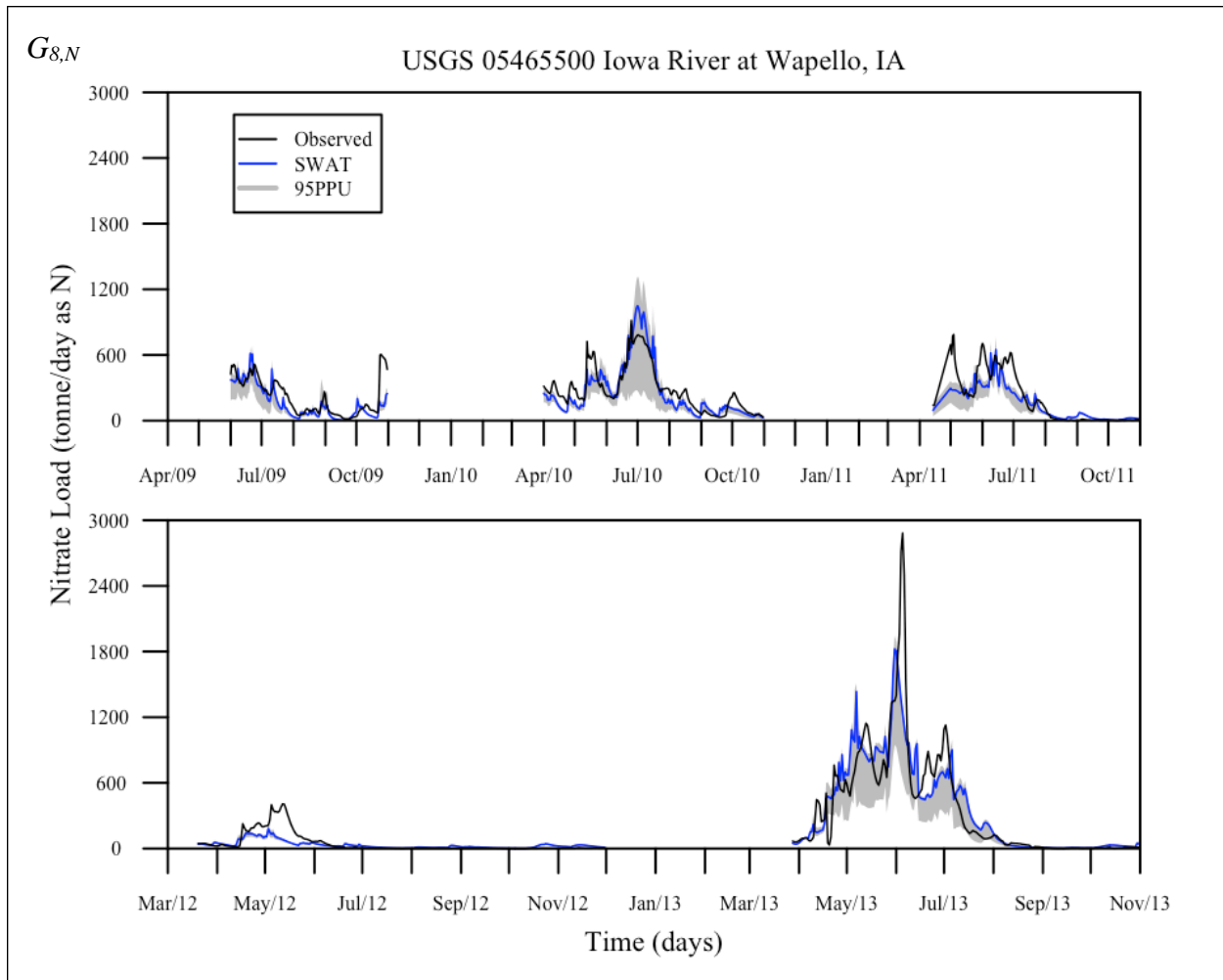
Figure 4-13   Simulated and observed nitrate load (tonne/day) at gage station USGS 0546550 Iowa River at Wapello, IA for (top) calibration period and (bottom) validation period
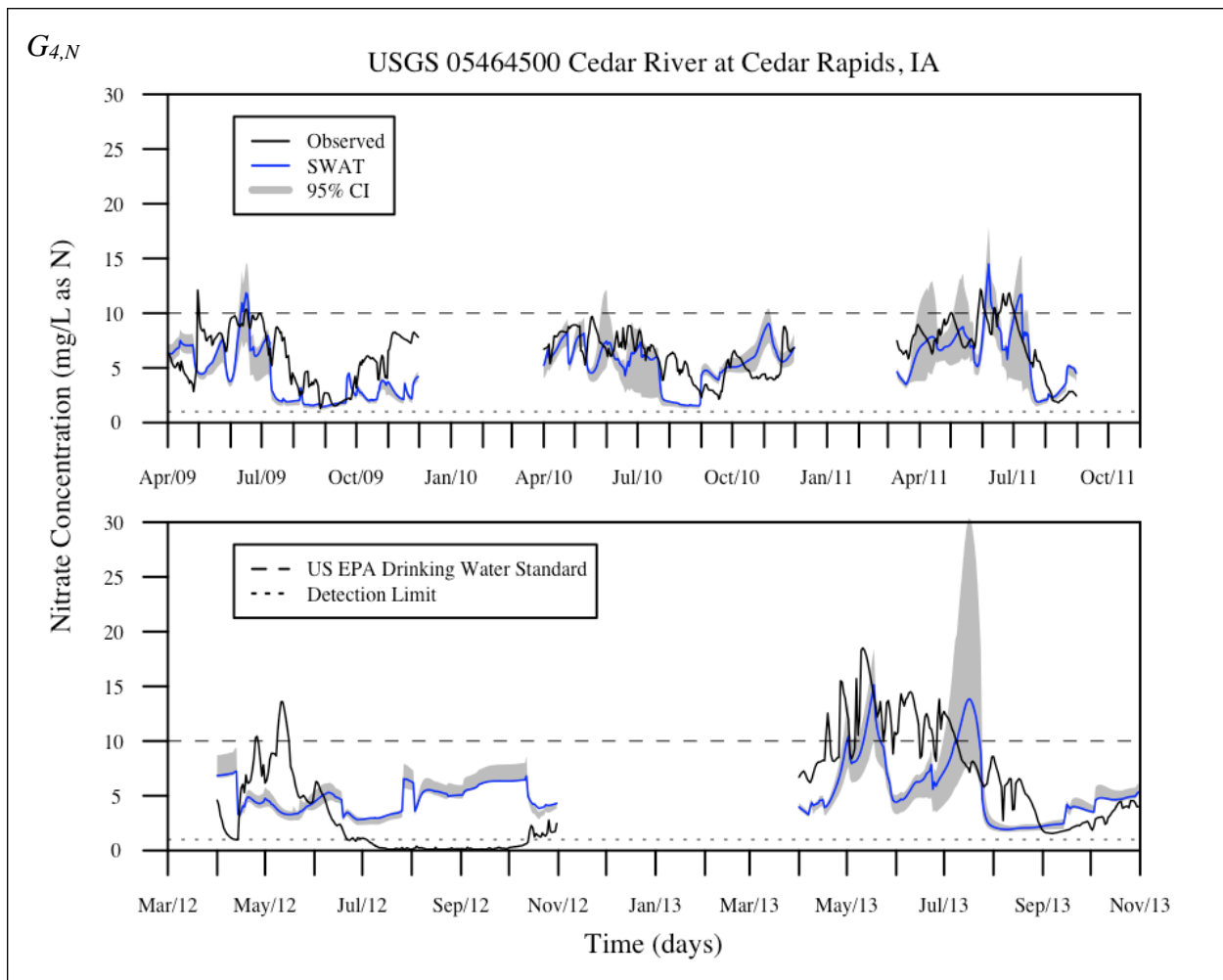
Figure 4-14   Simulated and observed nitrate concentrations (mg/L) at gage station USGS 05464500 Cedar River at Cedar Rapids, IA for (top) calibration period and (bottom) validation period with US EPA drinking water standard (10 mg/L) and detection limit (1 mg/L)
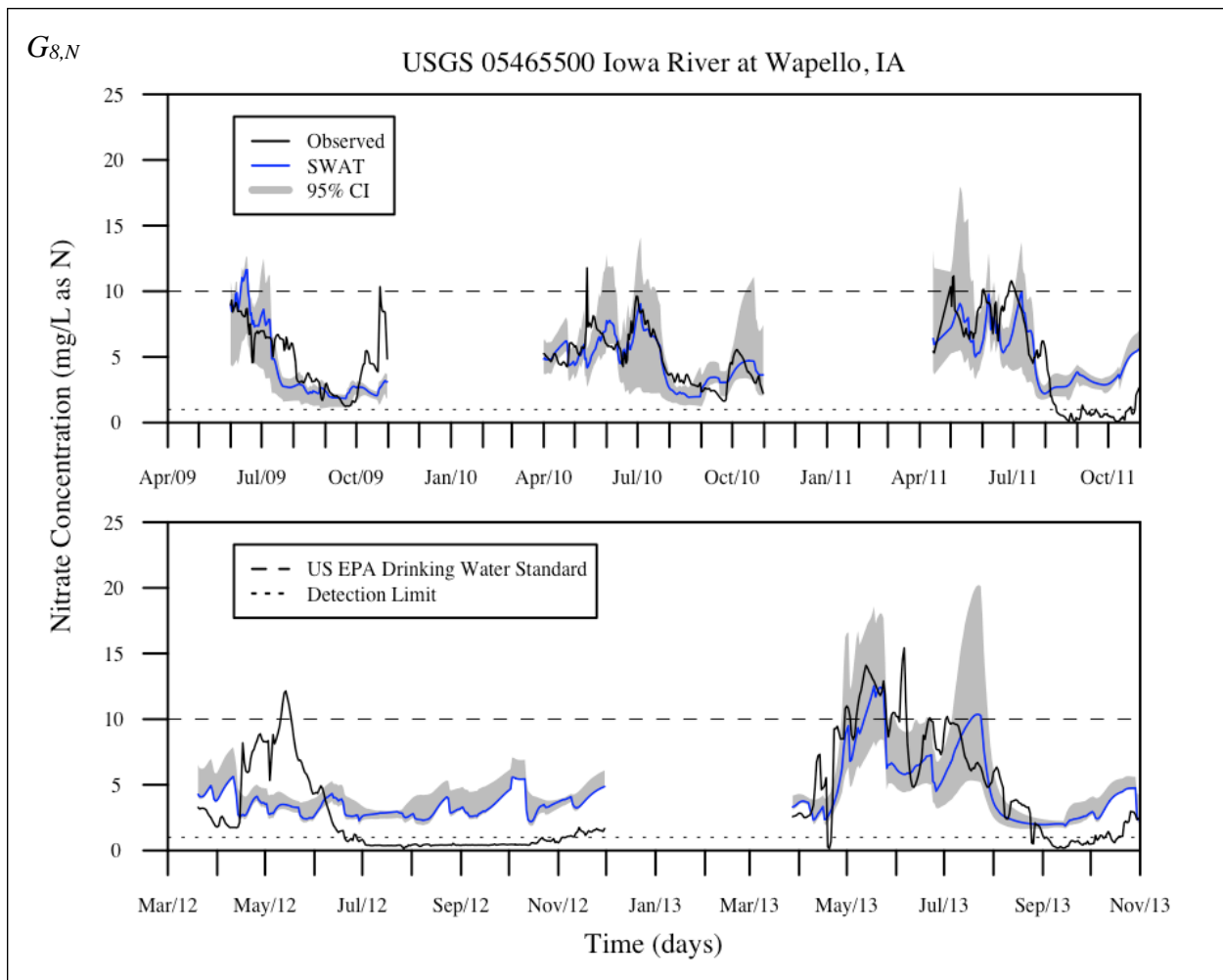
Figure 4-15   Simulated and observed nitrate concentrations (mg/L) at gage station USGS 0546550 Iowa River at Wapello, IA for (top) calibration period and (bottom) validation period with US EPA drinking water standard (10 mg/L) and detection limit (1 mg/L)

CHAPTER 5: ARTIFICIAL NEURAL NETWORKS FOR DATA
GAP TREATMENT AND WATER QUALITY MODELING

Introduction

Underlying the shift to "big data" in contemporary scientific investigation was the increased capabilities for collection, storage, and analysis (Manyika et al., 2011). For environmental data the deployment of instruments that can rapidly sample and transmit measurements to a data center was responsible for the collection aspect (Corke et al., 2010) and the ever decreasing costs of data storage and computational power were responsible for the latter. Some mathematical algorithms and problem-solving methods developed decades ago and infeasible to implement at the time had now become commonplace (Wu et al., 2008). One of these methods was the artificial neural network (ANN); the ANN was based on a biological neural network composed of neurons that interact and feed each other data to arrive at solutions to complex problems (Hassoun, 1995).

Artificial neurons formed the basic components for ANNs, but could have many different architectures (Hagan et al., 1996). Each neuron may exist alone and accept inputs from other neurons or input data directly or neurons grouped as layers whose cumulative outputs transferred between layers. Biological neurons transmitted information across axons via action potentials and neurotransmitters and the artificial neuron's analogous components were digital data and a transfer function that transforms the data before passing them on to other neurons (Hecht-Nielson, 1989). What kind of transfer function, the number of neurons, the number of layers, and the network links and directionality together defined the ANN's architecture. The types of problem to be solved dictated the ANN architecture. Regardless of architecture all ANNs required "training," a term equivalent to calibration where the ANN "learns" from the training dataset and validates on a "testing" dataset.

ANNs have been applied to a variety of problems including pattern recognition, operating control systems, and regression analysis (Patterson, 1998). ANNs have also seen increasingly

common usage in hydrological studies (Hsu et al., 1995; Govindaraju & Rao, 2010), especially comparing the performance of common watershed models such as SWAT to their ANN counterparts. This chapter dealt with two applications of ANNs: filling in time series data gaps and modeling in-stream nitrate concentrations.

Data Gap Treatment

While the high frequency stations provided a large amount of data, gaps still existed in the record due to instrument malfunction or removal for maintenance. An estimation method was helpful in preparing a more complete record for calibration and validation as the reliability of GOF statistics benefit from larger and complete datasets (Yapo et al., 1996). For filling in data gaps statistical models were typically sufficient and straightforward to use without the need for physical modeling beyond time and the readily available covariates such as stream discharge (Cohn et al., 1989). The classic statistical model was parametric where the constituent is approximated by the product of coefficients and covariates or their transformations:

Equation 5-1 $\qquad \hat{C}_i \sim \beta_0 + \vec{\beta} \cdot \vec{f}(Q_i, t_i)$

$\vec{\beta}$ was a vector coefficient and f some function of the explanatory variables. The coefficients were determined through least squares method that minimizes the sum of squared errors between model and observations or other techniques such as maximum likelihood estimation. The drawbacks of parametric models came from their assumptions: the model errors followed a normal distribution, the response variable was the sum of linear covariates, and the equation was determined *a priori*.

Non-parametric methods overcame some drawbacks of classical parametric model, but introduced their own (Cheng, 1976). A non-parametric model relaxed the assumptions of linearity and did require determining the probability distribution of the response variable, an often necessary step in parametric statistical modeling. A non-parametric method avoided the need to define the right hand side of the equation, dependent solely on the available data

107

themselves. The resulting non-parametric model may be opaque in the sense that there were many terms on the right side of the equation and the coefficients of those terms did reveal much information about how the response variables physically relate to the explanatory variables. As such non-parametric methods fell victim to "overfitting" where the model accurately predicts the observations but poorly generalizes to new data (Sarle, 1995). Of the non-parametric methods the ANN may be the most opaque. The lack of formula, terms, and coefficients explicitly tied to those terms place ANNs in the far extreme of non-parametric methods.

While Chapter 3 already walked through the SWAT model calibration and validation, a pre-processing step occurred before the calibration where the data gaps in the daily nitrate loads and concentrations were filled. The raw observations for daily nitrate concentrations and loads covered only five years with many gaps. The largest and consistent gaps occurred during the winter months and those gaps were not filled because a calibration or training dataset cannot be compiled for those periods. Any model trained on the non-winter months would be woefully biased and unreliable. Instead, the gaps during the time periods where the instrument was employed were filled to complete the seasonal records. The first step was justifying the use of the ANN over parametric methods. The Load Estimator (LOADEST) software was developed by the USGS and commonly used for estimating loads (Runkel et al., 2004). While designed for loads, the software implicitly modeled concentrations as the explanatory variables usually contain stream discharge.

The process of evaluating a method's efficacy at filling data gaps was as followed. The existing daily data were partitioned into calibration and validation sets through random sampling with equal probabilities for any given day. The size of the calibration dataset changed with the percent data gaps. That is, at 10% data coverage, only 10% of the data were selected for model calibration and 90% were for model validation. The percent data gaps chosen were ϵ {10, 11… 89, 90}. For each data gap percentage value, fifty sample sets and subsequent calibration runs prevented the sampling procedure from producing an unrepresentative sample of the hydrological and temporal conditions at the monitoring station.

The total number of simulations for an estimation method was 4050: 81 data coverage percentages and 50 sample sets each. The GOF statistic was the NSE, but its distribution and median were used for comparison. The interquartile range (IQR) can be calculated from the fifty NSE replicates to approximate the variability of an estimation model's performance. That is, given a random sample set, the IQR represents the variability of an estimation method's performance in predicting the rest of the dataset. The median NSE gave a sense of the overall accuracy of the gap treatment method. The following values were used to judge the generalizability of either models: the best median validation NSE, the percent data gap in which the NSE is found, Kendall's τ rank correlation coefficient for median validation NSE with percent data gaps, and the τ-test's *p*-value for the probability that the calculated τ was significantly different from zero. Kendall's τ was non-parametric and showed whether the median NSE was increasing or decreasing with data gaps without regard to the NSE's probability distribution.

The gage stations are the same as the SWAT calibration: Cedar Rapids and Wapello. The general relationship mapped by the ANN was:

Equation 5-2 $\qquad \ln C \sim f(\ln Q, \sin \pi t_d)$

C was the mean daily nitrate concentration, *Q* the mean daily stream discharge, and t_d the day of the year mapped from an interval of [0,366] to [0,1] to account for periodicity. As for actually filling in data gaps versus a comparison between filling methods, the ANN training data set was split into 70% of the observations and the validation 30%, randomly selected from the entire record. The <u>Methods</u> section of this chapter detailed the mechanics and procedure for both ANN and LOADEST regression.

<u>Water Quality Modeling</u>

With the "learning" of the data for the training period completed, the neural network can estimate the missing data. Another potential application of neural networks is coupling with a

physically-based model with known and meaningful parameters to aid in any deficiencies of the latter model. Chapter 4 showed that SWAT could effectively simulate stream discharge and nitrate loads, but nitrate concentrations were not simulated with the same degree of accuracy, especially at low concentrations.

An experimental procedure coupled SWAT and ANN by using SWAT's stream discharge as inputs into the ANN. First, 5000 ANNs were trained on the following inputs: the natural log of the observed discharge Q_t at the current time step, the natural log of discharges lagged by three days $Q_{t-1..3}$, the day of the year t_d mapped to [0,1] for periodicity, and the daily mean temperature of the five nearest contributing basins to the gage station, $\theta_1, ..., \theta_5$. The target was the natural log of the observed concentrations excluding those filled in by the data gap treatment:

Equation 5-3 $\qquad \ln C \sim f(\ln Q_t, \ln Q_{t-1}, \ln Q_{t-2}, \ln Q_{t-3}, \sin \pi t_d, \theta_1, ..., \theta_5)$

The lagged discharges accounted for prior rainfall-runoff events, the day of year accounted for the fertilizer application on agricultural lands, and temperature at the nearest subbasins in the gage's group accounted for nearby nitrogen dynamics. The outputs of the multiple networks were also used to construct 95% uncertainty intervals (95PPU) via the 2.5 and 97.5 percentile of the 5000 network outputs of each simulated time step's ECDF. This interval is equivalent to those found in the time series plots in Chapter 4. A calibrated SWAT model's output daily discharge was used to replace the observed discharge to link the two models.

<div align="center">Methods</div>

<div align="center">*Artificial Neural Networks*</div>

The multilayer feed-forward ANN was the architecture class used for both the data gap treatment and the ANN-SWAT coupling. As universal function approximators (Hornik et al., 1989), these ANN architectures were the most suitable for regression type problems where the outputs were a function of the inputs. The ANN architecture employed three layers: an input

<div align="center">110</div>

layer, a "hidden" layer, and output layer. The number of neurons in the input layer was equal to the number of input variables. The output layer was a single neuron as nitrate concentration was the sole variable of interest. The hidden layer contains ten neurons that act as nodes, collecting input data multiplied by weights with numerical interval of [0,1].

Figure 5-1 shows a schematic of the ANN architecture with input x_i and weights $w_{i,j}$ denoting the weight for i'th variable to the j'th node or neuron. The circles were neurons and the boxes were transfer functions. The neurons summed the products and weights from each input vector plus a bias term, equivalent to a constant in an ordinary regression analysis. Transfer functions transformed the neurons' sums with a tan-sigmoid function that mapped the sum from an interval of $(-\infty, +\infty)$ to $(-1,1)$:

Equation 5-4 $$f_t^H(\Sigma) = \frac{2}{1 + e^{-2\Sigma}} - 1$$

Σ was the sum of the weights and inputs to the j'th neuron or $\sum_i^n x_i w_{j,i}$ and f_t^H was the transfer function for the hidden layer. A second set of weights $w_{j,O}$ were multiplied with the outputs of the hidden layer and were summed at the output node before undergoing the output transfer function, f_t^O, which was simply the identity function:

Equation 5-5 $$f_t^O\left(\sum_j^{10} w_{j,o} f_{t,j}^H(\Sigma)\right) = \sum_j^{10} w_{j,o} f_{t,j}^H(\Sigma) = \hat{y}$$

The flow of inputs through the hidden layer to the output neuron and finally an output $\hat{y}$ was one iteration of the ANN training. The training initialized with a randomized weights that change with each iteration by comparing the ANN estimated $\hat{y}$ and target output, y. ANN training was an optimization routine of finding the best weights with respect to an objective function. The objective function for the ANN in this dissertation was the mean squared error (MSE):

111

Equation 5-6

$$\text{MSE} = \frac{1}{n}\sum_{k=1}^{n}(y - \hat{y})^2$$

The algorithm to optimize the weights was the Levenberg-Marquardt or damped least-squares method common in non-linear least squares curve fitting (Hagan & Menhaj, 1994). As the inputs propagated through the network for the estimated outputs, the errors between the outputs and the targets propagated backwards to update the weights. The backwards propagation required a constant learning parameter η and transfer functions that are differentiable. The weight update algorithm can be summarized as:

Equation 5-7

$$\mathbf{w}^* = \mathbf{w} - (\mathbf{J}^T\mathbf{J} + \eta\mathbf{I})^{-1}\mathbf{J}\mathbf{e} \;\bigg|\; \mathbf{J} = \left\{\frac{\Delta(y - \hat{y})}{\Delta w_{i,j}}, \frac{\partial f_t}{\partial w_{i,j}} : i = 1\ldots M, j = 1\ldots 10\right\}$$

w was the vector of weights, **J** the Jacobian matrix, **I** the identity matrix, and **e** the vector of absolute error between the target and outputs. In simpler language the update to the weights was a function of the partial change in the error and the derivative of the transfer function for a layer. These partial changes or derivatives were the elements of the Jacobian matrix.

Complete details of the Levenberg-Marquardt algorithm was beyond the scope of this dissertation and can be found in most texts describing numerical methods for neural networks (Yu & Wilamowski, 2011). The stopping point for the algorithm depended on the test dataset. The ANN used the inputs from the validation dataset to calculate outputs for the validation targets for each iteration. If the MSE for the validation increased consecutively for five iterations, the training stopped. Although the validation MSE was used as the stopping point, the errors from the validation outputs were not used to update the weights, ensuring that the weights and the ANN as a whole can generalize outside the training data.

Load Estimator

The USGS's LOADEST software for estimating constituent loads offered several parametric models whose coefficients or parameters were determined using adjusted maximum

112

likelihood estimation (AMLE), which maximized the log-likelihood function of a parametric model given censored constituent data (Cohn et al., 1989). The likelihood function was equal to the probability of a response variable value given a set of parameters. AMLE iteratively sampled from the parameter space and calculated the log-likelihood until convergence to a parameter set with no change in the log-likelihood estimate. For comparison a least squares regression method minimizes the sum of squared errors between the observations and a parametric model's predictions. LOADEST offers 11 preloaded formulas, but the user could also define a custom formula.

Equation 5-8 included all terms used in the premade formulas:

Equation 5-8
$$L = a_0 + \sum_{i=1}^{2} a_i \ln Q^{i-1} + \sum_{j=3}^{4} a_i \theta \ln Q^{j-2} + \sum_{k=4}^{5} a_j d_t^{j-3} + a_5 \sin 2\pi d_t + a_6 \cos 2\pi d_t$$

Q was centered stream discharge, θ a seasonal term typically defined as certain months out of the year, and d_t centered decimal time. Some explanatory variables such as flow and time may correlate with one another so centering pre-processed the data to eliminate this relationship (Cohn et al., 1992):

Equation 5-9
$$\tilde{Q} = \bar{Q} + \frac{\sum_{k=1}^{N}(Q - \bar{Q})^3}{2 \sum_{k=1}^{N}(Q - \bar{Q})^2}$$

Q was stream discharge or any other variable, $\bar{Q}$ the mean, and $\tilde{Q}$ the centered form.

To choose the best formula from the preloaded for each station, a preliminary formula selection was done using 50 sample sets per formula at 50% data gap for each station. The best median calibration NSE was the decision metric. Table 5-1 shows the formulas for the Cedar Rapids and Wapello station after this preliminary procedure and the NSE statistics attached to them. Cedar Rapids had a briefer formula that depended less on time periodicity while Wapello had heavy dependence on time periodicity with both periodic (sine and cosine) terms included.

<u>Results and Discussion</u>

Data Gap Treatment

Figure 5-3a-d show the median NSE and the interquartile range of the sample sets'
validation NSE for the LOADEST and ANN models as a function of percent data gap or missing
data. The parametric models in LOADEST do not seem to change with the percent data gap with
low Kendall's τ rank correlation coefficients: 0.30 and 0.01 for Cedar Rapids and Wapello,
respectively (Table 5-2). The *p*-value in Kendall's τ for Wapello were not statistically significant
at α=0.05. The Kendall's τ coefficients for the ANNs were 0.74 and 0.70 for the two stations
with the low *p*-value indicating highly significant correlations. The median validation NSE plot
in Figure 5-3b for the ANNs shows that ANN were sensitive to amount of data available and
asymptotically improve as data gaps decreased. With few data gaps the ANNs performed better
than their parametric counterparts with the highest median NSE for the ANN occurring at data
gaps ≤ 20%. The LOADEST models did not have the same trend with Wapello having its highest
median NSE at 68% data missing and Cedar Rapids at 36%.

As for model variability in terms of the IQR in Figure 5-3c-d, a slight quadratic
relationship appeared to exist between data coverage and an estimation model's variability. For
both LOADEST and ANNs, the variability was greatest at low data coverage <30%, least around
40-60%, and increased above 60%; however, the ANN curves in Figure 5-3d show this
relationship less strongly than LOADEST. The relationship could indicate that at high data
coverage the estimation models begin to "overfit" to the calibration dataset and perform poorly
on new data. The variability in the low data coverage was more intuitive as a small sample size
was more likely to be unrepresentative.

Considered in the context of data collection, if the resources for a project only allowed
for grab sampling with uncertain frequency, then a parametric model for estimation of data gaps
may be more appropriate as it is less sensitive to number and length of data gaps for a given site.
If the resources for sampling design allowed for high data coverage or high-frequency sampling,

114

ANN or other non-parametric models may be more accurate, exceeding that of the parametric models at very high data coverage. For either estimation method a risk of overfitting occurred at low and high data coverages, especially if the samples did not cover the temporal range of interest. In the case of high frequency sensors which had fewer gaps and a larger amount of data, the non-parametric ANN was superior for filling in data gaps. The ANN with the maximum NSE at 30% from this comparison exercise was then used to fill in the data gaps for the observed nitrate concentration time series. The NSE and R^2 all exceeded 0.90 for both stations. The time series plot in Figure 5-4 shows the training data set as gray circles, the ANN estimated outputs as red, and the missing data filled in by the ANN in blue. The estimates matched the training or observations well except for 2012, the drought year that also presented problems for the SWAT autocalibration.

Water Quality Modeling

ANNs demonstrated their worth in filling gaps in comparison to purely statistical models. For prediction the ANN required more input variables and had greater dependency on SWAT's discharge outputs. The ANN-SWAT coupling and the SWAT nitrate calibrated outputs were compared to each other to evaluate whether resorting to ANN for nitrate prediction would be a better alternative than using SWAT's nitrate dynamics. From Table 5-4 and for the best networks, the calibration period NSEs for nitrate concentrations were 0.49 and 0.64 at Cedar Rapids and Wapello, respectively. The R^2 were 0.60 and 0.65. The PBIAS under-predicted at -7.3 and -5.3 percent. The validation period NSEs for nitrate concentrations were 0.70 and 0.53 at Cedar Rapids and Wapello, respectively. The R^2 statistics were 0.79 and 0.63. The validation PBIAS under-predicted at -17.4 and -18.0 percent.

From a numerical GOF standpoint, the ANN coupled with SWAT's stream discharge outputs performed far better than SWAT's nitrate autocalibration. Cedar Rapids' calibration period NSE for SWAT by itself was negative while the ANN coupling had an NSE just short of the acceptable limit at NSE=0.50. The validation NSEs for the two stations also met the

115

acceptable limit with Cedar Rapids's NSE exceeding that of its calibration period. The PBIAS also looked moderate, but the PBIAS for Wapello's calibration period and Cedar Rapids's validation period are greater in magnitude than SWAT by itself, which yielded PBIAS of -0.90 and 0.30 percent for Cedar Rapids and Wapello, respectively.

The time series plots told a very different story. Figure 5-5 and Figure 5-6 show the coupled ANN-SWAT nitrate concentrations for the calibration period (2009-2011) on top and the validation period (2011-2012) on bottom with the black lines being the observations, blue being the best ANN with the highest NSE, and the gray being the 95PPU. Compared to the SWAT nitrate autocalibration in Figure 4-14 and Figure 4-15, the coupled ANN-SWAT plots had a more noisy appearance as both the simulations and the 95PPU had pronounced day to day fluctuations. Despite the noisy appearance the coupled ANN-SWAT did appear to approximate the nitrate concentrations well in the calibration period for both Cedar Rapids and Wapello. The calibration 95PPU also had a narrow range around the simulations. The noisy appearance was perhaps due to the large number of ANNs trained (5000). With so many networks the continuity between each time step became less smooth; that is, the networks which produced the 97.5 and 2.5 percentile networks between two consecutive time-steps may behave very differently.

The validation time-series suffered an issue opposite that of SWAT's nitrate autocalibration. Whereas the autocalibration hardly allowed concentrations to dip below 1 mg·L^{-1}, the coupled ANN-SWAT validation period did not mimic the nitrate spikes found in 2013. The low concentrations were consistent with concurrent lab samples reported at similar USGS gage stations (Pellerin et al., 2014). Instead the ANN simulated the low concentrations well. Cedar Rapids in this case performed better than Wapello with some nitrate concentrations going above 10 mg·L^{-1} and an overall pattern that resembled the observations. ANN-SWAT's Wapello in 2013 completely missed the May-June spike. The 95PPU for the validation was also wider and noisier, indicating greater uncertainty compared to the calibration. For example in October 2012 for both stations, the 97.5 percentile greatly exceeded the observations, some points exceeding the observed maximum daily concentration for their respective stations.

116

Conclusion

ANNs had great utility in improving high-frequency datasets, but the sensitivity of the ANN to initial weights and their optimization hindered their use when attempting to fill-in values or interpolate missing data during a time period when the ANN had no training. Parametric models such as LOADEST would be better with a sparser dataset, but to effectively use LOADEST one would need samples equally spaced in time to reduce the sensitivity of a parametric model's coefficients to the calibration data. The ANN did not have the same variability with data gaps that are random or have no particular pattern; their only requirement was that the training data cover the entire time frame of interest.

The coupling of ANN with SWAT yielded mixed results for nitrate concentrations. The ANN-SWAT coupling simulated low nitrate concentrations where SWAT alone could not. Yet the coupled model failed to simulate the spikes in nitrate after a drought year, a phenomenon that a physically-based model can. The coupled model also had a greater degree of noise in the outputs, even from a single network. The number of explanatory variables may account for this noise because the ANN was "blind" to what were the important variables. With a large number of networks trained, the results may vary wildly as seen in the time series plots. While the statistics for the coupled ANN-SWAT exceeded that of SWAT alone, the visual inspection proved valuable in pointing out the flaws of a model that depended too much on numerical values, ignoring the actual attributes of the physical environment or special circumstances of each year.

117

Table 5-1   LOADEST results from preliminary model selection and the NSE for calibration and validation

Location	Calibration NSE	Validation NSE	Model
Cedar Rapids	0.74	0.73	$\alpha_0 + \alpha_1 \ln Q + \alpha_2 \ln Q^2 + \alpha_3 d_t$
Wapello	0.55	0.59	$\alpha_0 + \alpha_1 \ln Q + \alpha_2 \ln Q^2 + \alpha_3 \sin 2\pi d_t + \alpha_4 \cos 2\pi d_t + \alpha_5 d_t$

Table 5-2   Best median validation NSE for the model replicates and their associated coverage

Model	Station	Validation NSE	% Data Gap	τ	p-value
LOADEST	Cedar Rapids	0.76	36	0.30	<0.001
LOADEST	Wapello	0.60	68	0.01	0.890
ANN	Cedar Rapids	0.76	20	0.74	<0.001
ANN	Wapello	0.89	19	0.70	<0.001

Table 5-3   Goodness of fit statistics for the best artificial neural network

	$\exp(\sqrt{MSE})$ (mg·L^{-1})	R^2	NSE	PBIAS
Cedar Rapids	1.43	0.97	0.97	-0.893
Wapello	1.06	0.92	0.92	-1.19

Table 5-4   Goodness of fit statistics for daily nitrate concentrations at Cedar Rapids and Wapello gage stations for the ANN-SWAT coupling

	Calibration			Validation		
Gage Station	NSE	R^2	PBIAS	NSE	R^2	PBIAS
Cedar Rapids	0.49	0.60	-7.3	0.70	0.79	-17.4
Wapello	0.64	0.65	-5.3	0.53	0.63	-18.0
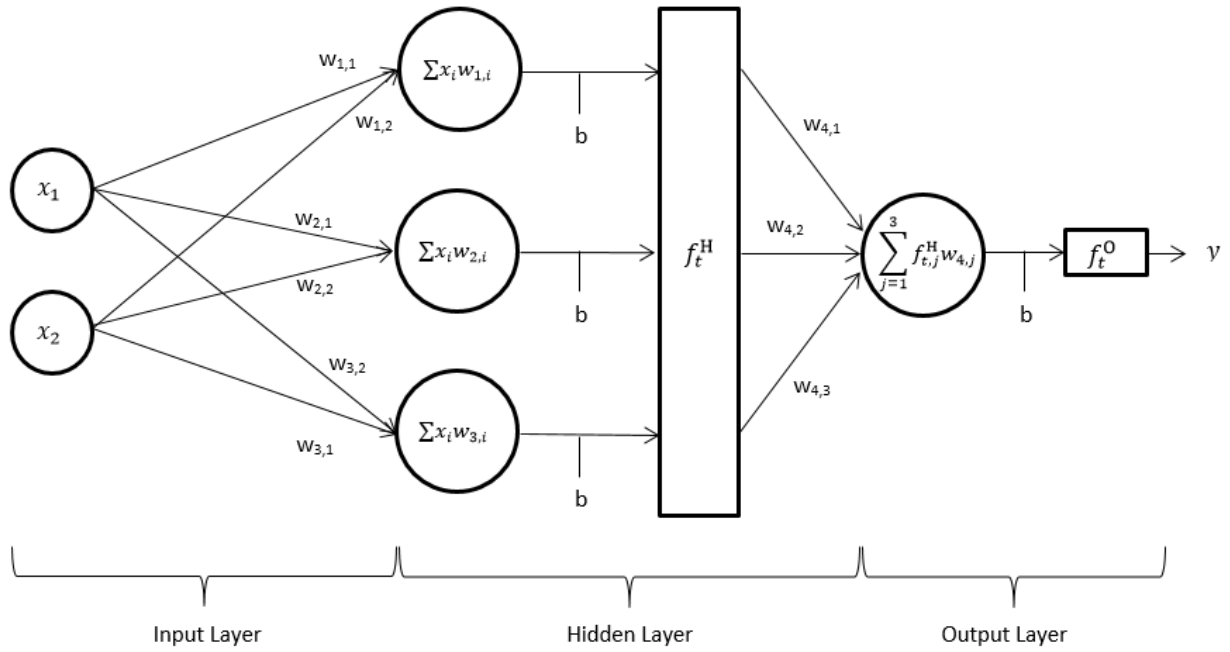
Figure 5-1   Schematic of a simple neural network with inputs x, weights w, and hidden (f_t^H) and output (f_t^O) transfer functions
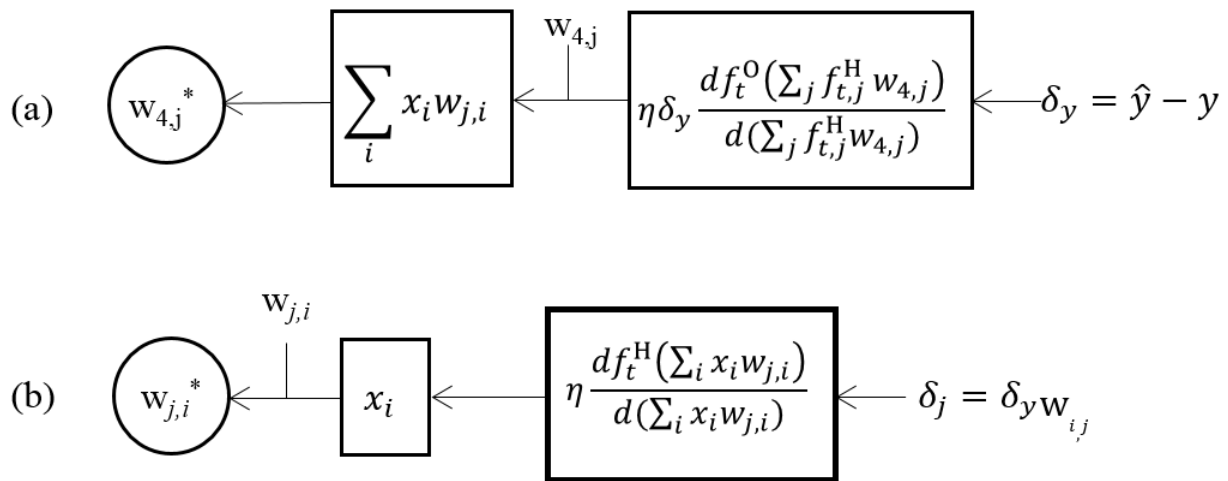
Figure 5-2   Updating schematic for the (a) j'th weight to the output neuron and (b) the j'th weight to the i'th variable
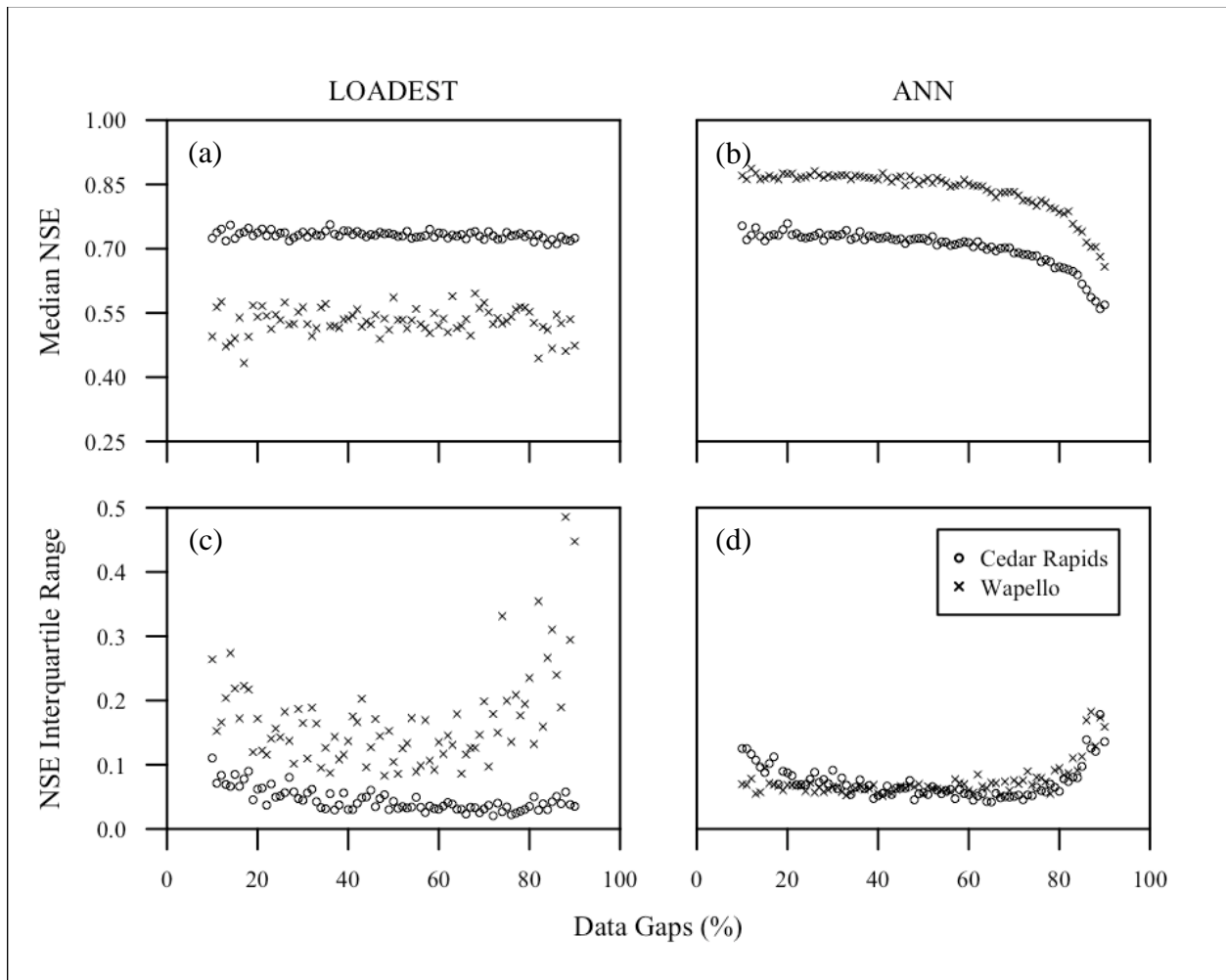
Figure 5-3   Comparison of NSE between LOADEST and ANN with respect to data gaps in terms of the (a,b) median NSE and (c,d) NSE interquartile range
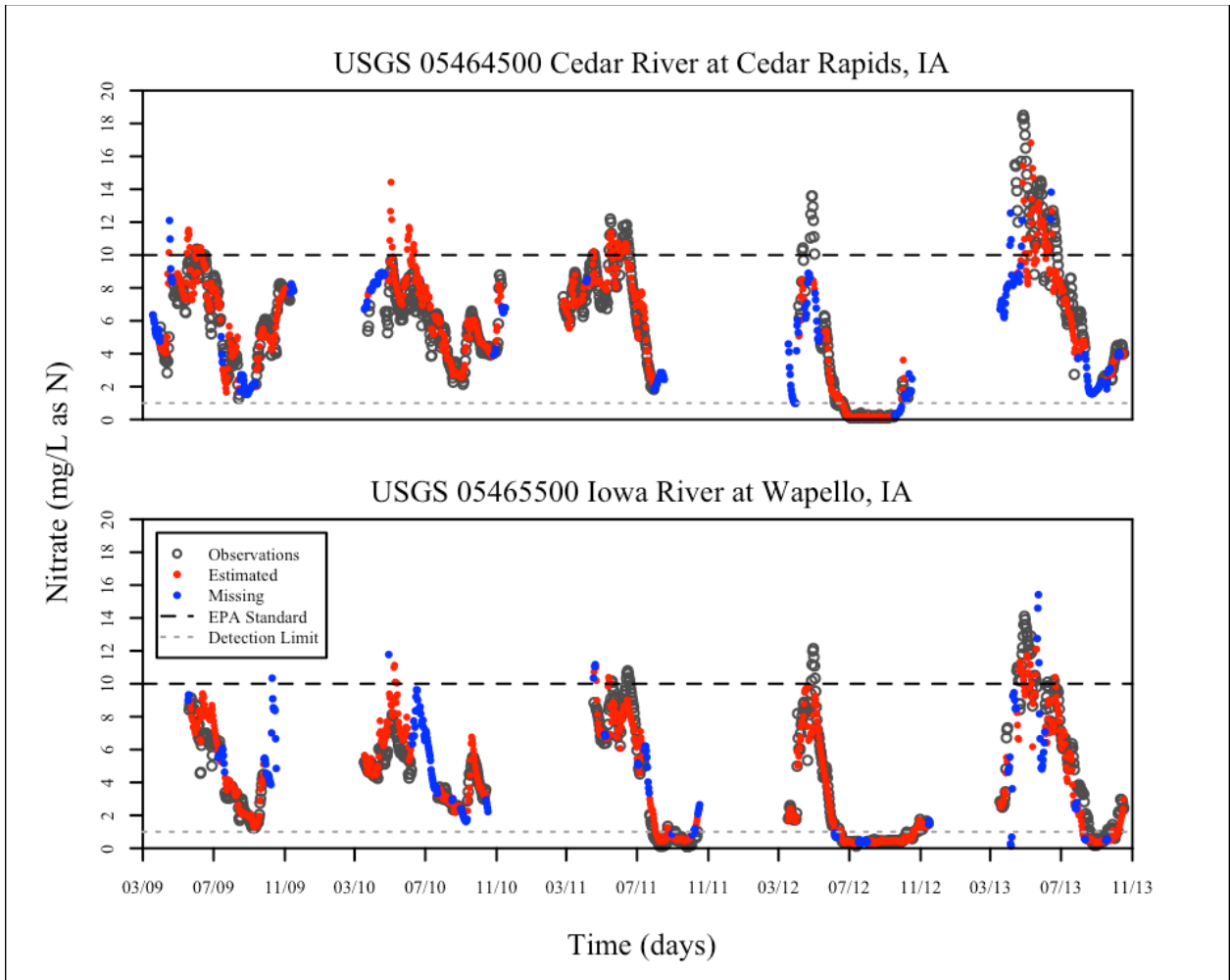
Figure 5-4   Time series of nitrate concentrations at Cedar Rapids and Wapello. In red are the estimated values for existing observations to judge network performance. In blue are the missing data that were in-filled by the neural network.
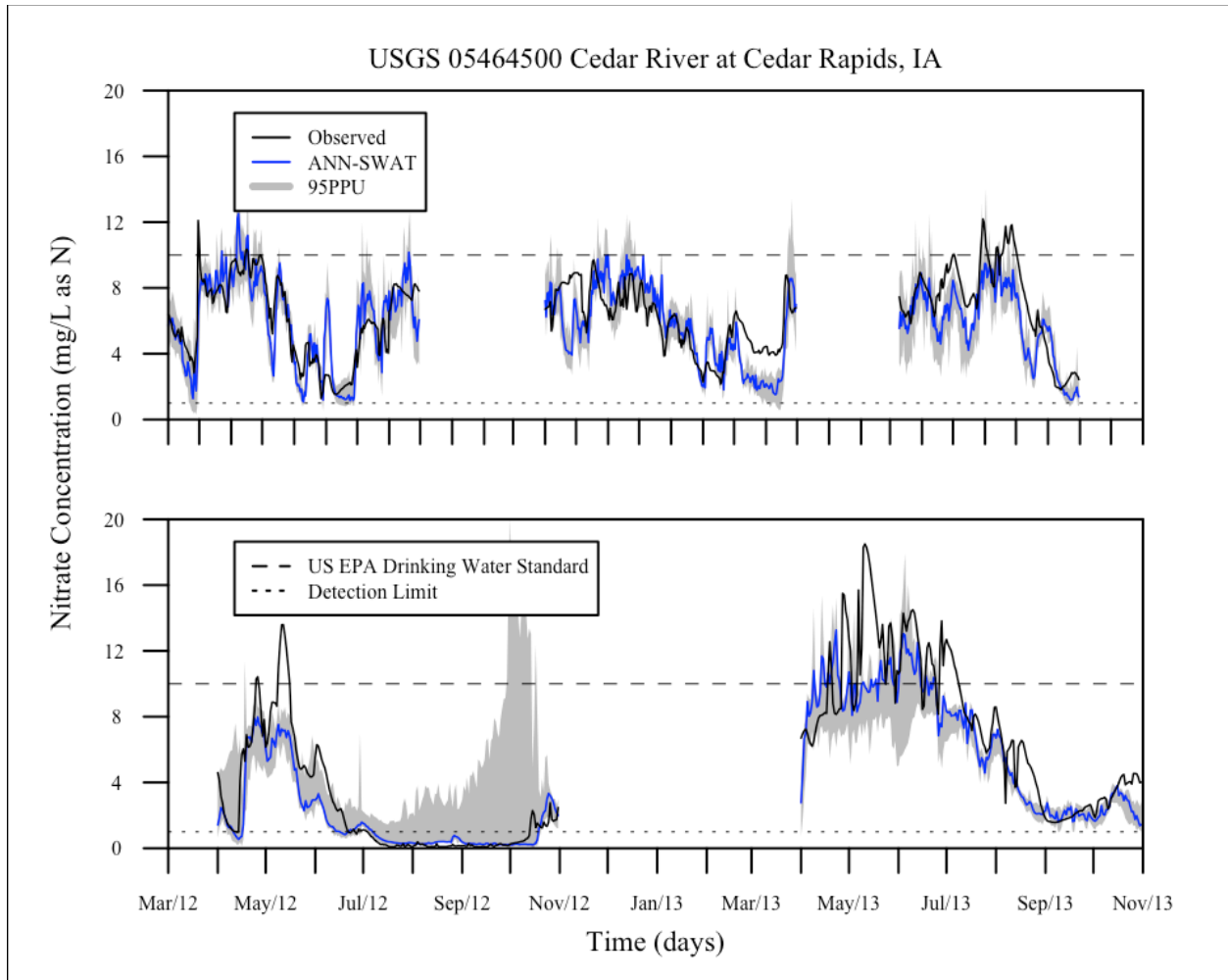
Figure 5-5   Coupled ANN-SWAT simulated daily nitrate concentration (mg/L) at gage station USGS 05464500 Cedar River at Cedar Rapids, IA for the (top) calibration period and (bottom) validation period with US EPA drinking water standard (10 mg/L), the detection limit (1 mg/L), and the 95PPU or uncertainty band from the 5000 neural networks
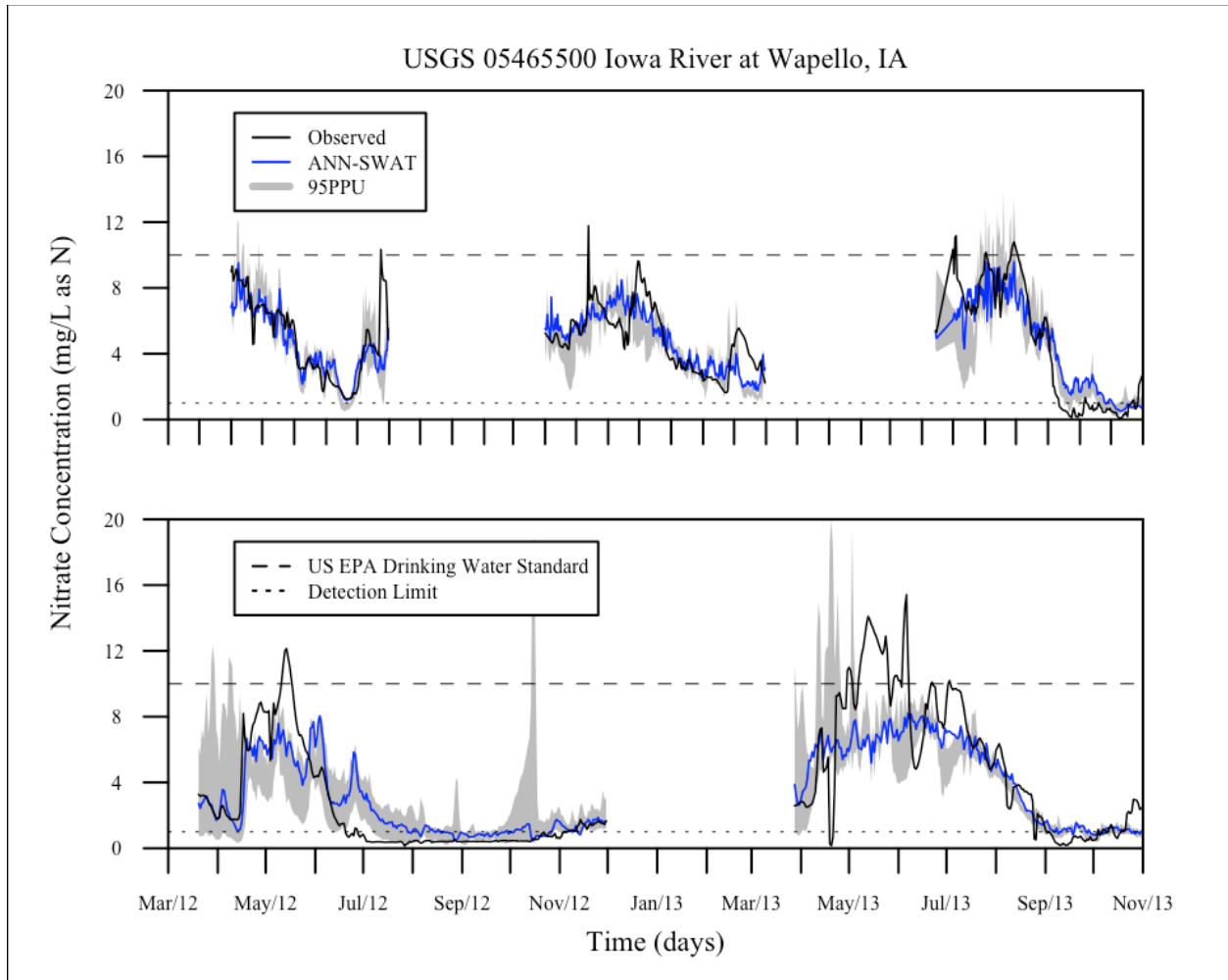
Figure 5-6   Coupled ANN-SWAT simulated daily nitrate concentration (mg/L) at gage station USGS 0546550 Iowa River at Wapello, IA for the (top) calibration period and (bottom) validation period with US EPA drinking water standard (10 mg/L), the detection limit (1 mg/L), and the 95PPU or uncertainty band from the 5000 neural networks

123

CHAPTER 6: APPLYING PROJECTIONS FROM THE NORTH AMERICAN REGIONAL CLIMATE CHANGE ASSESSMENT PROGRAM (NARCCAP)

Introduction

Climate modeling had its beginnings in the 1950s meteorology literature and the prediction of atmospheric events by explicitly solving the equations related to the conservation energy, conservation of momentum, mass balance, and the behavior of gases: the first ever attempt at a "general circulation model" (Phillips, 1956; Manabe & Wetherald, 1975) or GCM. These equations were otherwise known as the first law of thermodynamics, Newton's second law of motion, the continuity equation, and the ideal gas law. Yet a formal definition of climate emerged only two decades after the first GCM, defined by the Global Atmospheric Research Program (GARP) of the World Meteorological Organization (WMO) as a system composed of the atmosphere, hydrosphere, cryosphere, land surface, and biosphere (Perry, 1975). Climate models have since diversified and can be characterized in one of four forms in order of increasing complexity (Shine & Henderson-Sellers 1983): (1) energy balance (EBM), (2) one-dimensional radiative-convective (RC), (3) two-dimensional zonally average dynamical models, often grouped with Earth system models with intermediate complexity (EMIC) and (4) three-dimensional general or global circulation.

While the history of climate models started from the most complex type in the GCMs, the difficulties in prediction, forecast, and computation prevented their wide adoption (Ferraro et al., 2003; Edwards, 2001). These difficulties included the necessary temporal and spatial scale for predictive utility, the extreme sensitivity of system variables to initial conditions, and the realizations that other systems such as the hydrosphere must also be modeled simultaneously (Lorenz, 1963). Thus climate modeling took a few steps backwards to investigate the individual components, birthing the other approaches addressing the equations used by Phillips (1956). The EBM simulated surface temperatures and was based on the black-body radiation applied in one or two dimensions (i.e. latitude and the Earth's surface) with parameters accounting for albedo

124

effects related to ice or cloud cover (Sellers, 1969). The RCs can be seen as a discrete unit of an EBM where the dimension is altitude, incorporating wavelength-dependent radiative heat transfer and vertical heat flux along the vertical column from a point on the Earth to any arbitrary distance into the atmosphere. The EMICs were a broad group of models whose structures may be empirical or mechanistic and their unifying features were that they were just short of a three-dimensional, time-continuous general circulation model (Claussen et al., 2000).

<center>Description of Climate Models</center>

As high-performance computing became more common, the GCMs returned and largely replaced the aforementioned models. The simpler models and their structures retained their usefulness because a typical 3º (~300 km) resolution GCM still incurred substantial computational resources. Personal computers could easily run the simpler models as either educational tools or for sensitivity before devoting resources to a full GCM simulation (McGuffie & Henderson-Sellers, 2005). The GCM category had varying levels of complexity. The original formulation dealt with only the atmosphere, equivalent to a computational fluid dynamics simulation on large temporal and spatial scales. As climate change became a more significant issue, many GCMs evolved into fully coupled ocean-atmospheric circulation models (OAGCM) with some including the biosphere and its carbon cycling (Sellers et al., 1986), leading to an alternate meaning for the acronym to stand for "global climate model." For the sake of brevity, further mentions of GCM include AOCGCM as the NARCCAP required the ocean-atmospheric coupling.

Despite the computing power and intense research into atmospheric, oceanic, and other climatic processes, the coarse spatial scales limited the utility and applications for entities operating within small geographic areas and mesoscale climates. This limitation prompted the need to downscale the GCM simulation outputs to a finer resolution, considering that, historically, the downscaling methods were empirical (Giorgi & Mearns, 1991). With resolutions in the range of 50-100 km, a regional climate model (RCM) nested within a GCM produced finer

<center>125</center>

details given their more realistic surface characteristics in topography or vegetation with most able to simulate additional processes such as soil hydrology (Giorgi, 1990). The general methodology for producing GCM-RCM simulations was to run the GCM and have their outputs (temperature, moisture flux, etc.) interpolated to the RCM scale as boundary conditions to drive the higher-resolution model (McGregor, 1996). NARCCAP members collaborated and produced an ensemble of GCM-RCM combination for North America, simulating the historical period from 1971-2000 to validate the models with existing data and then simulating a projected period from 2041-2070 using the IPCC A2 emission scenario (Mearns et al., 2007). The NARCCAP repository at the time of their retrieval in 2013 totaled eleven combinations.

The GCMs were the Community Climate System Model (CCSM), the Third Generation Coupled Global climate model (CGCM3), Geophysical Fluid Dynamics Laboratory (GFDL), and the Hadley Centre Coupled Model version 3 (HadCM3). CCSM (Collins et al., 2006) had a $1.4°\varphi \times 1.4°\lambda$ resolution and 26 uneven vertical layers measured in air pressure with the top layer at 220 Pa; the ocean grid varied between 0.3° to 1°, depending on location, with 40 vertical layers. CGCM3 (Flato, 2005) had a $1.9°\varphi \times 1.9°\lambda$ surface resolution with 31 vertical layers with the top layer at 100 Pa; the ocean grid underlain the surface atmosphere lied and its resolution was $0.9°\varphi \times 1.4°\lambda$ with 29 vertical layers. CGCM3 also adjusted the ocean-atmospheric coupling for heat and fresh water input from rain and land runoff. GFDL (GFDL GAMDT, 2004) had a $2.0°\varphi \times 2.5°\lambda$ grid with 24 vertical layers with the top layer at 300 Pa; the ocean grid varied between 0.3° to 1°. HadCM3 (Gordon et al., 2000) had a $2.0°\varphi \times 2.5°\lambda$ grid with 24 vertical layers with the top layer at 500 Pa; the ocean grid's resolution was $1.25°\varphi \times 1.25°\lambda$ with 20 vertical layers. All GCMs except HadCM3 modeled sea ice via rheology or as viscous plastic; HadCM3 modeled sea ice as freely drifting with the ocean currents. All GCMs had land components featuring soil layers, vegetation/canopy, runoff routing. GFDL employed the "bucket" method for soil water wherein above critical threshold, water ponds (Manabe, 1969) while the other GCMs employed soil columns with differing layers and infiltration rates (Liang et al., 1994). Table A-2 in the Appendix summarizes the features of the GCMs.

The RCMs were the Canadian Regional Climate Model (CRCM), the Experimental Climate Prediction Center (ECP2), the Hadley Regional Model 3 (HRM3), the National Center for Atmospheric Research's mesoscale model (MM5I), the Regional Climate Model version 3 (RCM3), and the Pacific Northwest National Laboratory Weather Research and Forecasting model (WRFG). The RCMs differed in resolution, hydrodynamic conditions, land surface and cover features, boundary layer determination methodology, atmospheric moisture and cloud formation, uniformity aerosol dynamics, length of time-step, and calculation of solar radiation spectra. Table A-3 in the Appendix summarizes their dimensional features.

<u>Methods</u>

Data Pre-Processing

The NARCCAP outputs were the daily maximum temperatures, minimum temperatures, and rainfall totals for grid points spaced approximately 50km apart. The location of the grid points did not coincide with the climate stations that provided data for the SWAT calibration runs. Simple spatial interpolation between climate model outputs would not accurately reflect the rainfall or temperature observed at climate stations (Najafi & Moradkhani, 2013). A bias-correction method (Teutschbein & Seibert, 2012) was applied to the NARCCAP outputs to prepare the data for usage in SWAT by way of distribution mapping. The bias-corrected time-series replaced the precipitation and temperature files SWAT used to simulate the historical data. The NARCCAP outputs had a control or "historical" period of 1971-1998 and a "projected" period of 2041-2068. The GCM-CRM historical time series served as a check on whether climate models and their SWAT implementations deviated from the calibrated model using actual historical data.

The bias-correction first performed an inverse distance weighting spatial interpolation between the RCM grid points to generate a synthetic historical time series for temperature and

127

precipitation matching the time-frame of the observed historical data and the location of the gauge stations:

Equation 6-1 $$P^* = \frac{\sum_{i=1}^{n} \frac{P_i}{d_i}}{\sum_{i=1}^{n} d_i^{-1}}$$

P^* was the daily precipitation for a climate station, P_i the daily precipitation for a GCM-RCM grid point, and d_i the Euclidean distance between the station and the grid point. Dry days with zero precipitation were abundant in climate time series and a correction prior to distribution mapping matched the observed and synthetic data's dry day counts. A threshold was defined for each synthetic time-series such that the number of days with rainfall below the threshold equals the number of observed days with zero precipitation. The dry day correction was a partial adaption from local intensity scaling (Schmidli et al., 2006). The procedure then adjusted synthetic time-series' values by way of percentile cumulative distribution function (CDF) mapping. The empirical CDF were constructed for both synthetic and observed time-series. The CDF location of each synthetic datum had a matching location with the observed CDF. The ratio of the two CDF produced a set of correction factors that were then applied to the synthetic time-series.

Figure 6-1 shows graphically the distribution mapping procedure. The projected time series underwent a similar procedure with modifications: no local intensity scaling for dry days and the use of correction factors from the historical time-series bias-correction. To generate new correction factors for the projected time-series with the observed time-series would defeat the purpose of having projected climate data; however, the correction factors did assume that the differences between an interpolated climate model output and the observations were non-stationary.

128

Precipitation, stream discharge, evapotranspiration (ET), and nitrate loads were the variables that evaluate the climate change scenarios using the bias-correct GCM-RCM inputs. Aside from nitrate loads, the variables were analyzed by seasons: December-January-February (DJF), March-April-May (MAM), June-July-August (JJA), and September-October-November (SON). Three graphical methods and one statistical method were used to analyze these outputs. A general measure was the mean annual percent change. Means for each year were calculated from outputs at the monthly time step:

Equation 6-2 $$\% \, Change = \frac{\sum_{i=1}^{28} \bar{Q}_{sim}}{\sum_{i=1}^{28} \bar{Q}_{ref}}$$

Q_{sim} was either the climate model-driven outputs (or inputs in the case of precipitation) for the historical and simulated period. Q_{ref} was a reference period that differed for the control and projected periods. For the control period, the reference values were the observations or outputs from the calibrated SWAT model if observations were not available such as the case with nitrate loads and evapotranspiration. For the projected period, the reference values were the historical NARCCAP-driven SWAT inputs/outputs. Because the probability distribution of these datasets, both observational and simulated, were unlikely to be normal, boxplots were alternative methods to look at the distribution of the outputs.

Quantile-quantile (Q-Q) plots were also an alternative when comparing two paired datasets in which one was a modified form of the other. Q-Q plots ranked two datasets in order from least to greatest and then plotted the ranked values on axes of the same units. Q-Q plots can be misleading for skewed data. For example in a Q-Q plot of stream discharge, the axes would necessarily encompass the largest or extreme values, but the configuration of the axes would obscure the distribution of flows on the lower end. To account for skewedness, the data were transformed by a median-normalization or mapping scheme from a reference dataset: the

129

reference median is set to zero, values above the median are scaled in reference to the maximum, and values below are scaled in reference to the minimum:

Equation 6-3
$$x^* = \begin{cases} \dfrac{y_{max} - x}{y_{max} - y_{med}} & \text{if } x > y_{med} \\ 0 & \text{if } x = y_{med} \\ \dfrac{y_{min} - x}{y_{med} - y_{min}} & \text{if } x < x_{med} \end{cases}$$

x^* was the transformed datum, y_{min} the reference minimum, y_{max} the reference maximum, and y_{med} the reference median. This transformation resulted in negative values for any original value smaller than the reference median and positive for values greater than the reference median. A single datum was the monthly mean (discharge, nitrate load) or cumulative sum (precipitation, ET).

The utility of these transformed Q-Q plots was two-fold. First, the data were separated into lower and upper portions which themselves may have different distributions and responses to climate change. Second, when x^* was above 1.0 or below -1.0, the dataset of interest can be said to "overshoot" or "undershoot" the reference. For example, if a transformed stream discharge datum for the projected period was above 1.0 with respect to the historical climate modeled period, then the projected period datum was above the maximum for the historical period. Like the mean percent annual change, the Q-Q reference values for the historical period were the observations and the historical outputs were the reference for the projected period.

Finally, the Mann-Whitney U-test was used as the quantitative method to check whether the climate change yielded statistically significant differences or if the modeled historical/control period was significantly different from the observations. The U-test was non-parametric and did not assume a probability distribution for the data. When the data were paired such as the time series comparison between historical/projected or historical/observation, the U-test checked the differences in the medians between the two datasets.

130

<u>Results and Discussion</u>

Precipitation

Table 6-1 shows the percent change between the historical and projected periods for 11 GCM-RCM climate models described previously for mean monthly cumulative precipitation. The precipitation data were bias-corrected inputs and did not have an added layer of modeling from SWAT. The model ensemble for the historical period featured small changes from the historical observations with the greatest deviation in MM5Ihadcm3 in the SON months. A seasonal trend existed where the climate models tend to over-predict for SON and under-predict for DJF months. The projected period displayed a climate signal between the periods as the model ensemble typically showed annual changes in excess of 5 percent. The trend was less seasonal and more model-based: CRCMccsm, HRM3gfdl, HRM3hadcm3, MM5Iccsm, MM5Ihadcm3, and WRFGccsm showed at least one season where the precipitation decreased. The greatest decrease was in CRCMccsm during JJA with a 20 percent decrease and the greatest increase is seen in HRM3hadcm3 during SON with a 28.1 percent increase. Overall, the model ensemble indicated increasing precipitation.

Table 6-2 shows the Mann-Whitney U-test *p*-values for historical/observation and historical/projected monthly cumulative precipitation. Shades of blue and orange indicate the magnitude of the *p*-values for medians greater or less than the reference data: the smaller the *p*-value, the darker the shade. The historical columns showed no model or season having statistically significant differences from the observations. For the projected period with historical climate simulated values as reference, only two models in two seasons total showed a statistically significant difference at $\alpha=0.05$; still, compared to the historical/observation columns, the *p*-values were lower. A seasonal trend did appear with MAM and SON having more models with lower *p*-values.

Figure 6-4 shows bar-plots of the average annual percent change from the observations. The climate models seem to succeed in simulating the historical period with SON having the

131

greater bias with consistently positive changes. Figure 6-5 shows bar plots for changes to the projected period with the reference being the simulated historical periods. The model ensemble showed positive trend with precipitation increasing for nearly all months except for JJA where 6 out of 11 models show a decrease in precipitation. CRCMcgcm3 and ECP2gfdl show a slight increase but quite small compared to the rest (1.2 and 0.5 percent, respectively).

Figure 6-6 and Figure 6-7 are boxplots for the historical and projected periods, respectively. The solid, dashed, and dotted horizontal lines were the maximum, median, and minimum values from the observations, respectively. The model maximums for the historical period tended to over-predict the observations for all seasons except for DJF, but the medians line up except for the SON months where the model medians were slightly lower than the observations' median. The projected periods' maximum monthly cumulative precipitation were mostly above the observations and the medians tended to be greater, but have high variability between climate models, especially for the JJA where there was no ensemble agreement on where the median monthly precipitation laid.

Figure 6-8 and Figure 6-9 contain the modified Q-Q plots for the historical and projected periods, respectively. The grid of plots had seasons as columns and climate models for rows. For each plot a single vertical line at zero indicated the dataset of interest's median and the two horizontal lines at the 1.0 and -1.0 marks indicated the "overshooting" or "undershooting" of the reference dataset. If the data points followed a diagonal line from (-1.0, -1.0) to (1.0, 1.0), the model had good agreement with the reference dataset at values above and below the reference median. The ensemble model control period showed good agreement with the observations; overshooting occurred sporadically across the models and season, but SON and JJA saw the most overshoots. Values below the observations' median agreed very well with few deviations. The projected periods' Q-Q plots show more differences. Overshooting occurred more frequently and towards the upper values while the lower values appeared similar to the historical simulations. The maximum for the projected tended to be above the maximum for the historical simulations, a result shared by the boxplots.

132

The plots for monthly mean stream discharge and evapotranspiration followed the same sequence and formatting as precipitation previously: two annual percent change bar plots, two box plots, and two Q-Q plots, with each pair evaluating the historical and projected periods. Table 6-3 showed the average annual percent change for GCM-RCM model-driven SWAT simulations for stream discharge for the historical period using the calibrated SWAT model's discharge as reference and the projected period using historical NARCCAP-driven simulations as reference. While historical climate model precipitation showed small changes compared to the observed discharge, stream discharge has greater variability. The greatest deviations were in JJA with CRCMccsm discharges the highest at 30.8 percent greater than the observations. Figure 6-10 shows bar plots for the historical period and while the deviations were greater than those seen in precipitation, they seemed to be randomly distributed between the models, indicating the changes were within the uncertainty SWAT adds to the outputs.

Figure 6-12 shows boxplots with same configurations as the precipitation boxplots with the horizontal lines being the calibrated model's maximum, median, and minimum discharge. The NARCCAP-driven model maximum discharges nearly all exceeded the observed maximums with the exception in JJA. The medians did not line up in a consistent manner through the seasons and models. SON and MAM's medians were slightly below the observed medians for those months. JJA agreed more with the observations with the medians lining up with the observations and only three models reporting maximums above the observations. Figure 6-14 contain the Q-Q plots with median-normalized discharges for the historical period with observations as reference. Discharges below the medians in all the models appear to agree with the calibrated model as they laid on the 1:1 line. Above the medians the models tend to deviate with values above the observations, especially for SON where the highest flows tend to be above the 1.0 horizontal line. Quantitatively from Table 6-2's historical columns, the *p*-values indicated

133

that although the medians may be off, they were not statistically significant except for three models in the SON months.

The projected period's percent change showed a more apparent climate change signal when compared to the historical NARCCAP-driven simulations. From Table 6-3 and Figure 6-11, all models reported a positive change for SON with CRCMccsm being the greatest at 83.3 percent increase in mean annual change. MAM sees the same trend across the models except for MM5Ihadcm3, which reported a small negative change at 0.1 percent. DJF has three models not reporting a positive annual change. JJA had more mixed results with 5 out of 11 models showing negative change and the other models showing positive: CRCMccsm had the greatest decrease in JJA at 30.8 percent and WRFGccsm greatest increase in JJA at 27.5 percent. The mixed results and large variation in both directions did show a model ensemble agreement for JJA in stream discharge in the mean annual stream discharge. The boxplots in Figure 6-13 told a similar story for JJA as the medians for the different models were scattered above and below and observed historical medians. The JJA maximums, however, only had one model reporting projected maximums lower than the historical maximums. Indeed, the maximums and medians for the other seasons were above the historical observations, agreeing with the story given by the percent changes in Figure 6-11.

Figure 6-15 contain the Q-Q plots for the projected period with simulated historical period as reference. Whereas the Q-Q plots in Figure 6-14 show historical NARCCAP-driven discharge values below the median agreeing with the observed low flows, the projected period had low flows consistently above the historical simulations. The only aberration from the trend was in JJA, which showed little change in the low discharges or decreased low discharge in the case of CRCMccsm. The discharges above the median for DJF, MAM, and SON consistently showed increases from the historical simulations with the highest discharges overshooting the 1.0 line. The exception was JJA where some models showed increase and other showed little change. The JJA story in the Q-Q plots was consistent with the other plots. Quantitatively, the *p*-values in Table 6-4 showed projected medians that were statistically significant above the

simulated historical medians. CRCMccsm showed the only difference with a median flow that was statistically significantly lower than the simulated median. DJF and SON had the most models showing statistically significant greater median discharges while the statistical significance was in the minority for MAM and JJA.

Evapotranspiration

Historical NARCCAP temperatures did not deviate from the observations as all but one model and season had percent differences less than one percent (Table 6-7, Figure 6-22). The boxplots in Figure 6-24 and the Q-Q plots in Figure 6-26 show a consistent comparison. For the projected period the mean annual (Figure 6-23) and median daily (Figure 6-25) temperatures increased for all seasons with DJF having the greatest relative increase. The lowest absolute mean temperature increase occurs in MAM in the ECP2gfdl model at 1.23°C and the greatest absolute increase occurs in JJA in the HRM3gfdl model at 5.11°C (Table 6-9). While daily mean temperatures increased overall, the Q-Q plots in Figure 6-27 do not show evidence of extremes at either end of the distribution. Increased temperatures were expected in the climate change inputs as the driving A2 emission scenario depicted greater or little slowdown in greenhouse gas emissions.

Actual evapotranspiration (ET) can be considered a proxy for watershed response to temperature increases due to climate change. Observations for actual ET were not available and so the horizontal lines for the historical period were all calibrated SWAT model outputs. Table 6-5 shows the mean annual percent change from the calibrated SWAT simulation. ET was more well-behaved than stream discharge in the historical NARCCAP-driven simulations as seen on Figure 6-16 where the deviations in mean annual percent change was less than 10 percent in all cases except for three models and seasons in DJF and SON. MAM and JJA showed the least deviations in ET from the calibration and DJF and SON showed the most. DJF's models had ET randomly distributed above and below zero while SON had ET consistently lower than the calibration. A reason for this might be that ET was already low for DJF and SON and small

135

changes in temperature from the NARCCAP time-series induced large changes in a watershed model outputs.

The historical period box plots in Figure 6-18 show a consistent story with the bar plot as the maximum monthly cumulative ET rarely exceeded the calibrated model's ET. DJF and SON did have lower raw ET values; DJF had low enough ET that the historical NARCCAP-driven ET had maximums that exceed the calibrated maximum. The Q-Q plots in Figure 6-20 show that MAM and JJA had distributions that generally align with the calibrated model's distribution; however, sub-median ET values for JJA seemed to undershoot the calibrated model's ET values. Between the models the ET distributions for DJF and SON were all strikingly similar, showing that despite the large percent changes, the distributions did not differ greatly from the observed temperature-driven calibrated model's ET. Quantitatively, the *p*-values from Table 6-6 show only four models having statistically significant different medians from the calibrations, one occurring in DJF and the other three occurring in SON.

The projected percent change in Figure 6-17 shows the greatest differences occurring in DJF with a majority of models reporting changes in exceedance of 25 percent. MAM had increased ET while JJA and SON had decreased ET, but the magnitudes of these changes were not as great as DJF and were all below 25 percent in either direction. MAM and SON showed a consistent trend across all models with increased and decreased ET, respectively. JJA had slightly mixed results with two models showing increased ET and others decreased; however, the magnitudes of the increases were small and below 5 percent. The projected period's boxplots in Figure 6-19 shows an uncertain climate change signal for DJF: the large percent changes were due to the already low ET. MAM and SON's median ET agreed with the bar plots as the models for those seasons were consistently above and below the calibrated model's, respectively. JJA showed a more mixed response with the median ET being scattered across the models, but the maximum projected cumulative ET for JJA months were all above the calibrated models.

The Q-Q plots in Figure 6-21 show a bimodal response with respect to the values below and above the median for DJF and JJA. The sub-median ET values for DJF were above the

136

historical NARCCAP-driven simulations, but the above median values did not deviate too much from the 1:1 line. JJA's trend was opposite from DJF: sub-median projected ETs agreed with the historical and the above median projected ETs were generally higher than the historical ET. SON Q-Q plots generally showed the projected ETs agreeing with the historical NARCCAP-driven ET with the maximum projected values sometimes smaller than the historical. MAM had a similar trend as SON between the models except the maximum ETs generally exceeded the historical. Quantitatively, the projected median ETs for DJF were statistically significantly greater than the historical across all models. Such a broad trend cannot be said for the other seasons as the majority of models did not have statistically significant p-values.

<div align="center">Nitrate Load</div>

Like evapotranspiration observed nitrate load data were not available for the historical period and horizontal lines for the boxplots are from the calibrated model outputs. Due to the low performance of the nitrate autocalibration for SWAT, the analysis here was different from those of the previous variables. Loads were summarized on an annual basis and not seasonal and Q-Q plots were not done for nitrate loads. The historical (1971-1998) percent change in Figure 6-28 shows a slight degree of model variability, but the majority did have relatively small changes (<15% in either direction). Nitrate loads for the historical period were not statistically significant from the calibrated models and the medians on the boxplots agreed. The maximum historical NARCCAP loads for the models tended to under-predict the calibration maximum.

The percent change for the projected period (2041-268) also on Figure 6-28 with the historical NARCCAP-driven simulations as the reference showed an ensemble agreement for increased nitrate loads on the annual basis. CRCMccsm reported decreased mean annual loads, but the decrease was small at 2.4 percent. The medians in projected period box plots also seemed to be higher for a few models and the maximum nitrate loads are mixed in their position below or above the calibration's maximums. The projected p-values have 6 out 11 models with statistically significant and greater medians than the historical NARCCAP medians. As

<div align="center">137</div>

mentioned in previous chapters, nitrate loads correlate with discharge and these result should not come as a surprise.

Conclusion

This chapter presented an enormous amount of information about the watershed response to climate change. With 11 GCM-RCM models, seasonal differences, considerations for what was the reference period, and the need to use multiple methods for data analysis, one can only provide general statements about the results. The enumeration of each and every percent change, median, *p*-value, etc. would be better read from tables and figures. That said, the general trends were that of changes in extreme values and of seasonal differences in the climate change signal. Inter-model comparison in the results and discussion suggested CRCMccsm as the model that appeared to be the exception to many trends in the results, despite the geographical home of the model being nearest to the ICRB. The discharge plots and tables showed a wetter climate except for JJA, which had enough inter-model variability to prevent a clear conclusion on the status of precipitation during the summer months. Statistically, the median monthly precipitation did not show many statistically significant differences between the historical and projected NARCCAP models (Table 6-1), but the overall trend as displayed by the figures showed that increases in the annual mean precipitation occurred in all months except JJA. The discharge results indicated a wetter 2041-2068 projected period for most months except JJA, which had mixed results similar to precipitation. The extreme discharges for the projected period also increased for the non-JJA months.

The evapotranspiration results showed the results of a warmer climate with the winter months the most affected, but it should be remembered that ET is low in the winter months of DJF. The ET plots did show that the distribution of ET in MAM and JJA were much wider than that of the calibrated SWAT model, supporting that changes in the extreme values of ET were projected for the period 2041-2068. Annual nitrate loads increased in a similar manner as discharge and this may be mostly due to load being a function of discharge at the basin outlet. In

general, nitrate loads are projected to increase in the period 2041-2068 relative to the reference. Such a condition could presumably cause greater export of nutrients to the Gulf of Mexico and Gulf Hypoxia.

Nevertheless, climate change and prediction cannot be exact and will always have uncertainty even with infinite computational power and speed. Another uncertain dimension to the future alongside climate change is land use change. Land use change can be induced by climate change and vice versa. It can also be induced by the choices of humans. Chapter 7 covers the ICRB and SWAT's sensitivity to land use distribution with a look at specific scenarios based on specific considerations. The final part of this dissertation was the application of both land use and climate change scenarios to explore their combined impacts.

Table 6-1   Precipitation mean annual percent change for historical and projected periods. Reference period for historical columns are observed values and reference for projected values are historical NARCCAP.

Model	Historical (%)				Projected (%)			
	DJF	MAM	JJA	SON	DJF	MAM	JJA	SON
CRCMccsm	-0.9	-0.4	1.5	0.9	-0.6	12.3	-20.0	26.2
CRCMcgcm3	0.2	0.3	-0.2	0.5	12.0	17.5	1.2	2.5
ECP2gfdl	-0.9	0.2	-1.0	0.2	19.0	1.0	0.5	14.6
HRM3gfdl	-0.4	0.6	1.1	0.3	21.0	8.6	-8.7	1.5
HRM3hadcm3	-0.7	-1.5	0.9	1.8	6.4	9.1	-3.1	28.1
MM5Iccsm	-1.3	-0.2	-0.1	0.6	-2.5	8.4	-11.0	16.3
MM5Ihadcm3	1.0	-0.8	0.1	2.0	-5.1	6.6	-4.6	-0.7
RCM3cgcm3	-0.7	0.5	0.1	0.1	11.5	14.5	8.7	10.8
RCM3gfdl	-0.6	0.0	0.6	0.3	21.1	22.7	4.4	14.3
WRFGccsm	1.5	0.6	1.1	1.5	10.8	20.2	-13.4	6.6
WRFGcgcm3	-0.8	0.1	0.5	1.2	22.2	6.1	11.3	18.2

Table 6-2   Mann-Whitney U-Test *p*-values. Blue highlights indicate medians statistically significantly greater than historical climate model. Reference period for historical columns are observed values and reference for projected values are historical NARCCAP.

Model	Historical				Projected			
	DJF	MAM	JJA	SON	DJF	MAM	JJA	SON
CRCMccsm	0.44	0.87	0.22	0.83	0.76	0.14	0.08	0.10
CRCMcgcm3	0.82	0.92	0.87	0.98	0.59	0.18	0.60	0.92
ECP2gfdl	0.69	0.80	0.74	0.58	0.21	0.91	0.83	0.07
HRM3gfdl	0.79	0.83	0.95	0.81	0.08	0.50	0.12	0.40
HRM3hadcm3	0.62	0.66	0.91	0.97	0.73	0.46	0.92	0.01
MM5Iccsm	0.16	0.92	0.87	0.65	0.57	0.27	0.16	0.43
MM5Ihadcm3	0.56	0.65	0.66	0.85	0.72	0.54	0.81	0.64
RCM3cgcm3	0.78	0.60	0.76	0.83	0.58	0.14	0.66	0.51
RCM3gfdl	1.00	0.98	0.91	0.80	0.25	0.06	0.52	0.11
WRFGccsm	0.39	0.95	0.66	0.60	0.25	0.02	0.10	0.81
WRFGcgcm3	0.67	1.00	0.82	0.83	0.17	0.52	0.24	0.19

Table 6-3   Stream discharge mean annual percent change for historical and projected periods. Reference period for historical columns are observed values and reference for projected values are SWAT simulations using the historical NARCCAP climate projections as input.

Model	Historical (%)				Projected (%)			
	DJF	MAM	JJA	SON	DJF	MAM	JJA	SON
CRCMccsm	-4.3	-9.8	30.8	-15.1	10.7	40.5	-35.7	83.3
CRCMcgcm3	-3.0	-6.7	5.5	-19.5	47.8	19.0	25.1	25.9
ECP2gfdl	6.3	-12.0	-13.0	10.8	30.3	13.9	15.0	28.8
HRM3gfdl	0.1	7.6	-4.4	-7.5	29.7	13.8	-4.0	14.7
HRM3hadcm3	-1.1	4.3	4.9	-1.2	46.3	26.1	-5.0	74.7
MM5Iccsm	-14.9	5.4	10.4	-6.3	-6.2	10.5	5.6	72.5
MM5Ihadcm3	17.2	0.4	12.2	-15.8	-15.4	-0.1	-13.7	31.4
RCM3cgcm3	16.2	-12.2	2.8	-0.9	24.1	26.1	40.9	39.3
RCM3gfdl	11.5	-10.5	-5.4	-1.1	31.9	50.8	31.3	51.0
WRFGccsm	10.8	3.8	27.5	-9.5	-10.4	40.2	-14.5	35.8
WRFGcgcm3	10.4	0.5	8.7	-5.1	49.4	21.4	26.9	80.7

Table 6-4   Stream discharge Mann-Whitney U-Test p-values. Shades of orange indicate medians statistically significantly less than historical climate model and shades of blue indicate greater. Reference period for historical columns are observed values and reference for projected values are SWAT simulations using the historical NARCCAP climate projections as input.

Model	Historical				Projected			
	DJF	MAM	JJA	SON	DJF	MAM	JJA	SON
CRCMccsm	0.42	0.30	0.98	<0.01	0.37	<0.01	<0.01	<0.01
CRCMcgcm3	0.98	0.34	0.89	0.15	0.02	0.27	0.64	0.98
ECP2gfdl	0.65	0.07	0.65	1.00	0.08	0.56	0.44	0.01
HRM3gfdl	0.74	0.52	0.62	0.13	<0.01	0.71	0.33	0.07
HRM3hadcm3	0.67	0.94	0.72	0.36	<0.01	0.13	0.94	<0.01
MM5Iccsm	0.08	0.88	0.67	0.26	0.72	0.21	0.75	<0.01
MM5Ihadcm3	0.73	0.65	0.71	0.02	0.29	0.84	0.39	0.08
RCM3cgcm3	0.30	0.16	0.80	0.46	0.14	0.08	0.01	0.15
RCM3gfdl	0.34	0.30	0.95	0.61	0.02	<0.01	0.02	<0.01
WRFGccsm	0.56	0.99	0.26	0.02	0.70	<0.01	0.17	0.02
WRFGcgcm3	0.65	0.89	0.95	0.38	<0.01	0.02	0.02	<0.01

Table 6-5   Evapotranspiration mean annual percent change for historical and projected
            periods. Reference period for historical columns are observed values and
            reference for projected values are SWAT simulations using the historical
            NARCCAP climate projections as input.

Model	Historical (%)				Projected (%)			
	DJF	MAM	JJA	SON	DJF	MAM	JJA	SON
CRCMccsm	2.7	4.8	-1.1	-8.5	25.7	13.6	-8.8	-5.4
CRCMcgcm3	-2.6	5.1	2.2	-3.9	57.8	15.2	-3.2	-18.6
ECP2gfdl	9.3	1.6	1.2	1.9	54.5	2.8	-1.6	-1.9
HRM3gfdl	-1.9	1.7	2.0	-2.5	62.1	19.1	-11.6	-6.6
HRM3hadcm3	3.3	-0.7	0.2	-4.7	40.2	10.7	-3.2	-0.9
MM5Iccsm	-6.6	0.5	0.1	-2.5	25.1	4.6	-13.0	-7.0
MM5Ihadcm3	-0.8	2.2	0.9	-11.1	51.9	10.0	-4.9	-6.2
RCM3cgcm3	6.1	3.4	0.5	-4.0	48.5	11.5	-0.5	-11.1
RCM3gfdl	13.2	4.7	0.7	0.6	40.8	6.9	1.6	-4.6
WRFGccsm	-5.1	0.2	-0.6	-10.1	40.9	9.8	-8.0	-1.4
WRFGcgcm3	8.8	1.3	-0.8	-5.5	12.5	6.4	2.2	-3.2

Table 6-6   Evapotranspiration Mann-Whitney U-Test p-values. Shades of orange indicate
            medians statistically significantly less than historical climate model and shades of
            blue indicate greater. Reference period for historical columns are observed values
            and reference for projected values are SWAT simulations using the historical
            NARCCAP climate projections as input.

Model	Historical				Projected			
	DJF	MAM	JJA	SON	DJF	MAM	JJA	SON
CRCMccsm	0.96	0.29	0.89	0.02	0.01	0.01	0.22	0.23
CRCMcgcm3	0.54	0.36	0.32	0.35	<0.01	0.01	0.60	<0.01
ECP2gfdl	0.02	0.77	0.84	0.56	<0.01	0.71	0.81	0.52
HRM3gfdl	0.94	0.75	0.56	0.56	<0.01	<0.01	0.15	0.16
HRM3hadcm3	0.86	0.84	0.82	0.26	<0.01	0.09	0.79	0.82
MM5Iccsm	0.59	0.95	0.68	0.65	<0.01	0.44	<0.01	0.12
MM5Ihadcm3	0.55	0.70	0.59	<0.01	<0.01	0.25	0.50	0.23
RCM3cgcm3	0.27	0.60	0.95	0.27	<0.01	0.09	0.60	<0.01
RCM3gfdl	0.21	0.40	0.79	0.80	<0.01	0.15	0.41	0.26
WRFGccsm	0.93	0.88	0.99	0.02	<0.01	0.08	0.53	0.82
WRFGcgcm3	0.95	0.78	0.86	0.17	0.23	0.23	0.26	0.55

Table 6-7   Mean annual percent change for mean daily temperature for historical and projected periods. Reference period for historical columns are observed values and reference for projected values are SWAT simulations using the historical NARCCAP climate projections as input.

Model	Historical (%)				Projected (%)			
	DJF	MAM	JJA	SON	DJF	MAM	JJA	SON
CRCMccsm	-0.4	0.1	0.0	0.0	43.0	29.4	16.7	26.4
CRCMcgcm3	-0.5	0.1	0.0	0.0	55.0	31.7	16.4	32.6
ECP2gfdl	-0.6	0.0	0.0	0.0	62.7	13.8	10.0	24.5
HRM3gfdl	-0.2	0.0	0.0	0.1	61.0	32.7	23.2	29.6
HRM3hadcm3	-1.4	-0.4	-0.1	0.2	38.4	19.6	15.3	32.4
MM5Iccsm	-0.4	0.0	0.0	0.1	36.4	19.0	8.6	23.2
MM5Ihadcm3	-0.4	-0.3	-0.2	0.2	62.6	20.4	12.4	37.0
RCM3cgcm3	-0.5	0.1	0.0	0.1	51.2	25.8	14.3	31.0
RCM3gfdl	-0.4	0.0	0.0	0.1	50.8	14.5	14.6	21.7
WRFGccsm	-0.4	0.0	0.0	0.0	55.1	19.3	12.0	35.0
WRFGcgcm3	-0.2	0.1	0.0	0.0	23.3	15.2	7.7	25.2

Table 6-8   Mean daily temperature Mann-Whitney U-Test p-values. Shades of blue indicate medians statistically significantly greater than historical climate model. Reference period for historical columns are observed values and reference for projected values are SWAT simulations using the historical NARCCAP climate projections as input.

Model	Historical				Projected			
	DJF	MAM	JJA	SON	DJF	MAM	JJA	SON
CRCMccsm	0.64	0.98	0.73	0.99	<0.01	<0.01	<0.01	<0.01
CRCMcgcm3	0.56	1.00	0.81	0.99	<0.01	<0.01	<0.01	<0.01
ECP2gfdl	0.68	0.94	0.99	0.93	<0.01	<0.01	<0.01	<0.01
HRM3gfdl	0.78	0.97	0.72	0.93	<0.01	<0.01	<0.01	<0.01
HRM3hadcm3	0.49	0.86	0.70	0.92	<0.01	<0.01	<0.01	<0.01
MM5Iccsm	0.70	0.95	0.64	0.99	<0.01	<0.01	<0.01	<0.01
MM5Ihadcm3	0.63	0.90	0.83	0.89	<0.01	<0.01	<0.01	<0.01
RCM3cgcm3	0.60	1.00	0.77	0.96	<0.01	<0.01	<0.01	<0.01
RCM3gfdl	0.50	0.99	0.55	0.92	<0.01	<0.01	<0.01	<0.01
WRFGccsm	0.58	0.77	0.98	0.88	<0.01	<0.01	<0.01	<0.01
WRFGcgcm3	0.63	0.96	0.74	0.92	<0.01	<0.01	<0.01	<0.01

Table 6-9   Absolute change (°C) in mean daily temperature by season between NARCCAP
            historical 1971-1998 and projected 2041-2068 period

Model	DJF (°C)	MAM (°C)	JJA (°C)	SON (°C)
CRCMccsm	2.70	2.60	3.67	2.63
CRCMcgcm3	3.47	2.81	3.62	3.26
ECP2gfdl	3.95	1.23	2.21	2.44
HRM3gfdl	3.82	2.91	5.11	2.96
HRM3hadcm3	2.43	1.73	3.37	3.24
MM5Iccsm	2.29	1.69	1.89	2.32
MM5Ihadcm3	3.93	1.81	2.74	3.70
RCM3cgcm3	3.22	2.30	3.15	3.08
RCM3gfdl	3.19	1.29	3.22	2.17
WRFGccsm	3.45	1.71	2.65	3.50
WRFGcgcm3	1.46	1.35	1.70	2.51

Table 6-10   Nitrate load mean annual percent change and Mann-Whitney U-test *p*-values for
             historical and projected periods. Blue highlights indicate medians statistically
             significantly greater than historical climate model and shades of blue indicate
             greater.

Model	Percent Change		*p*-value	
	Historical	Projected	Historical	Projected
CRCMccsm	15.8	-2.7	0.27	0.26
CRCMcgcm3	-0.8	20.4	0.52	0.38
ECP2gfdl	-15.8	23.7	0.29	<0.01
HRM3gfdl	-7.7	2.7	0.42	0.38
HRM3hadcm3	2.4	12.8	0.49	<0.01
MM5Iccsm	-2.8	16.5	0.43	<0.01
MM5Ihadcm3	-4.3	3.1	0.14	0.20
RCM3cgcm3	-0.5	30.6	0.79	<0.01
RCM3gfdl	-6.9	48.9	0.46	<0.01
WRFGccsm	10.5	11.9	0.51	0.13
WRFGcgcm3	-0.5	27.7	0.54	<0.01
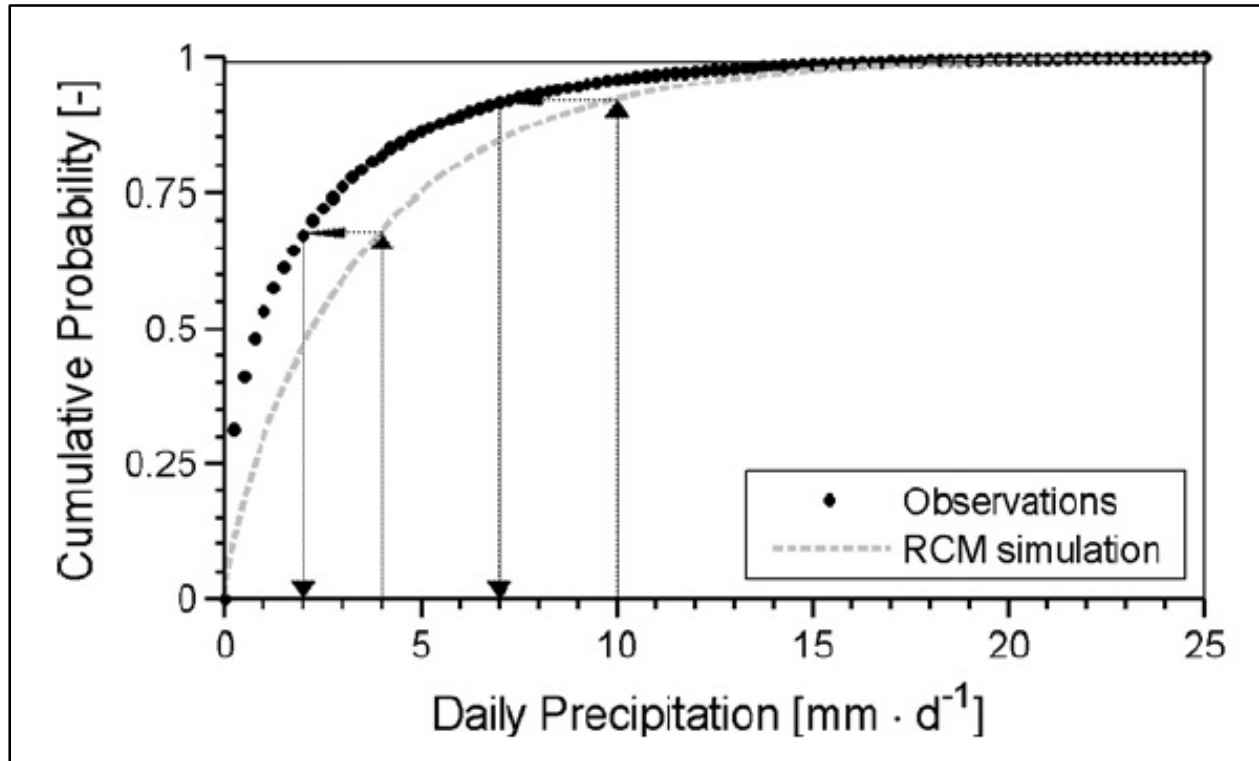
Figure 6-1   Bias-correction of precipitation by distribution mapping adapted from
               Teustchbein & Seibert (2012, Figure 6)
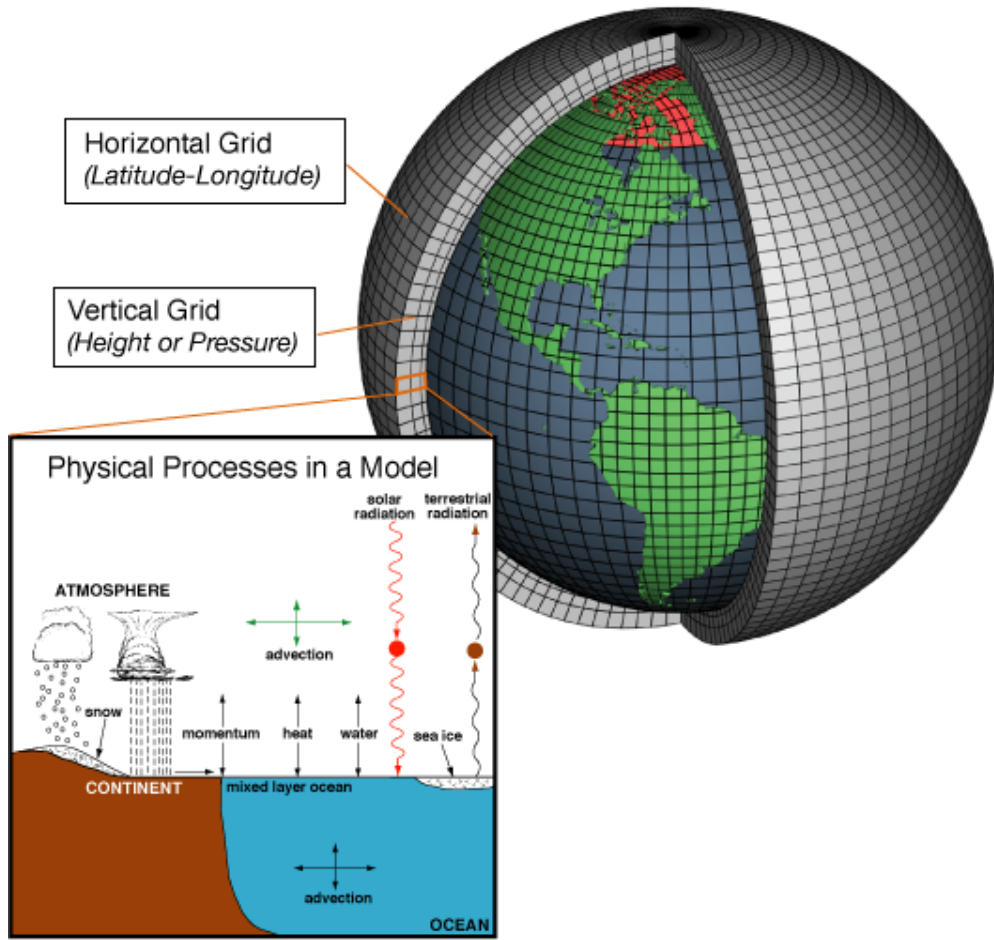
Figure 6-2   A model based on ocean and atmosphere interactions (NOAA, 2012)
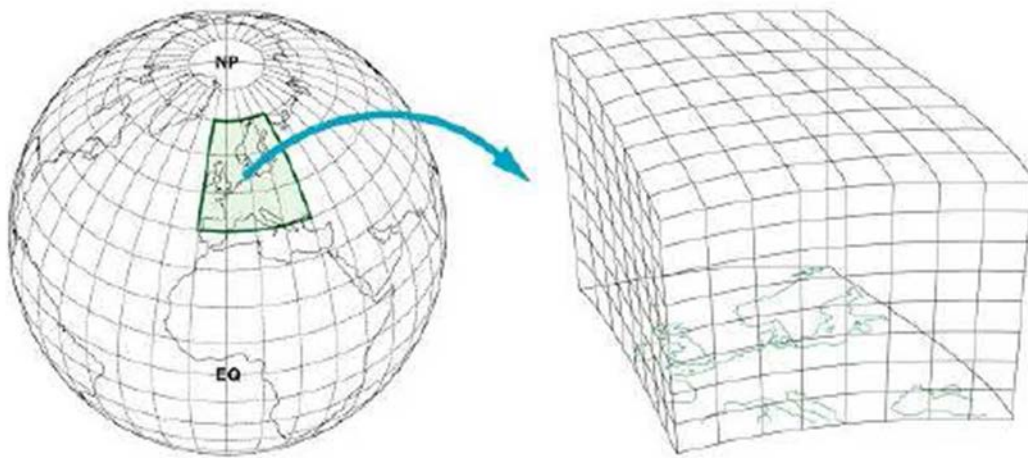
Figure 6-3   Downscaling of GCM to RCM (Gebetsroither et al., 2013)

Figure 6-4   Mean annual percent change of monthly cumulative precipitation of 1971-1998 NARCCAP historical period for 11 GCM-RCM model combinations and 4 seasons. The reference period is the 1971-1998 precipitation input data from the actual historical record.

Figure 6-5   Mean annual percent change of monthly cumulative precipitation of 2041-2068
              NARCCAP projected period for 11 GCM-RCM model combinations and 4
              seasons. The reference period is the 1971-1998 NARCCAP precipitation.

Figure 6-6   Boxplot of cumulative monthly precipitations over the 1971-1998 NARCCAP historical period for 11 GCM-RCM model combinations and 4 seasons. The reference period for the horizontal lines is the 1971-1998 precipitation input data from the actual historical record

149
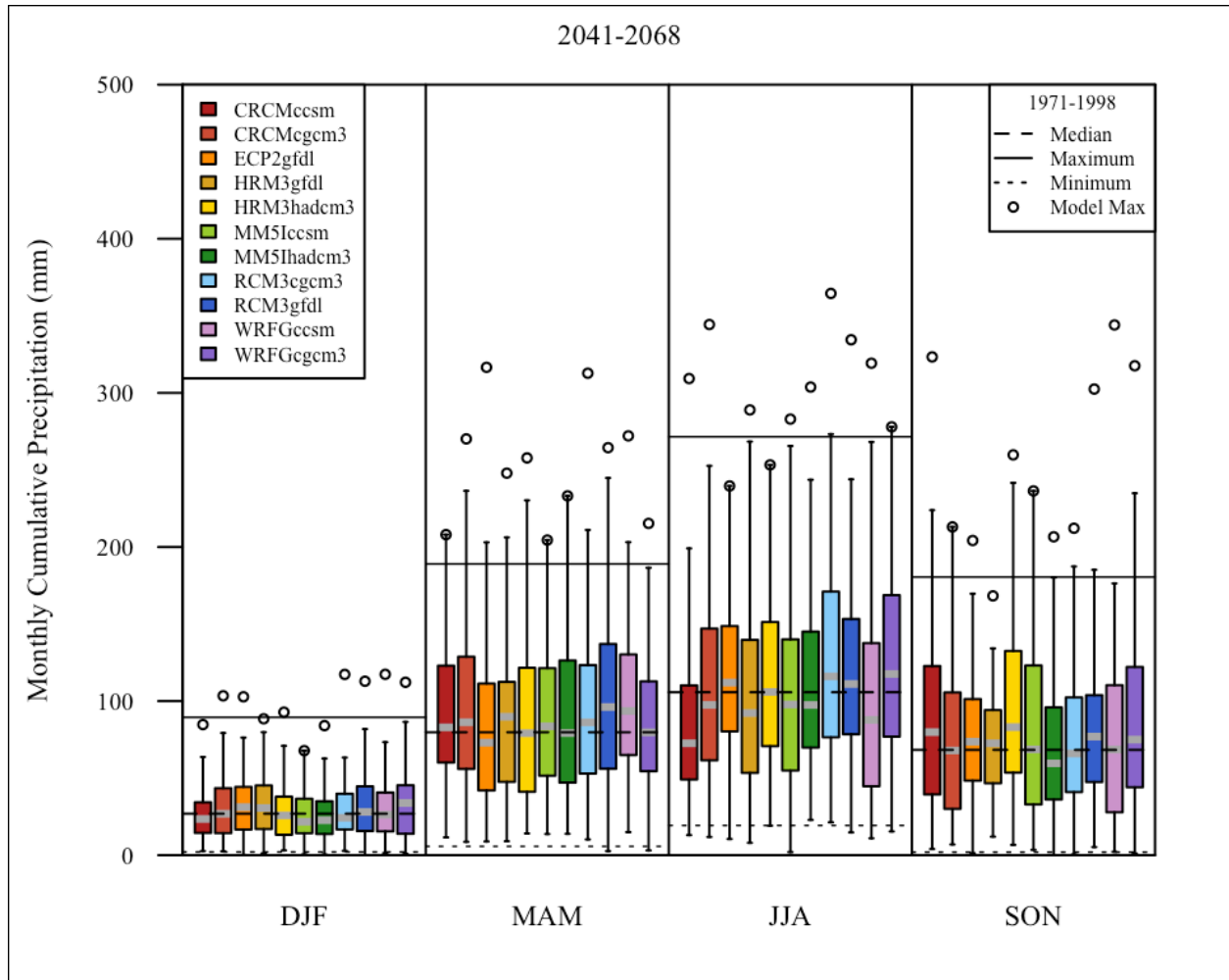
Figure 6-7   Boxplot of cumulative monthly precipitations over the 2041-2068 NARCCAP historical period for 11 GCM-RCM model combinations and 4 seasons. The reference period for the horizontal lines is the 1971-1998 precipitation input data from the actual historical record.

150
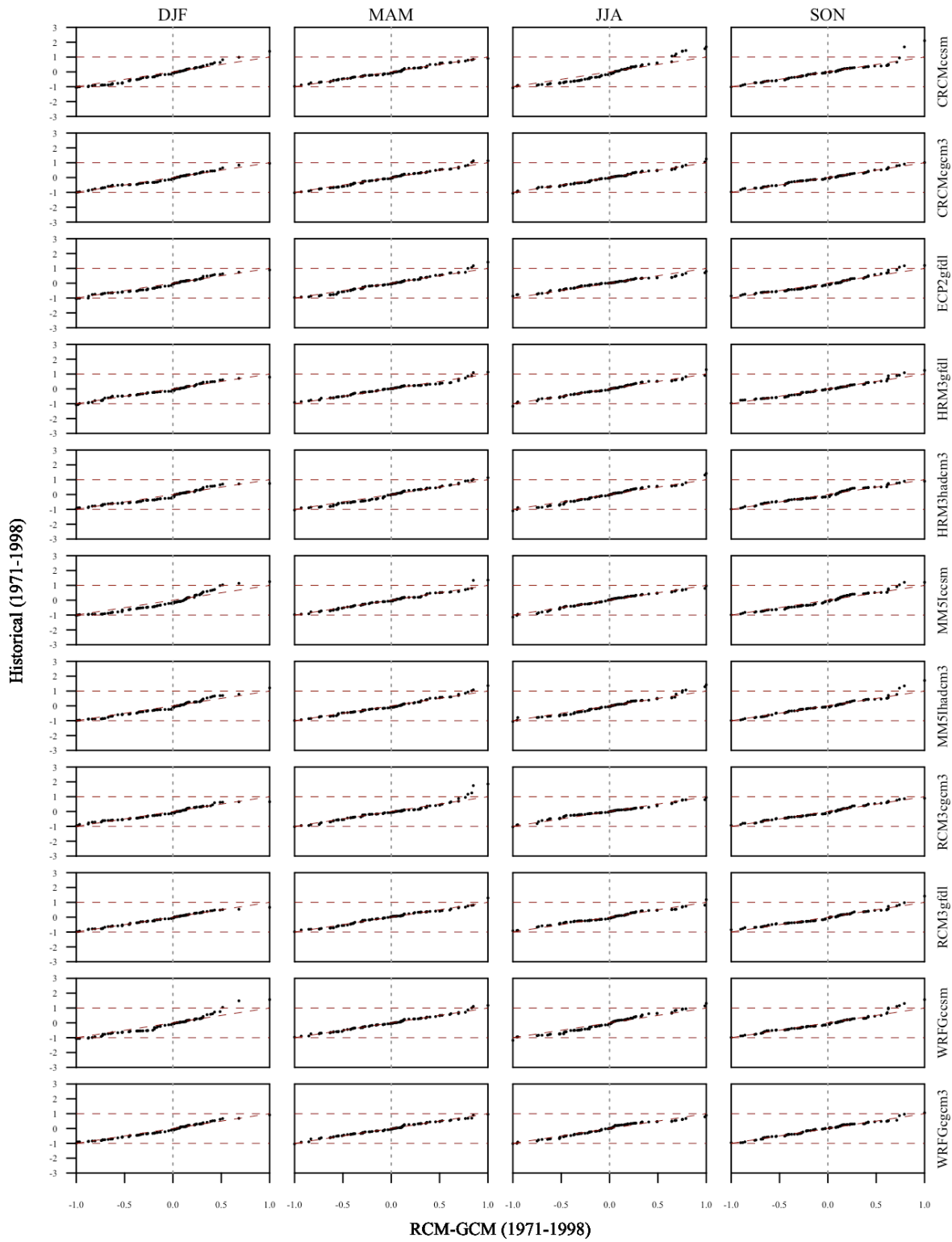
Figure 6-8   Quantile-quantile plots of median normalized monthly precipitation by season for
               the historical 1971-1998 simulation period with historical observations as
               reference. Horizontal lines at -1 and 1 indicate the min and max observations.

151

Figure 6-9   Quantile-quantile plots of median normalized monthly precipitation by season for the projected 2041-2068 simulation period with 1971-1998 model values as reference. Horizontal lines at -1 and 1 indicate the min and max reference values.
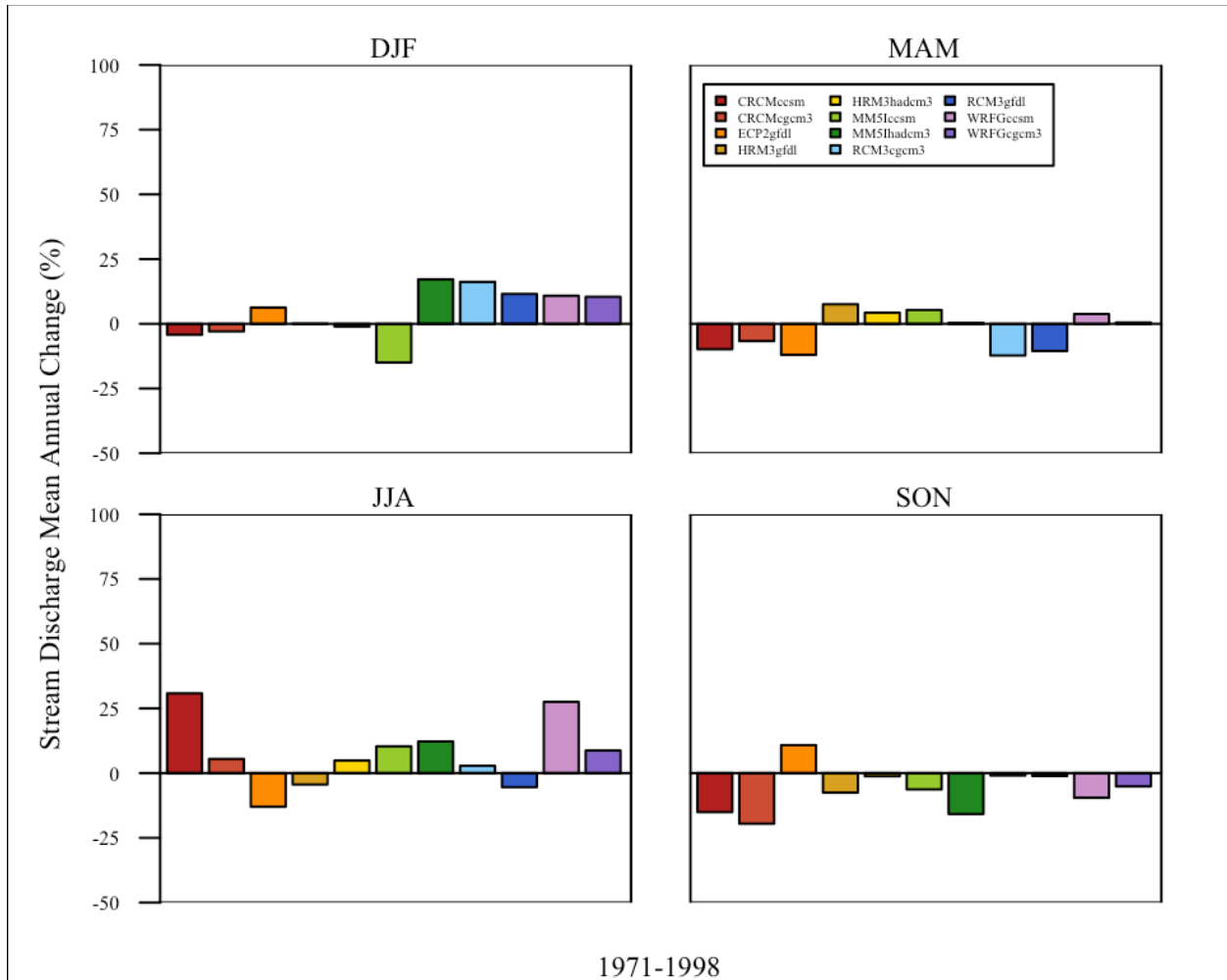
Figure 6-10   Mean annual percent change of monthly stream discharge of 1971-1998
               NARCCAP historical period for 11 GCM-RCM model combinations and 4
               seasons. The reference discharge is from the 1971-1998 simulation from the
               calibrated SWAT model.

153
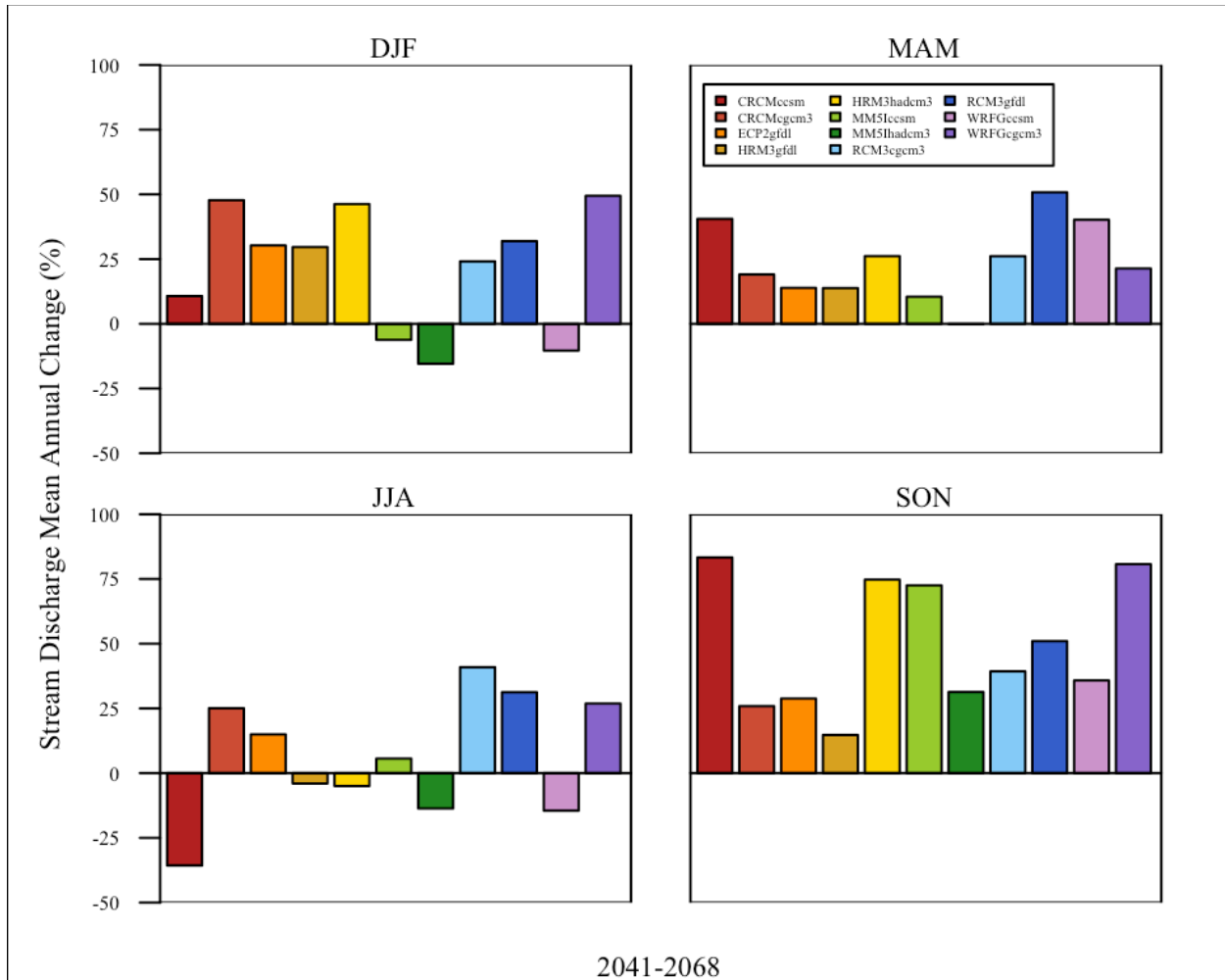
Figure 6-11   Mean annual percent change of stream discharge at the basin outlet over the
projected 2041-2068 NARCCAP simulation period for eleven GCM-RCM model
combinations. The reference discharge is from the 1971-1998 NARCCAP-driven
simulations for each model.

154
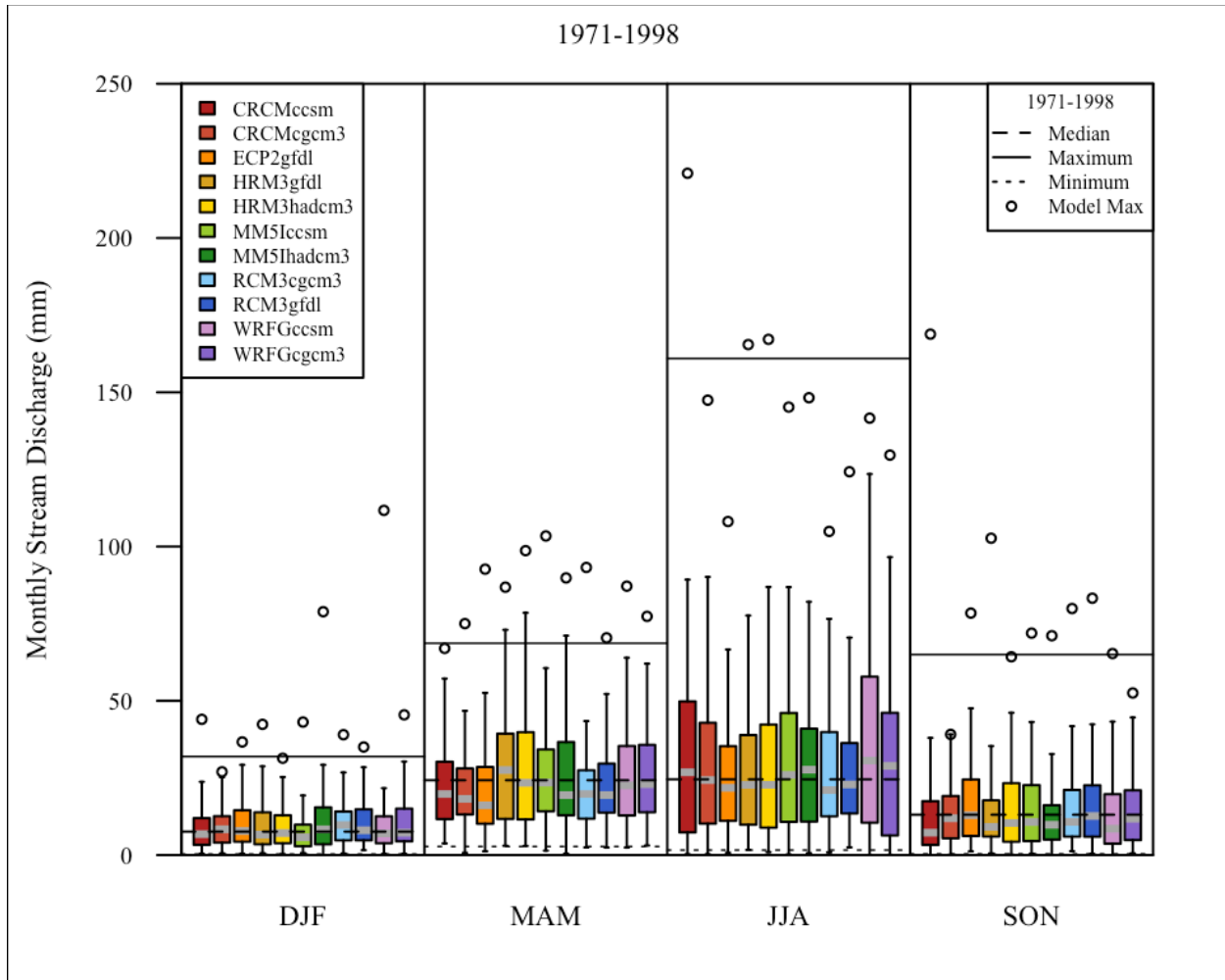
Figure 6-12   Boxplot of monthly stream discharge over the 1971-1998 NARCCAP historical
               period for 11 GCM-RCM model combinations and 4 seasons. The reference
               discharge for the horizontal lines is from the 1971-1998 simulation from the
               calibrated SWAT model.
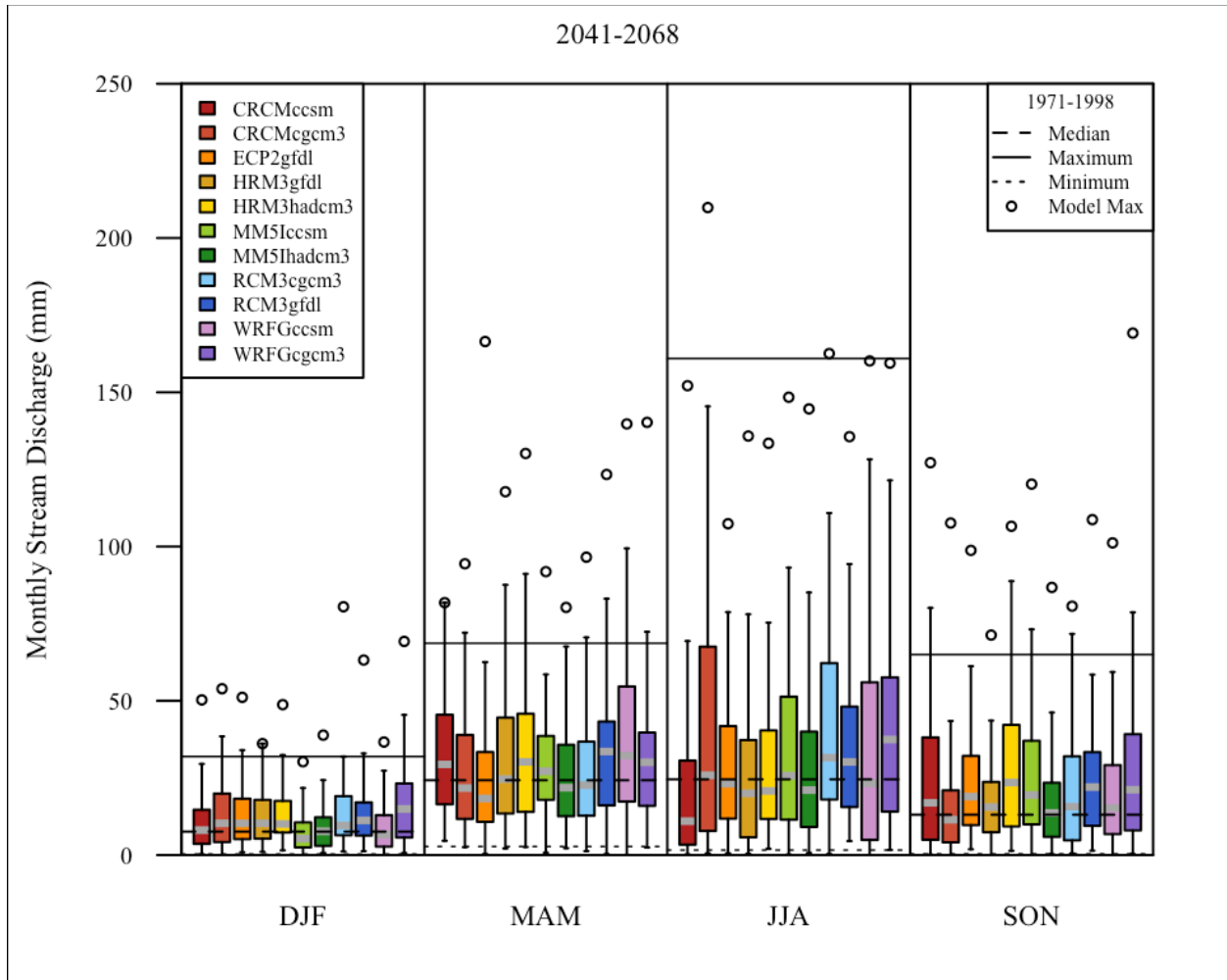
Figure 6-13   Boxplot of monthly stream discharge over the 2041-2068 NARCCAP projected period for 11 GCM-RCM model combinations and 4 seasons. The reference discharge for the horizontal lines is from the 1971-1998 simulation from the calibrated SWAT model.
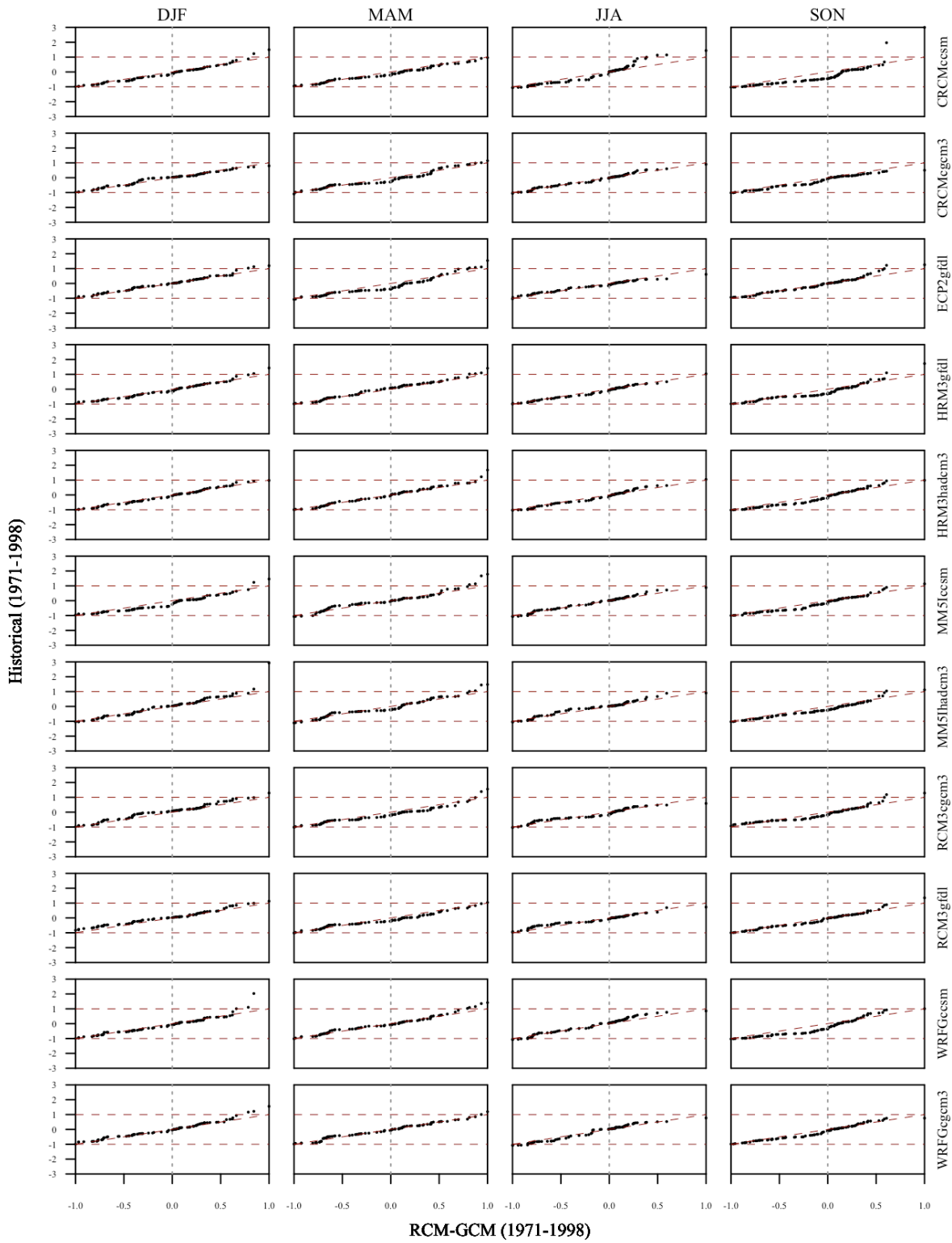
Figure 6-14   Quantile-quantile plots of median normalized monthly stream discharge by season for the historical 1971-1998 simulation period with calibrated model as reference. Horizontal lines at -1 and 1 indicate the min and max calibration values.

157
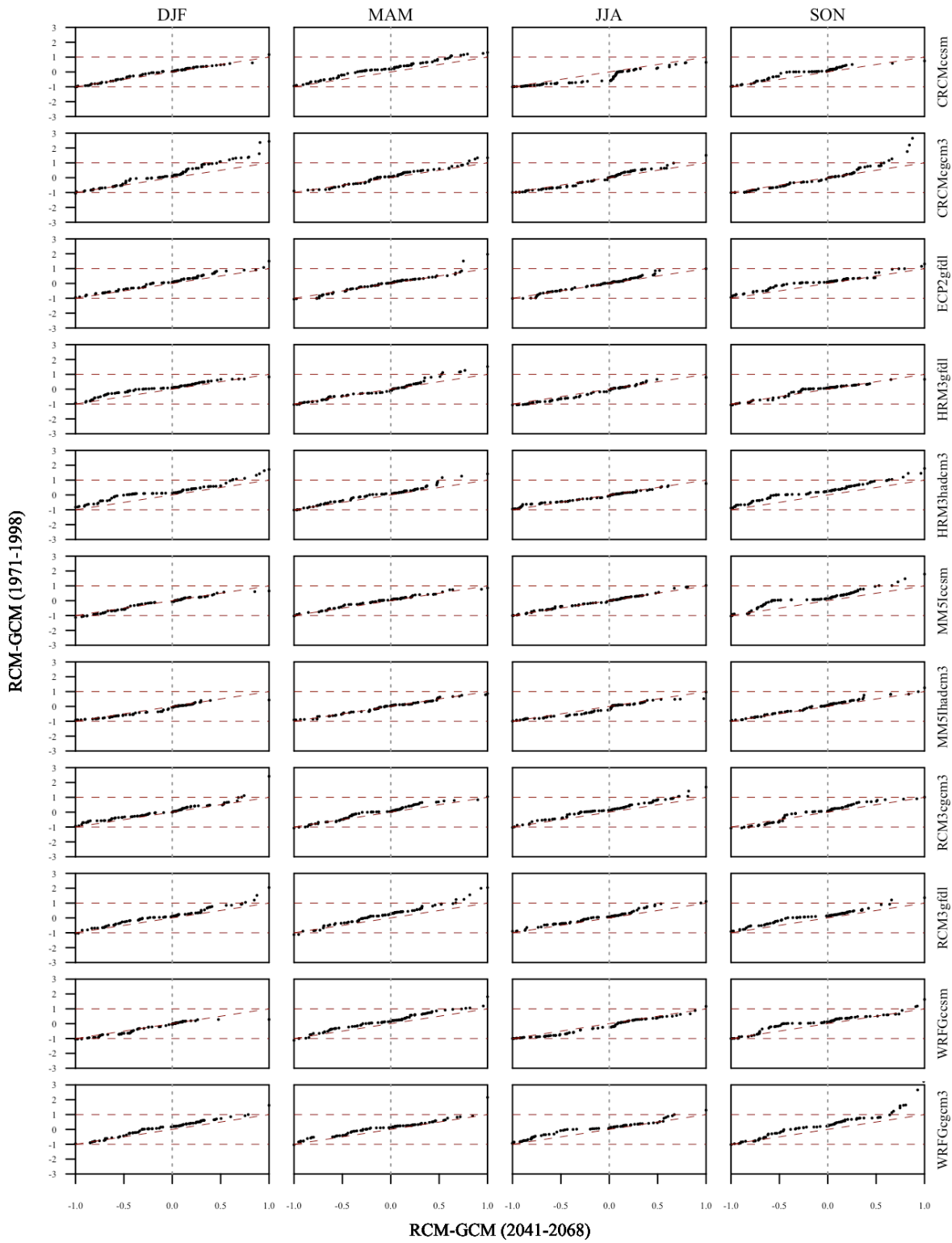
Figure 6-15   Quantile-quantile plots of median normalized monthly stream discharge by season for the projected 2041-2068 simulation period with historical NARCCAP as reference. Horizontal lines indicate the min and max historical model values.
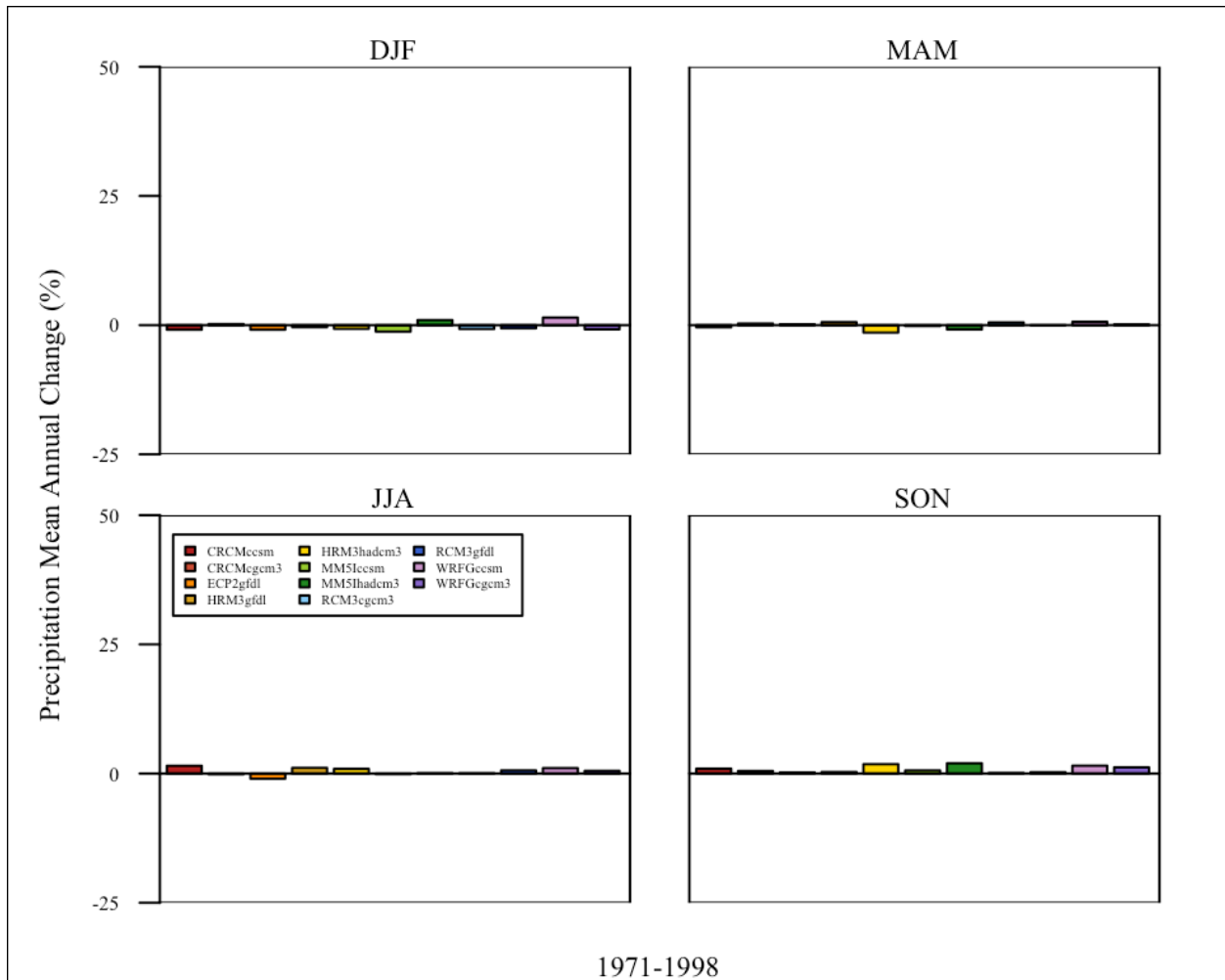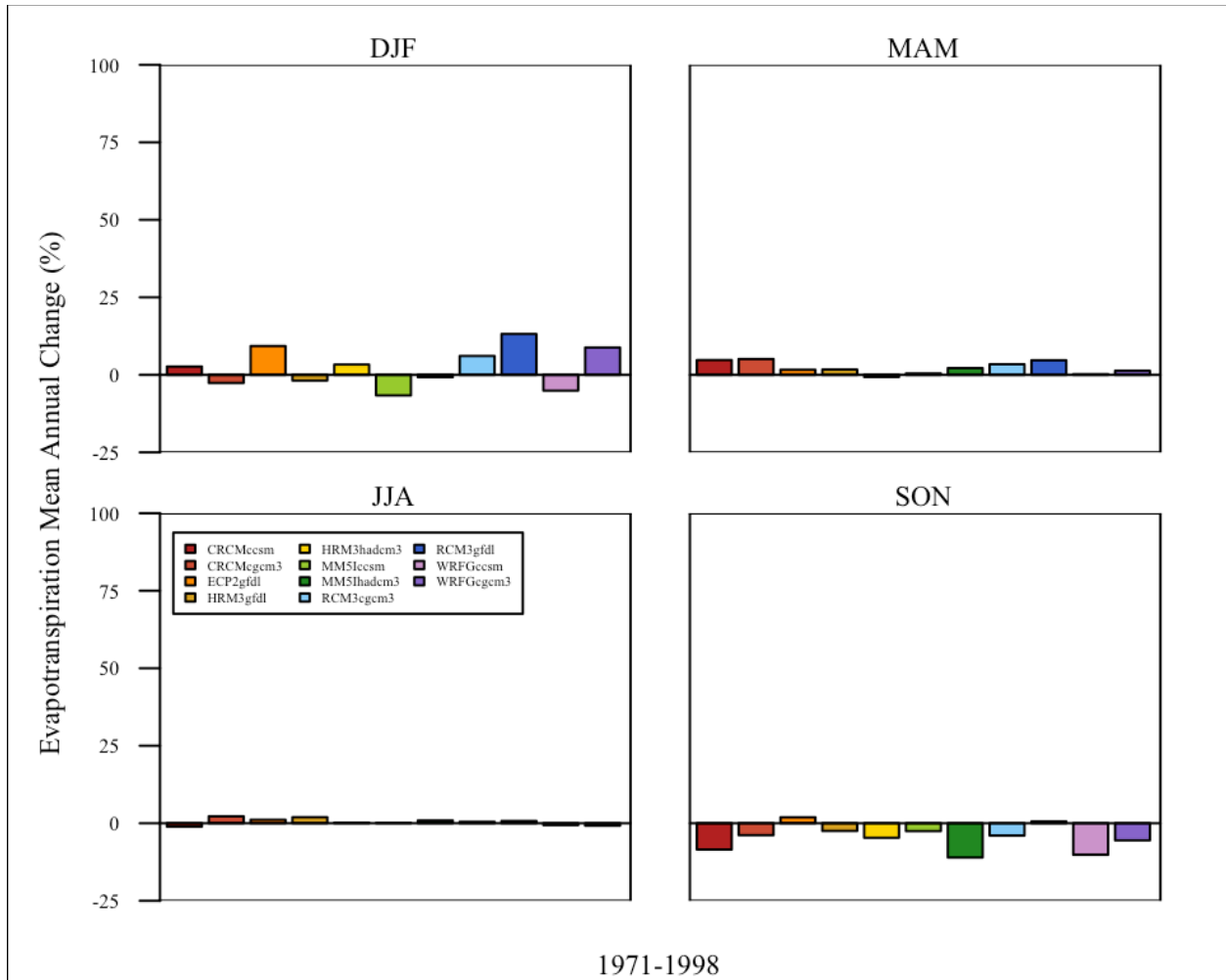
Figure 6-16   Mean annual percent change of cumulative evapotranspiration (ET) of 1971-1998
              NARCCAP historical period for 11 GCM-RCM model combinations and 4
              seasons. The reference ET is from the 1971-1998 simulation from the calibrated
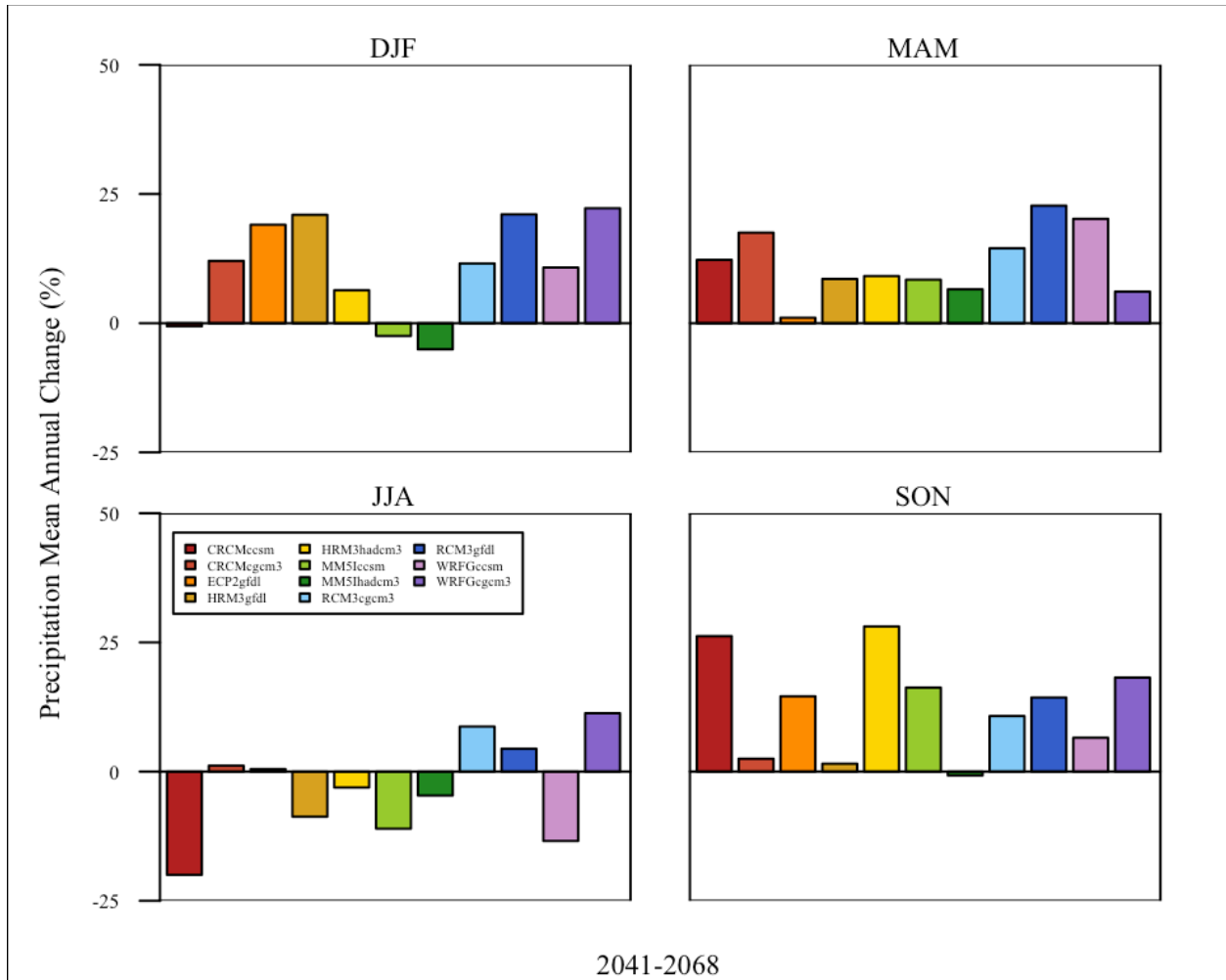   SWAT model.
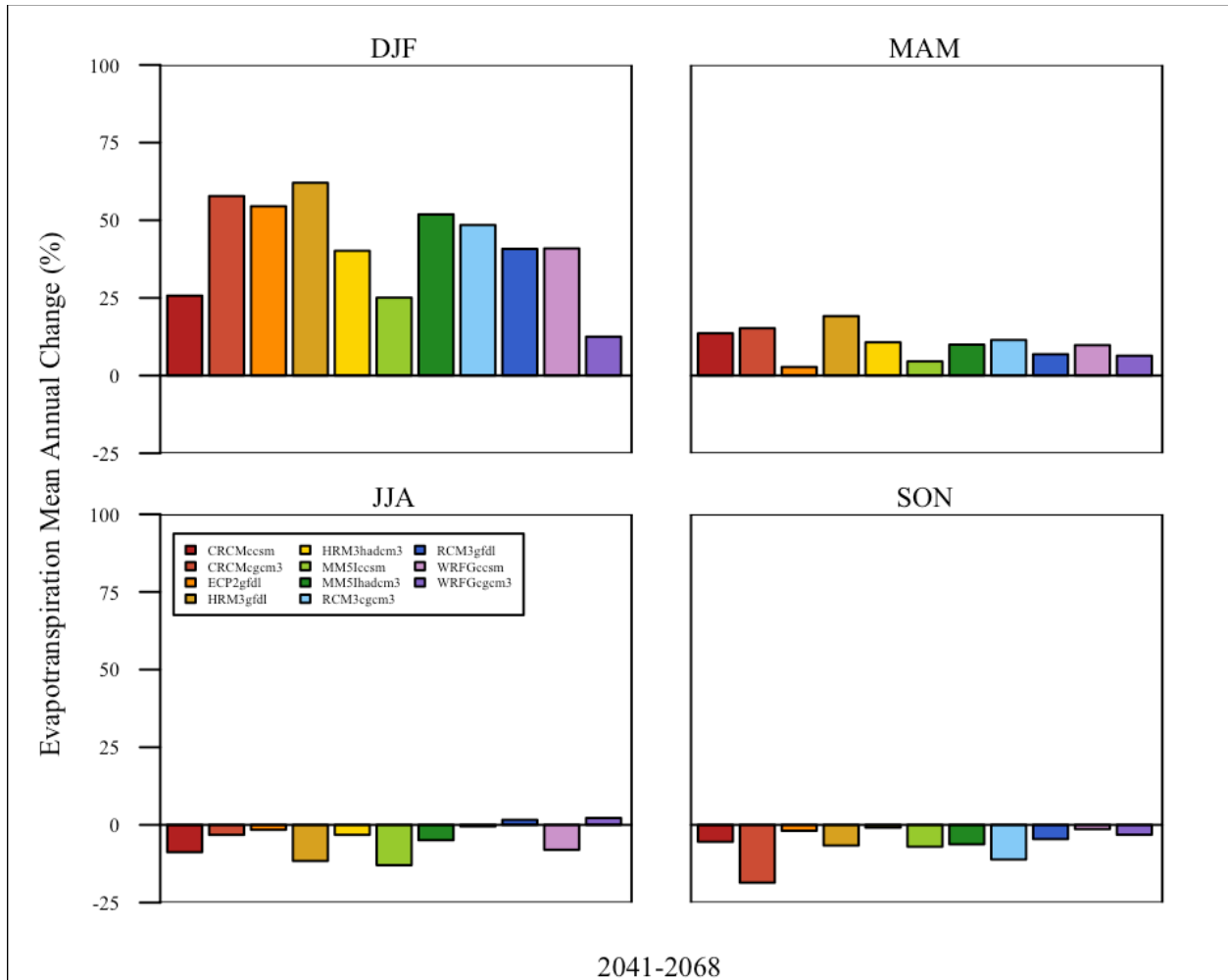
Figure 6-17   Mean annual percent change of cumulative evapotranspiration (ET) of 2041-2068
NARCCAP period for 11 GCM-RCM model combinations and 4 seasons. The
reference ET is from the 1971-1998 simulation from the historical NARCCAP
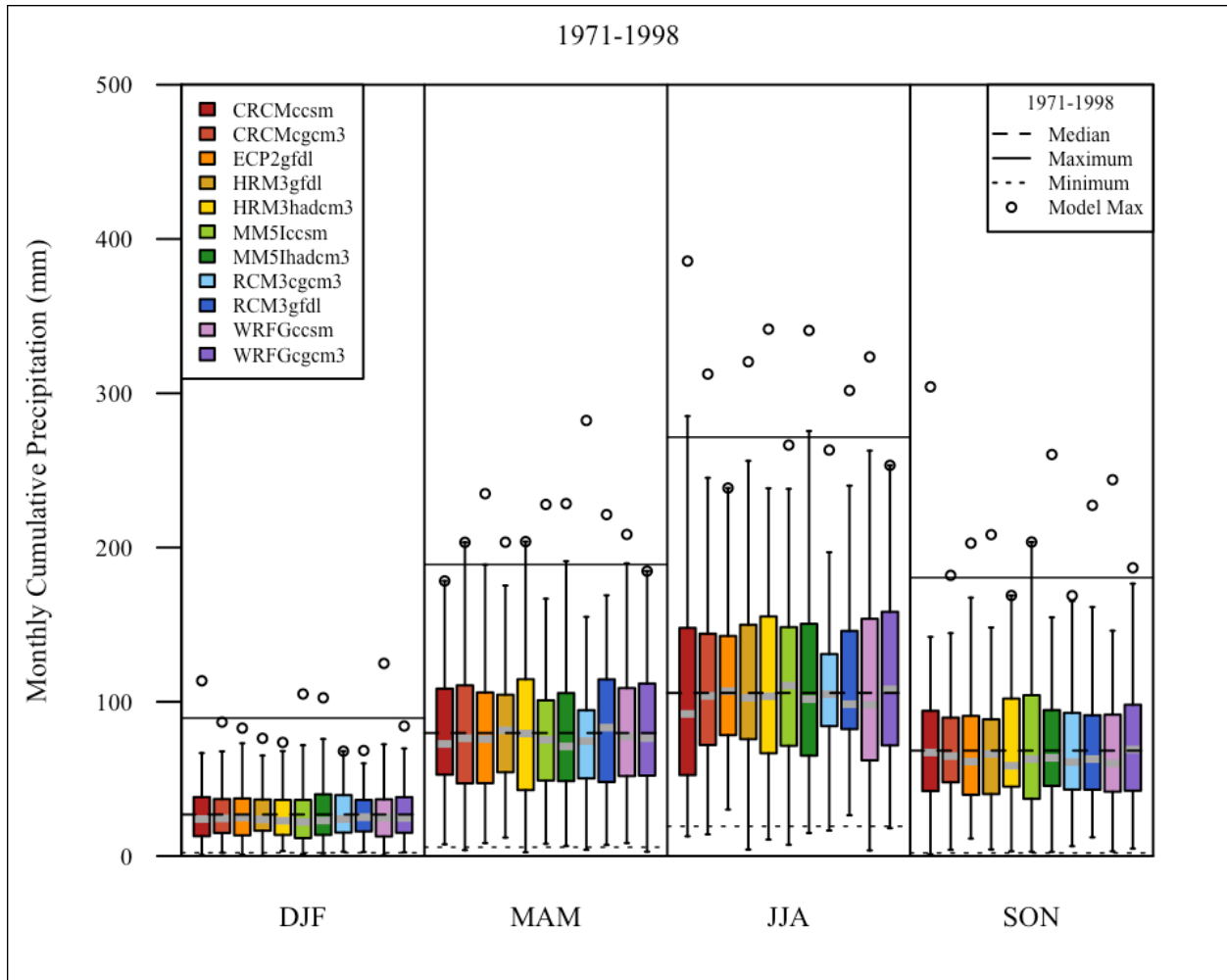driven SWAT outputs.
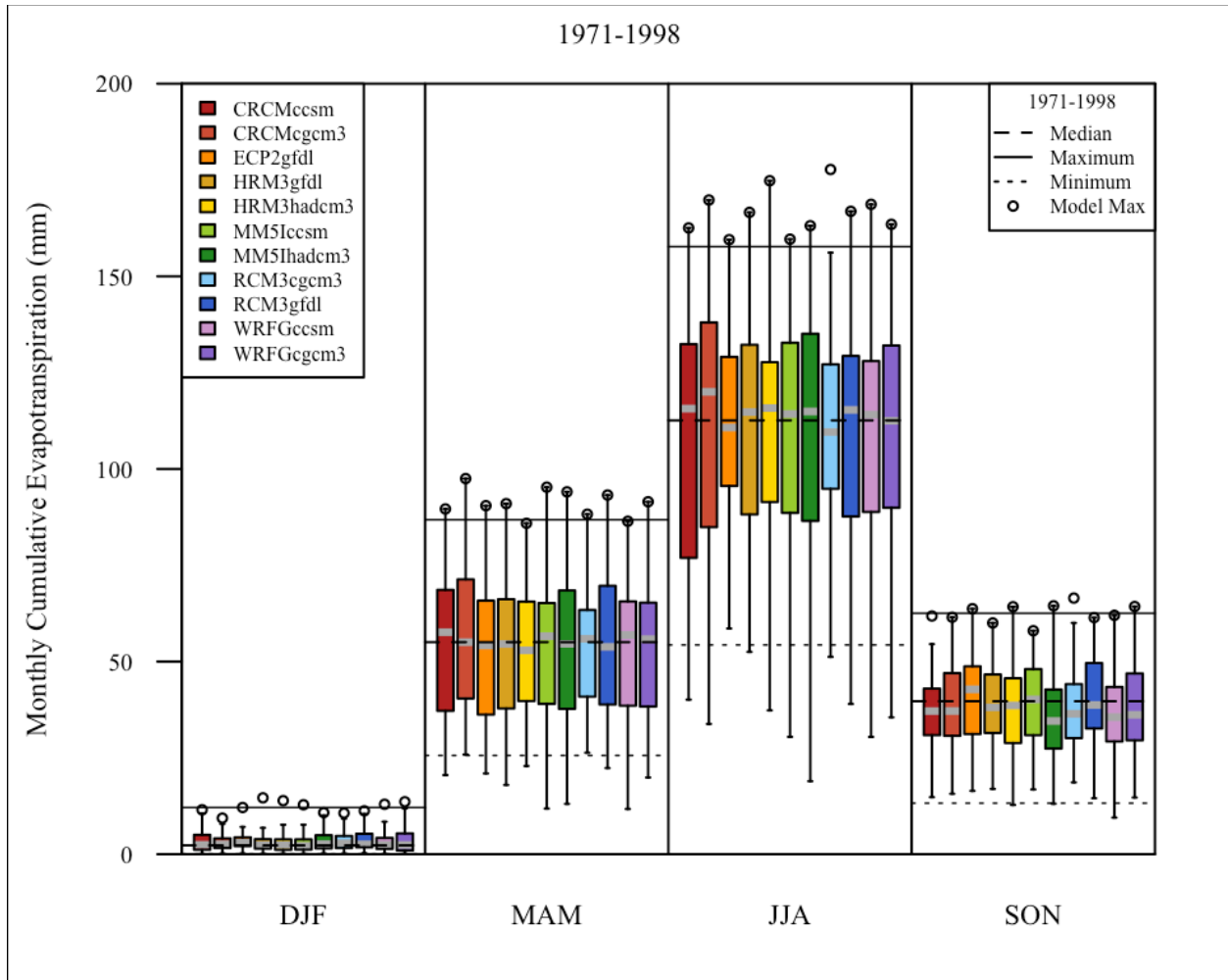
Figure 6-18   Boxplot of cumulative monthly evapotranspiration (ET) over the 1971-1998
NARCCAP historical period for 11 GCM-RCM model combinations and 4
seasons. The reference (ET) for the horizontal lines is from the 1971-1998
simulation from the calibrated SWAT model.
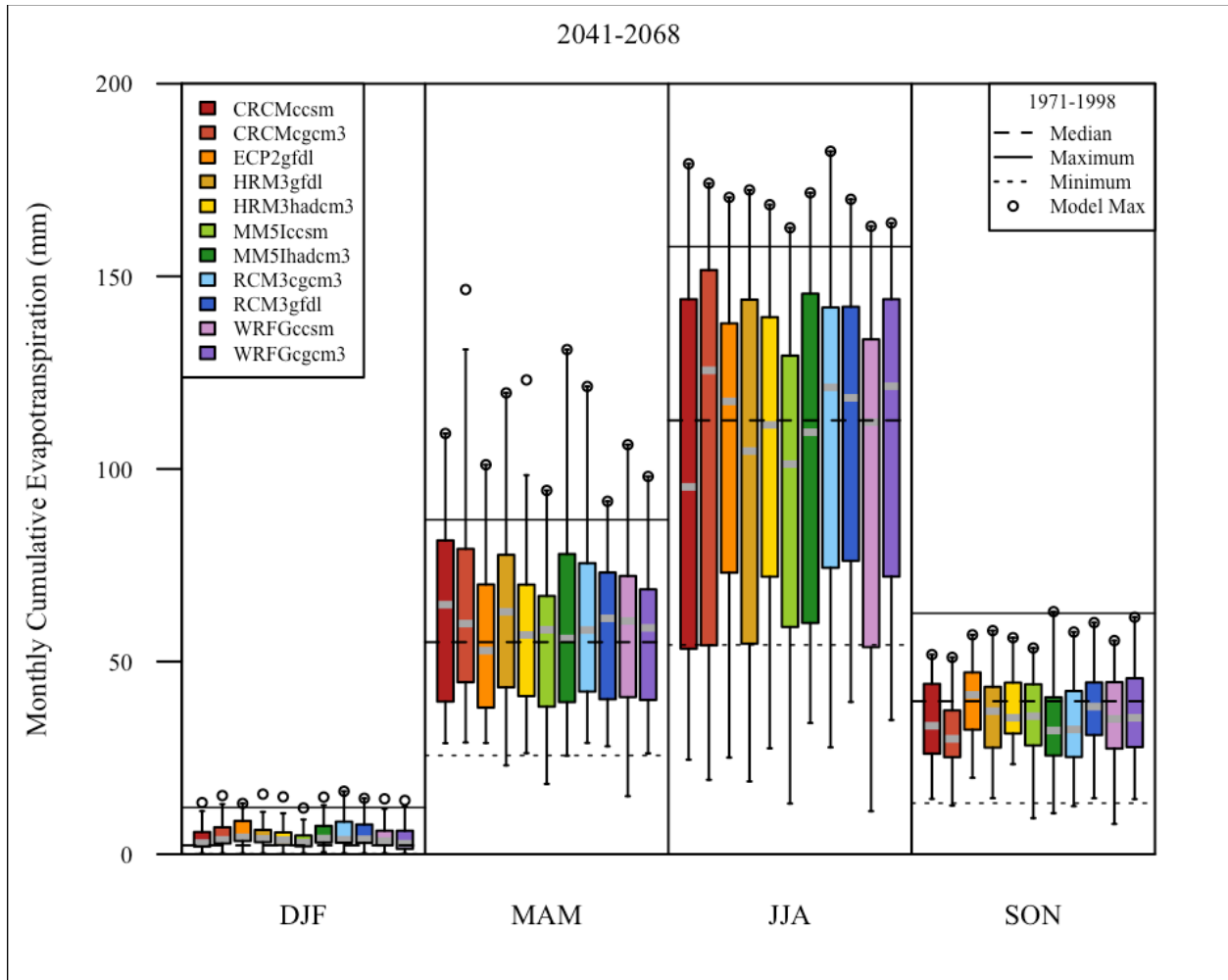
Figure 6-19   Boxplot of cumulative monthly evapotranspiration (ET) over the 2041-2068
NARCCAP projected period for 11 GCM-RCM model combinations and 4
seasons. The reference (ET) for the horizontal lines is from the 1971-1998
simulation from the calibrated SWAT model.
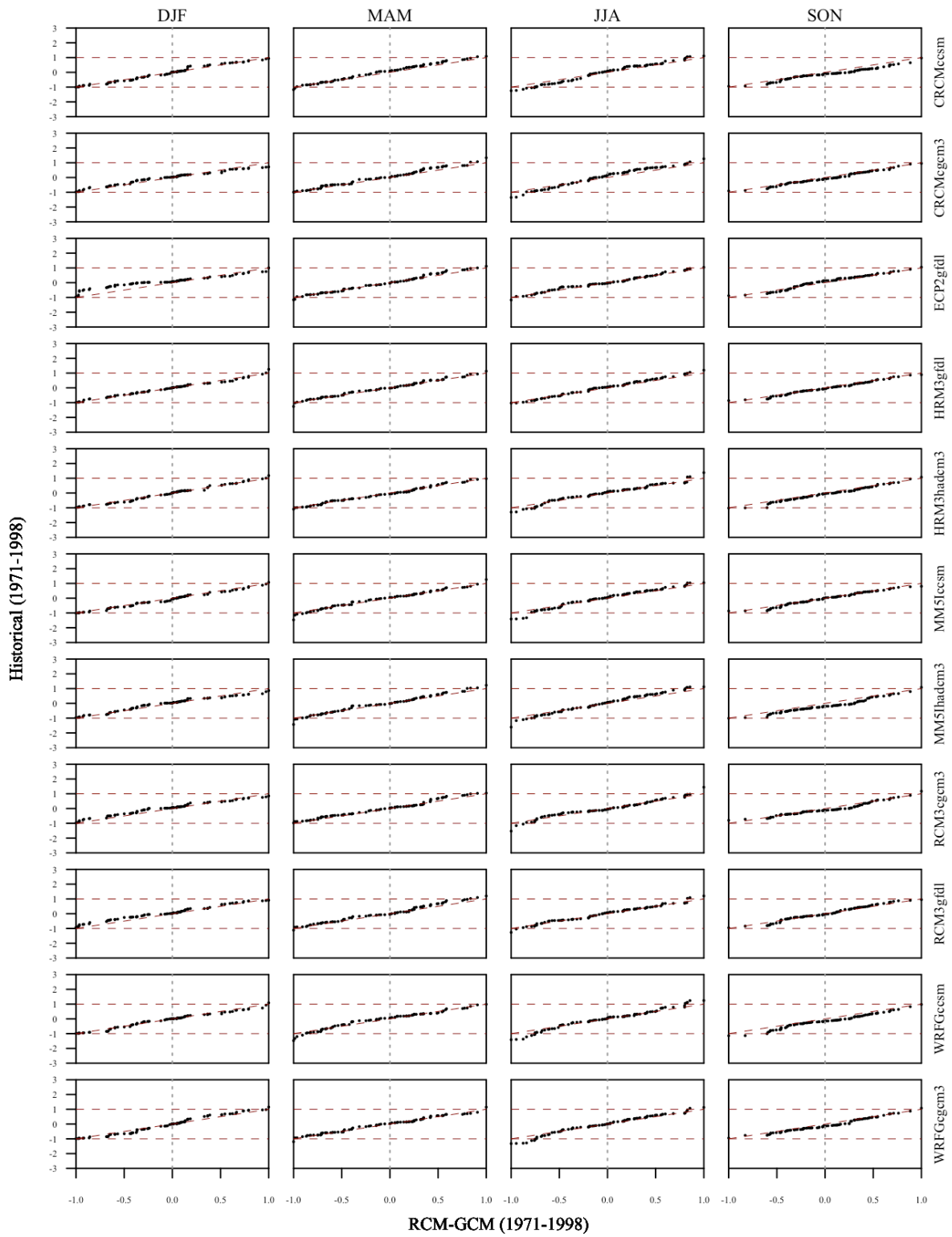
Figure 6-20   Quantile-quantile plots of median normalized evapotranspiration by season for historical 1971-1998 simulation period with calibrated model as reference. Horizontal lines at -1 and 1 indicate the min and max calibration values.

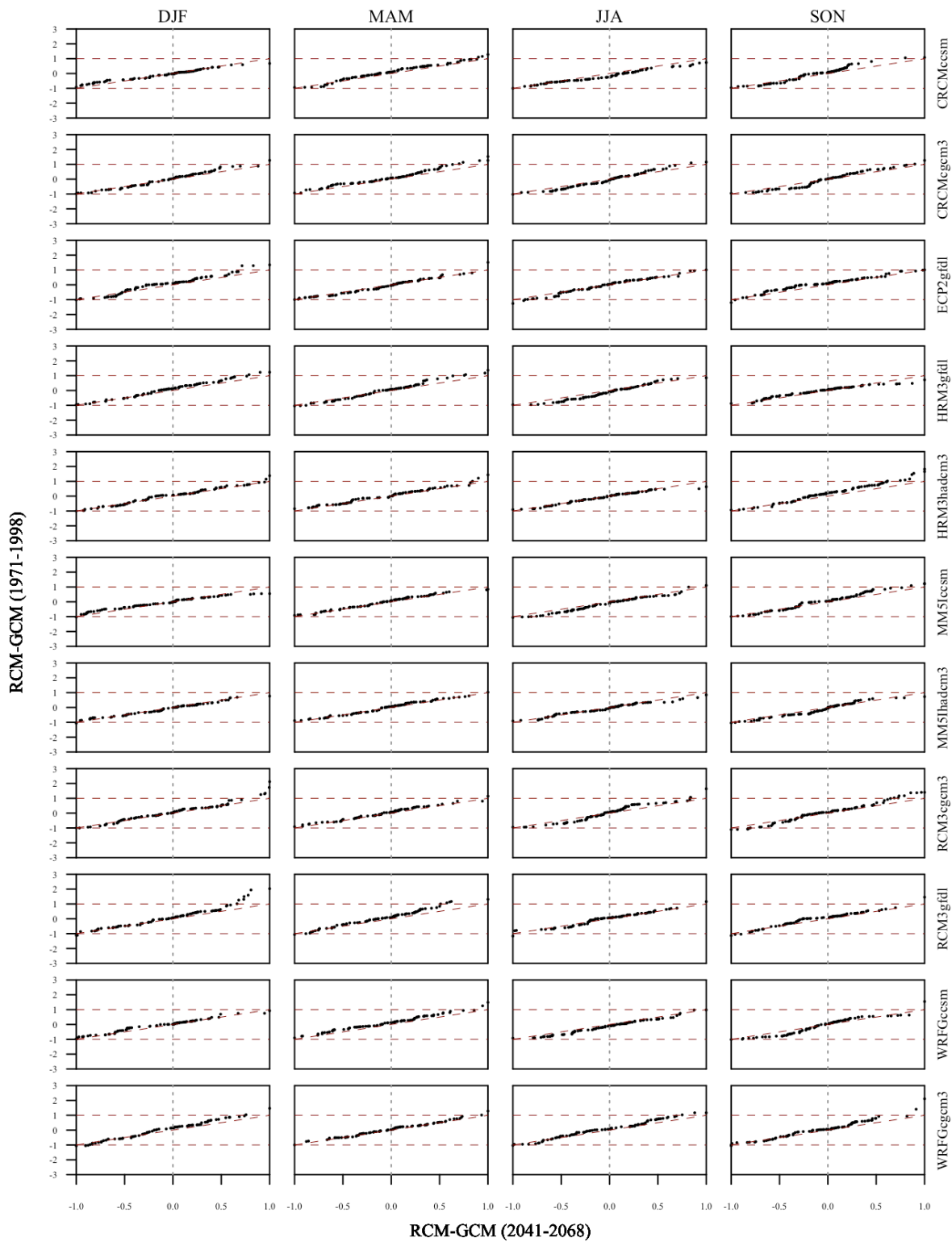163
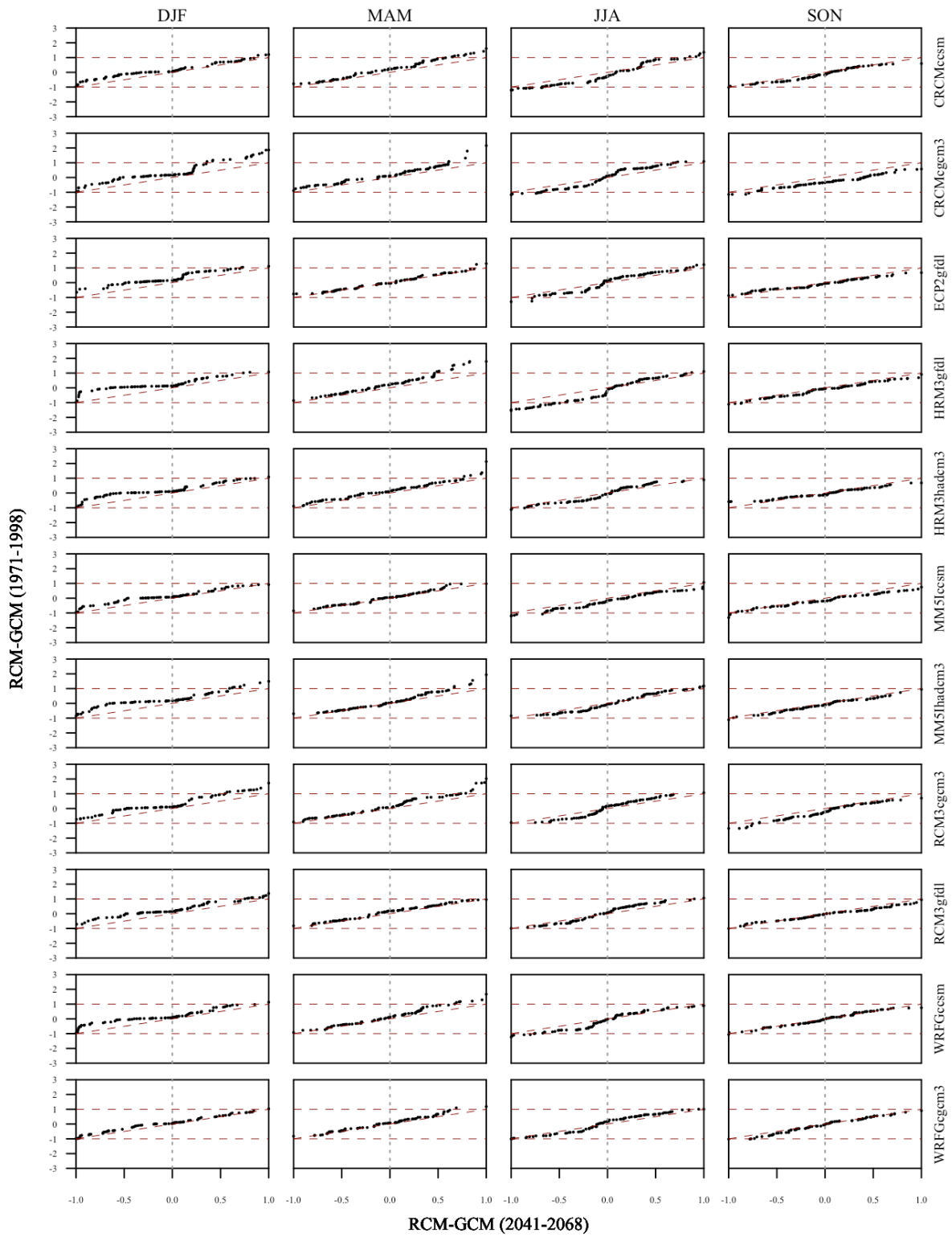
Figure 6-21   Quantile-quantile plots of median normalized evapotranspiration by season for the projected 2041-2068 simulation period with historical NARCCAP as reference. Horizontal lines indicate the min and max historical model values.
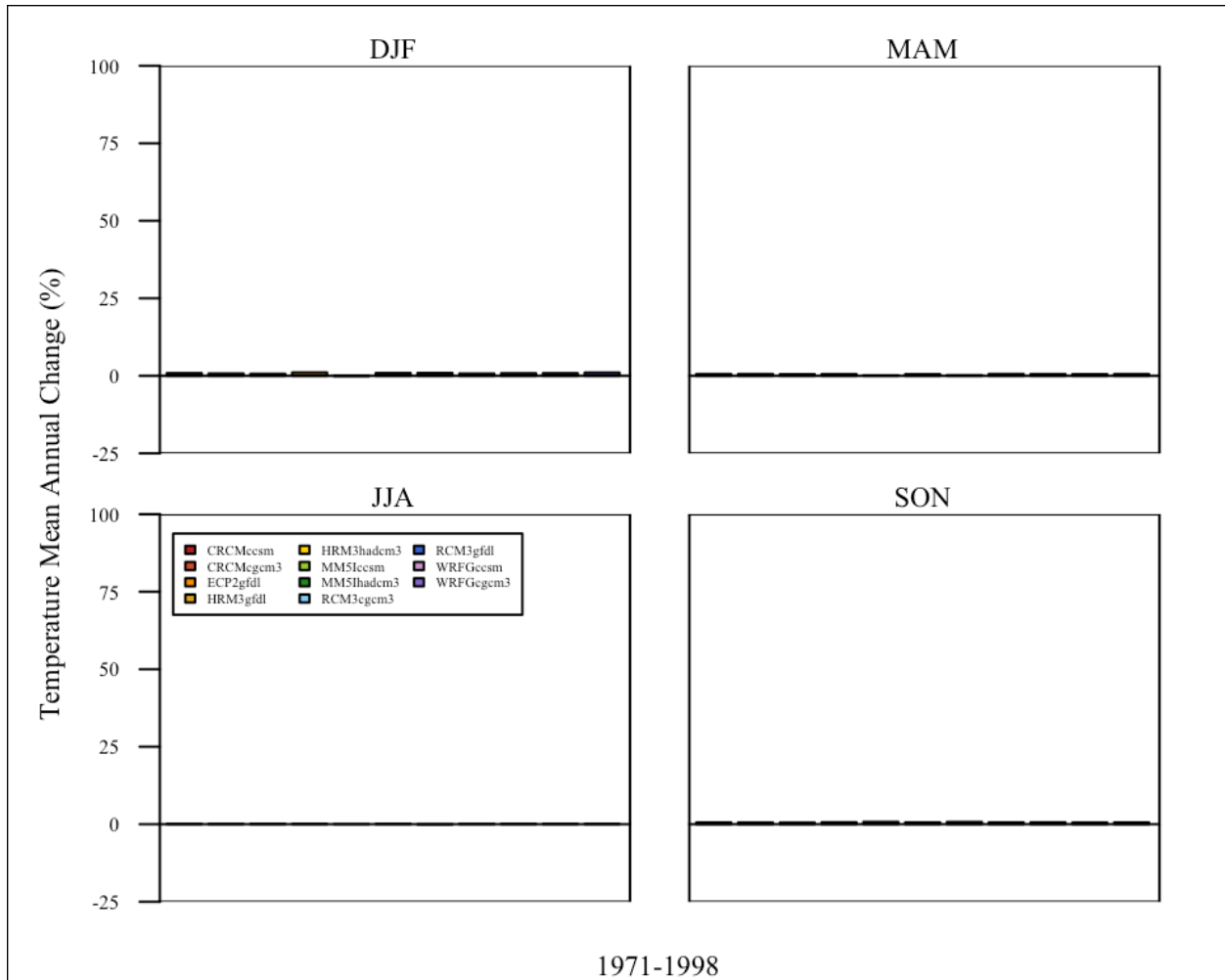
Figure 6-22   Mean annual percent change of mean daily temperature of 1971-1998 NARCCAP historical period for 11 GCM-RCM model combinations and 4 seasons. The reference ET is from the 1971-1998 simulation from the calibrated SWAT model.
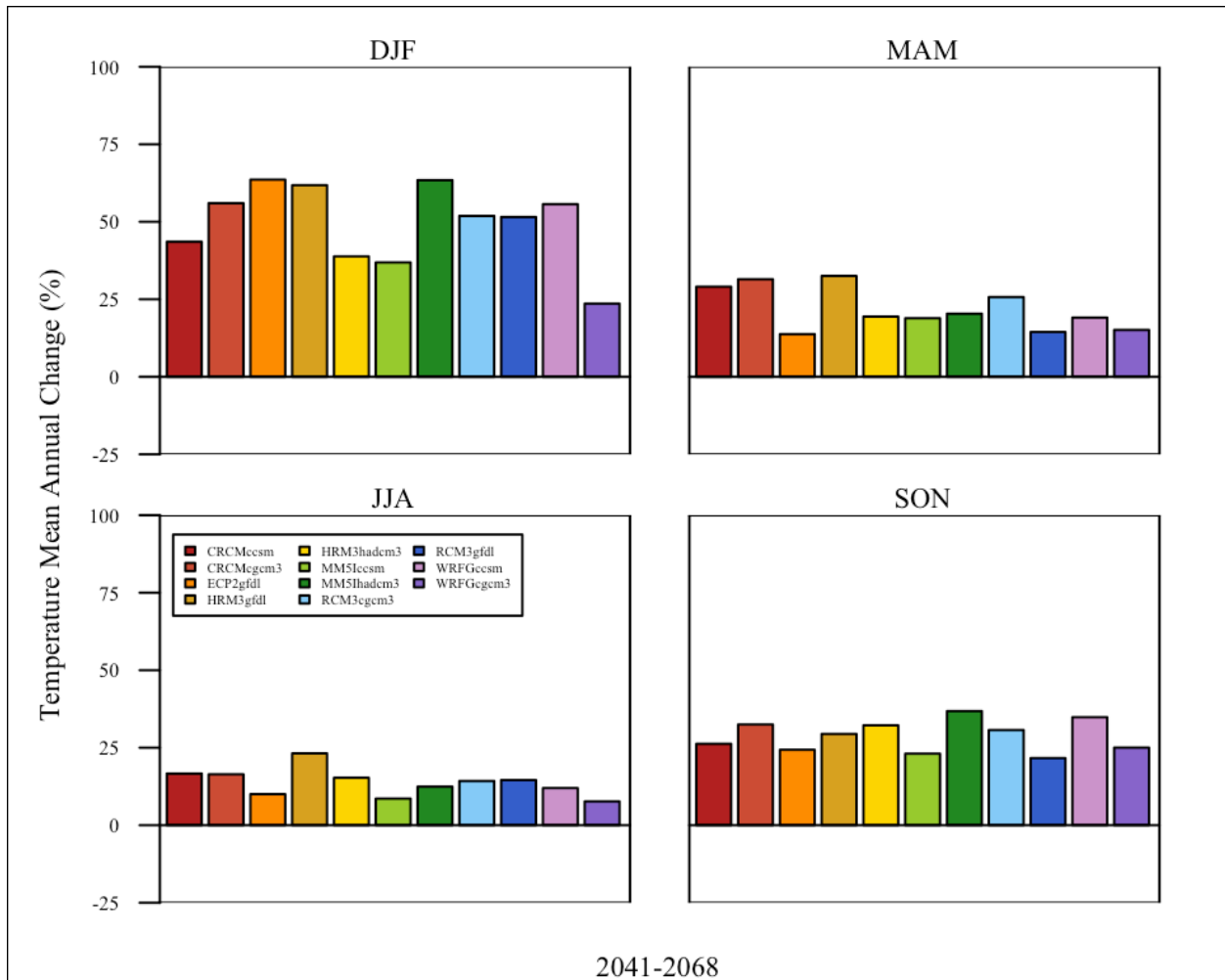
Figure 6-23   Mean annual percent change of mean daily temperature of 2041-2068 NARCCAP
               projected period for 11 GCM-RCM model combinations and 4 seasons. The
               reference period is the 1971-1998 NARCCAP precipitation.
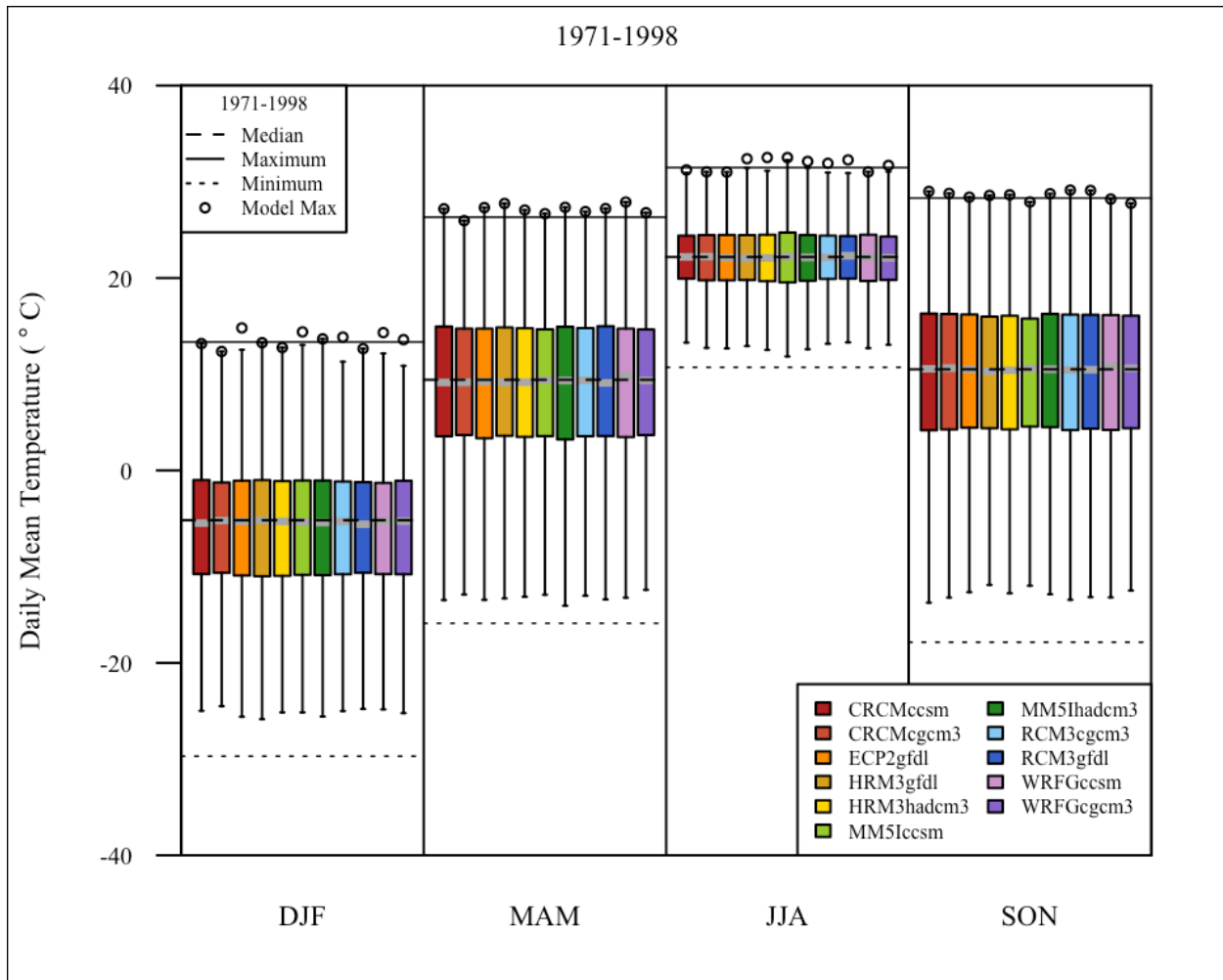
Figure 6-24   Boxplot of mean daily temperatures over the 1971-1998 NARCCAP historical
period for 11 GCM-RCM model combinations and 4 seasons. The reference
period for the horizontal lines is the 1971-1998 precipitation input data from the
actual historical record
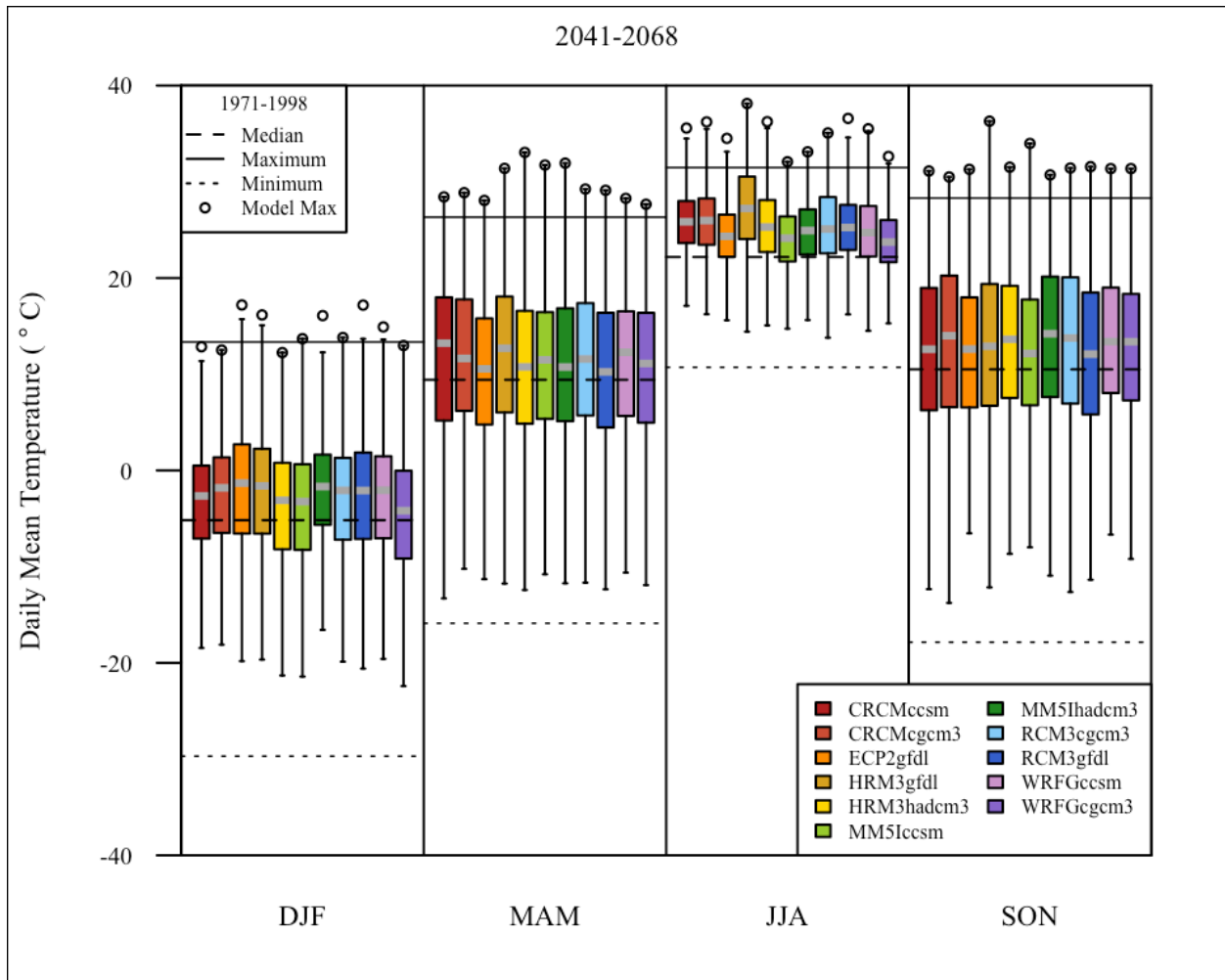
Figure 6-25   Boxplot of mean daily temperatures over the 2041-2068 NARCCAP historical period for 11 GCM-RCM model combinations and 4 seasons. The reference period for the horizontal lines is the 1971-1998 precipitation input data from the actual historical record
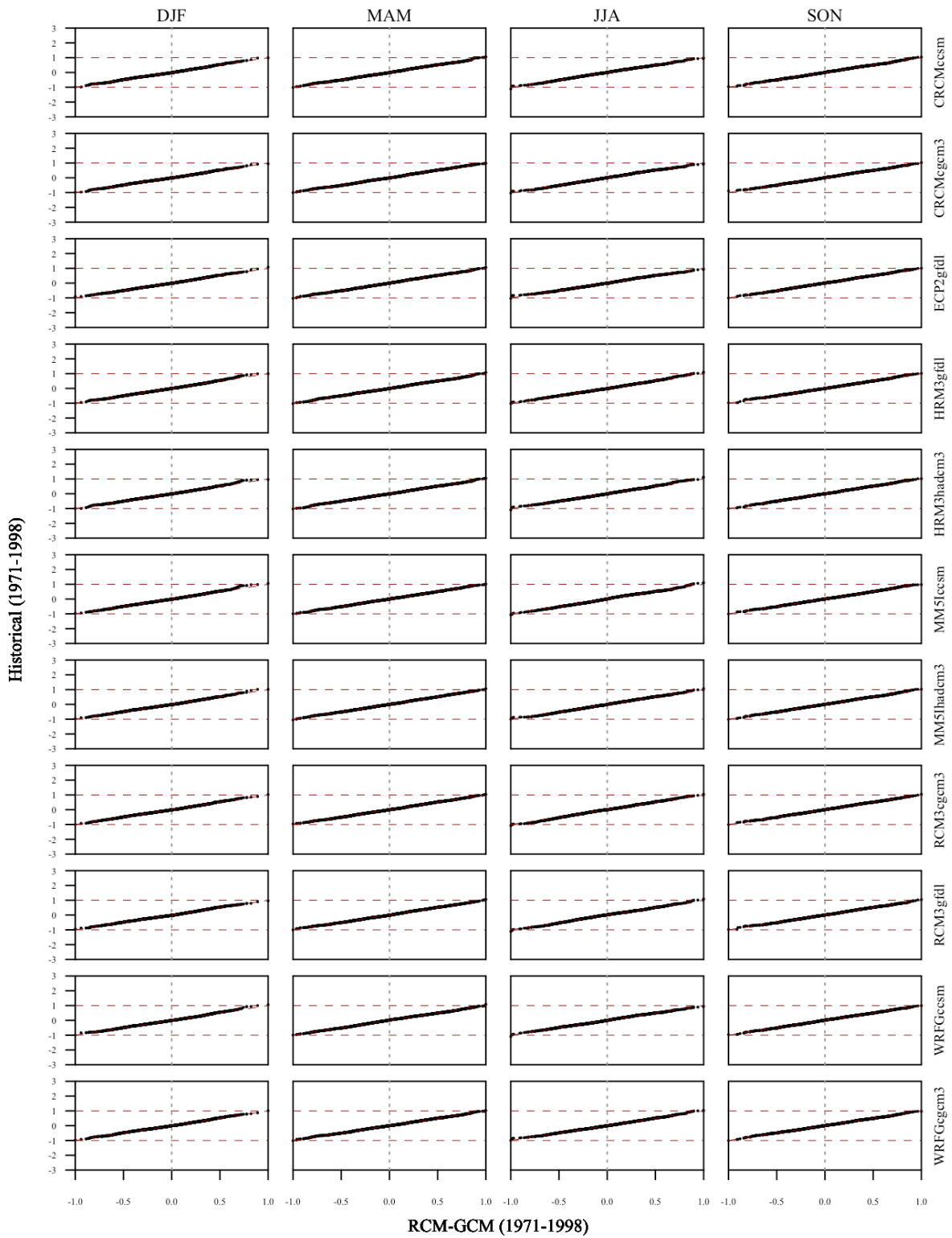
Figure 6-26   Quantile-quantile plots of median normalized daily mean temperature by season for the historical 1971-1998 simulation period with historical observations as reference. Horizontal lines at -1 and 1 indicate the min and max observations.

169
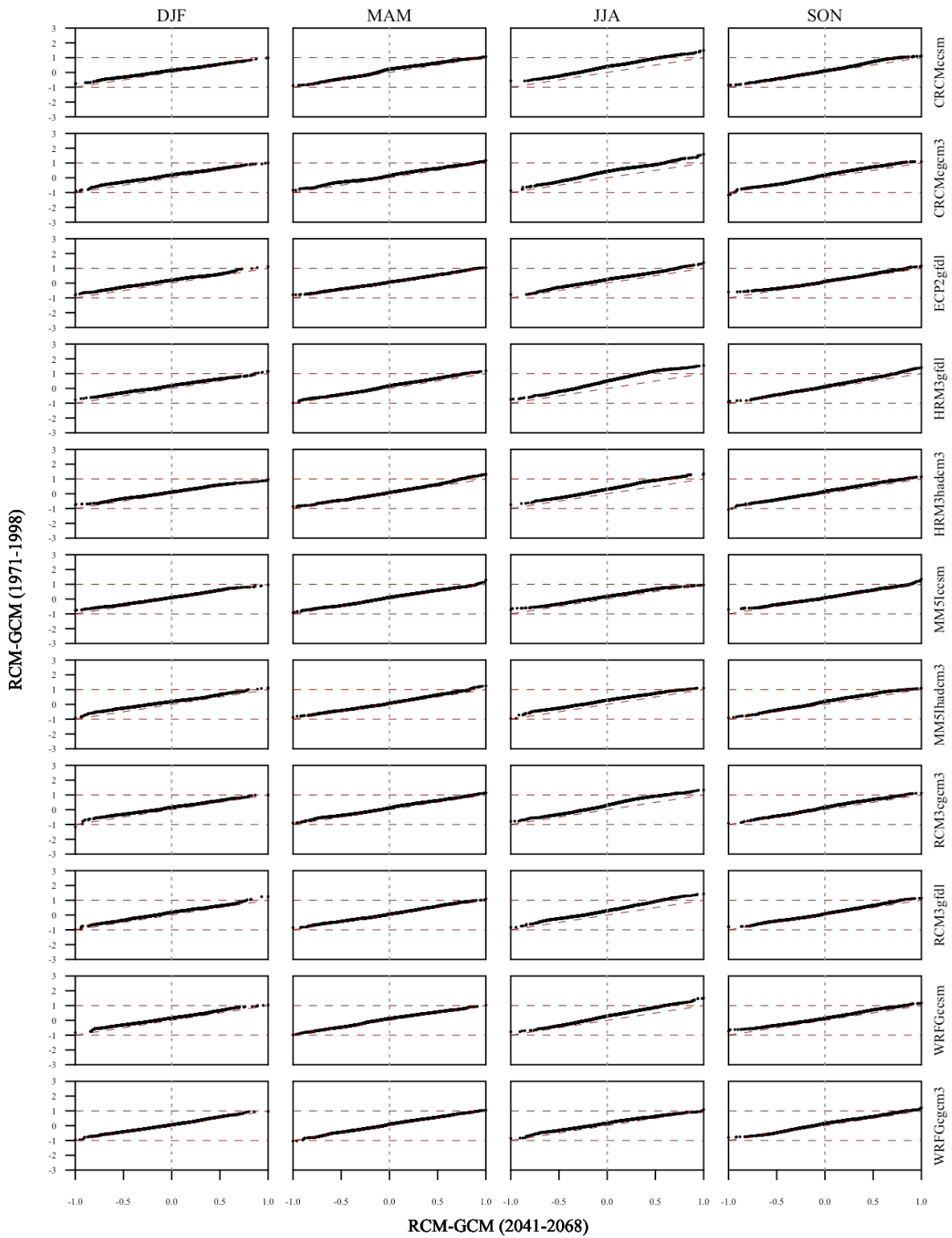
Figure 6-27   Quantile-quantile plots of median normalized daily mean temperature by season
for the projected 2041-2068 simulation period with 1971-1998 model values as
reference. Horizontal lines at -1 and 1 indicate the min and max reference values.
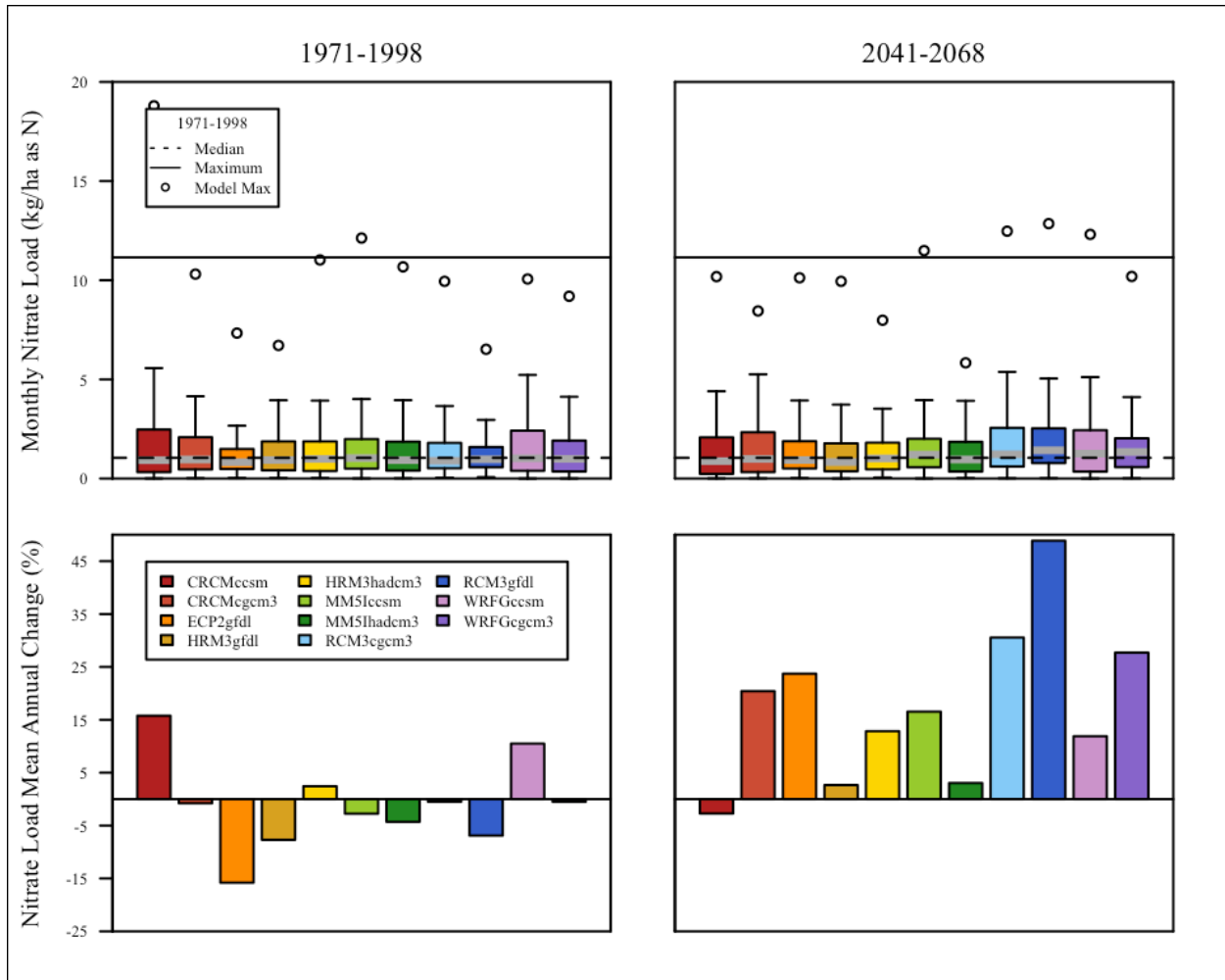
Figure 6-28   Boxplots and annual percent change for nitrate loads for the NARCCAP
simulation periods. The reference for the 1971-1998 percent change is the
calibrated SWAT model. The reference for the 2041-2068 percent change is the
historical NARCCAP-driven SWAT outputs.

CHAPTER 7: IMPLEMENTING LAND USE SCENARIOS
WITH CLIMATE CHANGE

Introduction

Climate change represented the atmospheric aspect of prediction and the boundaries were large, covering vast geographic and altitudinal dimensions. At the surface land use and cover (LULC) were the other aspects or axis that affects water quality and quantity. Excepting geological considerations for aquifers, the ridges that form the boundaries of watersheds gave a convenient focus area where the water that falls anywhere in this boundary will route and collect the constituents to a single point at the outlet by gravity. Thus the upstream inhabitants' activities were responsible for any positive or negative effect to those downstream. Land use change was in some ways more complicated than climate change. While anthropogenic activities drove the current climate change, these activities were typically wide-spread and by definition global in scale. Barring catastrophic events, humans instigated land use change and the decisions that guide these changes were already complex for the individual human, but together with institutions, regulatory agencies, and the economy, the human system provided a complex challenge in computation and the modeling of physical systems.

This chapter accessed the LULC impacts on water quality and water quantity through two tasks. The first task took a guided approach with LULC scenarios that met certain objectives: LULC distributions that maximized agricultural output, water quality, or biodiversity. With the 11 climate models and a "base" LULC, the first task produced 44 land and climate change scenarios. The ICRB's dominant LULC was agriculture, which was the primary culprit for poor water quality through fertilizer application and the subsequent runoff. SWAT's allows LULC update by modifying percent or fraction of land area an HRU occupies in a subbasin. The second task generalized the first by changing or updating the HRU fractions such that the basin-wide percent of agriculture LULC changed linearly. Each update was a SWAT scenario, creating $N \times$ 11 simulations with N changes to percent agricultural land. The dependent variables were stream

172

discharge and nitrate load. Because these scenarios required a complete representation of the ICRB, the SWAT simulations utilize the "full" model that did not lump small parcels, keeping all LULC and HRUS in the basin, regardless of their size. Agricultural land was defined as all LULC and their HRUs in SWAT that received fertilizer inputs, listed in Table 3-3 as corn, soybeans, lima beans, oats, peas, rye, sugarbeets, spring wheat, and winter wheat.

Methods

USACE Land Use Scenarios

The production of guided or objective based land use scenarios was a collaboration with the United States Army Corps of Engineers (USACE). The USACE adapted a rule-based GIS method from Nassauer et al. (2007) that addressed agricultural watersheds in Iowa. This method yielded three scenarios that (1) maximizes agricultural commodity production (AGRP), (2) improves water quality and reduces flooding (WATQ) and (3) enhances biodiversity (BIOD). The creation of these three scenarios required several data manipulation efforts drawn from the following geographical data: the 2006 National Land Cover Dataset (NLCD), the National Wetland Inventory (NWI), the National Hydrography Dataset (NHD), NAVTEQ company's physical infrastructure maps, the Protected Areas Database (PAD), and the U.S. soil survey geographic database (SSURGO).

The most important drivers for the USACE scenarios were the SSURGO and NLCD. The SSURGO dataset was not present in SWAT model development and the NLCD played a minor role in filling gaps in the LULC time series. The NLCD classes and the SWAT equivalent were found in Table 3-5 in Chapter 3. From the NLCD classes, the USACE implementation produced maps that consolidate previously sub-divided LULC into 9 general classes: water, urban, forest, range/grassland, pasture, agriculture, wetlands, riparia and bioreserves. Riparia and bioreserves were completely new LULC designations that had no clear SWAT equivalent. For implementation in SWAT simulations and land use update, the SWAT equivalent LULC for

173

bioreserve was Range-grass or RNGE and riparia was non-forested wetland or WETN. The rationale for designating bioreserves as generic grassland stemmed from Iowa's native, pre-development biome being mostly prairie grassland, and the riparia were generalized riparian buffer zones around streams adjacent to agricultural land. The SSURGO Non-Irrigated Capability Class (NICC) provided a starting point for designating land suitable for agricultural development. The classes described restrictions to cultivation based on soil productivity, erosion potential, and impact on native wildlife where Class 1 had fewest restrictions and Class 8 had the most. Table 7-2 summarizes these classes (USDA, 2002).

Along with the three scenarios, the USDA 2012 CDL and unmodified 2006 NLCD were the base scenarios. These two served as control scenarios: the CDL for the calibrated SWAT model and the NLCD because it was the base map for the USACE scenarios. Table 7-1 summarizes the LULC distribution for the scenarios. Figure 7-1 contains maps for the NLCD, AGRP, WATQ, and BIOD scenarios. Figure 3-8 in 2012 was the USDA CDL base scenario. The AGRP scenario replaced most pasture and grasslands with agriculture when compared to the NLCD in Figure 7-1a; however, the total agriculture land is 76.9 percent from 73 percent in the NLCD. This limited increase was due to the creation of bioreserves where the NLCD originally had none. The wide crop buffer zones in WATQ greatly reduced agricultural land in favor of a predominantly pasture watershed at 40 percent coverage in Figure 7-1c. The BIOD map in Figure 7-1d is a mix of WATQ and AGRP, adding pasture land and expanding bioreserves at the expense of agricultural land, but agriculture still had the highest coverage at 38 percent.

The USACE staff at Rock Island District deserve all credit for implementing the methodology described in this subsection to create the initial scenario maps before their processing to SWAT inputs (USACE, 2013). The following paragraphs summarize their work as well as describing how the scenario maps processed into SWAT inputs. Each scenario had a set of rules and assumptions that automated the map creation. The SWAT_2009LUC tool processed these USACE maps in the same manner as Chapter 3's *Land Use Update* subsection. The methods to analyze the stream discharge and nitrate load outputs for the USACE scenarios were

the same from Chapter 6: boxplots for visuals and the Mann-Whitney U-test for quantitative statistics.

AGRP

The AGRP scenario assumed that corn and soybeans were in continuous rotation, farms were less numerous but larger and highly industrialized, confined animal feeding operations (CAFO) replaced most grazing livestock, and cultivated land was only barred by steep slopes, public infrastructure, protected areas, and highly unproductive soils. The LULC conversion rules were that for NLCD cultivated or agricultural land, the SSURGO NICC 1-5 remained cultivated, Classes 6-7 became grasslands, and Class 8 changed to forests. For areas with steep slopes (>10% grade), the NICC 1-4 became pasture, 5-6 became grassland, and 7-8 became forests. The existing forests in the NLCD remained forest. A 10 meter buffer zone surrounded all streams, water bodies, and wetlands defined in the NHD and NWI; this buffer zone became the riparia LULC. The public lands in PAD became bioreserves. The developed areas in the NLCD became or remained the urban LULC and the wetlands from the NWI, NHD, and NLCD remained wetlands.

WATQ

The assumptions for WATQ included the dominance of pasture-based livestock production, corn and soybean rotations occured only on highly productive soils, and wide-spread adoption of riparian buffer zones on streams along with other water quality Best Management Practices (BMP). The rules followed a similar format as AGRP. NLCD cultivated land with NICC 1-3 remained cultivated, Classes 4-5 became pasture, Classes 6-7 became grassland, and Class 8 became forests. Steep slopes with NICC 1-4 became pasture, 5-6 became grassland, and 7-8 became forests. The existing forests in the NLCD remained forest. 30 meter buffer zone or riparia surrounded all streams, water bodies, and wetlands. Cultivated lands had a 200 m buffer zone whose LULC depend on the NICCC: 1-4 became pasture, 5-6 became grassland, and 7-8

175

became forests. The public lands in PAD became bioreserves. The developed areas in the NLCD became or remain urban LULC and the wetlands from the NWI, NHD, and NLCD remained wetlands.

BIOD

The assumptions for the BIOD scenario included the creation of bioreserves via purchase of unproductive lands, adoption of moderate riparian buffers and BMPs that connect to bioreserves, agricultural lands remained dominant enterprise in areas with productive soils and unhindered by steep slopes, and CAFOs replaced grazing livestock. New bioreserves were created through the following process: (1) consolidate PAD, public lands, riparian areas, and existing forest into bioreserves, (2) fragment those areas using roads, (3) eliminate the fragments' edges by 100 m and return the eedge area to the original LULC, (4) identify remaining "core" bioreserves whose area exceeded 12 acres, and (5) add 100 m edge to these core areas by reclassifying the boundary areas to bioreserve.

Again, the reclassification rules followed AGRP and WATQ in pattern. NLCD cultivated land with NICC 1-2 remained cultivated, Classes 3-4 became pasture, Classes 5-6 became grassland, and Class 7-8 became forests. Steep slopes with NICC 1-4 became pasture, 5-6 became grassland, and 7-8 became forests. The existing forests in the NLCD remained forest. 90 meter buffer zone or riparia surround all streams, water bodies, and wetlands. The public lands in PAD became bioreserves in addition to new bioreserves described above. The developed areas in the NLCD became or remained the urban LULC and the wetlands from the NWI, NHD, and NLCD remained wetlands.

Generalizing Agricultural LULC

The ICRB's dominant land use classes in NLCD were row crop agriculture thus the most change would come about by varying the total percent cover of agriculture over the basin. The goal was to create a series of LULC update files that changed total agricultural area by an equal

interval for each file. First, the LULC classes from Table 3-3 were separated into three groups: agricultural, non-agricultural, and static or constant HRUs. Constant LULC are the urban, barren, and water classes; their areas do not change in any of files. The agricultural lands were those HRUs that have fertilizer inputs, which included any LULC that were specific crops or were generic agriculture. The rest were non-agricultural, including pasture and alfalfa, because they did not have fertilizer inputs coded in the model. For each subbasin the agricultural HRUs' areas were adjusted by a factor x:

Equation 7-1 $$A^*_{sub,ag} = A_{sub,ag} \cdot (1 + x)$$

$A^*_{sub,ag}$ was the new area and $A_{sub,ag}$ was the original area of a given agricultural HRU using the USDA 2012 CDL as the reference.

A non-zero x adjustment factor would change the total area of all the HRUs once summed. This increase or decrease, depending on the x's sign, was offset by the non-agricultural lands:

Equation 7-2 $$A^*_{sub,nag} = A_{sub,nag} + \frac{A_{sub,nag}}{\sum A_{sub,nag}} \cdot \left(\sum A_{sub,ag} - \sum A^*_{sub,ag} \right)$$

$A^*_{sub,nag}$ was the new area and $A_{sub,nag}$ was the original area of a given non-agricultural HRU. Each non-agricultural HRU changed proportionally according to its original fraction with respect to the total non-agricultural land area. The second term on the right side of Equation 7-2 ensured that the offset gained or lost by the non-agricultural HRUs would result in the sum of all HRUs being equal to the subbasin area. For the simulations SWAT used the area fraction as the input and not the area itself:

Equation 7-3 $$f^*_{sub,LU} = \frac{A^*_{sub,LU}}{\sum A^*_{sub,nag} + \sum A^*_{sub,ag} + \sum A_{sub,const}}$$

$f^*_{sub,LU}$ was the new fraction of a given HRU. The area terms in the previous equations were actually the fraction of a given HRU multiplied with the area: $A_{HRU} = f_{HRU}A_{sub}$.

177

The values for the adjustment factor had the sequence $x \in [-0.90, -0.80, \ldots, 0.10, 0.20]$, excluding the base scenario zero. So, for example, at $x=-0.90$ the basin saw a 90 percent decrease in agricultural land from the 2012 CDL reference. 0.20 was the upper limit because any higher than a 20 percent increase, the total non-agricultural land area became negative. Spacing out x at 10 percent intervals yields 11 LULC $\times$ 11 climate models = 121 total scenarios for the 2041-2068 projected period. Due to the large number of simulations, the outputs were summarized to the mean of the entire period for each scenario. This generalization and modification of agricultural land area was exploratory in nature—the objective was to qualitatively assess the model's sensitivity to changes in HRU area among different climate change models.

Results and Discussion

USACE Land Use Scenarios

Figure 7-2 contains boxplots of the monthly stream discharge at the Wapello station for each LULC scenario, separated by season. Each box-and-whisker plot and their maximums covered the outputs from all NARCCAP models. The WATQ and BIOD scenarios showed a decrease in maximum discharges as well as decreases in medians for all seasons and models. BIOD had a less pronounced change relative to WATQ probably due to more cultivated land in the former. The USDA and NLCD distributions were similar to each other, but differ slightly in SON where NLCD reported a higher median. AGRP was also similar to the base scenarios, but had a lower maximum in all seasons. Although AGRP had slightly more agricultural land, the scenario also introduced the bioreserve and riparia LULC that did not exist in NLCD or USDA. Additionally, the USACE scenario generation procedure increased water area due to the spatial datasets the procedure used.

Table 7-3 summarizes the *p*-values for the Mann-Whitney U-test for stream discharge; specifically, if the median of a scenario is significantly different from a reference. The reference was the historical NARCCAP-driven simulated discharges for the USDA base scenario. Table

178

7-3 was organized by climate models by rows, LULC scenarios by columns, and seasons by quadrants. The USDA columns were the same from the "Projected" columns in Table 6-4. The colors and their shades were aids for finding trends in the numbers. A seasonal trend appeared in all scenarios where statistically significantly higher median discharges were in the DJF and SON months for all climate models. MAM had less agreement and JJA had mixed results where CRCMccsm reports statistically significantly lower median discharge. In the LULC axis, NLCD and AGRP were similar to each other, at least with respect to the historical NARCCAP. The WATQ scenarios resulted in a majority of models showing few significantly different medians from the historical. BIOD showed a similar effect on median discharges, but the effect was less pronounced in DJF and MAM. If one accepted that JJA and CRCMccsm were non-conclusive, the climate change signal appeared to overwhelm the land use scenarios designed to address impacts to water quantity from agriculture. That is, the LULC scenarios mitigated increases in discharge due to climate change, but did not reduce them. The differences in the median discharges between climate models in Figure 6-13 were greater than medians between the land use scenarios in Figure 7-2, suggesting that changes in climate model configurations would have greater influence than land use alone.

Figure 7-3 contains boxplots for monthly nitrate loads for the projected period by scenario. Here the differences between the USDA CDL map and NLCD-based maps were considerable. The USDA showed a maximum and median load exceeding all the other scenarios. The reason for this was likely due to the NLCD not having differentiated crops. The generic agricultural HRUs did not have the same calibration parameters as the corn and soybean HRUs in the USDA model. This decision to not include the crop-specific parameters was due to not knowing what the generic agricultural land is—applying crop-specific parameter edits to unknown LULC would bias the model results in an uncertain direction. A more conservative approach was to exclude the crop-specific parameters and simply have the USDA and NLCD results for comparison. NLCD and AGRP showed little difference, reflecting their comparable amount of agricultural land, but the median loads were higher than the historical medians.

179

WATQ scenario somewhat achieved its objective because the median load was right on the historical median and the maximum load was lower than AGRP or NLCD. BIOD's median and maximum were also lower than NLCD, but BIOD's median was higher than the historical. The boxplots indicated that despite the differences in results, the climate signal still showed with increased loads.

Table 7-4 shows the *p*-values for the Mann-Whitney U-test for each scenario and climate models. The USDA column contains the same values from Table 6-10. Here one sees that despite the overall similarities across all climate models in the boxplot, the NLCD-based scenarios were not comparable due to USDA and NLCD yielding different results. NLCD had mixed results for median loads with no model ensemble agreement whereas USDA had a majority of climate models showing increased loads. Despite the *p*-values not being very meaningful by themselves, they can still be a point of reference for the other scenarios. AGRP displays a similar behavior as NLCD in *p*-values while WATQ showed decreases in median loads across all the climate models. BIOD had a similar behavior to WATQ. Overall, the scenarios seem to be behaving as they were designed: reduced median discharges suggested fewer flood events and the reduction in agricultural land in BIOD and WATQ lowered nitrate loads.

Generalizing Agricultural LULC

Figure 7-4 shows the projected period mean annual stream discharge as a function of percent agricultural land area over the basin, separated into seasons. While slopes for individual climate models may be different, SWAT exhibited a positive linear response to discharge as agricultural land area changed. A seasonal difference appeared in overall slope magnitudes and inter-model variation. DJF typically had low discharge due to water locked in snow or ice and no crops were grown in winter. Thus changes to agricultural land area had little influence in the winter months. MAM also had a small vertical width between models, but changes in discharge scaled steeply with agricultural land. JJA had the greatest magnitude in inter-model variability

180

given the differences in slopes and intercepts for each of the lines. SON exhibited a similar

behavior to MAM and had a wide intercept range like JJA. Overall, when summarized as annual

means, SWAT's discharge increased linearly with agricultural land cover. This result likely came

from the curve number (CN) method for surface runoff being the predominant contributor to

discharge as well as how SWAT calculates the total discharge from an HRU. The CN stayed

constant for the agricultural lands and their HRUs, thus leading to a constant runoff per area

($Q_{surf} = mm \cdot ha^{-1}$) regardless of percent coverage. If the area changed linearly, then the total

contribution to discharge would increase linearly ($Q_{surf,tot} = A_{HRU} \times Q_{surf}$).

Figure 7-5 shows the mean annual nitrate loads at Wapello as a function of agricultural

land area. SWAT added fertilizer on a per area basis, similar to the surface runoff calculation in

discharge. Despite very low percentage of agricultural land, the nitrate loads never went to zero

as there were background sources of nitrogen as well as non-zero inputs from rainfall (wet and

dry nitrogen deposition). Nevertheless, load followed discharge and so the plots here were also

linear. To see how SWAT actually relates nitrate dynamics and agriculture, one should look at

the concentrations. Figure 7-6 shows the mean daily concentration at Wapello as a function of

agricultural land area. The different models all exhibited a similar behavior: a steeply linear trend

at agricultural land area above 30 percent and then a sharp drop in concentration below that

number. The lines also converged around 10-15 percent to a daily concentration slightly above 2

$mg \cdot L^{-1}$. One reason that could explain the sharp changes was the elimination of agriculture

altogether in subbasins with prominent non-agricultural HRUs. The difference between the

lowest and highest concentration was not great: 1.75 $mg \cdot L^{-1}$ and 3.75 $mg \cdot L^{-1}$, an increase of

about two-fold. These concentrations were low because they also included the non-growing

season when nitrogen levels were expected to be very low. For comparison, the observed mean

daily nitrate concentrations at Wapello for months excluding DJF was 4.26 $mg \cdot L^{-1}$ (Table 2-3).

The USACE scenarios proposed drastic changes to the ICRB; an Iowan landscape with cultivated land reduced to less than half of its current condition would be difficult to imagine. But the year 2068 is far into the future, and the changes wrought on the natural landscape over the last 200 years could very well change again in the same magnitude in the next century. Even with the large reduction in agriculture, the change in discharge and loads were modest, perhaps due to the climate change signal being greater than that of land use. Conclusions were difficult to draw for the USACE scenarios as the NLCD base and the calibrated model native USDA base yielded different distributions with the same climate inputs. While instructive the USACE scenarios cannot be fully incorporated into the existing calibrated SWAT model due to the NLCD creating a different HRU distribution than those for the USDA CDL. Despite this non-comparability, the USACE scenarios led to an observation that SWAT's discharge and nitrogen dynamics responded monotonically with agricultural land: as agriculture increased, so did discharge and nitrate. While agricultural land was the variable being modified, the actual culprit in increased nitrate was nitrogen fertilizer application whose inputs into the stream network increased proportionally to the HRU area.

The USACE scenarios themselves consisted of files that modify the existing model's HRU distribution. So when the files were modified directly and the agricultural land area coverage scaled at equal intervals, any decrease in nitrate from the basin or decrease in discharge was proportional to the agricultural land cover. In the case of stream discharge, the relationship was linear when averaged from three decades, but the slope displayed a definite seasonal variation, a variation likely explained by the input data. The linear response of nitrate load to percent change in agricultural land was similar to but weaker than Yaeger et al. (2014), whose SWAT model application and analysis showed a 1:1 correspondence between percent reduction in nitrate load and percent reduction in cropland or agriculture. Chapter 6 showed that summer months or JJA had the greatest variation between climate models—enough variation as to escape

a conclusion on whether discharge decreases or increases. This variation showed up again in Figure 7-4 with the wide range the minimum and maximum discharges take during JJA.

Nitrate concentration and agricultural land area had a more complex relationship. Spatial variability was not considered in this analysis like Ewing & Runck (2015) where the trade-off between water quality and crop yields in Iowa had differences between counties. Instead, the focus of the evaluation was concentration at the terminal gage station averaged decades. The data aggregation would obfuscate the relationship between local water quality and agriculture. Still, if one were to set all agricultural land area in the basin to zero, the nitrate concentrations would not drop to zero. Legacy nitrogen in the soil hard-coded as the initial soil organic nitrogen parameter (SOL_ORGN, Table 4-4), natural background cycling, and a non-zero wet deposition (RCN) would maintain a minimum nitrate export. Additionally, one must consider that these were model outputs from an autocalibration that generally under-predicted nitrate loads and concentration over a five year span. Between land use and climate change the latter had a greater impact, often muting extreme changes to the landscape. Nevertheless, to meaningfully simulate the impacts of LULC change, SWAT required more comprehensive management information or a method or model to dynamically produce the management information. Changing the inputs or modifying the HRU distribution yielded results that have a more exploratory research narrative, as opposed to a predictive one useful in policy and engineering.

183

Table 7-1   Land use class distribution (%) over ICRB with the USACE scenarios and the base NLCD map.

Land Use	NLCD Base	Agriculture	Biodiversity	Water Quality
Agriculture	73.0	76.9	38.0	28.4
Pasture	6.1	0.2	16.4	40.0
Range	5.6	0.3	0.9	1.5
Forest	3.4	3.0	1.7	3.3
Water	0.8	2.1	0.8	2.1
Wetlands	2.5	3.0	7.3	7.3
Urban	8.7	8.6	8.6	8.6
Bioreserve	0.0	5.0	18.8	8.1
Riparia	0.0	0.9	6.3	0.7

Table 7-2   SSURGO Non-Irrigated Class Definitions

Class	Description
1	Soils have slight limitations that restrict their use.
2	Soils have moderate limitations that reduce the choice of plants or require moderate conservation practices.
3	Soils have severe limitations that reduce the choice of plants or require special conservation practices, or both.
4	Soils have very severe limitations that restrict the choice of plants or require very careful management, or both.
5	Soils have little or no hazard of erosion but have other limitations, impractical to remove, that limit their use mainly to pasture, range, forestland, or wildlife food and cover.
6	Soils have severe limitations that make them generally unsuited to cultivation and that limit their use mainly to pasture, range, forestland, or wildlife food and cover.
7	Soils have very severe limitations that make them unsuited to cultivation and that restrict their use mainly to grazing, forestland, or wildlife.
8	Soils and miscellaneous areas have limitations that preclude their use for commercial plant production and limit their use to recreation, wildlife, or water supply or for esthetic purposes.

184

Table 7-3   Stream discharge Mann-Whitney U-test *p*-values for climate and land use change scenarios with historical NARCCAP-driven discharge as reference. Shades of orange indicate medians statistically significantly less than historical climate model and shades of blue indicate greater.

	USDA	NLCD	AGRP	WATQ	BIOD	USDA	NLCD	AGRP	WATQ	BIOD
			DJF					MAM		
CRCMccsm	0.37	0.13	0.24	0.34	0.22	<0.01	<0.01	<0.01	0.16	0.02
CRCMcgcm3	0.02	<0.01	<0.01	0.06	0.01	0.27	0.13	0.18	0.66	0.73
ECP2gfdl	0.08	<0.01	0.02	0.17	0.08	0.56	0.34	0.46	0.37	0.79
HRM3gfdl	<0.01	<0.01	<0.01	0.08	0.01	0.71	0.57	0.72	0.21	0.57
HRM3hadcm3	<0.01	<0.01	<0.01	<0.01	<0.01	0.13	0.08	0.15	0.79	0.46
MM5Iccsm	0.72	0.63	0.80	0.51	0.77	0.21	0.13	0.18	0.36	0.97
MM5Ihadcm3	0.29	0.61	0.44	0.17	0.33	0.84	0.63	0.78	0.16	0.46
RCM3cgcm3	0.14	0.01	0.02	0.27	0.12	0.08	0.02	0.06	0.97	0.44
RCM3gfdl	0.02	<0.01	<0.01	0.08	0.02	<0.01	<0.01	<0.01	0.06	<0.01
WRFGccsm	0.70	0.91	0.98	0.40	0.71	<0.01	<0.01	<0.01	0.33	0.09
WRFGcgcm3	<0.01	<0.01	<0.01	<0.01	<0.01	0.02	0.01	0.05	0.93	0.41
			JJA					SON		
CRCMccsm	<0.01	<0.01	<0.01	<0.01	<0.01	<0.01	<0.01	<0.01	0.02	<0.01
CRCMcgcm3	0.64	0.35	0.44	0.66	0.57	0.98	0.32	0.33	0.12	0.61
ECP2gfdl	0.44	0.17	0.24	0.90	0.60	0.01	<0.01	<0.01	0.26	0.02
HRM3gfdl	0.33	0.67	0.56	0.18	0.33	0.07	<0.01	<0.01	0.96	0.24
HRM3hadcm3	0.94	0.51	0.63	0.81	0.97	<0.01	<0.01	<0.01	<0.01	<0.01
MM5Iccsm	0.75	0.37	0.47	0.93	0.82	<0.01	<0.01	<0.01	0.02	<0.01
MM5Ihadcm3	0.39	0.75	0.62	0.20	0.34	0.08	0.01	0.01	0.84	0.22
RCM3cgcm3	<0.01	<0.01	<0.01	0.02	0.01	0.15	0.01	0.01	0.90	0.30
RCM3gfdl	0.02	<0.01	<0.01	0.19	0.08	<0.01	<0.01	<0.01	0.07	<0.01
WRFGccsm	0.17	0.27	0.24	0.09	0.13	0.02	<0.01	<0.01	0.52	0.12
WRFGcgcm3	0.02	<0.01	<0.01	0.07	0.02	<0.01	<0.01	<0.01	0.09	<0.01

185

Table 7-4   Nitrate load Mann-Whitney U-test p-values for climate and land use change scenarios with historical NARCCAP-driven discharge as reference. Shades of orange indicate medians statistically significantly less than historical climate model and shades of blue indicate greater

	USDA	NLCD	AGRP	WATQ	BIOD
CRCMccsm	0.26	0.01	<0.01	<0.01	<0.01
CRCMcgcm3	0.38	0.10	0.03	<0.01	<0.01
ECP2gfdl	<0.01	0.66	0.55	<0.01	<0.01
HRM3gfdl	0.38	0.04	0.03	<0.01	<0.01
HRM3hadcm3	<0.01	0.44	0.58	<0.01	0.02
MM5Iccsm	<0.01	0.78	0.59	<0.01	<0.01
MM5Ihadcm3	0.20	0.01	<0.01	<0.01	<0.01
RCM3cgcm3	<0.01	0.60	0.79	<0.01	0.01
RCM3gfdl	<0.01	0.01	0.03	<0.01	0.58
WRFGccsm	0.13	0.21	0.14	<0.01	<0.01
WRFGcgcm3	<0.01	0.04	0.15	<0.01	0.35
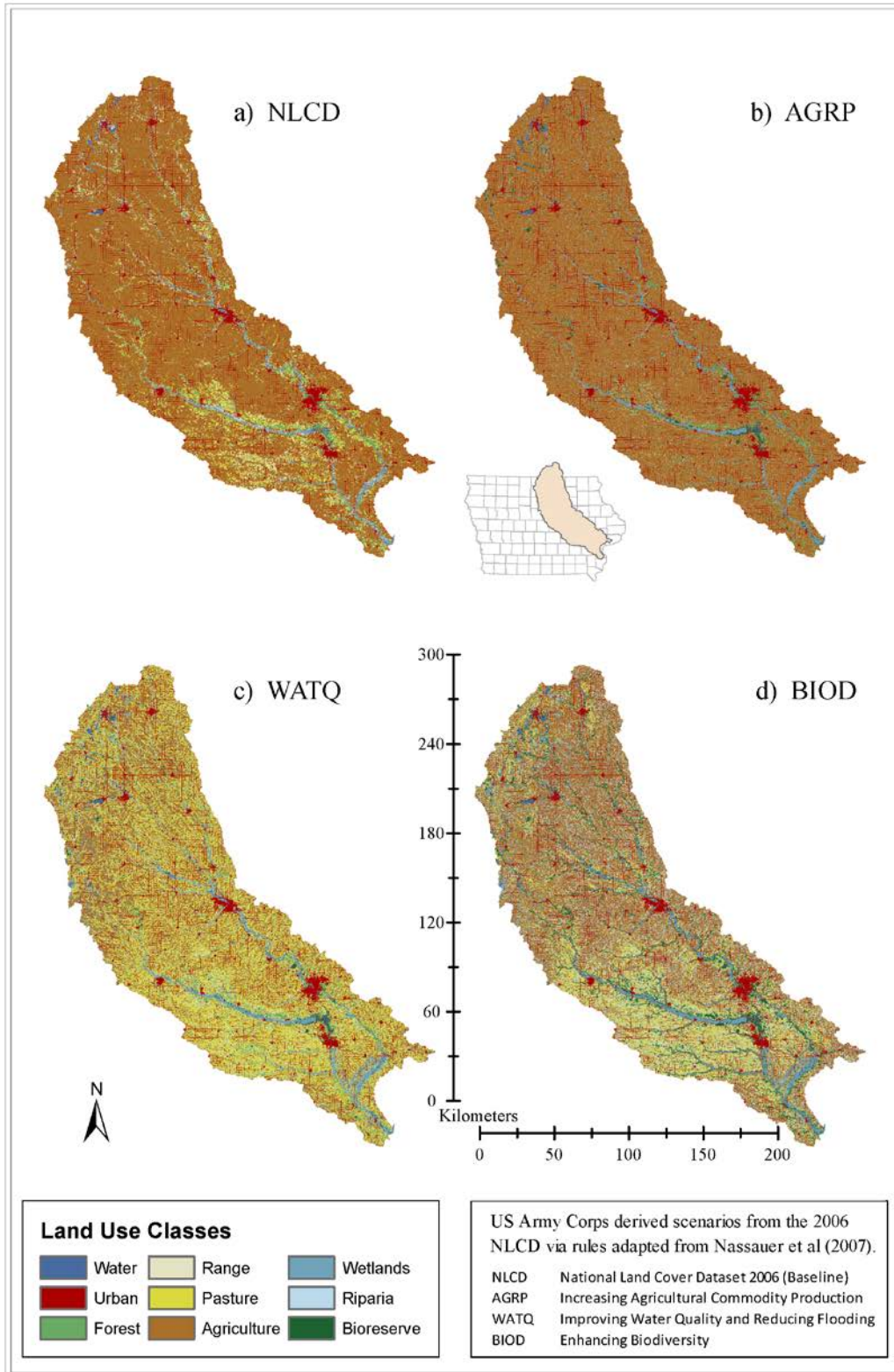
Figure 7-1   LULC scenarios generated by the U.S. Army Corps of Engineers
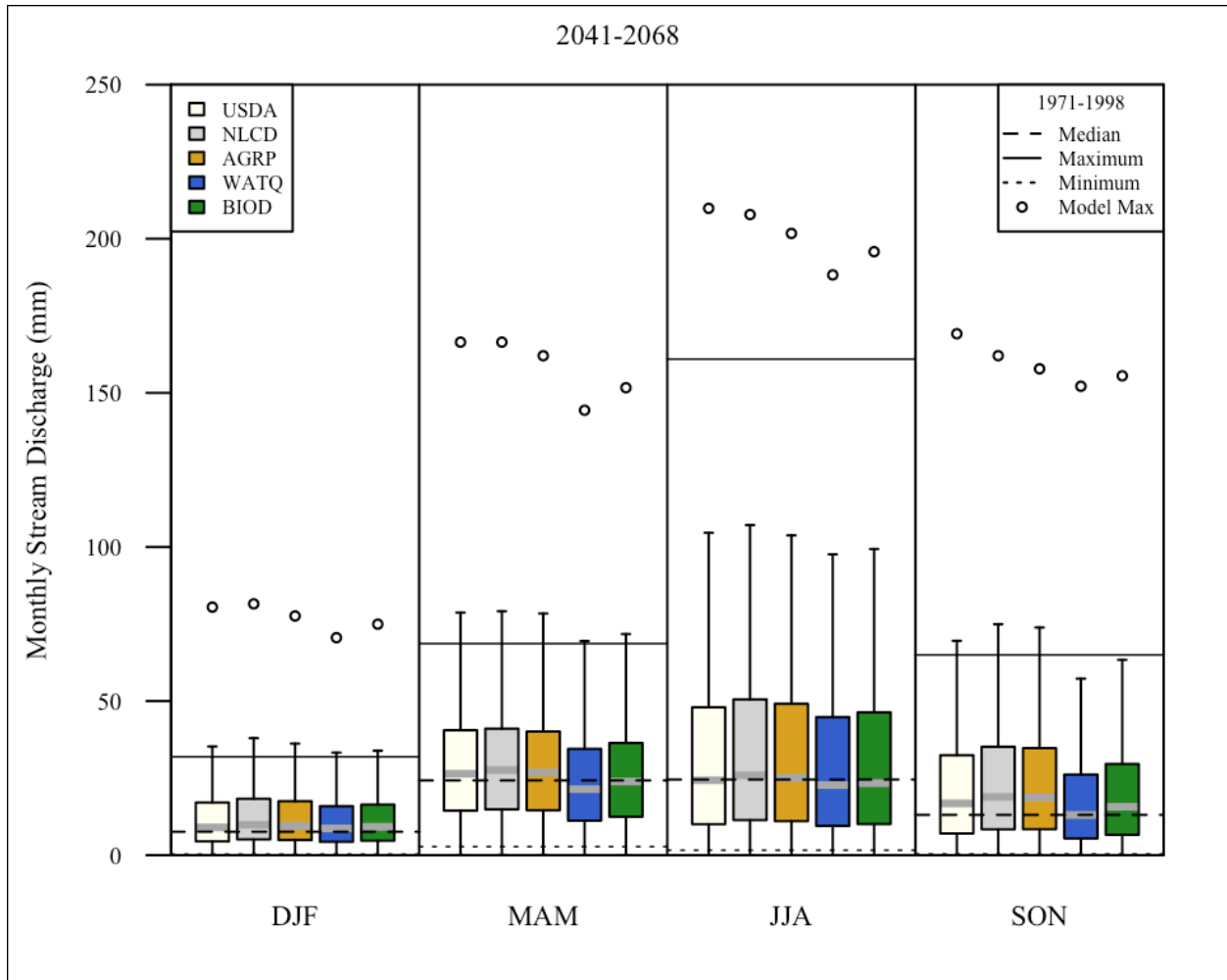
Figure 7-2   Boxplots of monthly stream discharge by season for the LULC scenarios and two base scenarios covering the projected 2041-2068 period. Each boxplot contains outputs from all 11 NARCCAP climate change models
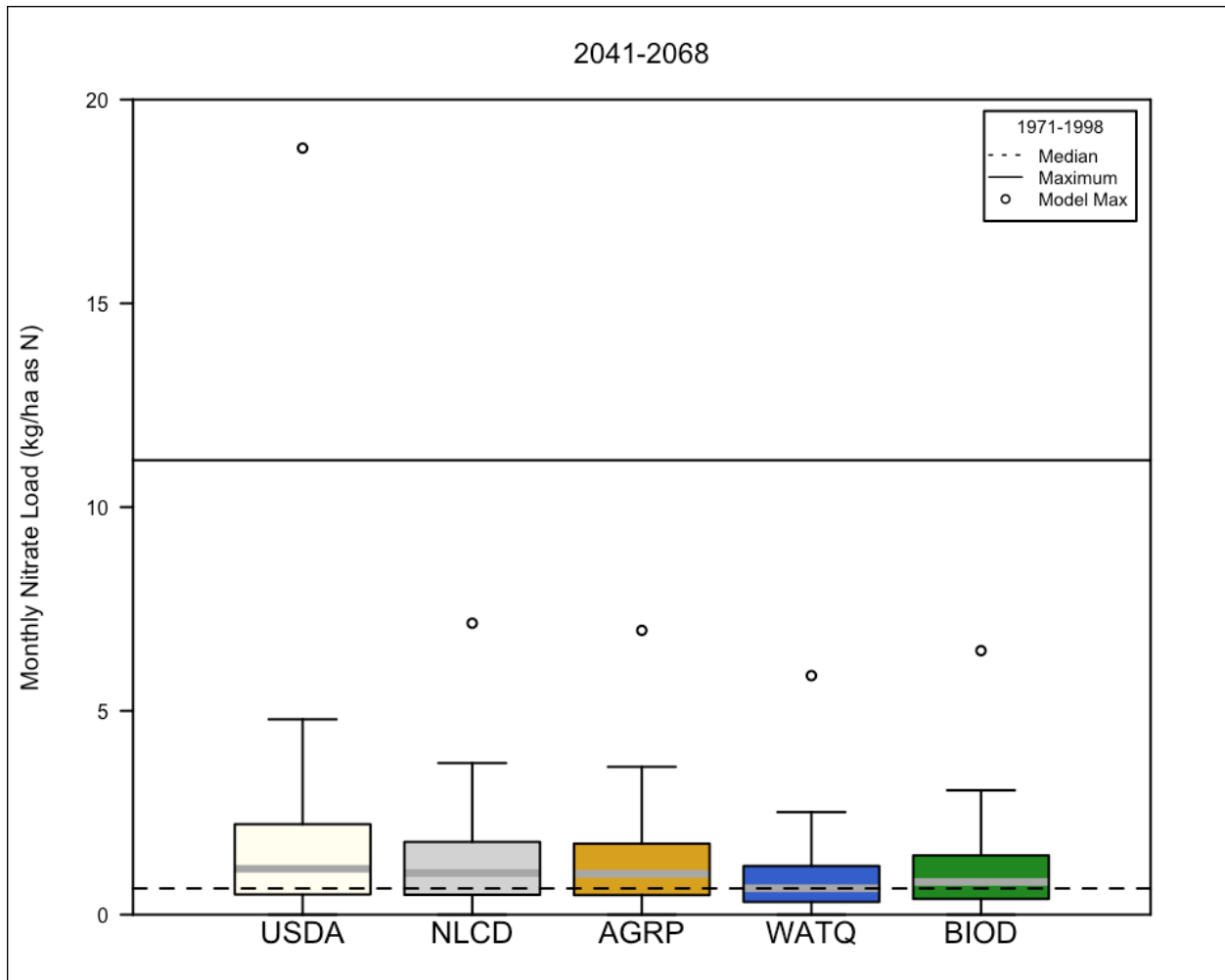
Figure 7-3   Boxplots of monthly nitrate loads for the LULC scenarios and two base scenarios
              covering the projected 2041-2068 period. Each boxplot contains outputs from all
              11 NARCCAP climate change models.
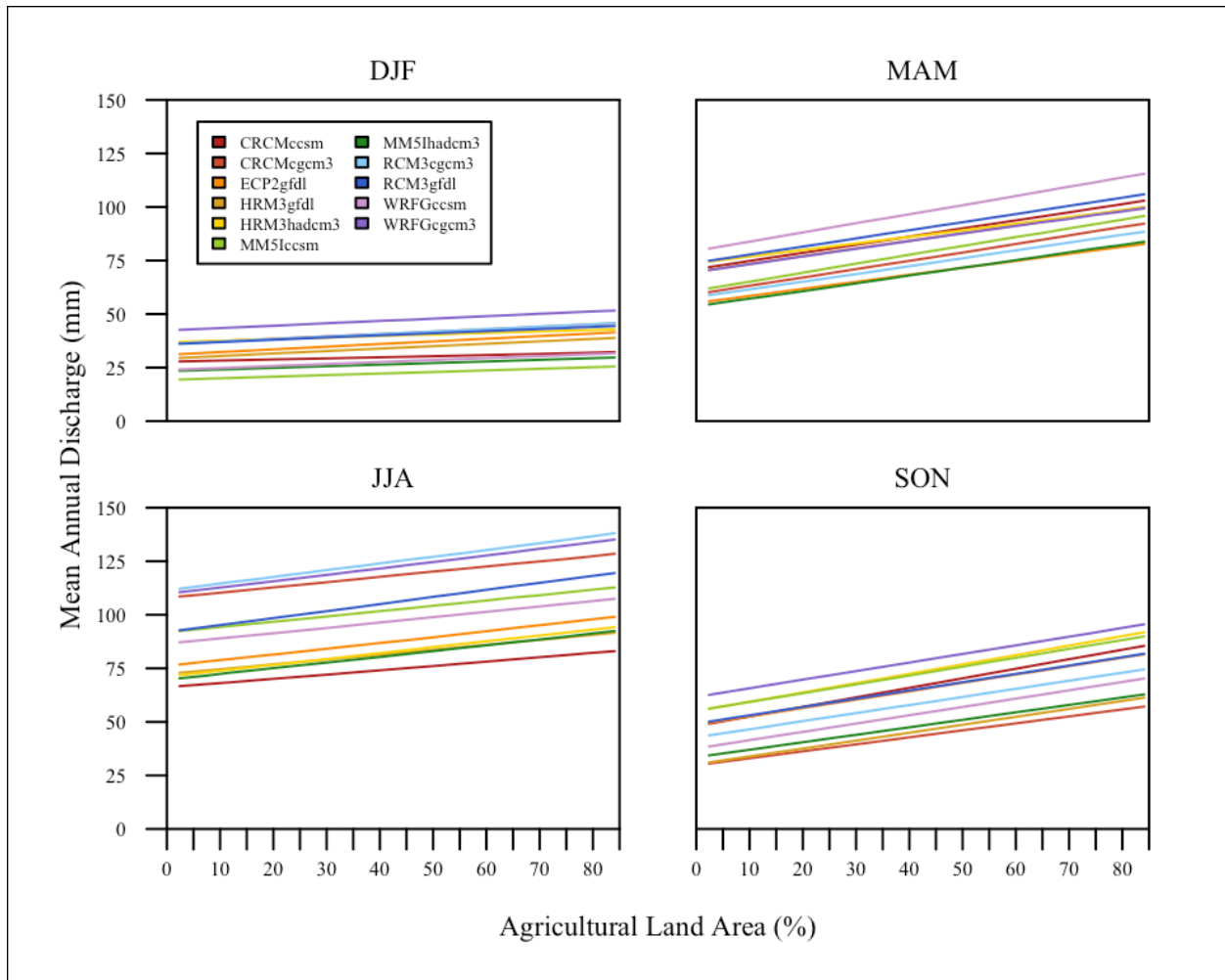
Figure 7-4   NARCCAP driven SWAT simulated mean annual discharge versus total percent agricultural land in the basin partitioned into seasons for projected period 2041-2068

190
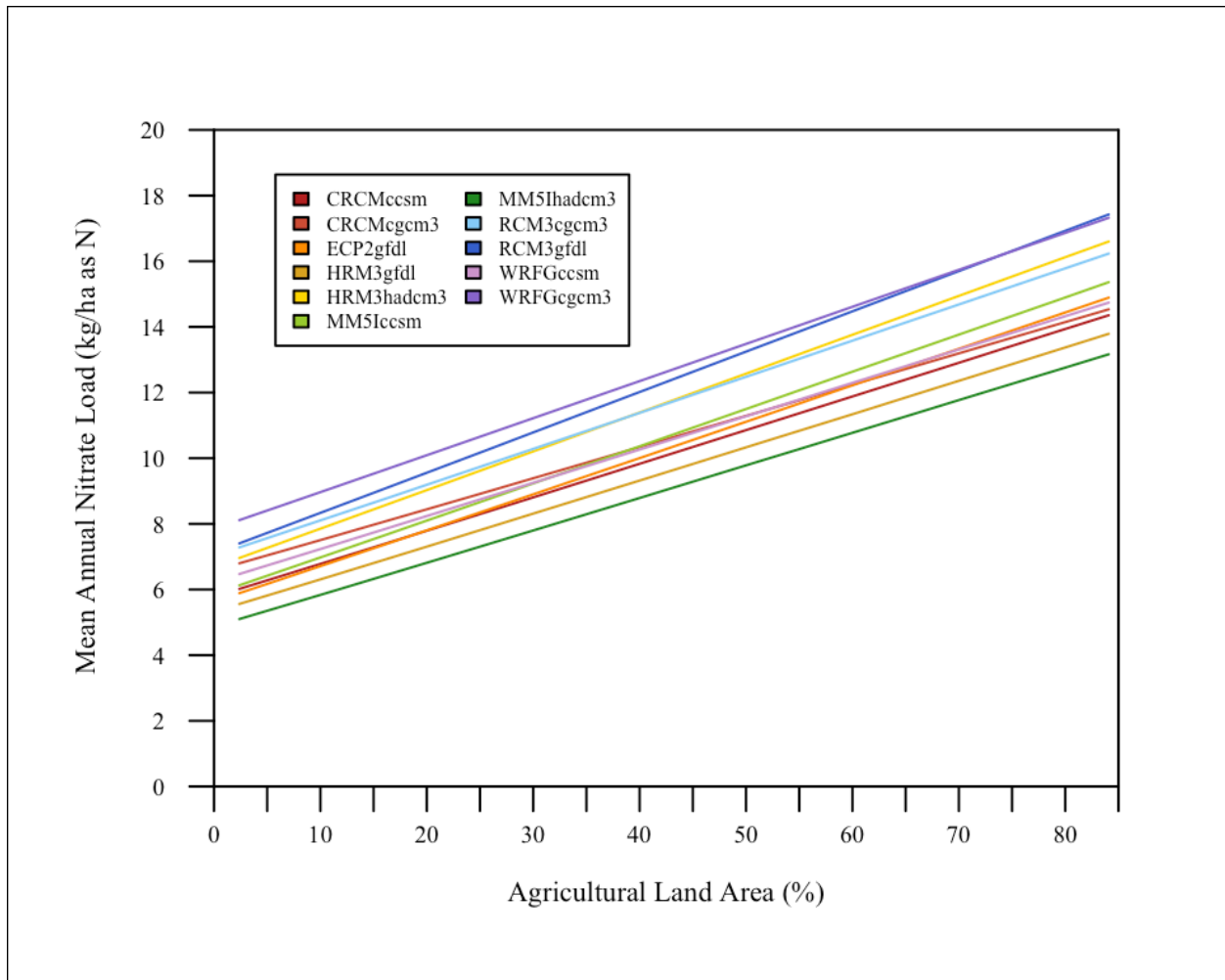
Figure 7-5   NARCCAP driven SWAT simulated mean annual nitrate as a function of total percent agricultural land in the basin for projected period 2041-2068
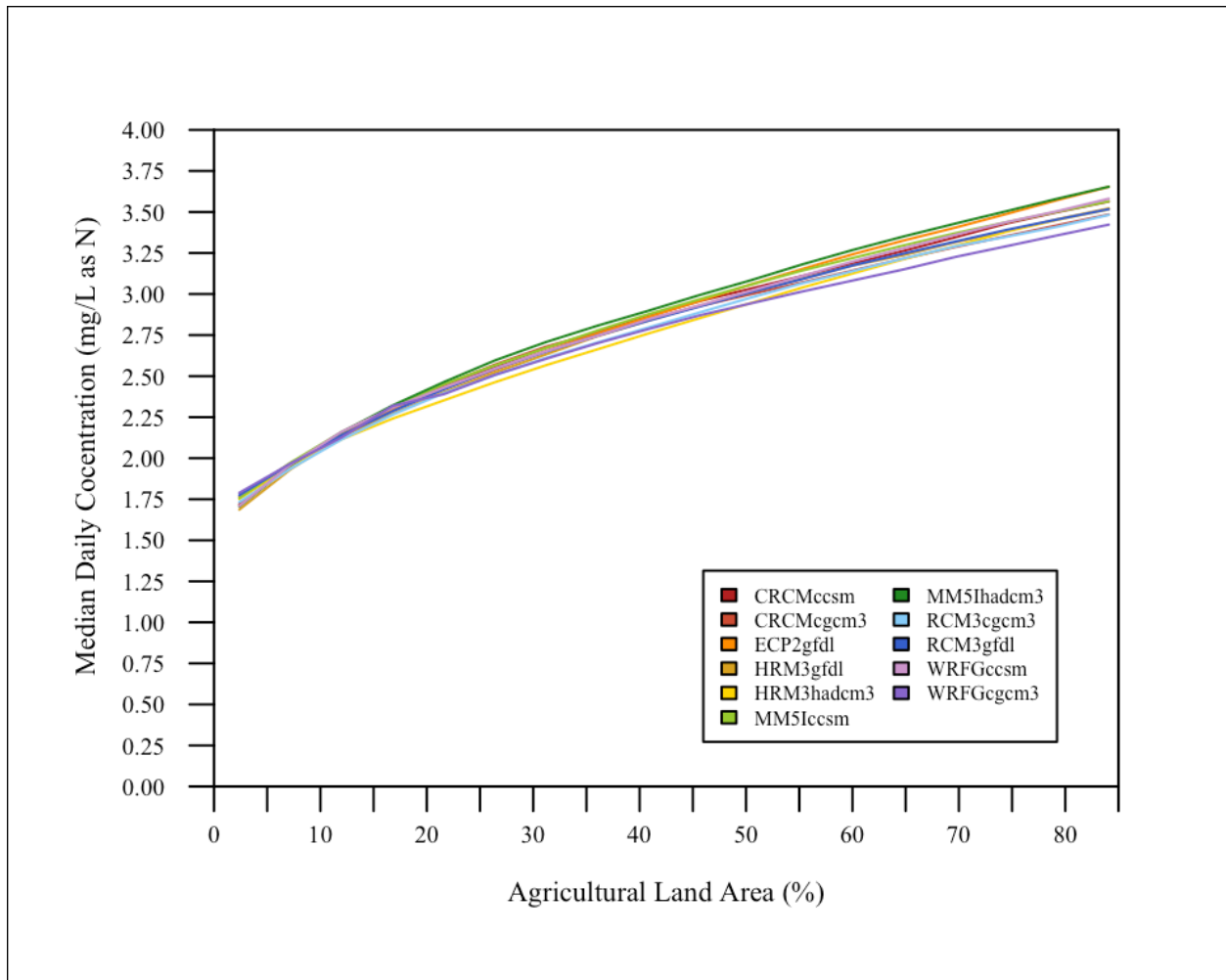
Figure 7-6   NARCCAP driven SWAT simulated mean daily nitrate concentration as a
function of total percent agricultural land in the basin for projected period 2041-
2068

192

CHAPTER 8: SUMMARY OF FINDINGS

To conclude this dissertation, the summary of findings is organized by the research questions and objectives listed at the beginning in Chapter 1:

(1)   For stream discharge and nitrate load, SWAT was an appropriate watershed model for the simulation of large spatial (HUC-4) and temporal (20+ years) domains which provided simulation results within accepted statistical criteria. As nitrate load is a function of stream discharge, one must also be able to simulate nitrate concentration (H1c) to gage the model's performance. SWAT did not simulate nitrogen as effectively, but the poorer performance seen for this parameter may be due to uncertainty in the input data rather than anything inherent in SWAT's theoretical basis or software implementation. Despite not meeting the literature goodness of fit criteria (NSE > 0.50), the nitrate concentration simulations successfully reproduced spikes seen in the observed time series.

(2)   The artificial neural network (ANN) used temperature, time, and simulated discharge as inputs in a weak coupling to attempt simulating nitrate concentrations, for which this particular SWAT model failed to achieve the necessary statistics. The ANN-SWAT coupling resulted in improved statistics for nitrate concentrations, exceeding that of literature values (NSE > 0.60). On inspection of the time-series, the coupling failed where SWAT succeeds and vice versa. That is, the calibrated SWAT model did not produce nitrate concentrations observed during the low flow periods in 2012, but the ANN could. The ANN, in turn, did not simulate the high concentrations during 2013 as well (or at all) in the case of Wapello.

(3)   For climate change modeling and projections, multiple models were utilized for assessment. The NARCCAP model ensemble passed the first test where the historical

period (1971-1998) was simulated and compared to the outputs from the calibrated model using observed climate data. The NARCCAP-driven precipitation, discharge, evapotranspiration, and nitrate loads showed no statistically significant difference from the model calibration. When applied to the projected time period (2041-2068), the model ensemble agreement depended on the season and on output variables. Projected monthly cumulative precipitation showed agreement on an increase except for June-July where the ensemble showed mixed results. Monthly mean discharges projections showed similar results. Projected monthly cumulative evapotranspiration values increased largely in Dec-Feb, and while agreement occurred for the other seasons, the differences were not large. The ensemble NARCCAP-driven SWAT model projections showed an agreement on projected nitrate loads which increased relative to the historical simulation.

(4)   Land use (LULC) change is a complex phenomenon for which SWAT was one piece. To accurately simulate the impacts, one must include other models. The impetus for this LULC investigation started with scenarios generated by the U.S. Army Corps of Engineers (USACE). The USACE scenarios yielded model results consistent with their objectives; e.g. the water quality and biodiversity scenarios reduced median flows and nitrate loads whereas in the agriculture scenario they increased. When translated to SWAT the scenarios were changes to the LULC distributions in the input data. Scenarios ranging from 20-90 percent of land in row-crop agriculture yielded a linear and increasing trend for discharge and nitrate loads. Nitrate concentrations behaved with more complexity and were only linear when agricultural land cover was greater than 30 percent.

<u>Further Research</u>

The issues with nitrate concentration as simulated by SWAT alone can be further explored if SWAT was allowed to run on high-performance computing platforms, because then

194

the limitation of having only so many subbasins or so many HRUs would not be an issue. For such a large basin, having only 67 computational elements for in-stream nitrogen cycling predictably leads to poor in-stream nitrogen concentration results. On the other hand, the ANN-SWAT approach could be reworked to use different ANN architectures. The architecture used in this dissertation is reliable but quite rudimentary. Modern methods for ANN are more involved and may yield better results. The number of NARCCAP models have only increased since the start of the climate change simulations. The limitation of 11 GCM-RCM was convenient because they were all available at the time. But if model ensembles are better for predicting the future, a chorus would only be an improvement. The LULC change methods could use some modeling themselves. Techniques such as agent-based modeling explicitly defines owners of land parcels and simulates their decision-making process. Dynamic simulation of LULC change versus static scenarios would expand on SWAT's utility.

Publication Potential

At the moment of this dissertation's submission, one manuscript is in progress for submission to a peer-review journal with the *Journal of Hydrology* as the target. The content of the manuscript is from Objective (3) of Chapter 6 of this dissertation. Chapter 6 was from a collaboration with William Gutowski and Sho Kawazoe of Iowa State University. The results from that chapter were indebted to their work on bias-correction and preparation of NARCCAP outputs for hydrological simulation. Given the number of climate models, figures, and methods of analysis, Chapter 6 is a novel and substantive submission for publication.

At least two methodology-related publications may result from this dissertation. First, Chapter 3 and Chapter 4 detailed the model development and calibration using a novel calibration technique combining SWAT-CUP, SUFI2, and GAM. While model development cycles logically separate sensitivity and calibration, an automation of both may hasten calibration as well as ensure the process is comprehensive, including all parameters at the start. Consolidated into a software library for R, the programming language of choice, this combined

autocalibration and sensitivity method is a good candidate of publication. Second, the use of artificial neural networks is not uncommon in hydrological research, but directly coupling them with physically-based models—in particular SWAT—is not commonly done. The results from Chapter 5 showed promise in the improved statistics and be viable for publication.

The last topic in land use change ends on an exploratory note. The future of this SWAT model lies in sharing it with other researchers. The tools and methods described in this dissertation do not fully address LULC change. While accurate maps of land cover exist, the actual land management practices would give a more complete picture of land use. The dissertation draws special attention to projections of climate change, collaboration and extension of scenarios for LULC change are important undertakings for understanding and predicting the future of the Iowa-Cedar River Basin.

Table A-1   Subbasin and channel dimensions

Subbasin	Subbasin Dimension			Channel Dimensions (m)		
	Absolute Area (km^2)	Drainage Area (km^2)	Mean Elevation (m)	Length	Width	Depth
1	395.8	395.8	377.6	19.4	46.7	1.4
2	640.7	640.7	390.0	16.7	62.3	1.7
3	371.4	1408.0	379.9	22.1	99.9	2.4
4	755.1	755.1	382.8	25.5	68.8	1.8
5	685.7	2093.7	369.1	19.9	126.8	2.8
6	595.4	595.4	384.8	17.6	59.6	1.7
7	147.5	2241.2	354.6	29.1	132.1	2.8
8	738.1	1333.5	371.2	50.8	96.7	2.3
9	539.5	2780.7	343.5	29.1	150.3	3.1
10	392.8	1726.3	354.4	32.8	112.9	2.6
11	597.5	1352.7	361.9	62.2	97.6	2.3
12	147.2	2927.9	317.9	65.8	72.0	1.9
13	815.1	815.1	362.2	17.3	45.7	1.4
14	382.0	382.0	375.3	26.5	54.4	1.6
15	511.4	511.4	375.2	41.6	177.6	3.5
16	593.4	3672.3	323.7	11.5	46.4	1.4
17	392.3	392.3	328.6	15.8	85.4	2.1
18	189.1	1082.5	369.6	41.3	73.5	1.9
19	843.5	843.5	352.1	19.1	52.5	1.5
20	482.1	482.1	355.0	7.3	104.2	2.4
21	184.2	1509.8	316.6	7.0	43.3	1.4
22	349.4	349.4	350.1	44.0	201.1	3.8
23	450.3	4514.9	300.3	62.2	196.9	3.7
24	422.7	6796.8	295.6	3.2	45.4	1.4
25	615.9	4358.9	302.7	37.2	82.6	2.1
26	377.5	377.5	334.5	18.0	75.4	2.0
27	648.1	1025.6	308.2	34.1	394.1	5.9
28	213.3	12394.6	276.9	22.7	69.8	1.9
29	105.7	879.4	278.1	18.4	58.6	1.7
30	583.4	13857.4	275.0	9.1	71.1	1.9
31	773.7	773.7	306.0	53.5	73.9	1.9
32	579.0	579.0	349.7	31.7	422.2	6.2
33	220.0	799.0	331.2	25.0	168.3	3.3

Table A-1   Subbasin and channel dimensions (continued)

Subbasin	Subbasin Dimension			Channel Dimensions (m)		
	Absolute Area (km^2)	Drainage Area (km^2)	Mean Elevation (m)	Length	Width	Depth
34	936.3	2018.7	353.8	12.0	48.2	1.5
35	850.7	850.7	299.3	38.4	432.0	6.3
36	835.2	15543.4	274.3	17.0	185.9	3.6
37	539.9	3357.6	316.3	11.0	194.4	3.7
38	417.6	417.6	325.7	0.2	42.3	1.3
39	603.0	16146.4	263.7	23.7	443.0	6.4
40	186.3	3961.6	293.9	33.4	57.1	1.6
41	305.9	4267.5	300.2	27.0	58.3	1.6
42	336.4	336.4	300.2	66.5	227.1	4.1
43	694.3	16840.7	259.4	21.2	155.1	3.2
44	553.5	553.5	263.8	49.4	257.0	4.4
45	573.6	573.6	280.6	24.9	368.6	5.6
46	927.0	5530.9	281.3	118.4	124.1	2.7
47	782.8	18177.1	254.8	36.0	463.8	6.6
48	548.3	6652.8	265.1	25.6	311.2	5.0
49	292.2	7516.7	244.5	34.2	648.5	8.2
50	571.7	571.7	276.8	27.6	253.7	4.4
51	936.1	8452.8	237.6	31.0	273.0	4.6
52	520.0	520.0	242.3	31.3	58.2	1.6
53	614.5	18791.6	236.0	45.8	292.9	4.8
54	576.6	576.6	228.4	18.9	55.0	1.6
55	166.5	8619.4	211.1	53.7	473.1	6.7
56	820.9	820.9	261.5	4.5	58.5	1.7
57	210.2	9349.5	213.3	19.1	296.4	4.9
58	330.7	330.7	256.3	35.8	72.3	1.9
59	496.9	1648.5	225.3	3.6	41.9	1.3
60	420.1	420.1	217.5	54.1	109.9	2.5
61	276.2	19644.4	204.2	8.0	48.4	1.5
62	102.4	11100.4	215.2	24.8	485.9	6.8
63	412.6	11513.0	204.6	9.2	345.0	5.4
64	206.7	31784.2	194.4	28.7	352.6	5.5
65	402.1	402.1	216.7	20.9	47.1	1.4
66	147.5	32333.7	193.6	12.3	655.2	8.3
67	332.4	32666.2	200.3	28.8	659.2	8.3

Table A-2   Comparisons between GCMs used in this thesis; adapted from Mearns et al. (2014)

Model	Resolution (Vertical Layers) Surface	Ocean	Highest Layer Pressure (Pa)	Land Soil
CCSM	$1.4° \times 1.4°$ (26)	$0.3° - 1.0°$ (40)	220	Layers
CGCM3	$1.9° \times 1.9°$ (31)	$0.9° \times 1.4°$ (29)	100	Layers
GFDL	$2.0° \times 2.5°$ (varies)	$0.3° - 1.0°$ (varies)	300	Bucket
HadCM3	$2.5° \times 3.75°$ (19)	$1.25° \times 1.25°$ (20)	500	Layers

Table A-3   Comparisons between RCMs used in this thesis; adapted from Mearns et al. (2014)*

Model	CRCM	ECP2	HRM3	MM5I	RCM3	WRFG
Resolution**	160×135	193×152	171×146	154×129	160×130	155×130
Vertical Layers	29	28	19	23	18	35
Time Step	900 s	100 s	300 s	120 s	150 s	150 s
Vegetation Classes	21	13	53	16	19	24

**Units units depend on the geographic coverage of the regional model

REFERENCES

Abbaspour, K. C., Johnson, C. A., & Van Genuchten, M. T. (2004). Estimating uncertain flow and transport parameters using a sequential uncertainty fitting procedure. *Vadose Zone Journal*, *3*(4), 1340-1352.

Abbaspour, K. C. (2005). Calibration of hydrologic models: when is a model calibrated? In Zerger, A. and Argent, R.M. (Eds), *MODSIM 2005 International Congress on Modelling and Simulation*. Modelling and Simulation Society of Australia and New Zealand. Retrieved from < http://www.mssanz.org.au/modsim05/papers/abbaspour.pdf>

Abbaspour, K. C., Vejdani, M., & Haghighat, S. (2007a). SWAT-CUP calibration and uncertainty programs for SWAT. In In Oxley, L. and Kulasiri, D. (Eds.) *MODSIM 2007 International Congress on Modelling and Simulation.* Modelling and Simulation Society of Australia and New Zealand. Retrieved from <http://www.mssanz.org.au/MODSIM07/papers/24_s17/SWAT-CUP_s17_Abbaspour_.pdf>

Abbaspour, K. C., Yang, J., Maximov, I., Siber, R., Bogner, K., Mieleitner, J., ... & Srinivasan, R. (2007b). Modelling hydrology and water quality in the pre-alpine/alpine Thur watershed using SWAT. *Journal of Hydrology*, *333*(2), 413-430.

Arnold, J. G., Allen, P. M., & Bernhardt, G. (1993). A comprehensive surface-groundwater flow model. *Journal of Hydrology*, *142*(1), 47-69.

Arnold, J.G., Srinivasan, R., Muttiah, R.S., & Williams, J.R. (1998). Large area hydrologic modeling and assessment—Part 1: Model development. *Journal of American Water Resources Association*, *34*(1), 73–89.

Beven, K. (1989). Changing ideas in hydrology—the case of physically-based models. *Journal of Hydrology*, *105*(1), 157-172.

Bogue, A. G. (1994). *From prairie to corn belt: farming on the Illinois and Iowa prairies in the nineteenth century*. Chicago, IL: University of Chicago Press.

Brown, L.C. & Barnwell, T.O. Jr. (1987). *The enhanced water quality models QUAL2E and QUAL2E-UNCAS documentation and user manual.* (EPA document EPA/600/3-87-007). Washington, DC: U.S. Environmental Protection Agency, Office of Research and Development, Environmental Research Laboratory. Retrieved from <nepis.epa.gov/Exe/ZyPURL.cgi?Dockey=30000KGT.TXT>

Chapra, S.C., Pelletier, G.J., & Tao, H. (2006) *QUAL2K: A Modeling Framework for Simulating River and Stream Water Quality, Version 2.04: Documentation and User's Manual*. Medford, OR: Department of Civil and Environmental Engineering, Tufts University.

Chattopadhyay, S., & Jha, M. K. (2014). Climate change impact assessment on watershed hydrology: A comparison of three approaches. *American Journal of Engineering and Applied Sciences*, *7*(1), 118.

Cheng, P. E. (1994). Nonparametric estimation of mean functionals with data missing at random. *Journal of the American Statistical Association*, *89*(425), 81-87.

Claussen, M., Ganopolski, A., Schellnhuber, J., & Cramer, W. (2000). Earth system models of intermediate complexity. *Global Change Newsletter*, *41*, 4-6.

Cohn, T. A., Delong, L. L., Gilroy, E. J., Hirsch, R. M., & Wells, D. K. (1989). Estimating constituent loads. *Water Resources Research*, *25*(5), 937-942.

Cohn, T.A., Caulder, D.L., Gilroy, E.J., Zynjuk, L.D. & Summers, R.M. (1992). The validity of a simple statistical model for estimating fluvial constituent loads—an empirical study involving nutrient loads entering Chesapeake Bay. *Water Resources Research, 28*(9), 2353–2363.

Cole, C. (1921). *A History of the People of Iowa*. Cedar Rapids, IA: Torch Press.

Collins, W. D., Bitz, C. M., Blackmon, M. L., Bonan, G. B., Bretherton, C. S., Carton, J. A., ... & Smith, R. D. (2006). The community climate system model version 3 (CCSM3*). Journal of Climate*, *19*(11), 2122-2143.

Corke, P., Wark, T., Jurdak, R., Hu, W., Valencia, P., & Moore, D. (2010). Environmental wireless sensor networks. *Proceedings of the IEEE*, *98*(11), 1903-1917. Retrieved from <http://www.jurdak.com/PIEEE10.pdf>.

Cotter, A. S., Chaubey, I., Costello, T. A., Soerens, T. S., & Nelson, M. A. (2003). Water quality model output uncertainty affected by spatial resolution of input data. *Journal of the American Water Resources Association*, *39*(4), 977-986.

Cukier, R. I., Levine, H. B., & Shuler, K. E. (1978). Nonlinear sensitivity analysis of multiparameter model systems. *Journal of Computational Physics*, *26*(1), 1-42.

Ding, D., Bennett, D., & Secchi, S. (2014). Investigating impacts of alternative crop market scenarios on land use change with an agent-based model. *Land, 3*(1), 33.

Douglas-Mankin, K. R., Srinivasan, R., & Arnold, J. G. (2010). Soil and Water Assessment Tool (SWAT) model: Current developments and applications. *Transactions of the ASABE*, *53*(5), 1423-1431.

Edwards, P.N. (2001). A brief history of atmospheric general circulation modeling. In Randall, D.A. (Eds). *General Circulation Model Development, Past Present and Future: The Proceedings of a Symposium in Honor of Akio Arakawa* (67-9). New York, NY: Academic Press.

Ewing, P. M., & Runck, B. C. (2015). Optimizing nitrogen rates in the midwestern United States for maximum ecosystem value. *Ecology and Society*, *20*(1), 18.

Ferraro, R., Sato, T., Brasseur, G., Deluca, C., & Guilyardi, E. (2003). Modeling the Earth system. Critical computational technologies that enable us to predict our planet's future. In *Geoscience and Remote Sensing Symposium, 2003. Proceedings. 2003 IEEE International, 1*, 630-633.

Flato, G. M., (2005). *The third generation coupled global climate model (CGCM3)*. Retrieved from <http://www.ec.gc.ca/ccmac-cccma/default.asp?n=1299529F-1>.

Foster, D., Swanson, F., Aber, J., Burke, I., Brokaw, N., Tilman, D., & Knapp, A. (2003). The importance of land-use legacies to ecology and conservation. *BioScience*, *53*(1), 77-88.

Fry, J., Xian, G., Jin, S., Dewitz, J., Homer, C., Yang, L., Barnes, C., Herold, N., & Wickham, J., 2011. Completion of the 2006 National Land Cover Database for the Conterminous United States. *Photogrammetric Engineering & Remote Sensing*, *77*(9), 858-864.

GARP (Global Atmospheric Research Programme). (1975). The physical basis of climate and climate modelling. In *GARP Publication Series No. 16*. Geneva, Switzerland: World Meteorological Organization.

Gassman, P.W., Reyes, M. R., Green, C. H., & Arnold, J. G. (2007). *The soil and water assessment tool: historical development, applications, and future research directions*. Ames, IA: Center for Agricultural and Rural Development, Iowa State University.

Gebetsroither, E., Johann Z., & Wolfgang L. (2013). *Drought in Alpine Areas Under Changing Climate Conditions*. In Cerbu, G. (Ed), *Management Strategies to Adapt Alpine Space Forests to Climate Change Risks*. InTechOpen. Retrieved from <http://www.intechopen.com/books/management-strategies-to-adapt-alpine-space-forests-to-climate-change-risks/drought-in-alpine-areas-under-changing-climate-conditions>.

Gesch, D.B., 2007. The National Elevation Dataset. In Maune, D. (Ed), *Digital Elevation Model Technologies and Applications: The DEM User's Manual* (99-118, 2nd ed). Bethesda, MD: American Society for Photogrammetry and Remote Sensing.

GFDL GAMDT (The GFDL Global Model Development Team). (2004). The new GFDL global atmospheric and land model AM2-LM2: Evaluation with prescribed SST simulations. *Journal of Climate*, *17*(24), 4641-4673.

Giorgi, F. (1990). Simulation of regional climate using a limited area model nested in a general circulation model. *Journal of Climate*, 3(9), 941-963.

Giorgi, F., & Mearns, L. O. (1991). Approaches to the simulation of regional climate change: a review. *Reviews of Geophysics*, *29*(2), 191-216.

Giorgi, F., Shields Brodeur, C., & Bates, G. T. (1994). Regional climate change scenarios over the United States produced with a nested regional climate model. *Journal of Climate, 7*(3), 375-399.

Glavan, M., White, S., & Holman, I. P. (2011). Evaluation of river water quality simulations at a daily time step–Experience with SWAT in the Axe Catchment, UK. *CLEAN–Soil, Air, Water*, *39*(1), 43-54.

Goolsby, D. A., Battaglin, W. A., Lawrence, G. B., Artz, R. S., Aulenbach, B. T., Hooper, R. P., ... & Stensland, G. J. (1999). Flux and sources of nutrients in the Mississippi-Atchafalaya River Basin. *White House Office of Science and Technology Policy Committee on Environmental and Natural Resources Hypoxia Work Group*. Washington, DC: U.S. Geological Survey, National Oceanic and Aeronautics Administration.

Goolsby, D. A. (2000). Mississippi basin nitrogen flux believed to cause Gulf hypoxia. *Eos, Transactions American Geophysical Union*, *81*(29), 321-327.

Goolsby, D. A., Battaglin, W. A., Aulenbach, B. T., & Hooper, R. P. (2001). Nitrogen input to the Gulf of Mexico. *Journal of Environmental Quality*, *30*(2), 329-336.

Gordon, C., Cooper, C., Senior, C. A., Banks, H., Gregory, J. M., Johns, T. C., Mitchell, J.F.B., & Wood, R. A. (2000). The simulation of SST, sea ice extents and ocean heat transports in a version of the Hadley Centre coupled model without flux adjustments. *Climate Dynamics*, 16(2-3), 147-168.

Govindaraju, R. S., & Rao, A. R. (2010). *Artificial neural networks in hydrology*. New York, NY: Springer Publishing Company, Inc.

Green, C. H., Tomer, M. D., Di Luzio, M., & Arnold, J. G. (2006). Hydrologic evaluation of the soil and water assessment tool for a large tile-drained watershed in Iowa. *Transactions of the ASABE*, *49*(2), 413-422.

Grotch, S. L., & MacCracken, M. C. (1991). The use of general circulation models to predict regional climatic change. *Journal of Climate*, *4*(3), 286-303.

HACH. (2011). *Nitratax UV Nitrate Sensor: Data Sheet*. Hach Company. Retrieved from <http://www.hach.com/asset-get.download.jsa?id=7639981839>.

Hagan, M. T., & Menhaj, M. B. (1994). Training feedforward networks with the Marquardt algorithm. *IEEE Transactions on Neural Networks*, *5*(6), 989-993.

Hagan, M. T., Demuth, H. B., & Beale, M. H. (1996). *Neural Network Design*. Boston, MA: PWS Publishing.

Harmel, D., Potter, S., Casebolt, P., Reckhow, K., Green, C. and Haney, R. (2006), Compilation of measured nutrient load data for agricultural land uses in the United States. *Journal of the American Water Resources Association*, *42*(5), 1163–1178.

Harmel, R. D., Smith, P. K., & Migliaccio, K. W. (2010). Modifying goodness-of-fit indicators to incorporate both measurement and model uncertainty in model calibration and validation. *Transactions of the ASABE*, *53*(1), 55-63.

Hassoun, M. H. (1995). *Fundamentals of artificial neural networks*. Cambridge, MA: MIT Press.

Hastie, T. J., & Tibshirani, R. J. (1990). *Generalized additive models*. Boca Raton, FL: CRC Press.

Hecht-Nielsen, R. (1989). Theory of the backpropagation neural network. In *Neural Networks, 1989, ICJNN International Joint Conference* (593-605). Washington, DC: Institute of Electrical and Electronics Engineers (IEEE).

Helsel, D.R., and Hirsch R.M., (2002). Statistical methods in water resources. (USGS Techniques of Water Resources Investigations, Book 4, Chapter A3). Washington, D.C.: U.S. Geological Survey. Retrieved from <http://water.usgs.gov/pubs/twri/twri4a3>.

Hendricks, N. P., Sinnathamby, S., Douglas-Mankin, K., Smith, A., Sumner, D. A., & Earnhart, D. H. (2014). The environmental effects of crop price increases: Nitrogen losses in the US Corn Belt. *Journal of Environmental Economics and Management*, *68*(3), 507-526.

Herzmann, D., Arritt, R., & Todey, D. (2013). *Iowa Environmental Mesonet*. Ames, IA: Department of Agronomy, Iowa State University. Data downloaded from <https://mesonet.agron.iastate.edu/>.

Hill, M. J. (1999). Nitrate toxicity: myth or reality? *British Journal of Nutrition*, *81*(05), 343-344.

Holland, P. W., & Welsch, R. E. (1977). Robust regression using iteratively reweighted least-squares. *Communications in Statistics-theory and Methods*, *6*(9), 813-827.

Hubbard, L., Kolpin, D. W., Kalkhoff, S. J., & Robertson, D. M. (2011). Nutrient and sediment concentrations and corresponding loads during the historic June 2008 flooding in eastern Iowa. *Journal of Environmental Quality*, *40*(1), 166-175.

Hornik, K., Stinchcombe, M., & White, H. (1989). Multilayer feedforward networks are universal approximators. *Neural Networks*, *2*(5), 359-366.

Hsu, K. L., Gupta, H. V., & Sorooshian, S. (1995). Artificial Neural Network Modeling of the Rainfall-Runoff Process. *Water Resources Research*, *31*(10), 2517-2530.

Iowa Department of Natural Resources (DNR). (2012.). *Natural Resources Geographic Information Systems Library*. Retrieved from <http://www.igsb.uiowa.edu/nrgislibx/>.

IPCC. (2007). *Climate Change 2007: The Physical Science Basis. Contribution of Working Group I to the Fourth Assessment Report of the Intergovernmental Panel on Climate Change* [Solomon, S., D. Qin, M. Manning, Z. Chen, M. Marquis, K.B. Averyt, M.Tignor and H.L. Miller (eds.)]. Cambridge University Press, Cambridge, United Kingdom and New York, NY, USA.

IPCC. (2012). *Managing the Risks of Extreme Events and Disasters to Advance Climate Change Adaptation*. A Special Report of Working Groups I and II of the Intergovernmental Panel on Climate Change [Field, C.B., V. Barros, T.F. Stocker, D. Qin, D.J. Dokken, K.L. Ebi, M.D. Mastrandrea, K.J. Mach, G.-K. Plattner, S.K. Allen, M. Tignor, and P.M. Midgley (eds.)]. Cambridge University Press, Cambridge, UK, and New York, NY, USA, 582 pp.

IPCC. (2013). *Climate change 2013: The physical science basis*. Cambridge, UK: Cambridge University Press.

Israelson, O.W. and West, F.L. (1922). Water holding capacity of irrigated soils. *Utah State Agricultural Experiment Station Bulletin 183* (1–24). Logan, Utah: Utah State University Press.

Jenson, S. K., & Domingue, J. O. (1988). Extracting topographic structure from digital elevation data for geographic information system analysis. *Photogrammetric Engineering and Remote Sensing*, *54*(11), 1593-1600.

Jha, M., Gassman, P. W., Secchi, S., Gu, R., & Arnold, J. (2004). Effect of watershed subdivision on SWAT flow, sediment, and nutrient predictions. *Journal of the American Water Resources Association, 40*(3), 811-825.

Jha, M. K., Gassman, P. W., & Panagopoulos, Y. (2015). Regional changes in nitrate loadings in the Upper Mississippi River Basin under predicted mid-century climate. *Regional Environmental Change, 15*(3), 449-460.

Karlen, D. L., Berry, E. C., Colvin, T. S., & Kanwar, R. S. (1991). Twelve-year tillage and crop rotation effects on yields and soil chemical properties in northeast Iowa. *Communications in Soil Science & Plant Analysis*, *22*(19-20), 1985-2003.

204

Katz, R. W. (2010). Statistics of extremes in climate change. *Climatic Change*, *100*(1), 71-76.

Kim, J. W., & Pachepsky, Y. A. (2010). Reconstructing missing daily precipitation data using regression trees and artificial neural networks for SWAT streamflow simulation. *Journal of Hydrology*, *394*(3), 305-314.

Knisel, W.G. (1980). *CREAMS, a field scale model for chemicals, runoff, and erosion from agricultural management systems* (USDA Conservation Research Report No. 26) Washington, DC: United States Department of Agriculture.

Krause, P., Boyle, D. P., & Bäse, F. (2005). Comparison of different efficiency criteria for hydrological model assessment. *Advances in Geosciences*, *2005*(5), 89-97.

Laprise, R. (2008). Regional climate modelling. *Journal of Computational Physics*, *227*(7), 3641-3666.

Lawrence, S., Giles, C. L., & Tsoi, A. C. (1997). Lessons in neural network training: Overfitting may be harder than expected. In *Proceedings of the Fourteenth National Conference on Artificial Intelligence* (540-545). Menlo Park, CA: AAAI.

Legates, D. R. & G. J. McCabe. (1999). Evaluating the use of "goodness-of-fit" measures in hydrologic and hydroclimatic model validation. *Water Resources Research, 35*(1), 233-241.

Leonard, R.A., Knisel, W.G., & Still, D.A. (1987). GLEAMS: Groundwater loading effects on agricultural management systems. *Transactions of the ASAE*, *30*(5), 1403-1428.

Liang, X., Lettenmaier, D. P., Wood, E. F., & Burges, S. J. (1994). A simple hydrologically based model of land surface water and energy fluxes for general circulation models. *Journal of Geophysical Research: Atmospheres* (1984–2012), *99*(D7), 14415-14428.

Lohr, S. (2009). *Sampling: design and analysis*. Boston, MA: Cengage Learning.

Loperfido, J. V. (2009). *High-frequency sensing of Clear Creek water quality: Mechanisms of dissolved oxygen and turbidity dynamics, and nutrient transport* (Doctoral dissertation). Retrieved from Iowa Research Online: The University of Iowa's Institutional Repository.

Lorenz, E. N. (1963). Deterministic nonperiodic flow. *Journal of the atmospheric sciences*, *20*(2), 130-141.

Maidment, D. R. (2002). *ArcHydro: GIS for water resources*. Redlands, CA: ESRI Press.

Manabe, S. (1969). Climate and the ocean circulation 1: I. The atmospheric circulation and the hydrology of the earth's surface. *Monthly Weather Review*, *97*(11), 739-774.

Manabe, S. & Wetherald, R.T. (1975). The effects of doubling CO_2 concentration on the climate of a general circulation model. *Journal of Atmospheric Sciences*, *32*(1), 3-15.

Manyika, J., Chui, M., Brown, B., Bughin, J., Dobbs, R., Roxburgh, C., & Byers, A. H. (2011). *Big data: The next frontier for innovation, competition, and productivity*. San Francisco, CA: Insights & Publications, McKinsey & Company.

Marquardt, D. W. (1963). An algorithm for least-squares estimation of nonlinear parameters. *Journal of the Society for Industrial & Applied Mathematics*, *11*(2), 431-441.

Martz, L. W., & Garbrecht, J. (1998). The treatment of flat areas and depressions in automated drainage analysis of raster digital elevation models. *Hydrological Processes*, 12(6), 843-85.

Matalas, N.C. (1967). Mathematical assessment of synthetic hydrology. *Water Resources Research, 3*(4), 937-945.

McElroy, A.D., Chiu, S.Y., Nebgen, J.W., Aleti, A., & Bennett, F.W. (1976*). Loading functions for assessment of water pollution from nonpoint sources* (EPA 600/2-76-151). Washington, DC: Environmental Protection Agency.

McKay, M. D., Beckman, R. J., & Conover, W. J. (1979). Comparison of three methods for selecting values of input variables in the analysis of output from a computer code. *Technometrics*, *21*(2), 239-245.

McCuen, R. H., Knight, Z., & Cutter, A. G. (2006). Evaluation of the Nash–Sutcliffe efficiency index. *Journal of Hydrologic Engineering*, *11*(6), 597-602.

McGregor, J. L. (1997). Regional climate modelling. *Meteorology and Atmospheric Physics, 63*(1-2), 105-117.

McGuffie, K., & Henderson-Sellers, A. (2005). *A climate modelling primer*. New York, NY: John Wiley & Sons.

Mearns, L. O., Bogardi, I., Giorgi, F., Matyasovszky, I., & Palecki, M. (1999). Comparison of climate change scenarios generated from regional climate model experiments and statistical downscaling. *Journal of Geophysical* Research*: Atmospheres (1984–2012)*, *104*(D6), 6603-6621.

Mearns, L. O., Gutowski, W. J., Jones, R., Leung, L. Y., McGinnis, S., Nunes, A. M. B., & Qian, Y. (2007, updated 2013). *The North American regional climate change assessment program dataset*. Boulder, CO: National Center for Atmospheric Research Earth System Grid Data Portal. Data downloaded from <http://www.narccap.ucar.edu/>.

Mearns, L. O., W. J. Gutowski, R. Jones, L.-Y. Leung, S. McGinnis, A. M. B. Nunes, and Y. Qian. (2014). *Atmosphere-Ocean General Circulation Models (AOGCMS).* Retrieved from <http://www.narccap.ucar.edu/about/aogcms.html>.

Menzel, R.G. (1980). Enrichment ratios for water quality modeling. In *CREAMS: a field scale model for chemicals, runoff, and erosion from agricultural management systems* (USDA Conservation Res. Rept. No. 26). Washington, DC: U.S. Department of Agriculture.

Miller, D. A., & White, R. A. (1998). A conterminous United States multilayer soil characteristics dataset for regional climate and hydrology modeling. *Earth Interactions*, *2*(2), 1-2.

Monteith, J. L. (1965). Evaporation and environment. In *Symposia of the Society of Experimental Biology, 19*(205-23), 4.

Moriasi, D. N., Arnold, J. G., Van Liew, M. W., Bingner, R. L., Harmel, R. D., & Veith, T. L. (2007). Model evaluation guidelines for systematic quantification of accuracy in watershed simulations. *Transactions of the ASABE*, *50*(3), 885-900.

Moriasi, D. N., Rossi, C. G., Arnold, J. G., & Tomer, M. D. (2012). Evaluating hydrology of the Soil and Water Assessment Tool (SWAT) with new tile drain equations. *Journal of soil and water conservation*, *67*(6), 513-524.

Najafi, M. R., & Moradkhani, H. (2014). A hierarchical Bayesian approach for the analysis of climate change impact on runoff extremes. *Hydrological Processes*, *28*(26), 6292-6308.

Nakicenovic, N., & Swart, R. (2000). *IPCC Special Report on Emissions Scenarios*. Cambridge, UK: Cambridge University Press.

Nassauer, J. I., Corry, R. C., & Cruse, R. M. (2007). Alternative scenarios for future Iowa agricultural landscapes. In *From the Corn Belt to the Gulf: Societal and Environmental Implications of Alternative Agricultural Futures* (41-55). Washington, DC: RFF Press.

Nassauer, J.I., et al. (2011). Iowa farmers' responses to transformative scenarios for Corn Belt agriculture. *Journal of Soil and Water Conservation*, *66*(1),18A-24A.

National Oceanic and Atmospheric Administration (NOAA). (2012*). A model based on ocean and atmosphere interactions*. Retrieved from <http://celebrating200years.noaa.gov/breakthroughs/climate_model>

Neitsch, S. L., Arnold, J.G., Kiniry, J.R., Wiliams, J.R. (2011). *Soil and Water Assessment Tool: Theoretical Documentation*. College Station, TX: Texas Water Resources Institute.

Nourani, V., Baghanam, A. H., & Gebremichael, M. (2012). Investigating the Ability of Artificial Neural Network (ANN) Models to Estimate Missing Rain-gauge Data. *Journal of Environmental Informatics*, *19*(1), 38-50.

Ocampo, C. J., Oldham, C. E., & Sivapalan, M. (2006). Nitrate attenuation in agricultural catchments: Shifting balances between transport and reaction. *Water Resources Research*, *42*(1).

Page, B., & Walker, R. (1991). From settlement to Fordism: the agro-industrial revolution in the American Midwest. *Economic Geography*, *67*(4), 281-315.

Pai, N., & D. Saraswat. 2011. SWAT2009 LUC: a tool to activate land use change module in SWAT 2009. *Transactions of the ASABE*. 54(5), 1649-1658.

Patterson, D. W. (1998). *Artificial neural networks: theory and applications*. Saddle River, NJ: Prentice Hall.

Pellerin, B.A., Bergamaschi, B.A., Downing, B.D., Saraceno, J.F., Garrett, J.A., & Olsen, L.D., (2013). *Optical techniques for the determination of nitrate in environmental waters: Guidelines for instrument selection, operation, deployment, maintenance, qualityassurance, and data reporting.* (USGS TM 1–D5). Washington DC: U.S. Geological Survey. Retrieved from <http://pubs.usgs.gov/tm/01/d5/pdf/tm1d5.pdf>.

Pellerin, B. A., Bergamaschi, B. A., Gilliom, R. J., Crawford, C. G., Saraceno, J., Frederick, C. P., ... & Murphy, J. C. (2014). Mississippi river nitrate loads from high frequency sensor

measurements and regression-based load estimation. *Environmental Science & Technology*, *48*(21), 12612-12619.

Perry, J. S. (1975). The Global Atmospheric Research Program. *Reviews of Geophysics 13*(3), 661-667.

Peterson, B. J., Wollheim, W. M., Mulholland, P. J., Webster, J. R., Meyer, J. L., Tank, J. L., ... & Morrall, D. D. (2001). Control of nitrogen export from watersheds by headwater streams. *Science*, *292*(5514), 86-90.

Phillips, N. A. (1956). The general circulation of the atmosphere: A numerical experiment. *Quarterly Journal of the Royal Meteorological Society, 82*(352), 123-164.

Ponce, V. M., & Hawkins, R. H. (1996). Runoff curve number: Has it reached maturity? *Journal of Hydrologic Engineering*, *1*(1), 11-19.

Press, W.H., Flannery, B.P., Teukolsky, S.A., Vetterling, W.T., (1992). *Numerical Recipe: The Art of Scientific Computation* (2nd ed). Cambridge, UK: Cambridge University Press.

Putney, M.K. (2010). *Using high frequency data collection to study nitrate on clear creek during high flow events* (Master's thesis). Retrieved from Iowa Research Online: The University of Iowa's Institutional Repository.

Richardson, C.W. (1981). Stochastic simulation of daily precipitation, temperature, and solar radiation. *Water Resources Research, 17*(1), 182-190.

Rosenzweig, C., Tubiello, F. N., Goldberg, R., Mills, E., & Bloomfield, J. (2002). Increased crop damage in the US from excess precipitation under climate change. *Global Environmental Change*, 12(3), 197-202.

Ross, E. D. (1951). *Iowa agriculture: an historical survey*. Des Moines, IA: State Historical Society of Iowa.

Rubin, D. B. (1976). Inference and missing data. *Biometrika*, *63*(3), 581-592.

Runkel, R.L., Crawford, C.G., and Cohn, T.A. (2004). *Load Estimator (LOADEST): A FORTRAN program for estimating constituent loads in streams and rivers.* (USGS Survey Techniques and Methods 4-A5). Washington, DC: U.S. Geological Survey

Ruppert, D., & Carroll, R. J. (1999). *Penalized regression splines*. Ithaca, NY: Cornell University Operations Research and Industrial Engineering.

Saltelli, A., Chan, K., & Scott, E. M. (Eds.). (2000). *Sensitivity analysis* (Vol. 134). New York, NY: John Wiley & Sons.

Santelmann, M. V., White, D., Freemark, K., Nassauer, J. I., Eilers, J. M., Vache, K. B., ... & Debinski, D. (2004). Assessing alternative futures for agriculture in Iowa, USA. *Landscape Ecology*, *19*(4), 357-374.

Sarle, W. S. (1995). Stopped training and other remedies for overfitting. In *Proceedings of the 27th Symposium on the Interface of Computing Science and Statistics.* (352-360). Fairfax, VA: Interface Foundation of North America.

Schilling, K. E., Jha, M. K., Zhang, Y. K., Gassman, P. W., & Wolter, C. F. (2008). Impact of land use and land cover change on the water balance of a large agricultural watershed: Historical effects and future directions. *Water Resources Research*, *44*(7).

Schmidli, J., Frei, C., & Vidale, P. L. (2006). Downscaling from GCM precipitation: a benchmark for dynamical and statistical downscaling methods. *International Journal of Climatology*, *26*(5), 679-689.

Seligamnd, N.G. & H., van Keulen. (1981). PAPRAN: a simulation model of annual pasture production limited by rainfall and nitrogen. In Frissel, M.J. and van Veeds, J.A. (Eds), *Simlulation of nitrogen behavior of soil-plant systems: papers of a workshop, Models for the behaviour of nitrogen in soil and uptake by plant, comparison between different approaches* (192-221). Wageningen, Netherlands: Centre for Agricultural Publishing and Documentation.

Sellers, W. D. (1969). A global climatic model based on the energy balance of the earth-atmosphere system. *Journal of Applied Meteorology*, *8*(3), 392-400.

Sellers, P. J., Mintz, Y. C. S. Y., Sud, Y. E. A., & Dalcher, A. (1986). A simple biosphere model (SiB) for use within general circulation models. *Journal of the Atmospheric Sciences, 43*(6), 505-531.

Seneviratne, S. I. (2012). Climate science: Historical drought trends revisited. *Nature, 491*(7424), 338-339.

Sharpley, A.N. & Williams, J.R (Eds). (1990). *EPIC-Erosion Productivity Impact Calculator, 1. model documentation.* (USDA ARS Technical Bulletin 1768). Washington, DC: Agricultural Research Service, U.S. Department of Agriculture.

Shine, K. P., & Henderson-Sellers, A. (1983). Modelling climate and the nature of climate models: a review. *Journal of Climatology*, 3(1), 81-94.

Sloan, P.G. & Moore, I.D. (1984). Modeling subsurface stormflow on steeply sloping forested watersheds. *Water Resources Research*. 20(12), 1815-1822.

Smedema, L.K. & Rycroft, D.W. (1983*). Land drainage—planning and design of agricultural drainage systems*. Ithaca, NY: Cornell University Press.

Soil Survey Staff (n.d.). *Web Soil Survey*. Washington, DC: Natural Resources Conservation Service, United States Department of Agriculture. Retrieved from <http://websoilsurvey.nrcs.usda.gov/>

Soil Survey Staff (1993). *Soil survey manual* (63–65). Washington, DC: Natural Resources Conservation Service, United States Department of Agriculture. Retrieved from <http://www.nrcs.usda.gov/wps/portal/nrcs/detail/national/nedc/training/soil/?cid=nrcs142p2054262>

Solomatine, D., & Ostfeld, A. (2008). Data-driven modelling: some past experiences and new approaches. *Journal of Hydroinformatics*, *10*(1), 3-22.

Tebaldi, C., & Knutti, R. (2007). The use of the multi-model ensemble in probabilistic climate projections. *Philosophical Transactions of the Royal Society A: Mathematical, Physical and Engineering Sciences*, *365*(1857), 2053-2075.

Teutschbein, C., & Seibert, J. (2012). Bias correction of regional climate model simulations for hydrological climate-change impact studies: Review and evaluation of different methods. *Journal of Hydrology*, *456*, 12-29.

Throne, M. (1949). Southern Iowa Agriculture, 1833-1890: The Progress from Subsistence to Commercial Corn-Belt Farming. *Agricultural History*, *23*(2), 124-130.

U.S. Army Corps of Engineers (USACE), Rock Island District. (2013). Appendix D: Alternative Landscape Scenarios. In *Conservation Reserve Program Flood Damage Reduction Benefits to Downstream Urban Areas*. Retrieved from <http://www.fsa.usda.gov/Internet/FSA_File/fsa_pilot_report_final.pdf>

U.S. Geological Survey (USGS). (2013). *National Elevation Dataset*. Data downloaded from <http://ned.usgs.gov>

U.S. Department of Agriculture (USDA). (1985). *SCS National engineering Handbook. Section 4: Hydrology.* Washington DC: Soil Conservation Service.

U.S. Department of Agriculture (USDA). (2002). *National Soil Survey Handbook, Title 430-VI.* Washington, DC: Natural Resources Conservation Service. Retrieved from <http://soils.usda.gov/technical/handbook/>

U.S. Department of Agriculture (USDA). (2010a). *Usual Planning and Harvesting Dates for U.S. Field Crops (October 2010)*. Washington DC: National Agricultural Statistics Service. Retrieved from <http://usda01.library.cornell.edu/usda/current/planting/planting-10-29-2010.pdf>

U.S. Department of Agriculture (USDA). (2010b). *US Climatic Data*. Washington, DC: Agricultural Research Service. Data downloaded from <http://ars.usda.gov/Research/docs.htm?docid=19388>

U.S. Department of Agriculture (USDA). (2012). *Crop Data Layer*. Washington, DC: National Agricultural Statistics Service. Data downloaded from <http://nassgeodata.gmu.edu/CropScape/>

U.S. Department of Agriculture (USDA). (2014). *2012 Census of Agriculture: Preliminary Report: U.S. and State Data.* Washington, DC: National Agricultural Statistics Service, Retrieved from <http://www.agcensus.usda.gov/Publications/2012/Preliminary_Report/Full_Report.pdf>

Vaché, K. B., Eilers, J. M., & Santelmann, M. V. (2002). Water Quality Modeling of Alternative Agricultural Scenarios in the US Corn Belt. *Journal of the American Water Resources Association*, *38*(3), 773-787.

Veihmeyer, F.J. and Hendrickson, A.H. (1928). Soil moisture at permanent wilting of plants. *Plant Physiology, 3*(3), 355–357.

White, K. L., & Chaubey, I. (2005). Sensitivity analysis, calibration, and validations for a multisite and multivariable SWAT model. *Journal of the American Water Resources Association*, *41*(5), 1077-1089.

Whittaker, G., Confesor, R., Di Luzio, M., & Arnold, J. G. (2010). Detection of overparameterization and overfitting in an automatic calibration of SWAT. *Transactions of the ASABE*, *53*(5), 1487-1499.

Williams, J.R. (1969). Flood routing with variable travel time or variable storage coefficients. *Transactions of the ASAE*, *12*(1), 100-103.

Williams, J.R., Jones, C.A., Dyke, P.T. (1984). A modeling approach to determining the relationship between erosion and soil productivity. *Transactions of the ASAE*, *27*(1), 129-144.

Williams, J.R., Nicks, A.D., Arnold, J.G. (1985). Simulator for water resources in rural basins. *Journal of Hydraulic Engineering*, *111*(6), 970-986

Winchell, M., Srinivasan, R., DiLuzio, M., & Arnold, J. (2009*). ArcSWAT 2.3.4 Interface for SWAT2005: User's Guide.* Temple, TX: Blackland Research Center.

Wood, S. N., & Augustin, N. H. (2002). GAMs with integrated model selection using penalized regression splines and applications to environmental modelling. *Ecological Modelling*, *157*(2), 157-177.

Wood, S. N. (2013). On p-values for smooth components of an extended generalized additive model. *Biometrika*, *100*(1), 221-228.

Wu, X., Kumar, V., Quinlan, J. R., Ghosh, J., Yang, Q., Motoda, H., ... & Steinberg, D. (2008). Top 10 algorithms in data mining. *Knowledge and Information Systems*, *14*(1), 1-37.

Wu, Y., & Liu, S. (2014). Improvement of the R-SWAT-FME framework to support multiple variables and multi-objective functions. *Science of the Total Environment*, *466*, 455-466.

Yapo, P. O., Gupta, H. V., & Sorooshian, S. (1996). Automatic calibration of conceptual rainfall-runoff models: sensitivity to calibration data. *Journal of Hydrology*, *181*(1), 23-48.

Yu, H., & Wilamowski, B. M. (2011). Levenberg-marquardt training. In Wilamowski B.M. & Irvin, J.D. (Eds), *Industrial Electronics Handbook*, *5*(12), 1-16.

Yaeger, M.A., Housh, M., Cai, X., Sivapalan, M. (2014). An integrated modeling framework for exploring flow regime and water quality changes with increasing biofuel crop production in the U.S. Corn Belt, *Water Resources Research*, *50*(12), 9385-9404

211